NBSIR 75-810

SEMI-ANNUAL REPORT ON MATERIALS RESEARCH IN SUPPORT OF SUPERCONDUCTING MACHINERY

R. P. Reed, J. G. Hust, M. B. Kasen, H. M. Ledbetter,
R. P. Mikesell, R. E. Schramm, L. L. Sparks, R. L. Tobler,
and W. F. Weston

Cryogenics Division
Institute for Basic Standards
National Bureau of Standards
Boulder, Colorado 80302

April 1975

Prepared for
Advanced Research Projects Agency
1400 Wilson Boulevard
Arlington, Virginia 22209

NBSIR 75-810

SEMI-ANNUAL REPORT ON MATERIALS RESEARCH IN SUPPORT OF SUPERCONDUCTING MACHINERY

R. P. Reed, J. G. Hust, M. B. Kasen, H. M. Ledbetter,
R. P. Mikesell, R. E. Schramm, L. L. Sparks, R. L. Tobler,
and W. F. Weston

Cryogenics Division
Institute for Basic Sandards
National Bureau of Standards
Boulder, Colorado 80302

April 1975

Prepared for
Advanced Research Projects Agency
1400 Wilson Boulevard
Arlington, Virginia 22209

U.S. DEPARTMENT OF COMMERCE, Frederick B. Dent, Secretary

NATIONAL BUREAU OF STANDARDS Richard W. Roberts, Director

SEMI-ANNUAL REPORT ON MATERIALS RESEARCH

IN SUPPORT OF SUPERCONDUCTING MACHINERY

Sponsored by
Advanced Research Projects Agency
ARPA Order No. 2569
Program Code 4D10
August 10, 1974 - August 9, 1975

Program Director
Dr. E. C. van Reuth
Materials Sciences
Advanced Research Projects Agency
1400 Wilson Boulevard
Arlington, Virginia 22209

Program Manager
Dr. R. P. Reed
Cryogenics Division
Institute for Basic Standards
National Bureau of Standards
Boulder, Colorado 80302

Abstract

Results of six months of study on materials in support of superconducting machinery (October 1974 through March 1975) are reported to the sponsor, the Advanced Research Projects Agency of the U.S. Department of Defense. The report is divided into five sections: Thermal conductivity, magnetothermal conductivity, fatigue and fracture-toughness properties, properties of advanced composites, and elastic properties. The temperature range 4 to 300 K is covered by the study. Materials studied are either being used or are candidates for use in superconducting machinery and include: aluminum alloys, composites, copper, age-hardened nickel-base superalloys, stainless steels, and titanium alloys.

Special results of the study include: thermal conductivity data for comparison of the effects of heat treatment on age-hardenable alloys, the first determination of a complete set of elastic constants for a composite at liquid helium temperature, boron-aluminum composite tensile data at 4 K, and a summary of fatigue crack-growth rate behavior at 4 K for a number of different structural alloys. These data provide considerable insight into material characteristics at extremely low temperatures, assisting in material selection and efficient design.

Keywords: Composites; elastic properties; fracture; liquid helium; mechanical properties; structural materials; superconducting machinery; thermal conductivity.

Report Contents

Page

THERMAL CONDUCTIVITY
J. G. Hust 1

MAGNETOTHERMAL CONDUCTIVITY
L. L. Sparks 11

FATIGUE AND FRACTURE-TOUGHNESS TESTING AT CRYOGENIC TEMPERATURES
R. L. Tobler, R. P. Mikesell, R. L. Durcholz, and R. P. Reed 23

Fracture Testing and Results for a Ti-6Al-4V Alloy at Liquid Helium Temperature
C. W. Fowlkes and R. L. Tobler 25

Fatigue Crack Growth and J-Integral Fracture Parameters of Ti-6Al-4V at Ambient and Cryogenic Temperatures
R. L. Tobler 56

Fatigue Crack Growth Rates of Structural Alloys at Four Kelvin
R. L. Tobler and R. P. Reed 87

The Fracture Toughness and Fatigue Crack Growth Rate of an Fe-Ni-Cr Superalloy at 298, 76 and 4 K
R. P. Reed, R. L. Tobler, and R. P. Mikesell 105

ADVANCED COMPOSITES
R. E. Schramm and M. B. Kasen 123

ELASTIC PROPERTIES OF ENGINEERING MATERIALS AT CRYOGENIC TEMPERATURES
H. M. Ledbetter and W. F. Weston 149

Low-Temperature Elastic Constants of a Superconducting Coil Composite
W. F. Weston 151

Iron-Molybdenum Alloy
W. F. Weston and H. M. Ledbetter 184

Disclaimer

Tradenames of equipment and materials are used in this report for clarity and to conform with standard usage in the scientific and engineering literature. Selection of materials for discussion and examination with regard to application in superconducting machinery is based on properties reported in the literature, and must be regarded as preliminary and tentative. In no case does such selection imply recommendation or endorsement by the National Bureau of Standards, nor does it imply that the material or equipment is necessarily the best available for the purpose.

NBSIR

Semi-Annual Report on Materials Research in Support of Superconducting Machinery

Thermal Conductivity

J. G. Hust

Cryogenics Division
Institute for Basic Standards
National Bureau of Standards
Boulder, Colorado 80302

April 1975

Summary: Thermal Conductivity

Thermal conductivity, electrical resistivity, thermopower, and Lorenz ratio data are reported for Inconel X-750 STDA. These data are compared to the previously reported data for Inconel X-750 ST. Data are presented in tabular and graphical form.

Contents: Thermal Conductivity

		Page
1.	Introduction	3
2.	Apparatus	3
3.	Specimen Characterization	4
4.	Results and Discussion	4
5.	Acknowledgements	4
6.	References	4
	List of Figures	5
	List of Tables	5

THERMAL CONDUCTIVITY

J. G. Hust

1. Introduction

Optimum design of superconducting machinery requires a knowledge of thermal properties of technically important materials at low temperatures. But often, components extend from ambient temperatures to low temperatures, and therefore, data are needed from 4 K to 300 K. Thermal conductivity of metals is a function of the host metal and its constituent elements and temperature. It also depends on the microstructure of the material, strain, fatigue, and heat treatment; and in some cases environmental effects are important (e.g., in the case of superconducting machinery, magnetic field intensities may produce significant changes). Thermal conductivity data for particular components are required to limit heat losses and thermal stresses in machines. With such a myriad of parameters it is difficult (at best) to determine accurately, by experiment, the thermal conductivity of each machine component. Instead, we often rely on a limited number of measurements on specific types of materials, characterized according to the above parameters. Due to material variability effects, these values are generally considered accurate to only about 10%.

It should be noted that accurate thermal conductivity measurements are much more expensive and time consuming relative to many other property measurements. The ease with which high accuracy can be obtained is primarily a function of temperature and the conductivity itself. The extremes of conductivity (both very high, such as in pure metals, and very low, such as in insulating materials) promote inaccuracies in measurement. Generally, low temperature data (below about 100 K) are more readily obtained with accuracy because radiation errors can be minimized.

For the above reasons, various methods of obtaining thermal conductivity data are used. The method used depends primarily on the accuracy dictated by the application. Usually accuracies of 10% are sufficient; in other cases values accurate to 50% suffice. The present state-of-the-art in thermal conductivity measurements is about 1% accuracy, but seldom is this required, except in theoretical or standardization work.

In this laboratory three methods of data determination are used:

(a) A variable-temperature apparatus, capable of measuring at any temperature from 4 to 300 K with an accuracy of about 2%. This is a multi-property apparatus used to simultaneously measure thermal conductivity, electrical resistivity, and thermopower at temperatures between 4 and 300 K. It is based on the longitudinal heat flow method. This apparatus will be used to measure materials that have not been sufficiently measured and characterized previously and for accurate temperature dependence determinations.

(b) A fixed point apparatus, capable of measuring only near the fixed temperatures of various boiling fluids (such as liquid helium and liquid nitrogen) and melting or subliming solids (such as ice and CO_2). The accuracy of this apparatus is about 10%, depending mainly on the conductivity of the specimen.

(c) Predictive methods such as those described by Hust and Clark [1] and Hust and Sparks [2]. The latter paper also contains data for many metals and alloys, necessary to carry out such predictions.

2. Apparatus

The variable-temperature apparatus was used for the measurements reported for Inconel* X-750 STDA. The specimen is a rod 23 cm long, with a diameter up to 3 cm depending on its conductivity. The top of the specimen is thermally connected to a temperature-controlled floating sink, and the gradient heater is connected at the bottom of the specimen. The specimen is surrounded with insulation and a temperature-controlled concentric shield. The longitudinal temperature distribution of the shield is adjusted to match that of the specimen. Eight equally spaced thermocouples are attached to the specimen to determine its longitudinal temperature distribution. These thermocouples are calibrated in-place

* Inconel is a tradename of International Nickel Corporation.

using accurately calibrated platinum and germanium resistance thermometers. Further details of this apparatus are documented in an unpublished NBS report available from Hust. A schematic diagram of the cryostat is shown in a previous semi-annual report to ARPA [3].

3. Specimen Characterization

The material investigated is Inconel X-750 STDA. This specimen is a heat treatment variation from the previously measured X-750 ST reported in the last ARPA report [4]. The STDA heat treatment is: ST (1800°F for one hour - air cooled) + 1350°F for eight hours - furnace cooled to 1150°F - hold for eight hours - air cooled. The Rockwell hardness and grain size of the STDA form are C-36 and 0.12 mm. This specimen was measured to determine the effect of heat treatments on the X-750 alloy. Very little is known about these effects on such alloys and the latest data will be helpful in predicting the effect on similar alloys.

This material was measured in the form of a 11.3 mm diameter machined rod, 23 cm long. The heat treatment was performed prior to the machining.

4. Results and Discussion

Measurements were performed using an ice bath, a liquid nitrogen bath, and a liquid helium bath. Usually a large number of runs (20-30) are taken to precisely define the thermal conductivity, electrical resistivity, and thermopower curves at temperatures from 4 to 300 K. However, in this case, because of the similarity of this specimen to the X-750 ST specimen, only a few runs (6) were performed. These runs were set up to match the conditions of the runs performed on the ST specimen to expedite data intercomparisons. The resultant experimental data were compared to the X-750 ST data and accurate property differences were calculated. From these differences and the results reported for X-750 ST we obtained data for X-750 STDA. These results are listed in Table 1 and illustrated in Figures 1, 2, 3, and 4. The data for X-750 ST are also shown in the figures for convenient comparison.

It is noted that thermal conductivity is affected very little by the STDA heat treatment. The relative effect is larger at low temperatures. Electrical resistivity has changed by about 4% over the entire temperature range. However, it is noted that while thermal conductivity decreased, electrical conductivity (reciprocal of electrical resistivity) increased. This is contrary to expectations but has been observed earlier on a similar alloy, Inconel 718. Because of this contradictory behavior, Lorenz ratio values are not useful for prediction of heat treatment effects in these alloys. Figure 3 shows that Lorenz ratio differences are larger than either thermal conductivity or electrical resistivity differences. For thermal conductivity predictions based on Lorenz ratio to be accurate, the opposite must be true.

5. Acknowledgements

I express appreciation to Joe Wells of Westinghouse Research Laboratories, Pittsburgh, Pennsylvania for supplying the Inconel X-750 STDA material.

6. References

1. Hust, J. G. and Clark, A. F., The Lorenz ratio as a tool for predicting the thermal conductivity of metals and alloys, Materials Research and Standards 11, (No. 8), 22-4 (Aug. 1971).

2. Hust, J. G. and Sparks, L. L., Lorenz ratios of technically important metals and alloys, Nat. Bur. Stand. (U.S.) Tech. Note 634, (Feb. 1973) 133 pp.

3. Hust, J. G. and Giarratano, P. J., Semi-annual report on materials research in support of superconducting machinery, pp. 29-43, Unpublished NBS report.

4. Hust, J. G. and Giarratano, P. J., Semi-annual report on materials research in support of superconducting machinery, pp. 1-35, Unpublished NBS report.

List of Figures

Figure — Page

1. Thermal conductivity of Inconel X-750 STDA compared to previously reported data for X-750 6

2. Electrical resistivity of Inconel X-750 STDA compared to previously reported data for X-750 ST 7

3. Lorenz ratio of Inconel X-750 STDA compared to previously reported data for X-750 ST 8

4. Thermopower of Inconel X-750 STDA compared to previously reported data for X-750 ST 9

List of Tables

Table — Page

1. Thermal and electrical properties of Inconel X-750 STDA as calculated by comparing six experimental runs to similar runs for X-750 ST 10

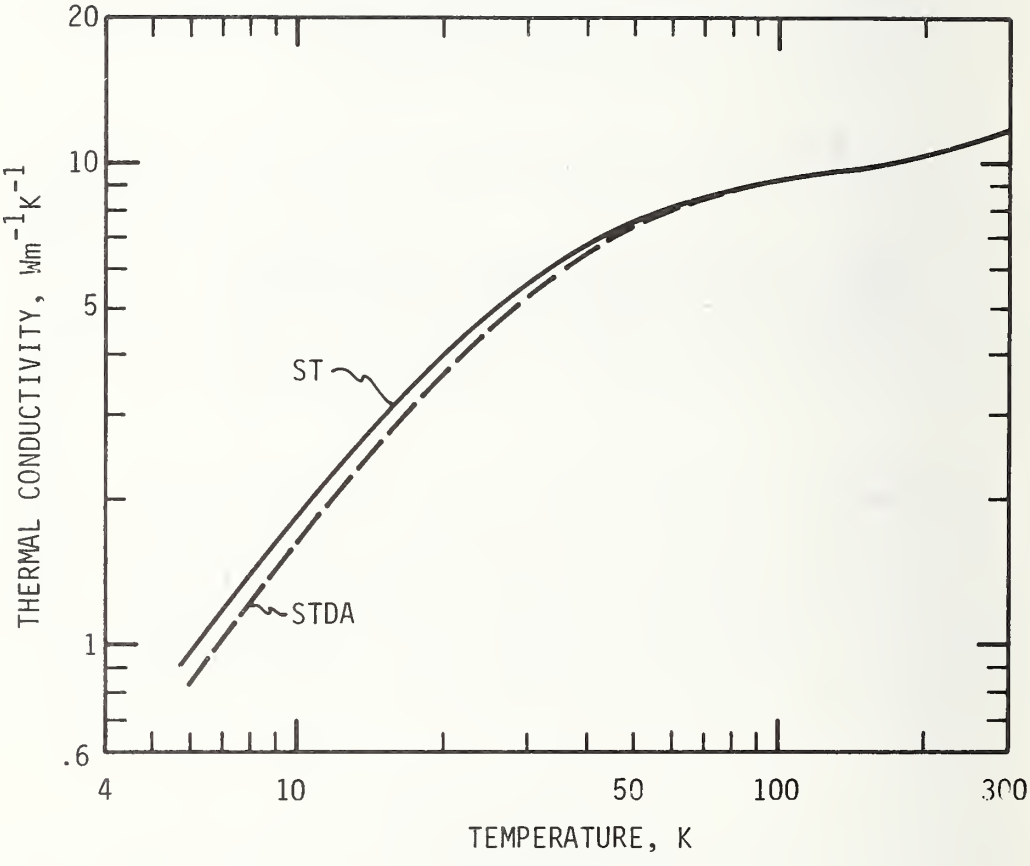

FIGURE 1. Thermal conductivity of Inconel X-750 STDA compared to previously reported data for X-750 ST.

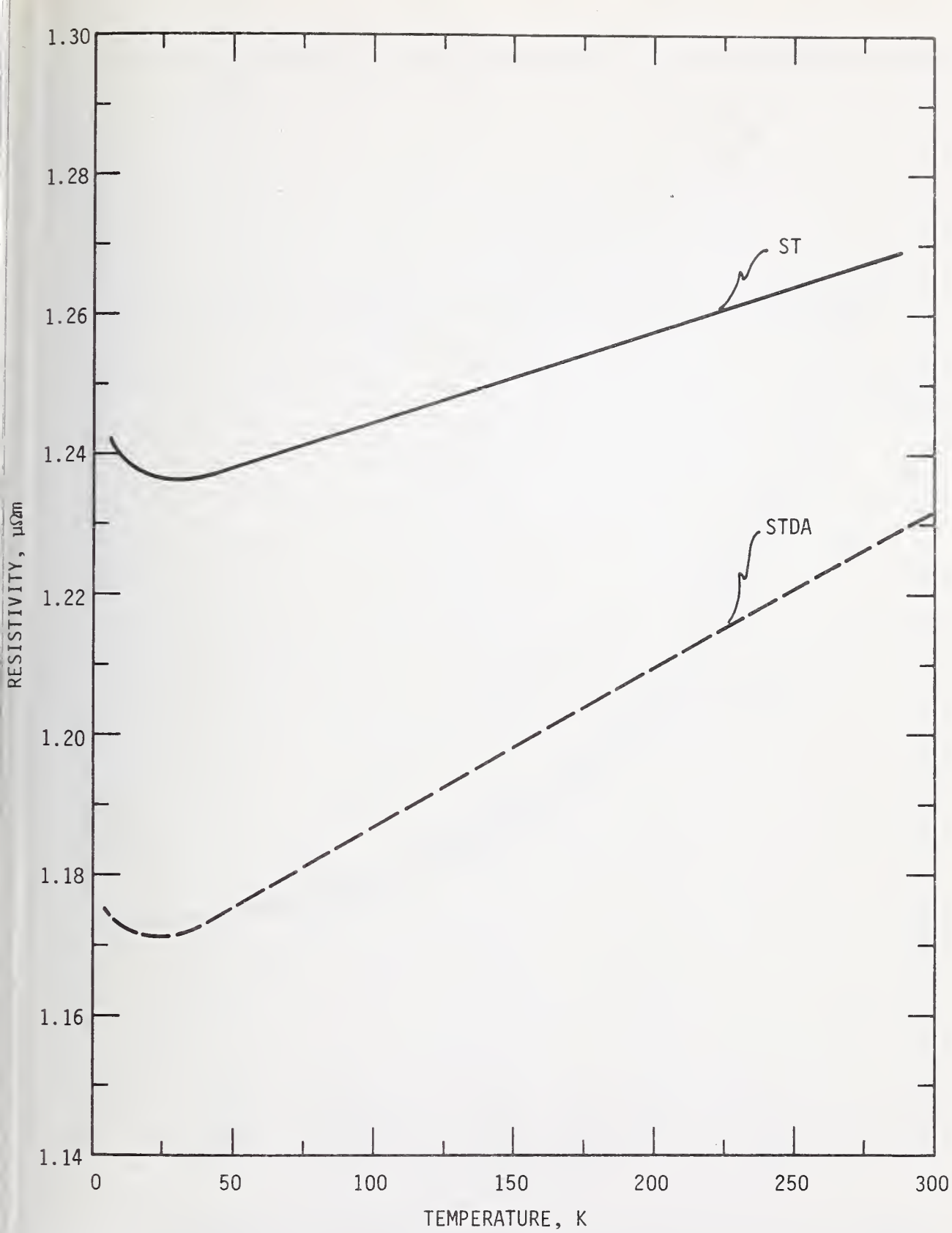

FIGURE 2. Electrical resistivity of Inconel X-750 STDA compared to previously reported data for X-750 ST.

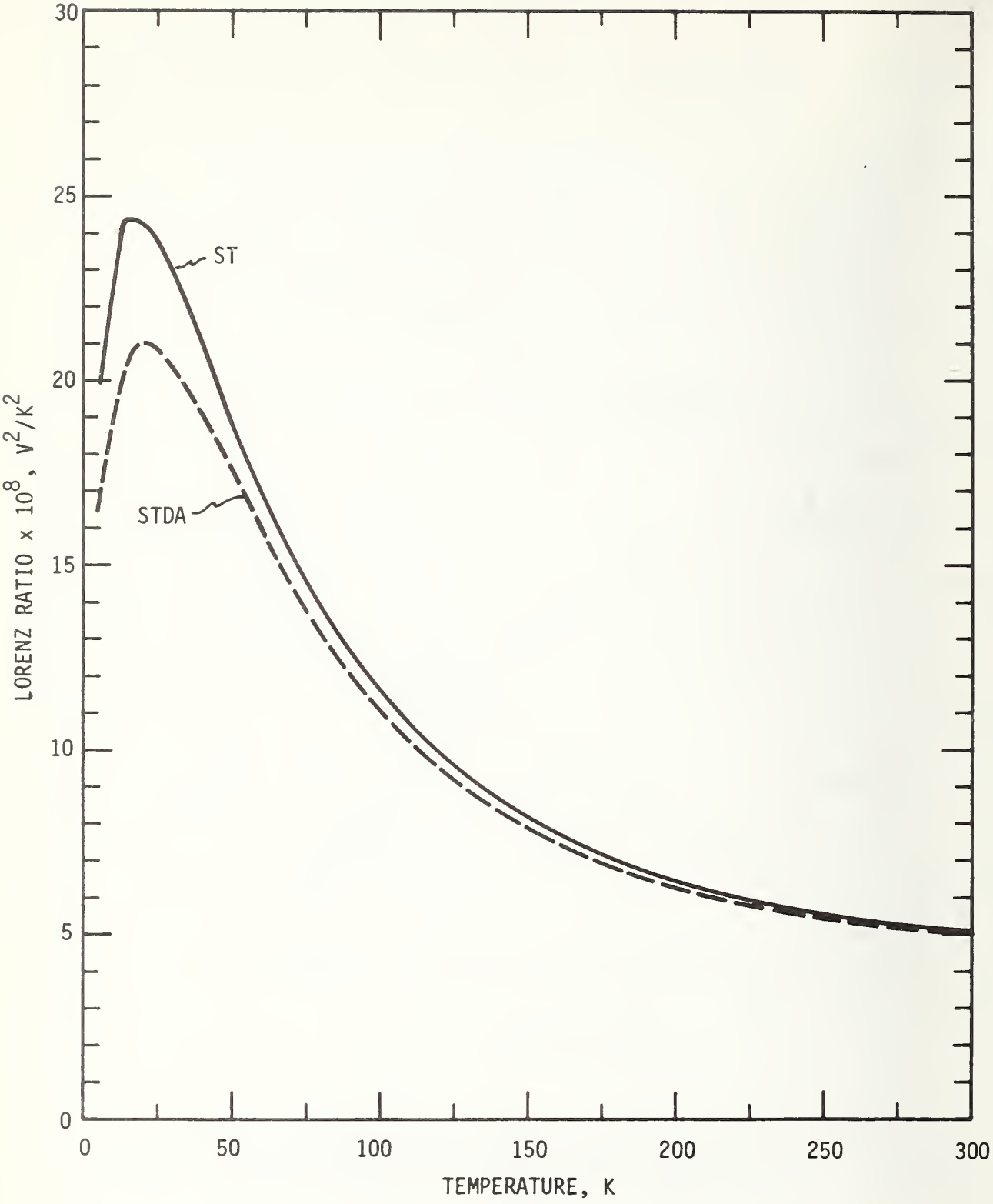

FIGURE 3. Lorenz ratio of Inconel X-750 STDA compared to previously reported data for X-750 ST.

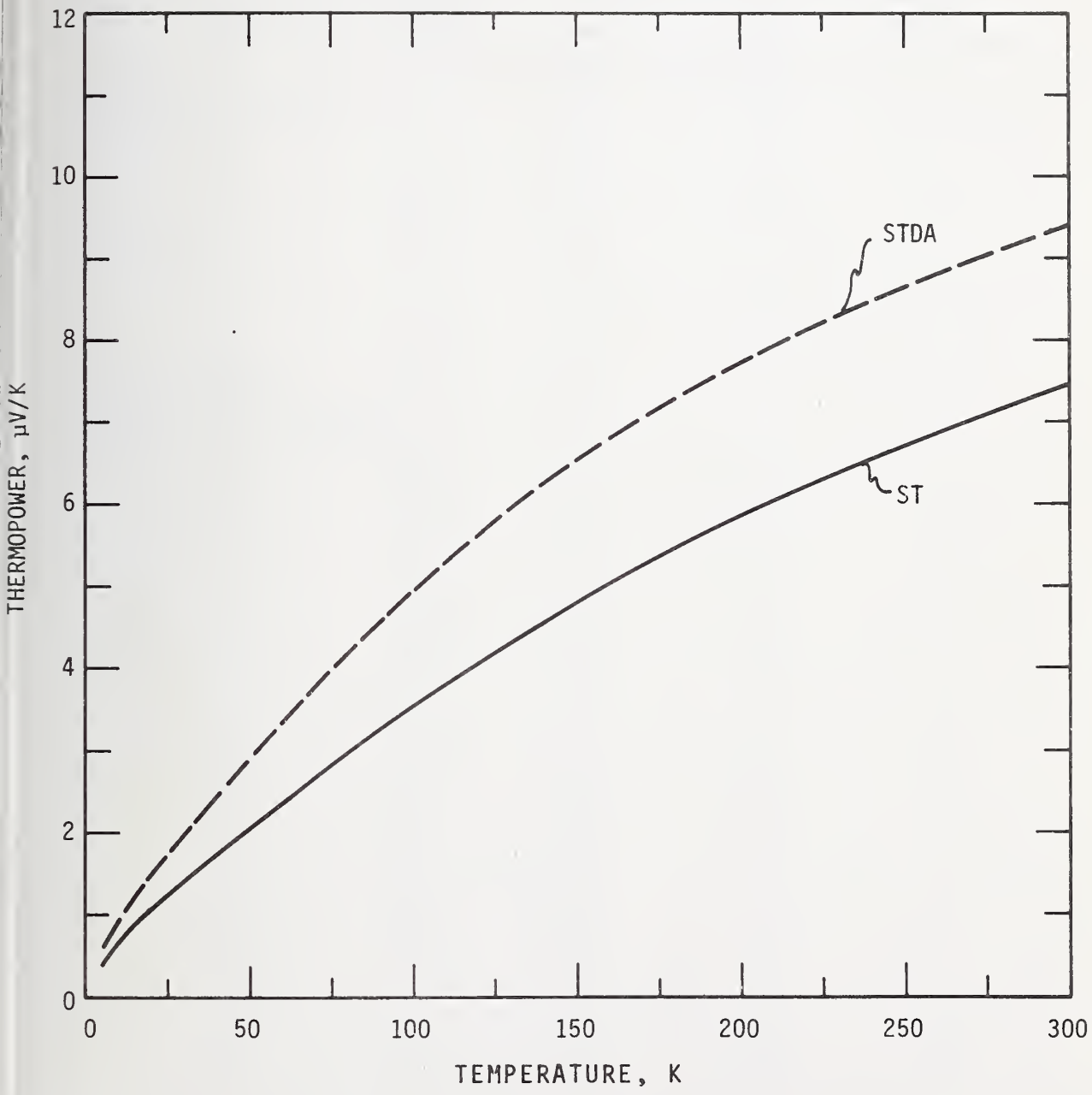

FIGURE 4. Thermopower of Inconel X-750 STDA compared to previously reported data for X-750 ST.

Table 1. - Thermal and electrical properties of Inconel X-750 STDA as calculated by comparing six experimental runs to similar runs for X-750 ST.

Temperature (K)	λ $Wm^{-1}K^{-1}$	ρ $n\Omega m$	$L \times 10^8$ V^2/K^2	S $\mu V/K$
6	0.846	1175	16.57	.57
7	1.03	1175	17.29	.69
8	1.22	1174	17.90	.77
9	1.42	1174	18.52	.84
10	1.61	1174	18.90	.91
12	2.03	1173	19.84	1.06
14	2.43	1173	20.36	1.19
16	2.85	1172	20.88	1.32
18	3.22	1172	20.96	1.44
20	3.62	1171	21.20	1.52
25	4.48	1171	20.98	1.73
30	5.24	1171	20.45	1.94
35	5.92	1171	19.80	2.17
40	6.52	1171	19.09	2.40
45	7.05	1172	18.36	2.64
50	7.51	1173	17.62	2.86
60	8.18	1176	16.03	3.34
70	8.66	1179	14.58	3.76
80	8.93	1182	13.19	4.17
90	9.12	1185	11.73	4.58
100	9.27	1188	11.01	4.93
120	9.50	1192	9.44	5.64
140	9.71	1196	8.30	6.23
160	9.92	1201	7.45	6.79
180	10.1	1205	6.76	7.30
200	10.4	1209	6.29	7.71
220	10.6	1214	5.85	8.12
240	11.2	1223	5.27	8.78
280	11.5	1227	5.04	9.09
300	11.8	1232	4.84	9.39

NBSIR

SEMI-ANNUAL REPORT ON MATERIALS RESEARCH IN SUPPORT OF SUPERCONDUCTING MACHINERY

MAGNETOTHERMAL CONDUCTIVITY

L. L. Sparks

Cryogenics Division
Institute for Basic Standards
National Bureau of Standards
Boulder, Colorado 80302

March 1975

Summary: Magnetothermal Conductivity

The effect of a longitudinal magnetic field on the thermal conductivity of Inconel 718, AISI 310, and high purity copper (RRR = 1520) are presented. The results indicate that the relative change in thermal resistivity ($\Delta W/W_o$) of Inconel 718 is 0.08 at 5 K and 0.03 at 19 K when an 80 kOe magnetic field is applied. The corresponding values for AISI 310 stainless steel are 0.28 at 5 K and 0.10 at 19 K. The effect of the magnetic field on the high purity copper specimen is much larger since its thermal conductivity is nearly all due to electrons. The relative change in thermal resistivity for the high purity copper specimen is 3.4 at 5 K and 2.8 at 19 K.

Contents: Magnetothermal Conductivity

		Page
1.	Introduction	13
2.	Procedures	13
	2.1 Apparatus	13
	2.2 Materials	14
3.	Results	14
4.	Discussion	14
5.	References	15
	List of Figures	16

MAGNETOTHERMAL CONDUCTIVITY

L. L. Sparks

Cryogenics Division
Institute for Basic Standards
National Bureau of Standards
Boulder, Colorado 80302

1. Introduction

The objective is to determine the effect of magnetic fields on the thermal conductivity of technically important metals. The need for this information arises from the development of rotating machinery operating at cryogenic temperatures. The existing world's literature on magnetothermal conductivity, $\lambda(H)$, is concerned almost exclusively with scientific materials, e.g., very pure materials and single crystals. A complete bibliography of the subject was given by Sparks and Fickett [1].

The materials studied in this program are being used in superconducting motors and generators. Optimum design of these machines, which must operate at low temperatures while in magnetic fields, requires a detailed knowledge of how the thermal properties of the constituent materials are affected by a magnetic field. The broad material categories of interest include superconductor stabilizing materials such as copper and aluminum, and structural materials such as nickel alloys, stainless steels, and metallic composites.

2. Procedures

2.1 Apparatus

The experimental determination of $\lambda(H)$ of metals in high magnetic fields is complicated by the requirement that the specimen be contained in a region of homogeneous field. For magnets of reasonable size, this restriction necessitates small specimen lengths and resultant small temperature differences along the specimens. Our $\lambda(H)$ probe is designed to be used in a superconducting solenoid with a 3.8 cm bore and a 2.5 cm homogeneous (1%) field sphere. Our specimen length is therefore limited to approximately 2.5 cm.

The principle components of the $\lambda(H)$ system are shown in figure 1. A specimen is shown with its axis mounted parallel to the magnetic field. This configuration is used to determine the longitudinal $\lambda(H)$. Provision for making transverse $\lambda(H)$ measurements (heat flow perpendicular to the direction of the field) have been included in the system design.

The basic operation of the system involves balancing electrical power supplied to three heaters with the heat leak to the liquid helium bath via the THERMAL LINKS (capitalized words refer to figure 1). The electrical heaters are wound one each on the TEMPERATURE CONTROLLED HEAT SINK (TCHS), the SPECIMEN, and the TEMPERING POST. The power supplied to the TCHS determines the approximate temperature of the specimen; the SPECIMEN HEATER is used to establish a temperature gradient along the specimen; and, the TEMPERING POST HEATER is used to eliminate any temperature difference between the specimen and the tempering post. The TEMPERING POST and TCHS heaters are automatically controlled during all tests, while a constant current is supplied to the SPECIMEN HEATER.

The thermometers used in the probe are three 1/8 watt, 100 ohm Allen Bradley[1] carbon resistors (CRT's) and a single calibrated germanium resistor (GRT). The CRT's are located, one each, in the TCHS and the two THERMOMETER BLOCKS, which are clamped to the specimen. The GRT is located in the TCHS and is used for zero-magnetic-field calibration of the CRT resistors. The effect of the magnetic field on the resistance of the CRT's is taken to be that published by Neuringer and Shapira [2]. Resistance measurements on the two specimen CRT's are made using a lock-in amplifier as both detector and power supply for an AC bridge. Both absolute and difference resistance measurements are possible using this system.

The thermal conductivity of a specimen is computed from the specimen geometry (Area/length), the specimen heater power ($\dot{Q}$), and the measured temperature difference along the

[1] Trade name of Allen Bradley Co.

specimen (ΔT). The relationship of λ to these parameters is given by

$$\lambda = \frac{\dot{Q}}{\frac{A}{\ell}\Delta T} .$$

A series of measurements of ΔT and $\dot{Q}$ at various fields ($0 \leq H \leq 80$ kOe) and temperatures ($4 < T < 20$ K) result in the data presented in this report.

2.2 Materials

A total of four materials have been tested--Inconel 718[2], OFHC[3] copper, AISI 310 stainless steel, and a high purity copper referred to as NBS-B stock 7. The Inconel 718 was in the age-hardened condition with a Rockwell hardness of C39 and an average grain diameter of 0.06 mm. The composition in weight percent for this material is: Ni = 54.57, Cr = 18.06, Fe = 17.08, Nb + Ta = 5.12, Mo = 3.18, Ti = 0.85, Al = 0.44, Mn = 0.29, Si = 0.24, Cu, C, and S < 0.1%. The residual resistance ratio (RRR = R_{273}/R_4) of the Inconel 718 specimen is 1.06. The AISI 310 specimen was measured in the cold worked condition; its Rockwell hardness was B48 and its RRR = 1.27. Chemical analysis and grain size determination of the AISI 310 specimen are being done. The high purity copper, NBS-B stock 7, was vacuum annealed at 850°C for one hour. The electrical resistivity of this copper specimen was too low to be measured in the $\lambda(H)$ system; however, extensive work on the electrical resistivity of NBS-B stock 7 copper by Fickett [3] indicates that RRR = 1520 for our specimen. The ratio for our particular specimen will be determined shortly.

3. Results

A large magnetic field effect on the thermal conductivity of Inconel 718 was reported in the previous ARPA semi-annual report [4]. Further analysis shows that the field was exaggerated. The re-evaluated data are given in figure 2. Data are shown only for 0 and 80 kOe fields; curves for H = 10, 20, and 40 kOe fall between the two curves shown. The estimated 10% uncertainty of the data would indicate that the data at 0 and 80 kOe are indistinguishable. However, as the curves drawn through the data points show, the precision of the measurements is sufficient to indicate a definite trend toward lower thermal conductivities at 80 kOe. The zero field data for Inconel 718 is within 10% of the zero field data by Hust, et al. [5] for a similar specimen.

Preliminary data for AISI 310 stainless steel are shown in figure 3. Again, only the 0 and 80 kOe curves are shown.

Preliminary data for NBS-B stock 7 copper are shown in figure 4. The experimental points at H = 0 represent averages, while the experimental points for $H \neq 0$ are single data points. The extremely high conductivity at zero field is near the limit of what can be measured in the present system. Repeat runs and data averaging were used to increase the reliability of the zero field results. The origin of the curve representing H = 0 data will be discussed later in this paper.

4. Discussion

Our data indicate that an 80 kOe magnetic field reduces the thermal conductivity of our Inconel 718 specimen by 8% at 5.5 K and by 3% at 19.5 K. An estimate of the electronic contribution to the thermal conductivity of this material can be made using Lorenz ratio data ($L = \rho\lambda/T$) given by Hust, et al. [5]. This estimate indicates that the electrons carry roughly 25% of the heat current at 5 K and 18% at 19 K. The Lorenz numbers for stainless steels are typically lower than those for the NiCrFe alloys by approximately a factor of 2. This would suggest a larger electronic component and consequently a larger field effect. The effect of a 80 kOe field on the AISI 310 stainless steel specimen is to reduce the conductivity by 20% at 5.25 K and 11% at 19.5 K. These percentages are determined at the extremes of temperature as shown in figure 3. At intermediate temperatures the conductivity at 80 kOe appears to be higher than at zero field. This effect is probably not real, but rather the conductivity should parallel the zero field data as was the case for Inconel 718. Further tests will be done on AISI 310 if a similar anomaly appears in the results for AISI 304.

---

[2] Trade name of International Nickel Corp.

[3] Trade name of AMAX Corp.

The very high thermal conductivity of the NBS-B stock 7 copper specimen causes experimental difficulties that result in lower accuracy in the zero field runs than was the case for the lower conductivity materials. The solid curve shown in figure 4 for H = 0 was derived using the relationship

$$1/\lambda = W = AT^n + B/T$$

and represents the data within the experimental accuracy. When put in the form $WT = AT^{n+1} + B$, B is the intercept and A is the slope of a WT vs T^{n+1} plot. Further details of this procedure, including determination of the constant n, are given by Powell, et al. [6]. The constants derived from the current zero field data are $A = 3.02 \times 10^{-8}$, $n = 2.55$, and $B = 4.7 \times 10^{-4}$ with the units of W being mK/W. The effect of a magnetic field is included in figure 4. The anomalous decrease shown in this figure for λ at 20 kOe and high temperatures is probably not real; the single data point at 21 K appears to be bad, but no reason can be found to discard it. Figure 5 presents the relative change in thermal resistivity ($\Delta W/Wo = \lambda_{H=0} - \lambda_H/\lambda_H$) as a function of magnetic field. The high temperature, 20 kOe data have been ignored in this figure due to its anomalously low value. This is unfortunate since the apparent knee in the $\Delta W/Wo$ data shown in figure 5 occurs in the 20 kOe field range. Although the exact placement and shape of the knee is somewhat questionable there, there is no doubt a rapid decrease in slope of $\Delta W/Wo$ in the 10 to 40 kOe range. A similar plot of $\Delta W/Wo$ for the previously reported OFHC copper is shown in figure 6; there is no rapid change in the slope of $\Delta W/Wo$ for this material. A magnetic field should affect the electronic conductivity strongly if the mean free path is long, e.g., $\omega\tau \geq 1$ where ω is the angular frequency and τ is the relaxation time. ω is proportional to the magnetic field as indicated by the cyclotron relationship $\omega = eH/mc$. Further, τ(high purity copper) $> \tau$ (low purity copper), so that $\omega\tau$ becomes large for the high purity stock 7 copper before it does for the OFHC specimen; consequently, the effect of a magnetic field should be seen at the lower fields for the stock 7 copper than for the OFHC material. A comparison of the data in figures 5 and 6 show this to be the case.

In conclusion, the effect of a magnetic field on structural alloys such as the Inconel 718 and stainless steel reported here is relatively small. The results are not inconsistent with estimates of the possible field effects using Lorenz ratio data. Good conductors such as the two copper specimens show greater field affects which are expected due to the large electronic component of the thermal conductivity.

The effort to detect and eliminate possible sources of error such as spurious control voltages, inadequate thermal contacts, and unwanted heat flow paths is continuing and will hopefully result in increased precision and reliability. Materials to be tested in the remainder of the year include AISI 304 stainless steel, an undesignated aluminum, and Ti-6Al-4V.

5. References

1. Sparks, L. L. and Fickett, F. R., Materials research in support of superconducting machinery, National Bureau of Standards, Boulder, Colorado, Cryogenics Division, March, 1974 NBSIR-74-359, AD-780 596/3WM.

2. Neuringer, L. J. and Shapira, Y., Low temperature thermometry in high magnetic fields, I. Carbon resistors, RSI 40, No. 10, 1314 (Oct., 1969).

3. Fickett, F. R., A preliminary investigation of the behavior of high purity copper in high magnetic fields, Annual report to INCRA, (August, 1973).

4. Sparks, L. L. and Fickett, F. R., Materials research in support of superconducting machinery, National Bureau of Standards, Boulder, Colorado, Cryogenics Division, October, 1974, NBSIR-74-393.

5. Hust, J. G., Weitzel, D. H., and Powell, R. L., Thermal Conductivity, Electrical Resistivity, and Thermopower of Aerospace Alloys from 4 to 300 K, J. Res. Nat. Bur. Stand. (U.S.), 75A, No. 6, 269 (July-August, 1971).

6. Powell, R. L., Roder, H. M., and Hall, W. J., Low-temperature Transport Properties of Copper and Its Dilute Alloys: Pure Copper, Annealed and Cold-Drawn, Phys. Rev. 115, No. 2, 314 (July 15, 1959).

List of Figures

Page

1. Magnetothermal conductivity probe and magnet 17

2. Thermal conductivity of Inconel 718 as a function of temperature for H = 0 and 80 kOe 18

3. Thermal conductivity of AISI 310 stainless steel as a function of temperature for H = 0 and 80 kOe 19

4. Thermal conductivity of high purity copper (RRR = 1520) as a function of temperature for H = 0, 10, 20, 40, and 80 kOe 20

5. Relative change in thermal resistance of high purity copper as a function of magnetic field 21

6. Relative change in thermal resistance of oxygen-free copper as a function of magnetic field 22

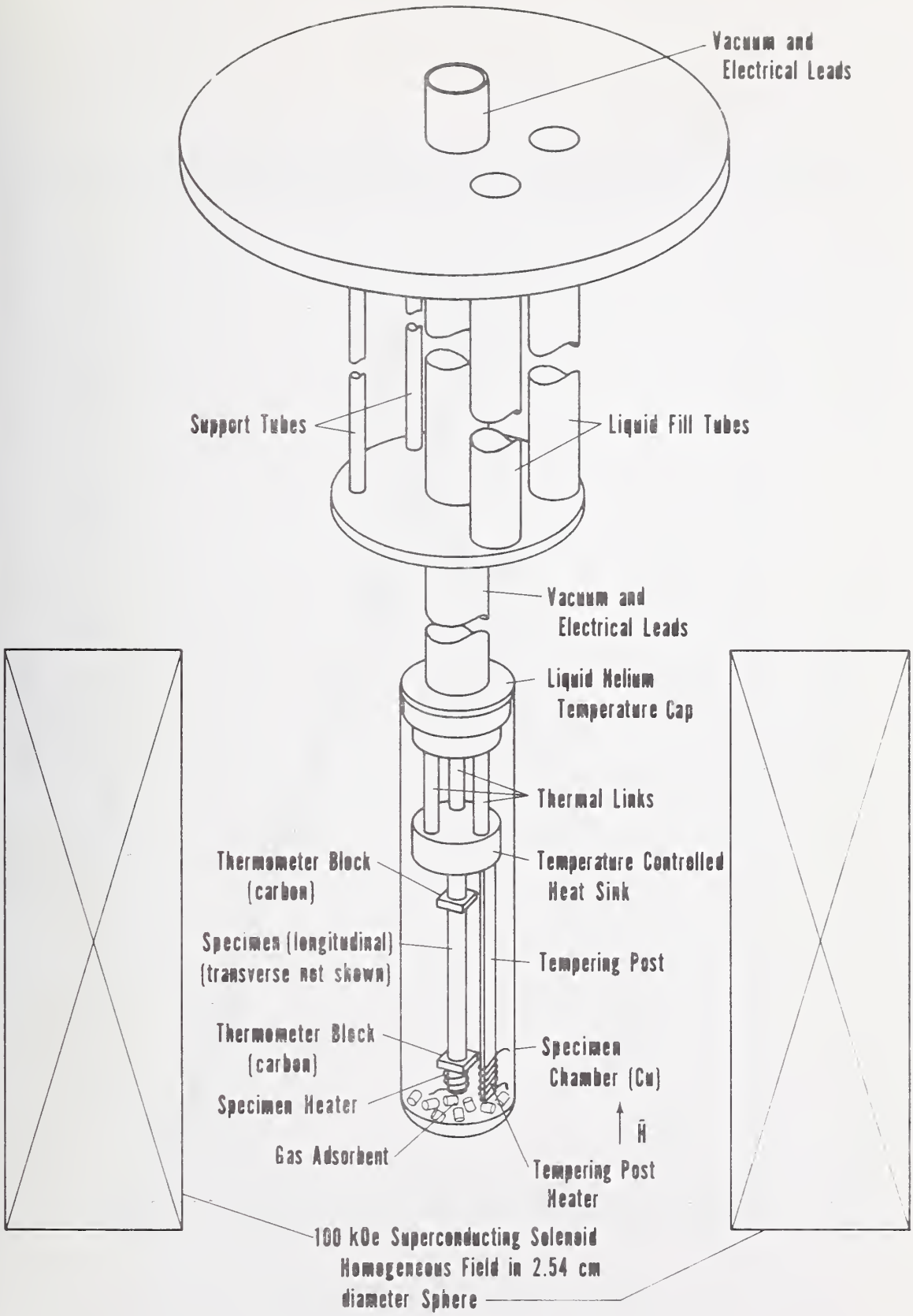

Figure 1. Magnetothermal conductivity probe and magnet.

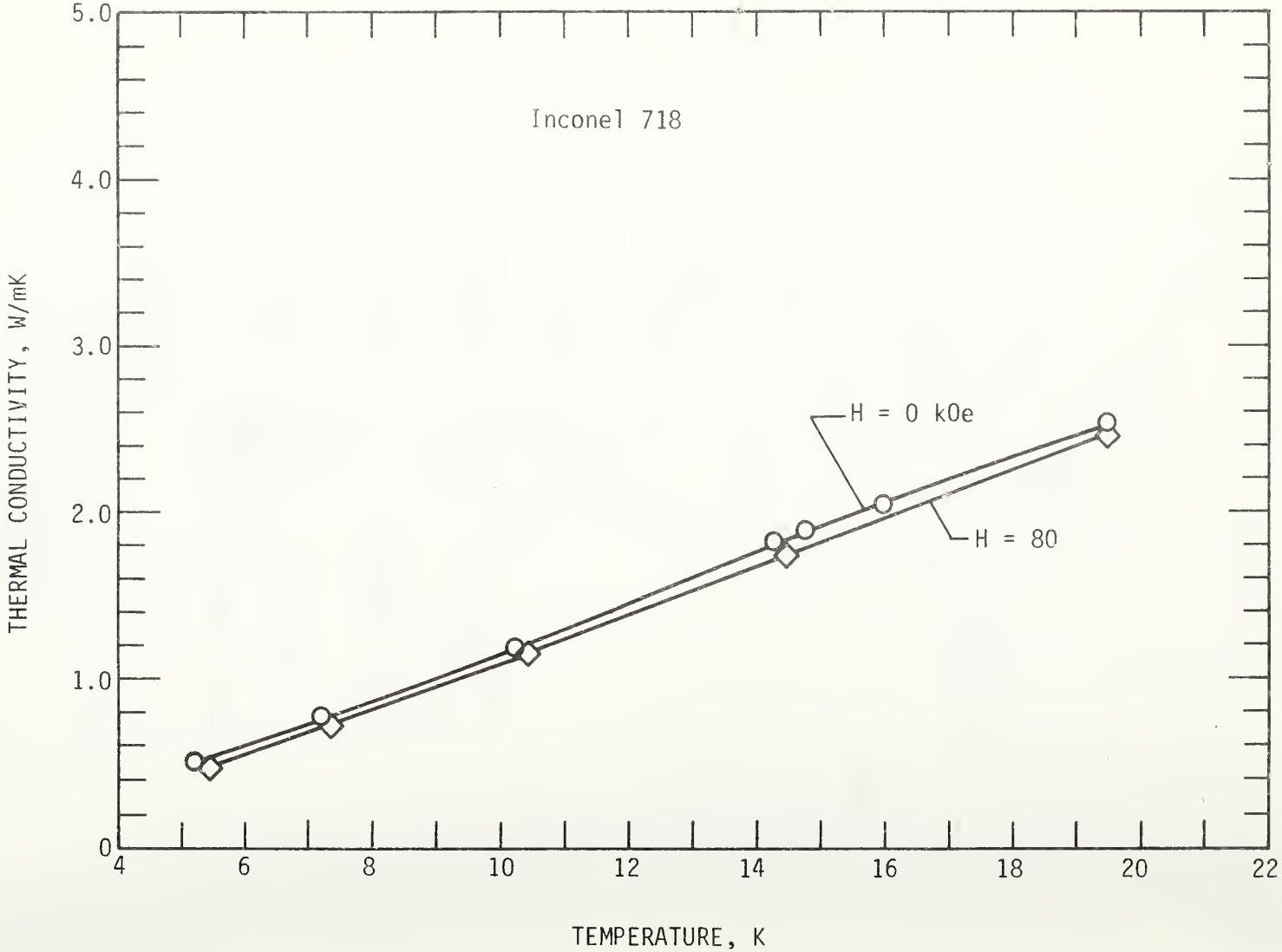

Figure 2. Thermal conductivity of Inconel 718 as a function of temperature for H = 0 and 80 kOe.

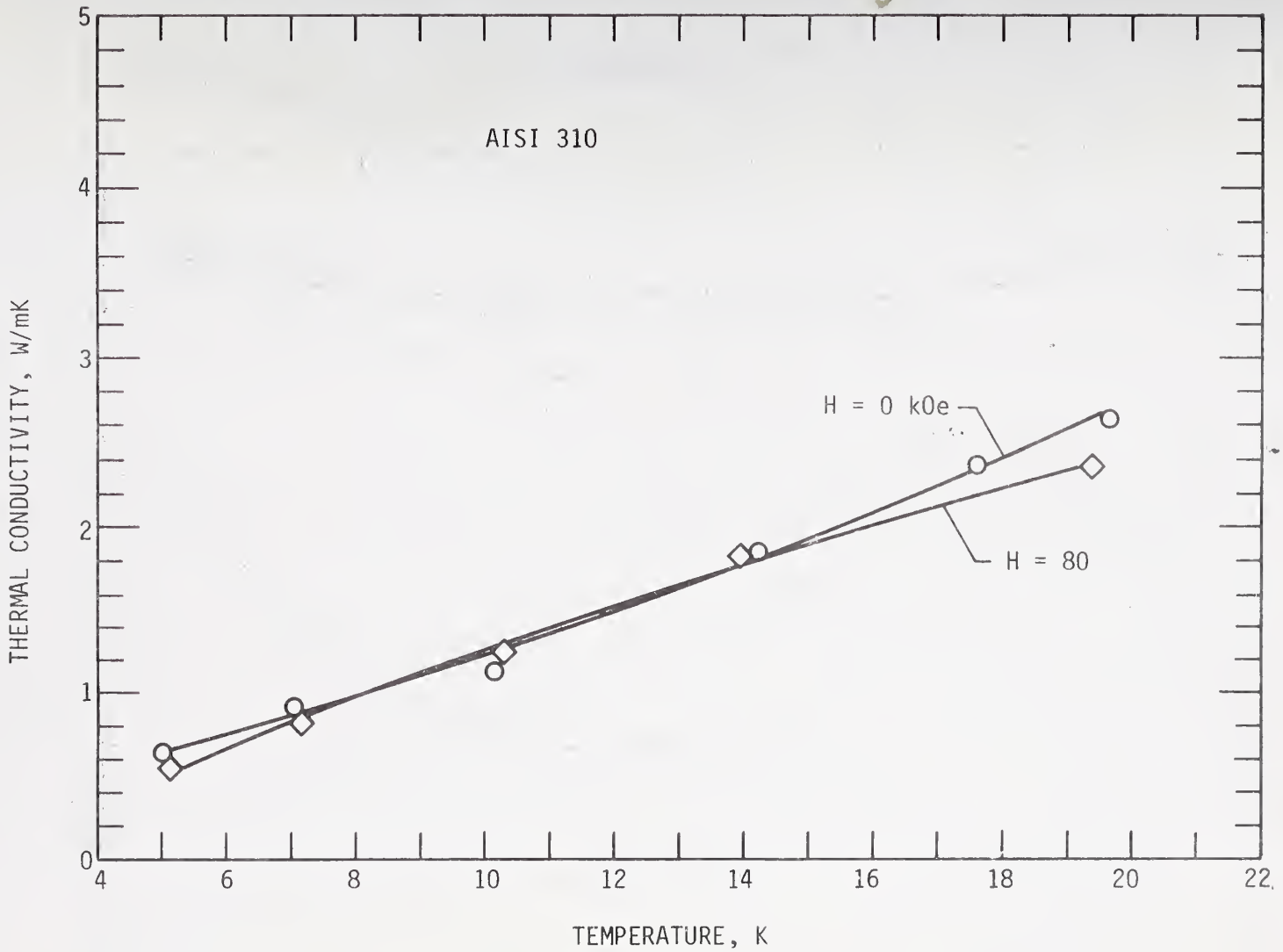

Figure 3. Thermal conductivity of AISI 310 stainless steel as a function of temperature for H = 0 and 80 kOe.

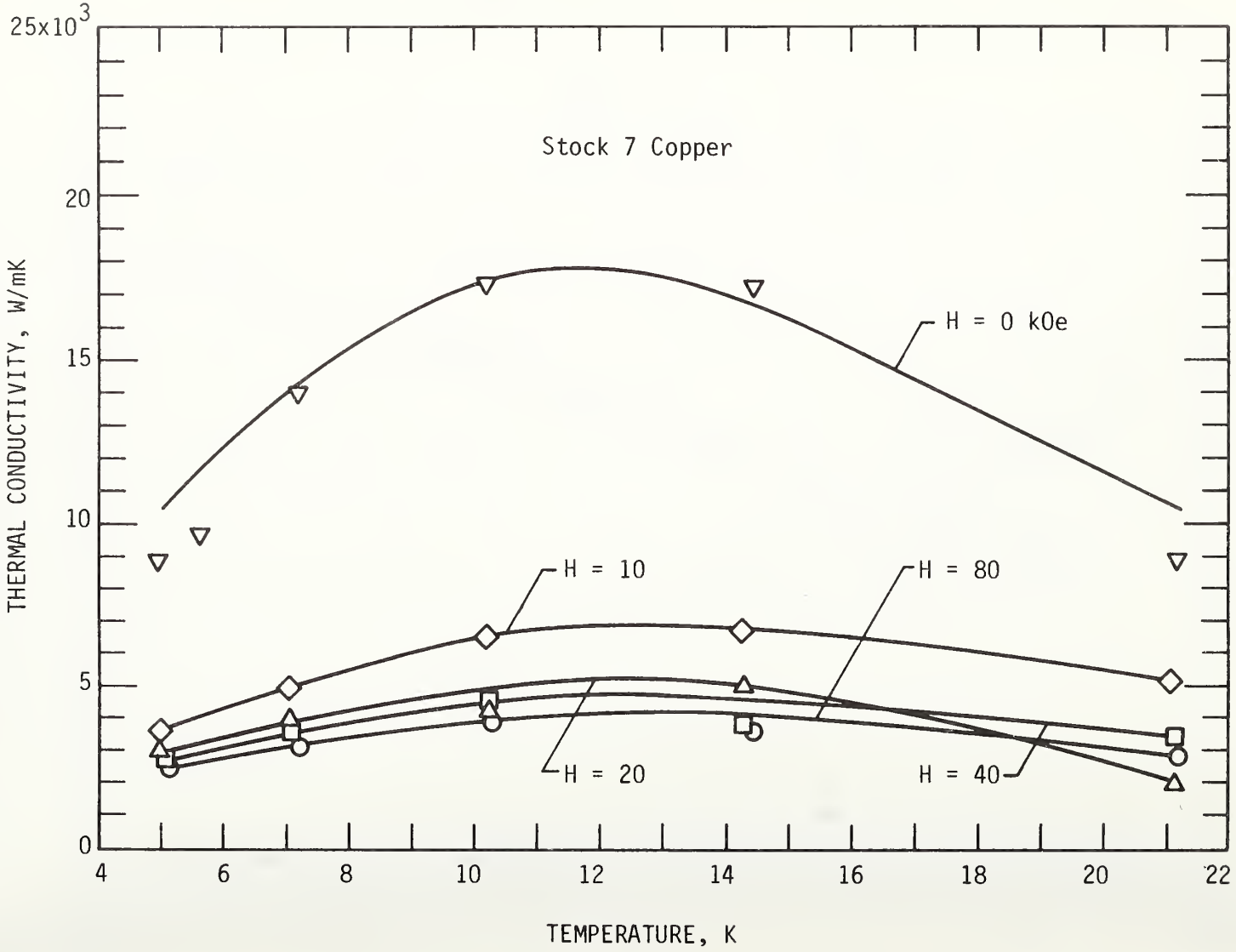

Figure 4. Thermal conductivity of high purity copper (RRR = 1520) as a function of temperature for H = 0, 10, 20, 40, and 80 kOe.

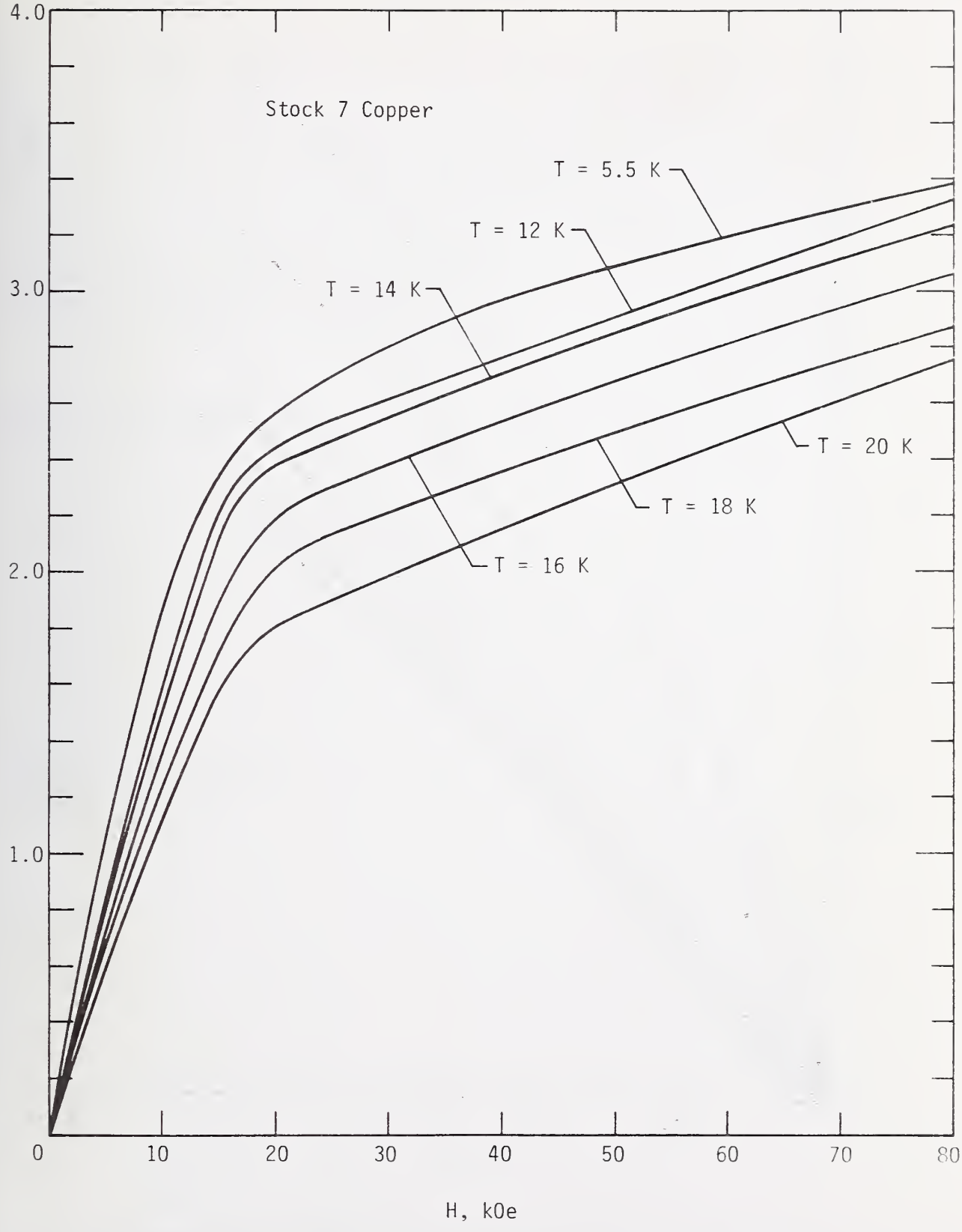

Figure 5. Relative change in thermal resistance of high purity copper as a function of magnetic field.

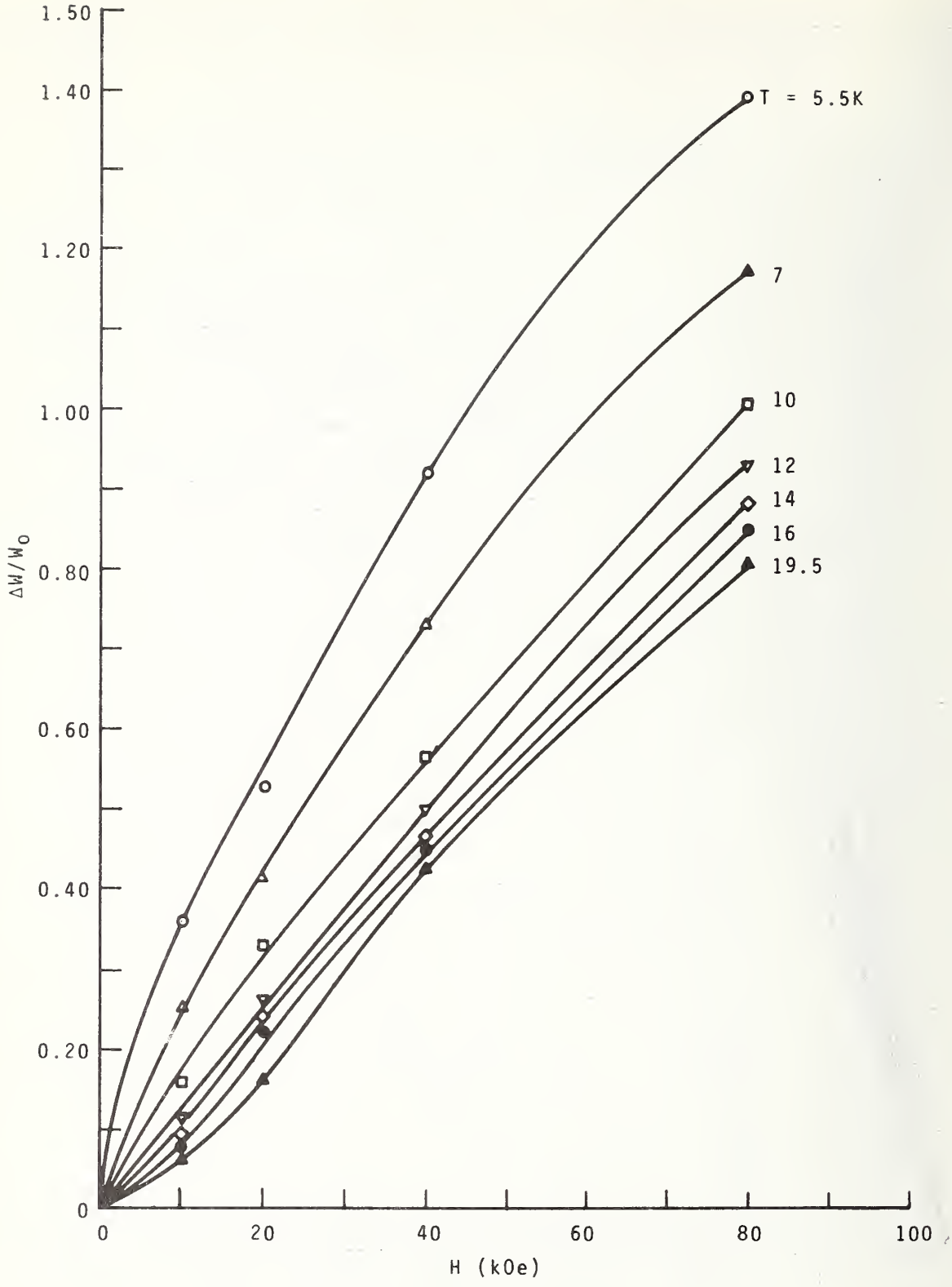

Figure 6. Relative change in thermal resistance of oxygen-free copper as a function of magnetic field.

NBSIR

SEMI-ANNUAL REPORT ON MATERIALS RESEARCH IN SUPPORT OF SUPERCONDUCTING MACHINERY

FATIGUE AND FRACTURE TOUGHNESS TESTING AT CRYOGENIC TEMPERATURES

R. L. Tobler, R. P. Mikesell, R. L. Durcholz, and R. P. Reed

Cryogenics Division
Institute for Basic Standards
National Bureau of Standards
Boulder, Colorado 80302

April 1974

SUMMARY

The report includes four manuscripts. Fracture mechanics design data are presented for a variety of cryogenic structural alloys having potential applications at 4 K. The plane strain fracture toughness parameters, K_{IC} and J_{IC}, and fatigue crack growth rates, da/dN, were measured at temperatures from 295 to 4 K using compact specimens and state-of-the-art test procedures. The results are summarized as follows:

1) Fracture toughness and fatigue crack growth tests lasting several hours were performed using about ten liters of helium per test and specially designed cryostats.

2) It was observed for the first time that the ELI (extra-low-interstitial) grade of Ti-6Al-4V exhibits a ductile-to-brittle transition between 125 and 76 K. Despite the transition, the toughness of the ELI grade exceeds that of the normal grade by a significant margin at all temperatures.

3) The fracture toughness of A 453, a precipitation-hardened austenitic stainless steel, decreased very slightly over the interval 295 to 4 K; its resistance to fatigue crack propagation was improved at cryogenic temperatures.

4) Fatigue crack growth rate results for ten alloys indicate that stable face-centered cubic (austenitic) alloys exhibit the best resistance to fatigue crack propagation at 4 K.

FRACTURE TESTING AND RESULTS FOR A Ti-6Al-4V ALLOY AT LIQUID HELIUM TEMPERATURE†

C. W. Fowlkes* and R. L. Tobler

Cryogenics Division
National Bureau of Standards
Boulder, Colorado 80302

† Contribution of NBS, not subject to copyright.

* Present address: Fowlkes Engineering, 12460 W. 82nd Ave., Arvada, Colorado 80005

ABSTRACT

This paper discusses fracture toughness and fatigue crack growth testing at liquid helium temperature, 4 K (-452°F). The design and performance of a fracture testing cryostat and associated instrumentation are described. Fracture toughness and fatigue crack growth data for Ti-6Al-4V from room temperature to 4 K are presented.

Key words: Crack propagation; cryostats; fracture tests; low temperature tests; mechanical tests; titanium alloys.

INTRODUCTION

The phenomenon of superconductivity is currently being applied in the design and construction of motors and generators, allowing a reduction in physical size of machinery for a given power output. Superconducting components are cooled with liquid helium, and, since some structural parts must operate at 4 K, a need for mechanical property data at this temperature has developed. Some existing data for structural alloys at 4 K describe fatigue and tensile properties [1-3].

Conventional tensile data do not provide an adequate basis for predicting the load carrying capability of structures where stresses are concentrated locally at fatigue cracks or other common flaws. In such cases, a fracture mechanics analysis may be the best method for determining the safe-operating lifetime of the structure. Fracture mechanics techniques utilize the concept of the stress intensity factor to characterize crack-tip stress fields, and this concept forms the basis of the ASTM Standard Method of Test for Plane Strain Fracture Toughness of Metallic Materials (ASTM E-399-74) [4]. The essential design parameters are the plane strain fracture toughness (K_{IC}) of a material and the fatigue crack growth rate (da/dn). A knowledge of these parameters for materials at 4 K is relevant to the optimum design of superconducting machinery since:

1) The investment in machinery is large, and fractures would be costly.

2) At low temperatures the yield strength of materials is increased and ductility may be decreased, increasing the probability of brittle fracture.

3) The materials in motors and generators are subject to high cycle fatigue; flaws in a structure, inherent or due to fabrication, may propagate to critical proportions during long-term operating conditions.

Programs have been initiated at the National Bureau of Standards to collect the needed fracture mechanics design data. The first step was to design test apparatus capable of efficient operation at 4 K. Experience gained during this phase of research is included in this report, which discusses: the optimum design of mechanical testing cryostats, the features and performance of the fatigue and fracture cryostat currently in use at NBS, and fracture data obtained for a Ti-6Al-4V alloy at 295, 77, and 4 K.

CRYOSTAT DESIGN CONSIDERATIONS

Systems Analysis

The cost of mechanical testing at 4 K depends on the amount of liquid helium consumed in cooling the specimen and cryostat. To insure a uniform temperature, the specimen must be submerged in the liquid and additional helium must be added to allow for evaporation during the test. The simple model of a fatigue and fracture testing cryostat shown in Figure 1 can be used to outline the mechanical and thermal trade-offs involved in cryostat design. The parameters of interest are the amount of heat to be removed during cool-down, the steady state heat gain, the load capacity, and the stiffness of the frame.

The initial heat, $Q_{cool\text{-}down}$, that must be removed from the dewar, the enclosed frame and the specimen can be approximated by:

$$Q_{cool\text{-}down} = (m_d c_d + m_s c_s + 2L_i A_f \rho_f c_f)\ \Delta T \qquad (1)$$

where where m is mass, c is average specific heat, ρ is density, A is cross-sectional area, $\Delta T = (T_{ambient} - T_{test})$, and the subscripts d, s, and f refer to the dewar, specimen, and frame respectively. The term L_i is defined in Figure 1.

The rate of heat gained by the cryostat during steady state operation can be separated into heat conducted along the frame, heat leaked into the dewar, q_d, and heat generated during fatigue operation, $q_{fatigue}$. The total steady state rate of heat gain, q_{steady}, can be approximated by:

$$q_{steady} = 2\left(k_f A_f \frac{\Delta T}{L_e}\right) + q_d + q_{fatigue} \qquad (2)$$

where k_f is the thermal conductivity of the frame members, and L_e is defined in Figure 1.

Heat is generated during fatigue due to plastic deformations of the test specimen. Cyclic operation will also stir and agitate the cryogenic fluid, increasing the heat

gained by the cryostat through dissipation and increased convection. The last term in Eq. (2), $q_{fatigue}$, includes these sources of heat. Such heat gains are significant in actual operation, tending to increase with the frequency and displacement of the test program, but for all practical applications they are independent of the cryostat design. For this reason, $q_{fatigue}$ will not enter in the optimization equations.

The strength and compliance of the cryostat frame are related to the size of the frame and therefore affect both cool-down and steady state heat gain. The load capacity, P_{max}, of the tension and compression members of the frame extending into the dewar will be taken as:

$$P_{max} = \sigma_{ds} A_f \tag{3}$$

where σ_{ds} is a design stress which can be represented as some fraction of the ultimate tensile stress of the material. The compliance (reciprocal of stiffness) of the load frame, C_f, can be approximated by considering the deflections of both tension and compression members. Neglecting bending, the compliance is given by

$$C_f = 2\left(\frac{L_e + L_i}{A_f E_f}\right) \tag{4}$$

where E_f is Young's modulus of the frame material. The compliance of the specimen is not included in Eq. (4); the specimen design is independently fixed, and its compliance will not affect the optimization of the cryostat.

The compliance of the cryostat is also important because it influences the performance of the fatigue actuator in the testing machine. The displacement-frequency behavior of the actuator used in these experiments, shown in Fig. 2, indicates that the frequency and hence the duration of a fatigue test is a strong function of actuator displacement.

Assume for example that the compliance of the system is such that the displacement at the required fatigue load is 1.27 mm. The corresponding maximum frequency from Fig. 2 is 50 Hz. If the frame is reduced in cross section by a factor of two in an effort to reduce heat gain and mass, the compliance will be doubled. Figure 2 shows that the maximum frequency will be reduced to approximately 25 Hz. This lower frequency doubles the test duration and the steady state heat gain.

Optimization

From the discussion above it can be seen that there is an interdependence among the design objectives. According to systems analysis procedures, an optimum design can be achieved by finding values of the controllable variables which minimize some objective function [5]. An objective function is a function that relates the design variables in a form such that their effects on optimization can be evaluated.

Case I. High-cycle fatigue cryostat

In a high-cycle fatigue cryostat we seek to minimize cool-down heat loss and steady state heat gain and simultaneously to maximize the load capacity and stiffness. One simple objective function which states this goal is:

$$\min z = \left[\frac{(Q_{cool\text{-}down})\ (q_{steady})\ (C_f)}{P_{max}}\right] \tag{5}$$

where min z indicates that the group of terms comprising the objective function is to be minimized subject to other system constraints [5].

The dewar heat gain, the specimen design, the specimen compliance, and the fatigue heat gain are independently fixed. Removing these terms from Eqs. (1) and (2) and substituting Eqs. (1) through (4) into Eq. (5) and simplifying yields:

$$\min z = \left[\left\{\frac{P_f c_f k_f}{E_f \sigma_{ds}}\right\}\left\{(\Delta T)^2\right\}\left\{\frac{(L_e + L_i)\ L_i}{L_e}\right\}\right] \tag{6}$$

where material properties are grouped separately from geometrical factors.

Clearly, the specific heat, density, and thermal conductivity of the frame should be minimized whereas the modulus and design strength should be maximized. All of these terms are linear in Eq. (6). The temperature difference is important since it is squared, but it cannot be changed. The total length of the frame ($L_e + L_i$) is also limited by the dimensions of the testing machine, but the internal length, L_i, should be minimized and the external length, L_e, maximized. Note that the cross-sectional area of the frame members does not appear in Eq. (6).

In addition to this particular result, it is instructive to briefly consider the outcome from Eq. (5) for three other cases.

Case II. Low-cycle fatigue cryostat

If compliance is removed from Eq. (5) the result is:

$$\min z = \left[\left\{ \frac{p_f c_f k_f}{\sigma_{ds}} \right\} \left\{ \frac{A_f L_i}{L_e} \right\} \left\{ (\Delta T)^2 \right\} \right] \tag{7}$$

showing that the ratio of internal to external lengths is to be minimized. The cross sectional area should also be minimized subject to other constraints, such as the load capacity of the cryostat. This objective function applies to the design of tensile cryostats and some fatigue cryostats. The low compliance implied by this objective function may affect some fracture measurements.

Case III. Creep Cryostat

If only the steady state heat gain and load capacity are considered, the objective function becomes:

$$\min z = \left[\left\{ \frac{k_f}{\sigma_{ds}} \right\} \left\{ \Delta T \right\} \left\{ \frac{1}{L_e + L_i} \right\} \right] \tag{8}$$

The only controllable variables are thermal conductivity and frame length. This objective function would be used to design a cryostat for creep and sustained load crack growth experiments.

Case IV. Tensile Cryostat

If the cryostat is not intended for long-term static or fatigue tests, the steady state heat gain and compliance terms can be removed from the objective function. The result:

$$\min z = \left[\left\{ \frac{p_f c_f}{\sigma_{ds}} \right\} \left\{ L_i \right\} \left\{ \Delta T \right\} \right] \tag{9}$$

suggests the use of a high strength structural material having low density and specific heat. The internal length of the frame should be minimized, the cross-sectional area of the frame members cancels, and there is only a linear dependence on temperature difference.

Cool-down Calculations

Unless the test duration exceeds several hours, the amount of heat removed from an efficient system in cooling from ambient temperature to liquid helium temperature is large compared to the steady-state heat gain. Particular attention must therefore be given to the details of the cool-down procedures [6].

Pertinent data on liquid nitrogen and liquid helium are shown in Tables 1 and 2. Four facts bear directly on design: (a) liquid helium is expensive, (b) liquid nitrogen is relatively cheap, (c) liquid helium has a relatively low heat of vaporization and (d) helium gas has a relatively large enthalpy compared to the heat of vaporization. Clearly, an optimum cool-down procedure should include precooling and cryostat with liquid nitrogen and effective utilization of the enthalpy of the helium gas.

The most efficient use of the enthalpy of the helium gas occurs for an isothermal cool-down where the vapor exhausted from the dewar is always at a temperature lower than the current temperature of the cryostat by only an infinitesimal amount. Here the term "cryostat" refers to the dewar and everything contained in it (the frame, specimen, grips, etc.). Assuming that the cryostat has been precooled to 77 K using liquid nitrogen, the subsequent cool-down to 4 K using evaporated helium will be considered.

Let an infinitesimal mass of liquid helium, dm_h, be vaporized at one atmosphere and then brought to a temperature T and an enthalpy H_h. The heat required is approximately $dm_h H_h$. If this heat is supplied by the cryostat of mass m_c initially at a temperature T + dT, the enthalpy of the cryostat will decrease by dH_c during the dT temperature change. The energy lost by the cryostat is $m_c dH_c$. The subscripts h and c refer to helium and cryostat, respectively.

The equation expressing the heat balance for this ideal cool-down is:

$$dm_h H_h = m_c dH_c \tag{10}$$

To simplify calculations the enthalpies in J/gm can be approximated by [7]:

$$H_c \approx 1.8 \times 10^{-7} \ (T)^{3.94} \tag{11}$$

and [8]:

$$H_h \approx 20.46 + 5.34 \ (T-4.2) \tag{12}$$

where the temperatures are Kelvin.

Taking the mass of the cryostat described in a later section as 9.1 kg, substituting Eqs. (11) and (12) into Eq. (10), and integrating the result yields:

$$\Delta m_h = 1.2 \times 10^{-6} \ [0.34T^{2.94} + 0.187T^{1.94} + \ldots \ ]_{T_2}^{T_1} \tag{13}$$

where T_1 and T_2 are the initial and final temperatures of the cryostat and Δm_h is the mass of liquid helium in kg.

As calculated from Eq. (13), the liquid helium consumed in ideal cooling from various temperatures to 4 K is shown in Figure 3. The minimum amount of liquid required for ideal cooling from 77 K is about 1.25 liters. In contrast, 20 liters would be consumed if the heat of vaporization alone were used for cool-down. Twenty liters represent the upper limit for extreme inefficiency.

The cryostat can be precooled to about 63 K using liquid nitrogen at a reduced pressure. Lowering the pressure from 1.0 to 0.18 atm reduces the equilibrium temperature to 63.14 K, the freezing point of nitrogen [9]. Figure 3 indicates that precooling the cryostat to 63 K will reduce the liquid helium required for subsequent cool-down by half a liter. As described later, this step can be incorporated in the cool-down procedures. Additional data for cool-down calculations are given by Jacobs [10].

FATIGUE AND FRACTURE CRYOSTAT

Description of Apparatus

The 100 kN capacity cryostat built for these tests, shown in Figures 4, 5, and 6, tends to minimize the objective function of Eq. (6). The load frame consists of two tubular, composite compression members that are linked at the lower ends with a maraging steel bridge. The lower sections of the compression members are AISI 304 having a wall thickness of 3.18 mm; the upper sections are fiberglass reinforced plastic (FRP) having a wall thickness of 6.35 mm. The maraging steel grips conform to ASTM E-399-74 specifications. The lower grip is pinned into the center of the bridge, while the upper grip is threaded to a titanium alloy loading rod.

A double dewar arrangement is used for tests in liquid helium, but conventional glass dewars were rejected because of fragility. Instead, an inner helium dewar was fabricated from fiberglass reinforced plastic. A vacuum is maintained in the space between the walls of this dewar by periodic mechanical pumping, and five layers of aluminized mylar line the vacuum space for added insulation. The foam insulated outer dewar for liquid nitrogen was fabricated from fiberglass and epoxy; the flared shape minimizes nitrogen consumption and facilitates assembly during testing.

Thin copper baffles may be attached along the frame with hose clamps. These baffles were designed for a close fit with the inner dewar. Staggered openings form a labyrinth for cold vapor introduced at the bottom of the dewar during helium transfer. Thus, the baffles direct the vapor flow and also serve as radiation shields.

A vacuum jacketed helium fill tube and a plastic purge tube extend to the bottom of the inner dewar. Other features include two vents, a carbon resistor liquid level indicator, a gas cylinder and pressure gage connection, and an instrumentation lead-through. With an O-ring placed under the cryostat lid and all vents closed, the helium dewar is sealed and its internal pressure may be raised or lowered.

A conventional double-beam ASTM E-399-74 clip gage was used to measure deflections at the specimen edge. Commercially available cryogenic strain gage films were bonded to the gage beams using an epoxy for low temperature applications. The gage films were left uncoated to reduce the probability of thermal cracking. The body of the clip gage was enclosed in a protective aluminum cage and tetrafluoroethylene coated lead wires in a woven glass fiber sheath linked the gage to external instrumentation. With the clip gage in liquid helium, a low excitation voltage (1.5 vdc) minimized the noise due to local boiling at the films. Direct calibrations using a dial micrometer verified that the gage satisfied ASTM E-399-74 linearity requirements and that there was only a small change in sensitivity with temperature. This clip gage has operated for 10^7 fatigue cycles at temperatures from 295 to 4 K, with about 10^6 cycles at 4 K.

Cryostat Operation and Performance

Liquid helium testing begins by filling both inner and outer dewars with liquid nitrogen. After reaching equilibrium at 1 atm, the pressure on the inner dewar is reduced to approximately 0.2 atm. On reaching equilibrium at this new pressure, the cryostat is pressurized with helium gas to purge the liquid nitrogen. Liquid helium is then slowly transferred into the dewar. When the required level has been reached, the transfer line is disconnected and the test begins. The helium transfer takes about thirty minutes and the entire cool-down procedure takes at least two hours.

An alternative procedure eliminates the use of baffles and the steps involving mechanical pumping and purging. After precooling the cryostat to 77 K, the inner dewar of liquid nitrogen can be removed, emptied, and replaced in less than thirty seconds. The outer dewar is then assembled and helium transfer begins. This reduces considerably the time to accomplish cool-down, at the cost of less than two additional liters of liquid helium.

The volume of liquid required to submerge the specimen in this cryostat is about 4 liters but a reserve of up to 5 additional liters can be added for long-term tests. Assuming ideal cool-down, the lower bound of liquid helium consumption per test is approximately 5.25 liters. In practice, some liquid is used in cooling the transfer lines. The actual liquid helium consumption per test for Ti-6Al-4V specimens varied between 7 and 11 liters, depending on the amount of reserve fluid added and the rate of helium transfer.

The steady state loss of liquid helium under static load is between 0.05 and 0.1 liter per hour. During the fatigue tests reported here, the loss increased about five times due to dissipation in the specimen and agitation of the liquid as discussed earlier.

The cryostat accepts specimens of the compact geometry (described below) up to 3.81 cm-thick, developing a stress intensity factor of 110 $MN/m^{3/2}$ on such a specimen at maximum load. The ASTM E-399-74 specimen thickness requirement will be satisfied for materials having a yield strength above 890 MN/m^2 and a K_{IC} value less than 110 $MN/m^{3/2}$.

The load-deflection behavior of the cryostat frame and load train, shown in Figure 7, was determined by replacing the specimen with a large rigid block. The frame was statically loaded to 110 kN, and approximately 10^7 fatigue cycles were applied at lower loads. The

main cantilever resonance of the frame is 17 Hz, but no difficulties are encountered in practice if the operating frequency during fatigue tests is kept above 19 Hz or below 15 Hz.

The entire apparatus, including the 100 kN servo-hydraulic test machine used in these tests, is shown in Figure 8. In this photograph the helium dewar is in place and the nitrogen dewar is lowered.

EXPERIMENTAL PROCEDURE

Material

The alloy Ti-6Al-4V was tested in this study. Stock was obtained in the form of a 2.54 cm x 6.40 cm cross-section bar which had been mill annealed at 977 K for two hours, air-cooled, and descaled. The microstructure consisted of primary alpha and beta, having a grain size of 0.006 mm. The mill analysis and room temperature mechanical properties of the material are shown in Tables 3 and 4.

Specimen

The crack growth and fracture tests were performed using 2.54 cm-thick compact specimens that were proportioned in accordance with the ASTM E-399-74 method as shown in Figure 9. The notch was machined in the TL orientation [4], and deflections were measured between attachable knife edges located at the specimen edge.

The compact specimen was chosen because it has the largest fracture toughness measurement capacity for its size of any of the common fracture specimens [11,12]. A relatively small load applied to the compact specimen produces a large stress intensity factor. This allows the mass of the grips, the cryostat frame, and the loading rods to be minimized which significantly reduces the liquid helium consumption and cost per test.

Relationships between load, crack length, stress intensity factor, dimensions, and deflections for this specimen were given by Roberts [13] and are reproduced in Table 5. The stress intensity factor is given by [4]:

$$K_I = \frac{P}{BW^{1/2}} \left[29.6 \left(\frac{a}{W}\right)^{1/2} - 185.5 \left(\frac{a}{W}\right)^{3/2} + 655.7 \left(\frac{a}{W}\right)^{5/2} - 1017.0 \left(\frac{a}{W}\right)^{7/2} + 638.9 \left(\frac{a}{W}\right)^{9/2}\right] \quad (14)$$

where P is the applied load and a, B, and W are defined in Figure 9.

Test Procedures

The test procedure consisted of cooling the specimen and the cryostat, initiating the crack, propagating the crack at various ranges of stress intensity, and finally loading the specimen to fracture. Tests were conducted in ambient air at room temperature, in alcohol and dry ice at 195 K, in liquid nitrogen at 77 K, and in liquid helium at 4 K. The specimens were allowed at least 20 minutes to reach thermal equilibrium in the cryogenic fluids, and data were not recorded until the crack had advanced at least 1.27 mm (0.05 in) from the machined notch.

The fatigue tests were performed in load control, using a sinusoidal load cycle. The loads were measured and controlled during the tests to ± 1% and the ratio, R, of minimum to maximum stress intensity (K_{min}/K_{max}) was maintained at 0.1 ± 0.05. The test frequency was 25 ± 5 Hz, except for a few high load tests at 10 Hz.

Monitoring the crack length at cryogenic temperatures presents some problems since the specimen cannot be visually observed without removing the dewars. In this study, the specimen compliance method [14] in conjunction with fracture surface fatigue marking was successfully employed. The room temperature results showed that experimentally determined crack length and compliance values for the Ti-6Al-4V specimens were in close agreement with the theoretical values derived from the data in Table 5. Thus, crack length could be inferred from compliance measurements made at intervals during the tests. The crack growth rates were determined by differentiating graphs of crack length versus fatigue cycles.

To translate the room temperature compliance curve to a curve for a different temperature, the changes in the clip gage calibration and in the Young's modulus of the specimen material must be known. Both variables are linear factors in the compliance relationship. Between 295 K and 77 K, the clip gage sensitivity changed by only 0.25% while Young's modulus of Ti-6Al-4V increases by about 9% [15]. The calibration curve at 77 K was constructed using these corrections and the values in Table 5.

A simple alternative can be employed if there is a well defined crack front (such as the final crack length) on the fracture surface of the specimen. The room temperature compliance curve can be shifted along the displacement or compliance axis to make it coincide with the measured value at the reference crack length. This compensates for the changes in clip gage sensitivity and Young's modulus, as well as automatically including an operational definition of crack length.

Using corrected compliance calibrations at each temperature, the predicted or inferred values of crack length were always within ± 1.3% of the values actually measured from the specimen fracture surfaces. This uncertainty is within the resolution for values of compliance read from the X-Y recorder. For all these tests, the actual crack length was measured as an average of readings at three points equidistant across the specimen thickness.

Dynamic measurements using representative loads and frequencies showed that no overloads greater than 2% occurred when the machine was turned on or off. Also, when the stress intensity factor was reduced to lower values the growth rate was allowed to stabilize before any data were considered valid. The criterion used was Irwin's formula for plastic zone radius, r_p [16]:

$$r_p = \frac{K_I^2}{2\pi\sigma_y^2} \tag{15}$$

where σ_y is the yield strength of the specimen material. When the stress intensity factor was reduced during a test, subsequent crack growth data were ignored until the crack had grown an increment equal to or greater than the value of r_p from Eq. (15). The effects of load changes were thus excluded from the test results [17].

The fracture toughness tests were performed in stroke control subsequent to precracking at the same temperature. The data interpretation followed the standard ASTM E-399-74 method, and the thickness requirement that $B \geq 2.5\ (K_{IC}/\sigma_y)^2$ was amply satisfied by the 2.54 cm-thick specimens.

RESULTS

Crack growth rates

Crack growth rates, $\frac{da}{dN}$, are often described by equations of the form:

$$\frac{da}{dN} = C(\Delta K_I)^n \tag{16}$$

where a is crack length, N is the number of fatigue cycles, ΔK_I is the range of stress intensity factor ($K_{max} - K_{min}$), and C and n are empirical constants. As discussed by Paris and Erdogan [18], this equation applies to a wide range of data if the stress ratio, R, is non-negative and relatively constant. Accordingly, log-log plots of da/dN versus ΔK_I should reveal linear trends, and are appropriate for illustrating the present results.

The room temperature crack growth results are shown in Figure 10 and the results at 77 K and 4 K are shown together in Figure 11. Superimposed on these curves is a shaded band representing data in the Damage Tolerant Design Handbook [19] and elsewhere [20]. The average values of K_{IC} shown in these graphs indicate the upper limit of slow growth.

As shown in Figure 10, the present room temperature data fall within the range of currently accepted handbook data. The results at liquid nitrogen and helium temperatures show that there is not a large change in the crack growth rates at these low temperatures.

The 77 K and 4 K data are plotted on the same graph since any variation due to temperature is of the same magnitude as variations between specimens. In relation to the apparent temperature independence of these growth rates, it is significant to note that Wei and Ritter found the growth rates of a similar Ti-6Al-4V alloy to be temperature independent over the interval 295 K to 563 K [21].

The crack growth curves show an increased slope at ΔK less than about 16.5 $MN/m^{3/2}$. If this trend is extrapolated another decade in crack growth rate, the intercept of stress intensity is about 8.8 $MN/m^{3/2}$. This value is termed the threshold value of stress intensity, the point below which crack growth rates become diminishingly small. Room temperature measurements [20] report threshold values for a similar Ti-6Al-4V alloy to be about 6.6 to 8.8 $MN/m^{3/2}$. This result compares well with an extrapolation of the present data.

Crack growth tests of two specimens immersed in a slush mixture of dry ice and alcohol at 195 K could not be interpreted because the compliance curves were non-linear. Moreover, the crack fronts were irregular, invalidating fracture toughness tests at this temperature. The dry ice and alcohol environment apparently caused these anomalous results.

Fracture toughness

A typical fracture test record at liquid helium temperature is shown in Figure 12, test records at 77 K were similar. A very slight departure from linearity during the last 5% of load was the only sign of slow crack growth at low temperatures. At room temperature, a more noticeable "pop-in" (increment of unstable crack extension) preceded fracture by a few seconds. The room temperature records resembled the Type III record described in ASTM E-399-74.

The surface appearance of specimens fractured at 295 K and 4 K are shown in Figure 13. The fracture surfaces were predominantly flat, with a gradual reduction in the extent of shear lips at lower temperatures. The room temperature specimens displayed 2% oblique fracture, while liquid helium test specimens displayed less than 1%. The flat fracture surfaces were relatively rough at the higher temperatures, becoming smoother as temperature was reduced.

The K_{IC} data are shown in Figure 14 and Table 6. Between 295 and 4 K, there is a uniform reduction in fracture toughness amounting to approximately 19%. However, the difference in toughness between 77 and 4 K is negligable for this material.

Also shown in Figure 14 are the results reported by Vishnevsky and Steigerwald [22]. They obtained valid K_{IC} data from bend specimens at temperatures as low as 77 K. Their alloy was beta processed Ti-6Al-4V, solution treated at 1227 K (1750°F) for one hour and aged for two hours at 811 K (1000°F). Comparing the valid results at 295 and 77 K, the present data are in excellent agreement with Vishnevsky and Steigerwald's data.

There are other cryogenic fracture data for Ti-6Al-4V alloys [23-28], but the variety of specimen designs and sizes as well as the material condition makes direct comparison difficult. Some of these data are for thin sheet specimens that do not satisfy the thickness requirement for linear-elastic plane strain, while other results pertain to alloys having extra-low-interstitial impurity contents. The data in these references are all higher than the K_{IC} values shown in Figure 14.

CONCLUSIONS

(1) Fracture toughness and fatigue crack growth tests were performed at 4 K using approximately 10 liters of helium for each test. Stress intensity factors up to 110 $MN/m^{3/2}$ (100.2 ksi $\cdot$ $in^{1/2}$) can be produced with the cryostat described, and fatigue tests spanning several hours are accomplished without refilling.

(2) The conventional clip gage instrumentation can be used for fracture and fatigue testing in liquid helium if cryogenic strain gages and wiring procedures are used.

(3) The crack length can be inferred to within ± 1% using the compliance method. Changes in the compliance calibration with temperature can be compensated by shifting the theoretical calibration curve by an amount determined during the test itself.

(4) The crack growth rates of Ti-6Al-4V at 77 K and 4 K showed no significant departure from room temperature results.

(5) The fracture toughness of Ti-6Al-4V decreased from 47.4 $MN/m^{3/2}$ (43.2 ksi $\cdot$ $in^{1/2}$) at room temperature to 38.5 $MN/m^{3/2}$ (35.1 ksi $\cdot$ $in^{1/2}$) at liquid helium temperature. The change in fracture toughness with temperature was monotonic and no anomalies were observed at 4 K.

ACKNOWLEDGMENTS

This work was sponsored by ARPA in cooperation with the Naval Ship Research and Development Center. The cooperation of Dr. H. V. Vanderveldt of NSRDC is acknowledged. The authors thank Ralph Trapani for assisting in the experiments and data reduction. The helium dewar was fabricated by George Wallace.

REFERENCES

[1] J. G. Kaufman and E. T. Wanderer, Tensile properties and notch toughness of some 7XXX alloys at -452°F, Advances in Cryogenic Engineering, Vol 16, Ed. K. D. Timmerhaus, 27-36, Plenum Press, (1970).

[2] A. J. Nachtigall, Strain-cycling fatigue behavior of ten structural metals tested in liquid helium (4 K), in liquid nitrogen (78 K) and in ambient air (300 K), NASA TN D-7532, National Aeronautics and Space Administration, (1974).

[3] F. R. Schwartzberg, S. H. Osgood, R. D. Keys, and T. F. Kiefer, Cryogenic Materials Data Handbook, AFML-TDR-64-280, Martin Marietta Co., AD 609562, (1964).

[4] Standard method of test for plane-strain fracture toughness of metallic materials, E 399-74, Annual Book of ASTM Standards, Part 10, 432-451, Amer. Soc. Test. Mater., (1974).

[5] Tung Au and T. E. Stelson, Introduction to Systems Engineering, Deterministic Models, Addison-Wesley Publishing Co., (1969).

[6] D. N. Lyon, D. B. McWhan, and A. L. Stevens, Cryostat for studies at 100 kilobars at liquid helium temperatures, Rev. Sci. Instrum., Vol 38, No. 9, 1234-1240, (1967).

[7] V. J. Johnson, ed., A compendium of the properties of materials at low temperature, (Phase 1) Part II, WADD Tech. Report 60-56, (1960).

[8] R. D. McCarty, Thermodynamic properties of helium 4 from 2 to 1500 K at pressures to 10 Pa, Jnl. Phys. Chem. Ref. Data, Vol 2, No. 4, (1973).

[9] R. T. Jacobson, R. B. Stewart, R. D. McCarty, and H.J.M. Hanley, Thermophysical properties of nitrogen from the fusion line to 3500 R (1944 K) for pressures to 150,000 Psia (10342 x 10^5 N/m^2), NBS Tech. Note. 648, (1973).

[10] R. B. Jacobs, Liquid requirements for the cool-down of cryogenic equipment, Paper J-6 in Advances in Cryogenic Engineering, Vol 8, Ed. K. D. Timmerhaus 529-535, Plenum Press, (1963).

[11] J. E. Srawley and W. F. Brown, Jr., Plane Strain Crack Toughness Testing of High Strength Metallic Materials, ASTM STP 410, Amer. Soc. Test. Mater., (1969).

[12] J. G. Kaufman, Progress in fracture testing of metallic materials, Review of Developments in Plain Strain Fracture Toughness Testing, ASTM STP 463, 3-21, Amer. Soc. Test. Mater., (1970).

[13] E. J. Roberts Jr., Elastic crack-edge displacements for the compact tension specimen, Materials Research and Standards, MTRSA, Vol 9, No. 2, 27, (1969).

[14] W. F. Brown Jr. and J. E. Srawley, Commentary on present practice, Review of Developments in Plane Strain Fracture Toughness Testing, ASTM STP 463, 216-248, Amer. Soc. Test. Mater., (1970).

[15] E. R. Naimon, W. F. Weston, and H. M. Ledbetter, Elastic properties of two titanium alloys at low temperatures, Cryogenics, Vol 14, 246-249, (1974).

[16] G. R. Irwin, Fracture, Handbuch der Physik, Vol 6, 551-590, Springer-Verlag, (1958).

[17] E. F. J. Von Euw, R. W. Hertzberg, and R. Roberts, Delay effects in fatigue crack propagation, in Stress Analysis and Growth of Cracks, ASTM STP 513, 230-259, Amer. Soc. Test. Mater., (1972).

[18] P. C. Paris and F. Erdogan, A critical analysis of crack propagation laws, Jnl. Basic Eng. Trans., ASME, Series D, Vol 85, No. 4, 528-534, (1963).

[19] Damage Tolerant Design Handbook - A Compilation of Fracture and Crack-Growth Data for High Strength Alloys, Metals and Ceramics Information Center, Battelle Memorial Institute, Columbus, Ohio, (1972).

[20] R. J. Bucci, P. C. Paris, R. W. Hertzberg, R. A. Schmidt, and A. F. Anderson, Fatigue threshold crack propagation in air and dry argon for a Ti-6Al-4V alloy, in Stress Analysis and Growth of Cracks, ASTM STP 513, 125-140, Amer. Soc. Test. Mater., (1972).

[21] R. P. Wei and D. L. Ritter, The influence of temperature on fatigue-crack growth in a mill annealed Ti-6Al-4V alloy, NASA-CR-127042, Lehigh Univ., (1972).

[22] C. Vishnevsky and E. A. Steigerwald, Fracture toughness of some cryogenic materials at room and subzero temperatures, Fracture Toughness Testing at Cryogenic Temperatures, ASTM STP 496, 3-26, Amer. Soc. Test. Mater. (1970).

[23] W. E. Witzell, Fracture data for materials at cryogenic temperatures, Tech. Report, AFML-TR-67-257, General Dynamics Convair, AD 825264, (1967).

[24] C. F. Tiffany and P. M. Lorenz, An investigation of low cycle fatigue failure using applied fracture mechanics, Tech. Doc. Report ML-TDR-64-53, Boeing Co., (1964).

[25] L. R. Hall, Plane-strain cyclic flaw growth in 2014-T62 aluminum and 6Al-4V(Eli) titanium, N69-20265, NASA-CR-72396, Boeing Co., (1968).

[26] E. T. Wessel, W. G. Clark, and W. K. Wilson, Engineering methods for the design and selection of materials against fracture, AD 801500, Westinghouse Research Labs., (1966).

[27] W. D. Bixler, Comparison of flaw growth characteristics under cryogenic proof and ambient test conditions for apollo titanium pressure vessels, N70-18309, Boeing Co., (1970).

[28] F. R. Schwartzberg, A review of cryogenic fracture toughness behavior, paper G-1 in Advances in Cryogenic Engineering, Vol 12, ed. K. D. Timmerhaus 453-472, Plenum Press (1967).

Table 1. Data for cryogenic fluids

Fluid	cost per liter[a] ($)	boiling point, 1 atm (K)	heat of vaporization [7] (kJ/ml)	density of liquid [7] (gm/ml)
Nitrogen	.25	77.4	1.410	0.808
Helium	5.50	4.2	2.562	0.125

[a] Can vary by a factor of two or three.

Table 2. Enthalpy of helium at 1 atm [8]

sat. liquid, 4 K (J/gm)	Sat. vapor, 4 K (J/gm)	75 K (J/gm)
9.71	30.13	404.4

Table 3. Chemical analysis of Ti-6Al-4V alloy (wt%)

Ti	Al	V	Fe	C	O	N	H
bal.	6.24	4.18	.174	.033	.155	.011	14ppm

Table 4. Mechanical properties at 295 K

0.2% yield stress (MN/m^2)	ultimate strength (MN/m^2)	elongation in 4D (%)	reduction in area (%)
942	993	16.3	26.4

Table 5. Dimensionless stress intensity factors and displacements for the compact specimen [13].

$\frac{a}{W}$	$\frac{KBW^{1/2}}{P}$	$\frac{EBv}{P}$[a]
0.30	5.85	25.1
0.35	6.54	30.1
0.40	7.33	36.0
0.45	8.34	43.4
0.50	9.60	53.0
0.55	11.26	66.4
0.60	13.62	85.8
0.65	16.84	115.4
0.70	21.56	162.8

[a] E is Young's modulus and v is deflection at the specimen edge.

Table 6. Fracture toughness results for Ti-6Al-4V

Specimen (No.)	Temperature (K)	Fracture toughness, K_{IC} $MN/m^{3/2}$
A12	295	47.3
A15	295	46.9
A16	295	49.4[a]
A18	295	48.1
		avg = 47.4
A13	195	42.2[b]
A14	195	39.8[b]
		avg = 41.0
A6	77	37.7
A7	77	38.1
A8	77	40.8
A9	77	38.7
		avg= 38.8
A10	4	39.0
A11	4	38.2
A21	4	38.2
		avg= 38.5

[a] Invalid; fatigue stress intensity exceeded 0.6 K_{IC}.

[b] Invalid; irregular crack front.

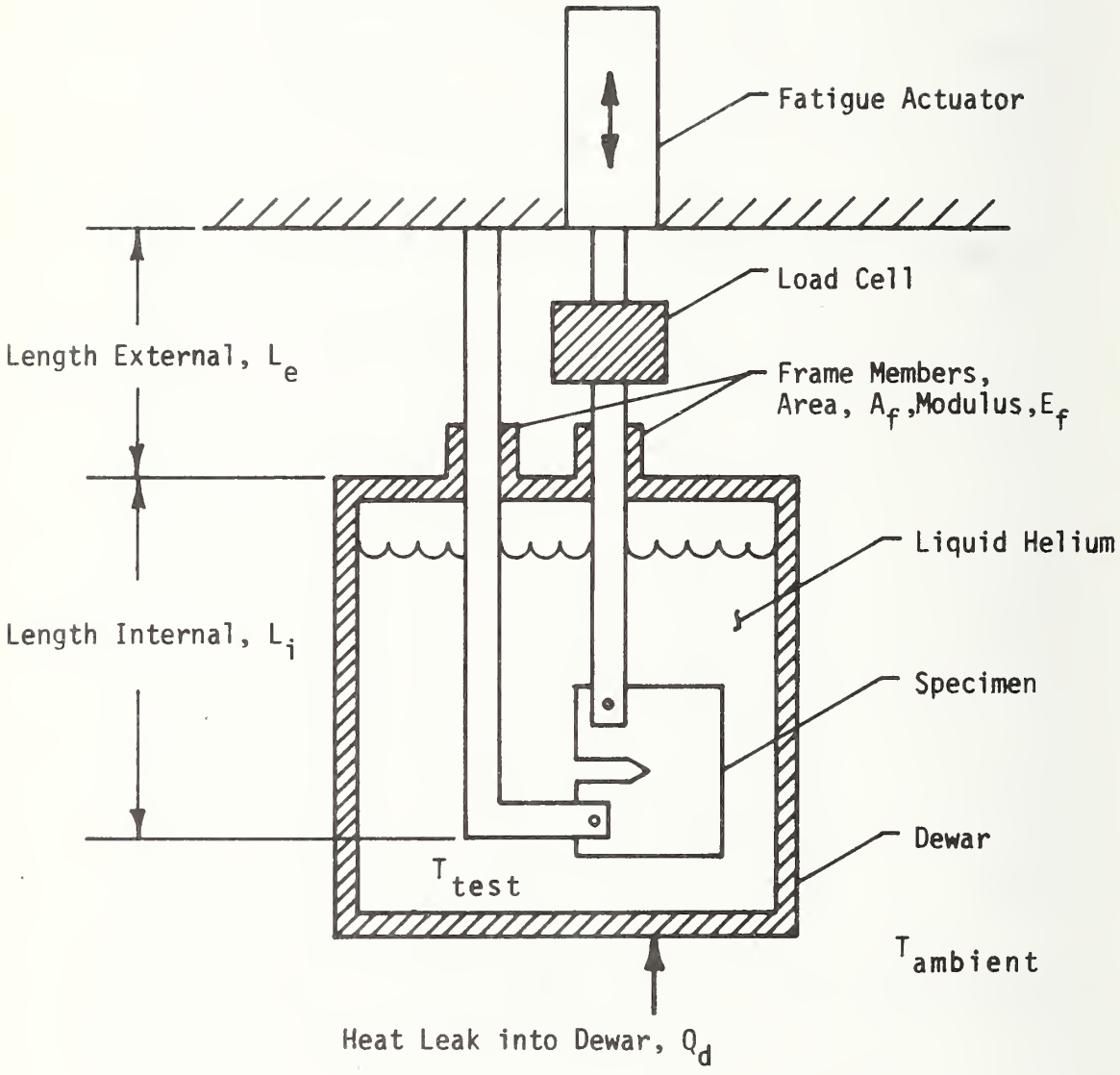

Figure 1. Simplified model of fatigue cryostat used in the optimization analysis.

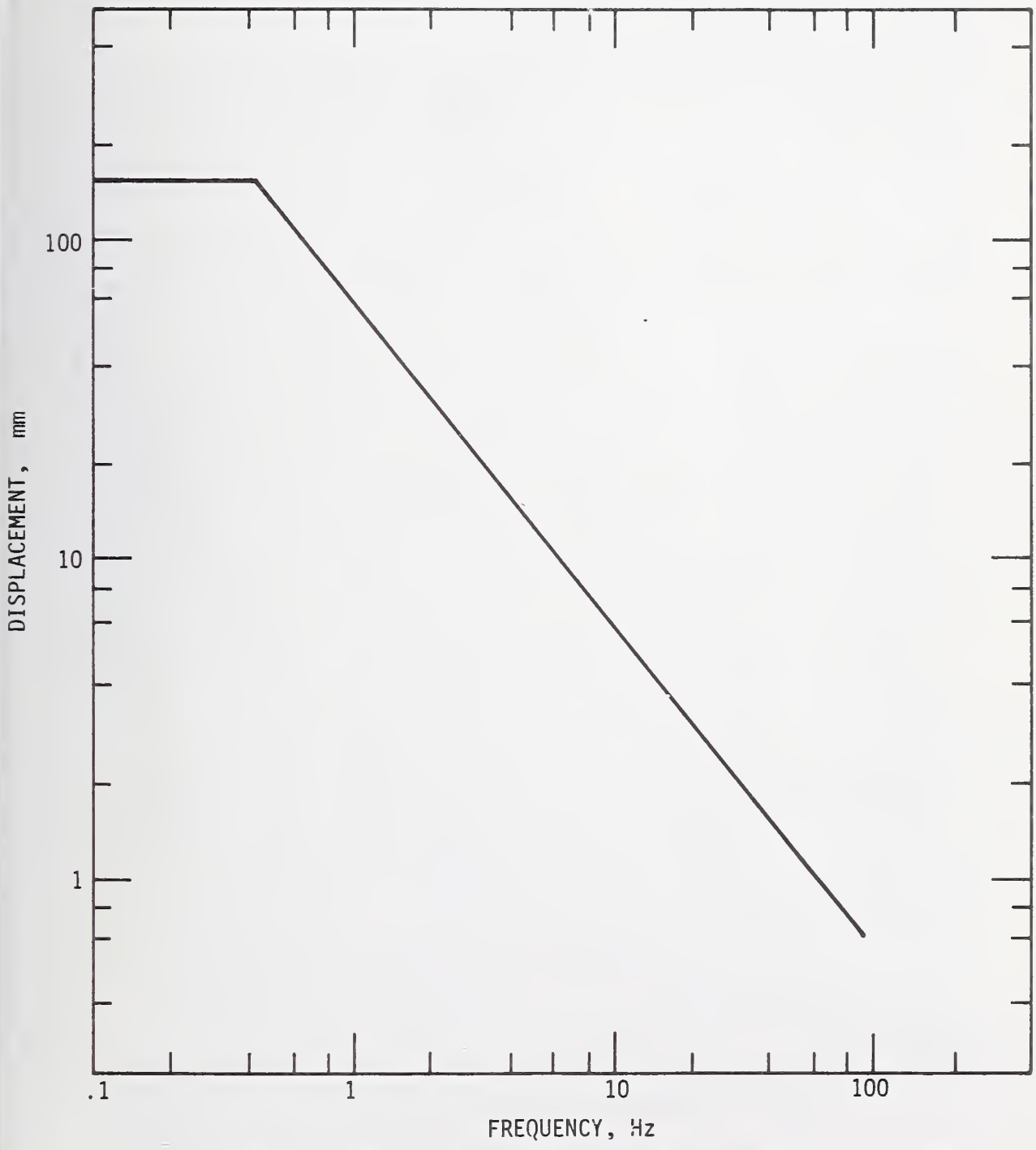

Figure 2. Performance of 100 kN fatigue testing machine

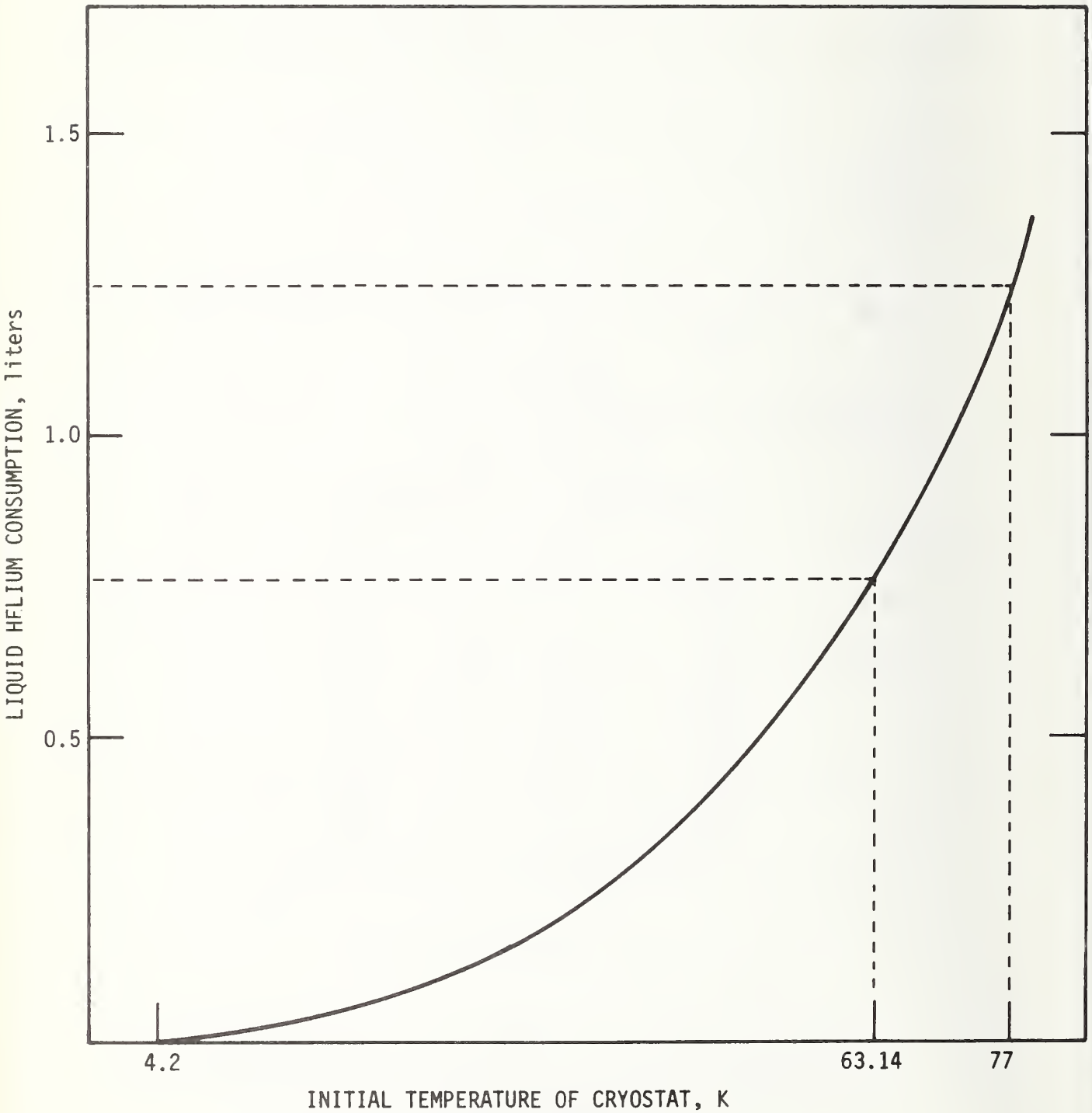

Figure 3. Liquid helium consumption for ideal or isothermal cool-down from various initial temperatures.

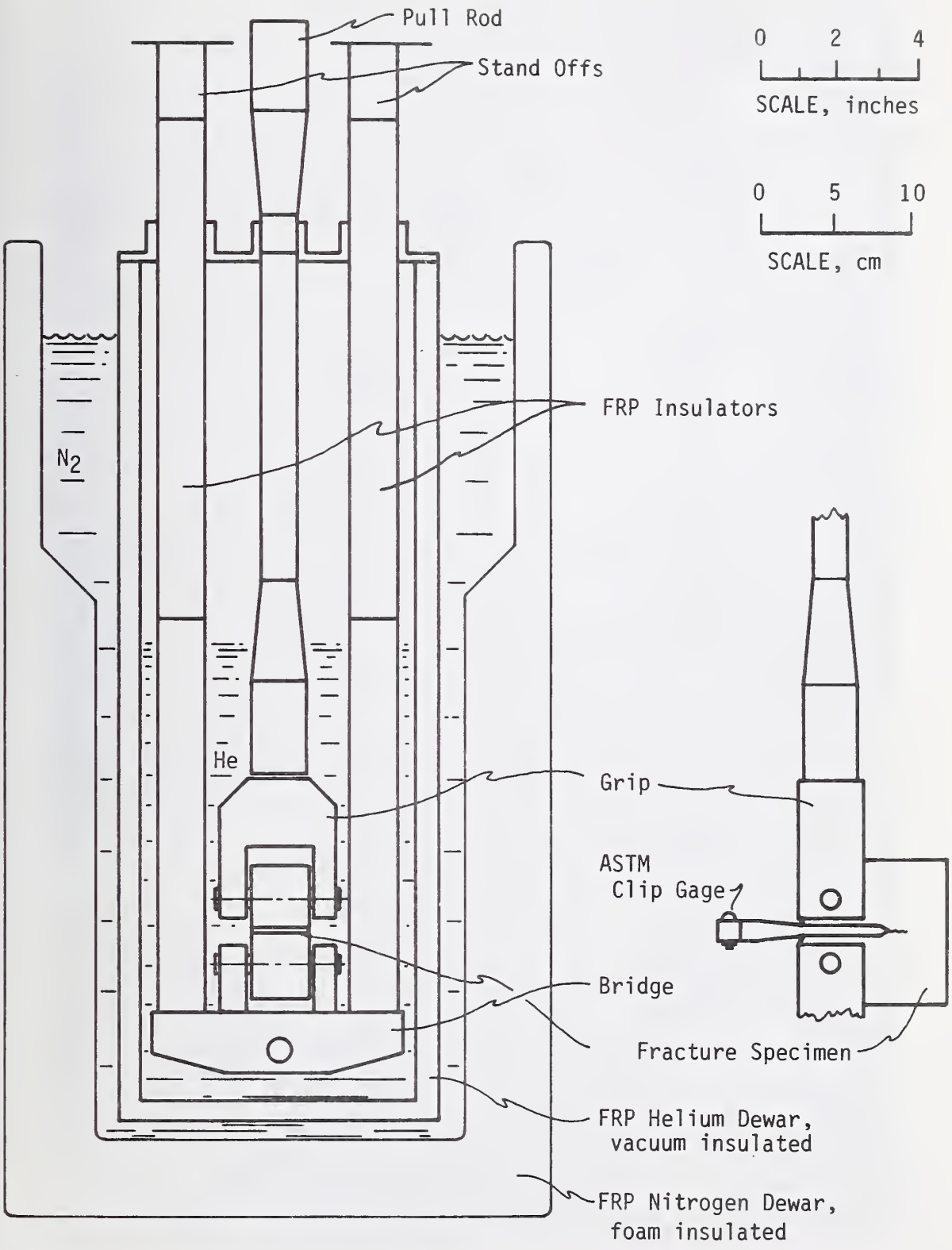

FIGURE 4 - Liquid helium fatigue cryostat.

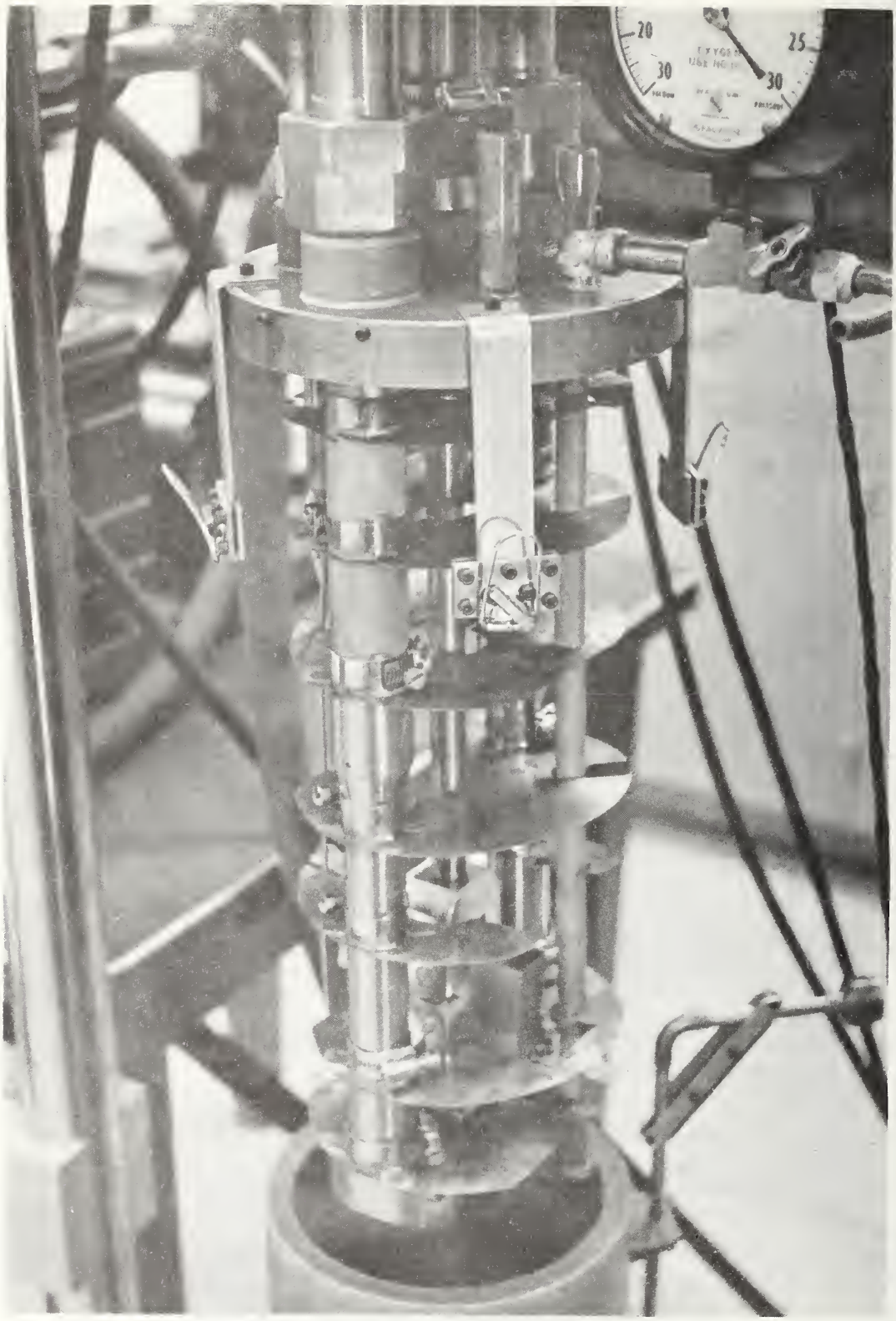

Figure 5. Helium fatigue cryostat (with copper baffles).

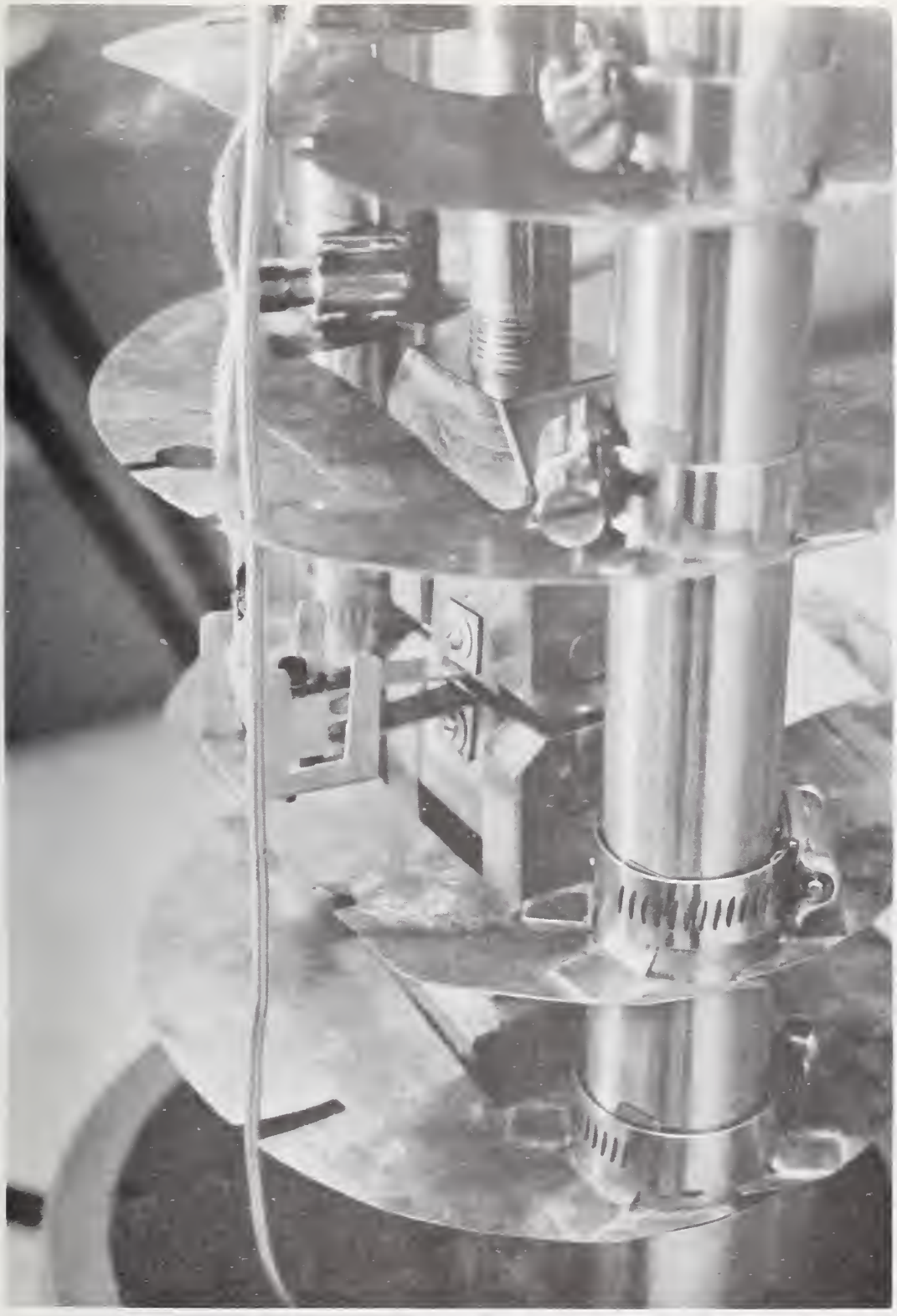

Figure 6. Specimen and clip gage positioned in fatigue cryostat.

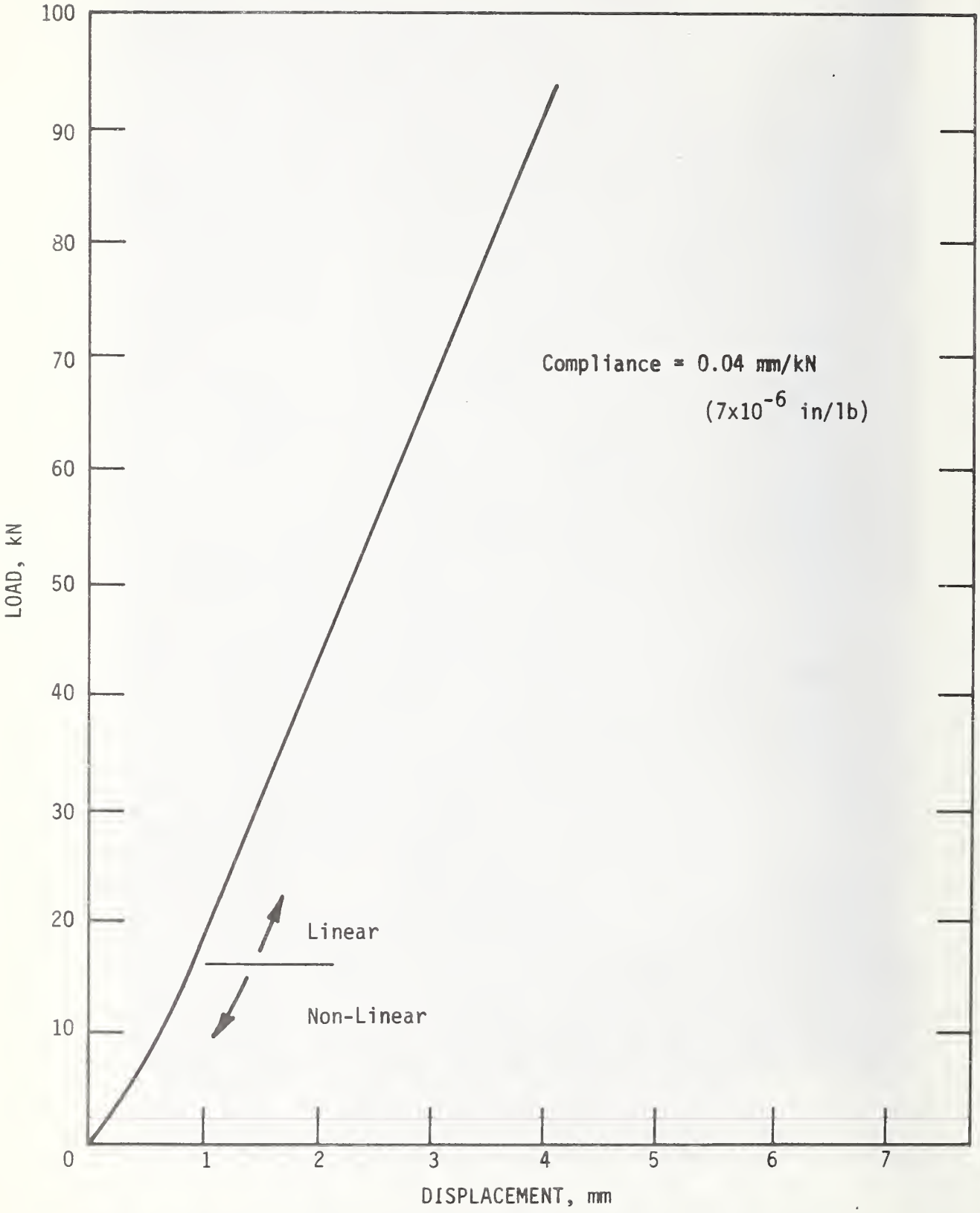

Figure 7. Compliance calibration of cryostat frame at 77 K.

Figure 8. Cryogenic fatigue testing apparatus.

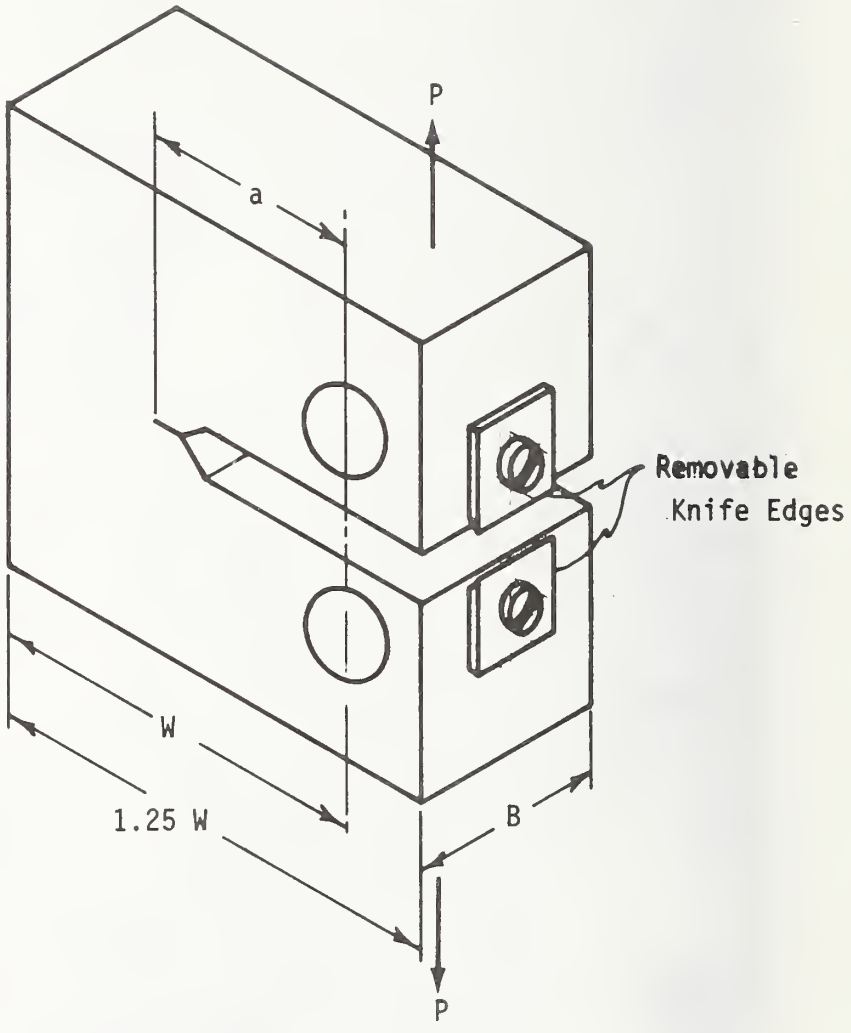

B = 2.54 cm

W = 5.08 cm

Figure 9. Compact specimen.

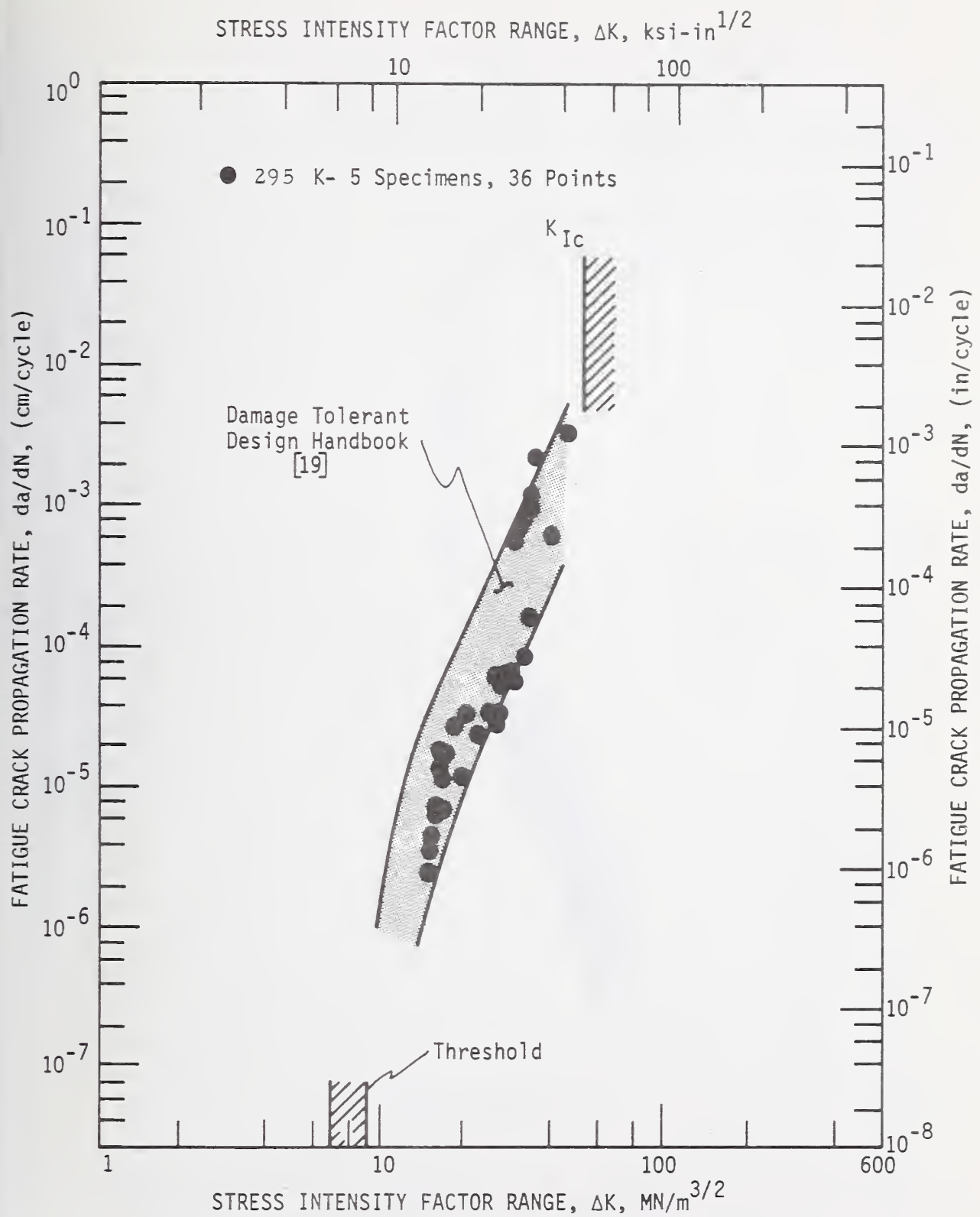

Figure 10. Room temperature growth rate data.

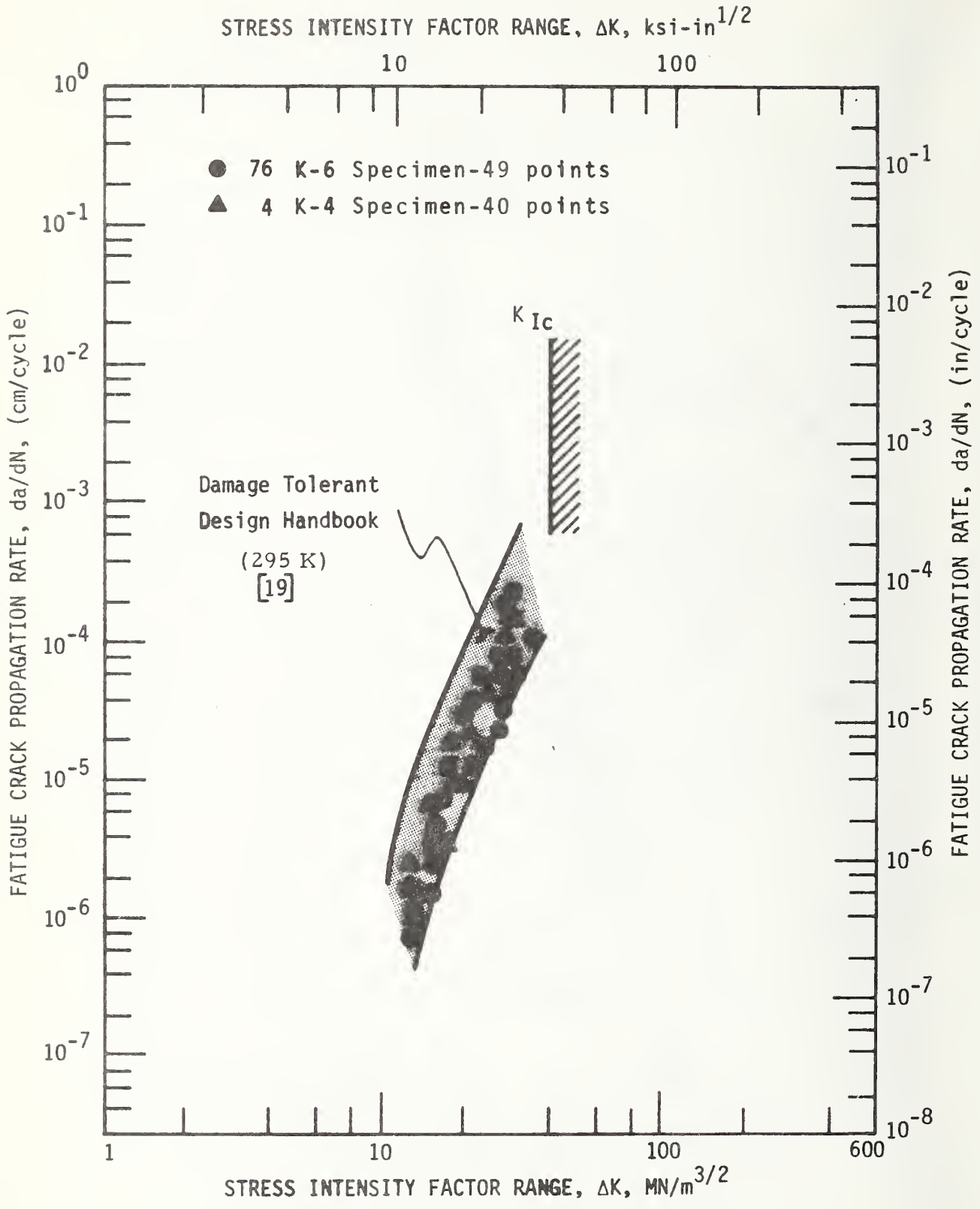

Figure 11. Crack growth data at 76 K and 4 K.

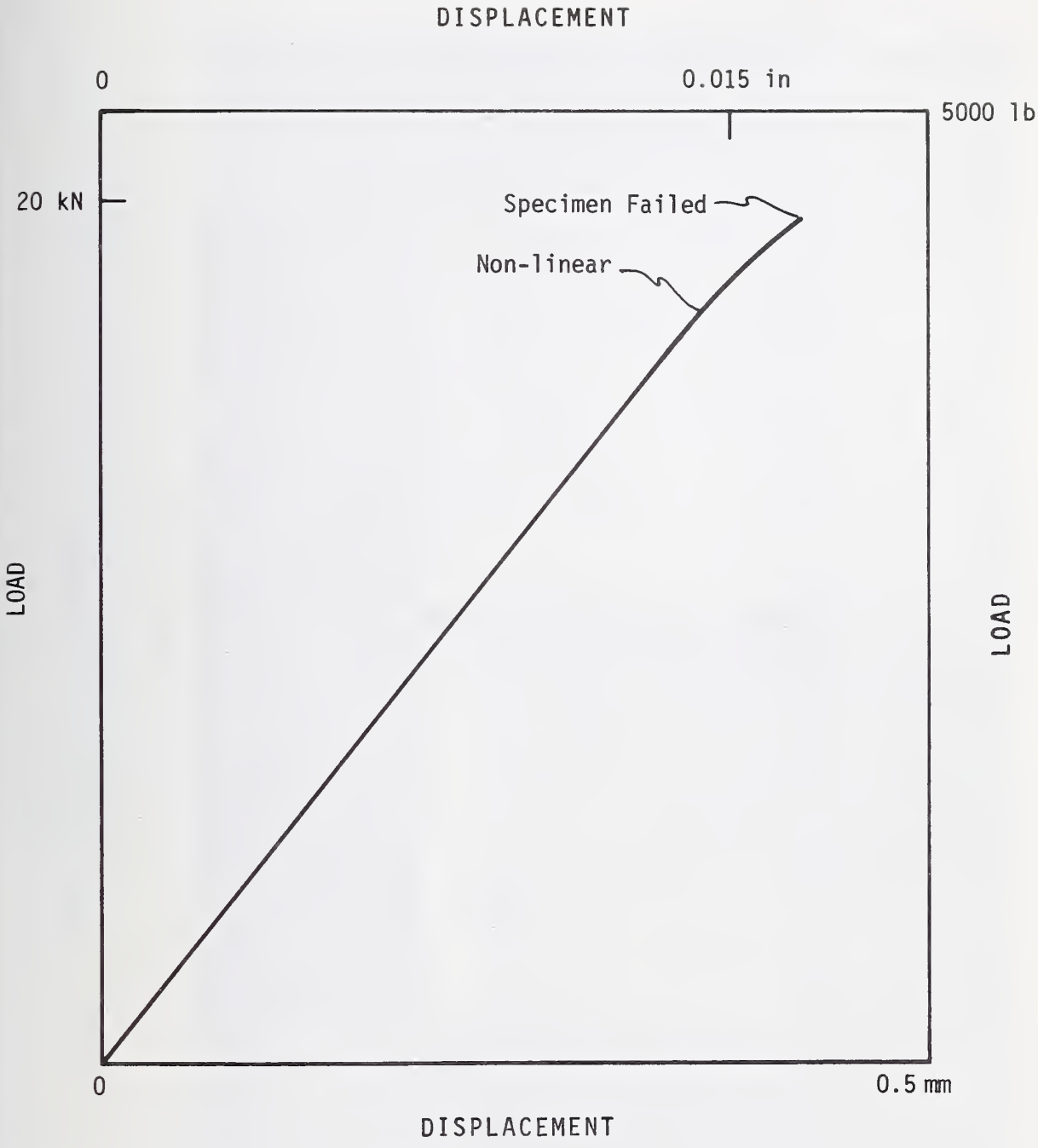

Figure 12. Typical load-displacement record at 4 K for Ti-6Al-4V.

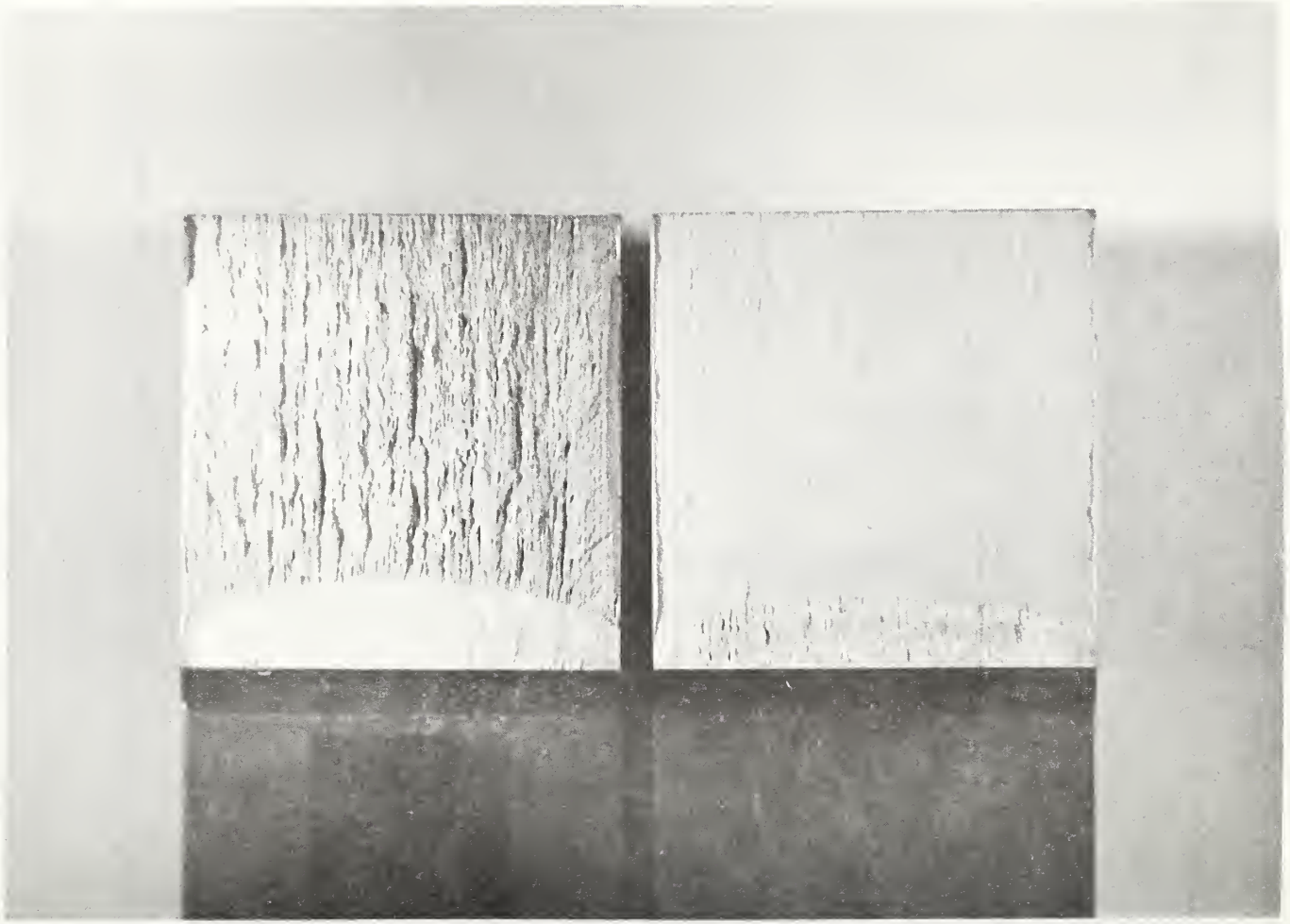

Figure 13. Surface appearance of Ti-6Al-4V specimens fractured at 295 K (left) and 4 K (right).

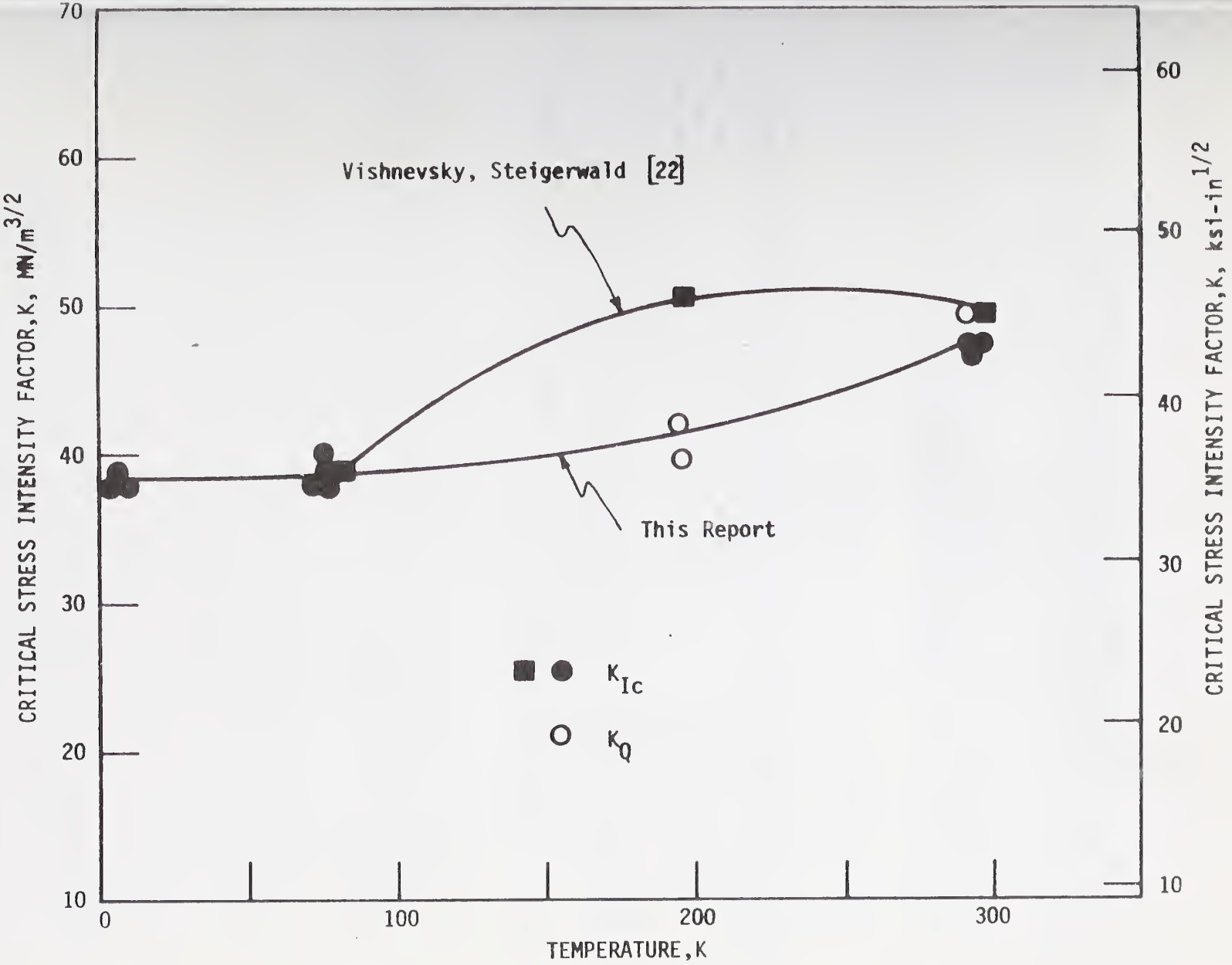

Figure 14. Temperature dependence of fracture toughness for Ti-6Al-4V.

FATIGUE CRACK GROWTH AND J-INTEGRAL FRACTURE PARAMETERS OF Ti-6Al-4V AT AMBIENT AND CRYOGENIC TEMPERATURES*

R. L. Tobler

Cryogenics Division
Institute for Basic Standards
National Bureau of Standards
Boulder, Colorado 80302

Abstract

Fatigue crack propagation and fracture parameters for 2.030 cm-thick compact specimens of an extra-low-interstitial Ti-6Al-4V alloy were measured at temperatures between 295 K and 4 K. The fatigue-crack growth rates (da/dN) were temperature independent at stress intensity ranges (ΔK) from 10 to 20 $MN/m^{3/2}$. Above 20 $MN/m^{3/2}$, the rates increased with decreasing temperature. Plane-strain linear-elastic and J-integral fracture test results were in good agreement: the fracture toughness of this alloy decreased from about 110 $MN/m^{3/2}$ at room temperature to 54 $MN/m^{3/2}$ at 4 K, with a ductile-to-brittle fracture transition occurring in the range 125 K to 76 K. These fatigue and fracture results are compared with data previously reported for a normal-interstitial Ti-6Al-4V alloy.

Key Words: Fatigue crack propagation; fracture toughness; J-integral; low temperature tests; titanium alloys.

* This work was sponsored by Kirtland Air Force Base and the Advanced Research Projects Agency; it is a contribution of NBS, not subject to copyright.

Introduction

High ratios of strength-to-density and strength-to-thermal conductivity make titanium-6% aluminum-4% vanadium (Ti-6Al-4V) an attractive aerospace and cryogenic structural material. Often, service temperatures span the ambient to cryogenic range, and the mechanical properties at low temperatures may be critical in design.

Temperature reductions increase the yield strength and decrease the ductility of Ti-6Al-4V [1], resulting in flaw-sensitive mechanical behavior. The normally ductile material may fail in a relatively brittle manner in the presence of a fatigue crack under conditions of plane strain. A fracture mechanics analysis is often the best means of assuring structural reliability and design efficiency.

The few fracture data for Ti-6Al-4V (ELI) alloys at cryogenic temperatures are insufficient: crack growth rate data at low temperatures are rare [2], fracture toughness data for thin sheet or plate [3-5] do not provide valid K_{IC} data over the entire cryogenic to ambient range, and no data exist below liquid hydrogen temperature. The present paper provides some needed fracture toughness and crack growth rate parameters with emphasis at the temperatures 295, 76 and 4 K. Linear-elastic fracture mechanics and J-integral test results are compared, and the existence of a ductile-to-brittle transition in this material is demonstrated.

Linear Elastic Fracture Mechanics

If a negligible amount of plastic deformation occurs prior to fracture, the ASTM Method of Test for Plane Strain Fracture Toughness of Metallic Materials (ASTM E-399-74) can be applied. This method utilizes the stress intensity factor, K, to describe fracture behavior. For specimens of a standard geometry, K is calculated from the relation:

$$K = \frac{P}{BW^{1/2}} \quad [f(a/W)] \tag{1}$$

where P is applied load, B is specimen thickness, W is specimen width, a is crack length, and f(a/W) is a factor dependent on relative crack length. Linear elastic conditions prevail for thick specimens where the plastic zone at the crack tip is constrained by the surrounding bulk of elastically loaded material. Under these conditions, materials loaded in tension exhibit a critical stress intensity K_{IC} at which failure occurs spontaneously without significant plastic deformation.

The parameter K_{IC} is a material property and a useful design criterion. Provided that specimen size requirements are met, K_{IC} can be calculated from Eq. (1) using the secant load P_Q, determined from the fracture test record according to ASTM E-399-74. The size criterion assuring linear elastic behavior and valid K_{IC} data is:

$$a,\ b,\ B \geq 2.5 \left(\frac{K_{IC}}{\sigma_y} \right)^2 \tag{2}$$

where σ_y is the 0.2% offset yield strength of the material and b is the specimen ligament (b = W-a). Subsized specimens yield invalid fracture toughness measurements that are denoted K_Q.

J-integral Analysis

Specimens that do not satisfy the thickness requirement of Eq. (2) exhibit nonlinear load-deflection behavior due to plastic deformation at the crack tip. In such a case, elastic stress field descriptors are not relevant, but the path-independent J-integral formulated by Rice [6] may be used to characterize fracture.

For nonlinear-elastic materials, J represents the change of potential energy with respect to crack extension. Experimentally, the J-integral can be evaluated as an energy proportional to the area (A) under the load-versus-loadline deflection (δ) curve of a precracked specimen tested in tension or bending. The critical value, J_{IC}, has been defined as the value of J required to initiate crack extension. Although a standard test procedure has not yet been developed, experiments by Begley and Landes [7-9] and others demonstrated that J_{IC} is a meaningful fracture parameter for linear-elastic, elastic-plastic, or fully plastic behavior. Recent applications include tests of Ti-6Al-4V at room temperature [10,11].

For standard compact specimens, J can be calculated using either of two equations. Assuming the specimen is in a state of pure bending, the following expression was derived [12]:

$$J = \frac{2A}{Bb} \tag{3}$$

This equation is conservative to some degree, but it yields adequate results for deeply cracked specimens where the assumption of pure bending is more appropriate [12]. Merkle and Corten pursued a more exact solution for the compact specimen, accounting for axial force as well as bending [13]:

$$J = \frac{\lambda_J A}{Bb} \tag{4}$$

Here, λ_J is a factor ranging from 2.55 to 2.31, dependent on relative crack length [13]. This expression applies to a wider range of a/W, but data quantifying the scope and accuracies of Eqs. (3) and (4) are lacking. Therefore, the present paper includes a comparison of critical J values calculated from both equations. The comparison is made for a range of a/W, in the linear-elastic case, where K_{IC} data are also calculated using ASTM E-399-74 methods.

Since the J-integral applies to plane strain, a size criterion is necessary to insure that results will be independent of specimen dimensions and geometry. A tentative criterion is [9]:

$$a,\ b,\ B \geq \alpha \left(\frac{J_{IC}}{\sigma_y} \right) \tag{5}$$

where α is a factor of 50. The specimen need not be as large as that required for linear-elastic tests; yet, the parameter J_{IC} can be converted to K_{IC} using the relation [7]:

$$K_{IC}^2 = \frac{E}{1 - \nu^2} \cdot J_{IC} \tag{6}$$

where E is Young's modulus and ν is Poisson's ratio. Thus, it is possible to derive the linear-elastic fracture toughness value from smaller, plastic J-integral test specimens. In this paper, the symbol $K_{IC}(J)$ distinguishes values obtained using Eq. (6) from K_{IC} data determined according to ASTM E-399-74.

Material and Specimen

Stock of an extra-low-interstitial (ELI) Ti-6Al-4V alloy produced to AMS 4930 specifications was obtained in the form of a 2.54 cm-thick forged ring, 101.6 cm I.D. by 106.7 cm O.D. The material was commercially annealed at 977 $\pm$ 14 K for two hours, air-cooled, and descaled. The microstructure, shown in Figure 1, was primary alpha and beta with an average alpha grain diameter of 0.013 mm. The chemical analysis is listed in

Table 1, and mechanical properties at primary temperatures of interest are listed in Table 2. The tensile properties were measured at room temperature according to ASTM method E8-69, or estimated at cryogenic temperatures from handbook data [1].

All tests were performed using compact specimens of the geometry shown in Figure 2. The specimen proportions were in general accordance with ASTM E-399-74, but a modified notch was introduced to enable loadline deflection measurements. The specimen thickness was 2.030 cm, the width-to-thickness ratio, W/B, was 2.0, and the orientation was LT [14].

Procedure

Young's modulus and Poisson's ratio were measured at room temperature using the ultrasonic pulse-superposition method. The results were equivalent ($\pm$ 1%) to those reported for a similar heat [15]. Since the elastic properties of Ti-6Al-4V are regular functions of temperature, Naimon, Weston, and Ledbetters' values of E and ν at low temperatures could be used with good accuracy [15].

Fatigue and fracture tests were performed using a 100 kN capacity servo-hydraulic testing machine and cryostat. As previously described [16], a vacuum insulated dewar containing liquid nitrogen or liquid helium encloses the load frame, specimen, and clip gage during tests at 76 K or 4 K. In this study, intermediate temperatures were obtained by admitting cold nitrogen vapor to the dewar. A chromel-constantan thermocouple was attached to the specimen during these tests and a servo-mechanical temperature controller regulated the vapor flow such that temperatures of 200, 125, and 110 K were maintained within $\pm$ 3 K. Clip gage calibrations at temperatures from 295 to 4 K verified that the gage sensitivity changed by only 1.5% and linearity corresponded to ASTM E-399-74 requirements.

Using load control, the specimens were precracked and then fractured at identical temperatures. The loading rate to fracture corresponded to a stress intensity factor increase of about 1.0 $MN/m^{3/2}$ per second. Critical stress intensity factors were calculated using Roberts' [17] solution for f(a/W). The J-integral calculations were performed for the same specimens using Eqs. (3) and (4) where the area, A, was measured with a planimeter at points of interest, and λ_J values were interpolated from the published solution [13].

For low temperature tests, fracture toughness calculations were performed at the load point P_Q, in accordance with ASTM E-399-74, and at other points described in the text. At room temperature, stable crack extension occurred and the J-resistance curve (J versus Δa) was determined following a procedure outlined by Begley and Landes [9]. Six identical specimens (a/W = 0.578 $\pm$ 1%) were loaded to cause decreasing amounts of crack extension. These specimens were then unloaded and heat tinted 15 minutes at 900 K to oxidize the surfaces where crack extension had taken place. The specimens were finally fractured into halves and the increments of crack extension, Δa, were measured with a traveling microscope at locations corresponding to 25, 50 and 75% of specimen thickness.

Most fatigue crack growth data were obtained during precracking of fracture toughness specimens. The maximum fatigue stress intensity, K_f, was maintained within ASTM E-399-74 specifications. At each temperature (295, 76 and 4 K), one additional specimen was tested solely for crack growth data at higher stress intensity factors.

Fatigue crack growth was monitored by elastic compliance measurements, an approach based on the fact that specimen compliance, δ/P, increases with increasing crack length. The correlation between crack length and compliance was determined experimentally by plotting the crack lengths of fractured specimens versus the dimensionless parameter EB δ/P. Changes in clip gage sensitivity and Young's modulus with temperature were accounted for in the term EB δ/P, and, as shown in Figure 3, the results were in agreement with predictions based on Roberts' solution [17].

Crack growth rates were determined by plotting the static compliance with an X-Y recorder at intervals during the fatigue tests. Using the correlation shown in Figure 3, the average crack length could be inferred at any time to $\pm$ 1%. The crack lengths were

plotted versus cycles, N, and the growth rates, da/dN, were obtained by graphical differentiation. Stress intensity factor ranges, ΔK, were calculated as the difference between the maximum and minimum fatigue stress intensities.

The loads during fatigue were measured to $\pm$ 1% by means of a digital peak load indicator. The load cycle was sinusoidal at a frequency of 20 Hz and a minimum/maximum load ratio of 0.1.

Results

Fatigue Crack Growth

Fatigue crack growth rates are shown in Figure 4. The data define a slightly curved scatter band that increases in width at higher stress intensity ranges. Below ΔK = 20 $MN/m^{3/2}$ the rates at 295, 200, 76 and 4 K are nearly equivalent and no effect of temperature can be distinguished from the scatter among specimens. Above 20 $MN/m^{3/2}$, the data appear to diverge according to temperature. In this region of high ΔK, the rates are lower at room temperature than at 76 K or 4 K.

As shown in Figure 4, the results are best approximated by straight line segments intersecting at ΔK = 20 $MN/m^{3/2}$. The equations describing these line segments are of the form suggested by Paris and Erdogan [18,19]:

$$\frac{da}{dN} = C(\Delta K)^n \qquad (7)$$

where C and n are empirical constants. The C and n values, which govern growth rates for various conditions of temperature and ΔK, were determined graphically and are specified in Table 3.

A single "Paris" equation, integrated, is sometimes preferred to calculate increments of crack growth over wide ranges of ΔK. The present data at 4 K could be closely approximated by a single straight line over the range of ΔK from 10 to 30 $MN/m^{3/2}$, but other data in Figure 4 and elsewhere [20-22] do not conform with a single-equation format. Since growth rates are highly sensitive to ΔK, practical applications of these data should incorporate duplicate sets of C and n values at each temperature, depending on the stress intensity factor range, as shown in Table 3.

A band representing data for a normal interstitial grade of Ti-6Al-4V is superimposed on the present results in Figure 5. Similarly, data for the normal grade were obtained at 295, 76, and 4 K, but the results were temperature-independent over the range of ΔK investigated [16]. The overlap of bands in Figure 5 suggests that a variation in the level of interstitials does not heavily influence the growth rates of these alloys.

Fracture Toughness

Macroscopic features of specimens loaded directly to failure are shown in Figure 6. The fracture surfaces indicate decreasing toughness at cryogenic temperatures. Slant and flat fracture modes are evident at each temperature, but the proportion of slant fracture at specimen edges decreases from 23% at room temperature to 5% at 4 K. Also, the flat fracture region becomes progressively smoother as temperature is lowered from 295 to 4 K. Similar trends but less noticeable changes were reported for the normal interstitial alloy [16].

The variety of P-δ behaviors observed is shown in Figure 7. A transition from elastic-plastic to linear-elastic behavior occurs at about 125 K, and at 110 K the behavior is ideally linear-elastic. At more extreme temperatures, fast fracture terminates the curves after a series of pop-ins, increments of unstable crack extension. The pop-ins, which were faint and sometimes barely perceptible, produced small step-like discontinuities

beginning at about 0.95 P_Q. Thus, specimens at 76 K and 4 K failed in linear-elastic plane-strain, but deviations from the initial P-δ slopes are evident. Table 4 cites the relationships among P_Q, P_{max}, and the load at the first noticeable pop-in, P_p.

Linear-elastic Fractures

Of all the results summarized in Tables 5-7, the test at 110 K affords the simplest interpretation. The K_{IC} and J_{IC} measurement point at this temperature is unambiguous since $P_p = P_Q = P_{max}$. The linear-elastic K_{IC} result (78 $MN/m^{3/2}$) is in good agreement with the $K_{IC}(J)$ value (81.4 $MN/m^{3/2}$) obtained using Eqs. (4) and (6). The ratio $K_{IC}(J)/K_{IC}$ is 1.04, indicating that the results from two test procedures are equivalent within 4% for an ideal linear-elastic P-δ record.

The K_{IC} data obtained at 76 and 4 K are shown in Table 5. The J-integral was evaluated at the K_{IC} measurement point, P_Q, and the results denoted J_Q are listed in Table 6. In comparison, the ratios of $K_Q(J)/K_{IC}$ ranged from 1.03 to 1.12, indicating wider disagreement than observed at 110 K. This is due to the effects of pop-ins on J-integral calculations. Pop-in phenomena at these lower temperatures violate the assumption of monotonic loading made in the J-integral formulation [6]. Complete agreement between J and K measurements is expected only if comparison is made at identical points on a perfectly linear P-δ record. At 76 and 4 K, the $K_Q(J)$ values exceed the values of K_{IC} because pop-ins prior to P_Q increase the area under the test records without proportionate increases in load.

In this study, errors in J-integral calculations at P_Q due to slight nonlinearity or pop-in were corrected as shown in Figure 8. According to this procedure, the initial linear slope of the P-δ record is extrapolated up to a point P_Q', which is equal in magnitude to P_Q, and J is calculated from the triangular area $OP_Q'\delta'$:

$$J = \frac{\lambda_J}{Bb} \left(\frac{1}{2} P_Q'\delta' \right) \tag{8}$$

where δ' is the hypothetical deflection associated with P_Q', as defined in the figure. Values of J adjusted by measuring at P_Q' are labelled J_{IC} in Table 8. The correction brings $K_{IC}(J)$ and K_{IC} data into agreement within 4%, which is equivalent to the agreement at 110 K where no correction was necessary. The correction procedure was also applied to the test record at 125 K where nonlinearity was apparently due to stable crack extension.

The J-integral calculations above incorporated the values of λ_J. Using $J = 2A/Bb$, where λ_J is replaced by the constant 2, yields underestimates of the fracture parameters. At 110 K, the critical stress intensity factor converted from $J = 2A/Bb$ underestimated K_{IC} by 6%. At 76 K and 4 K, similar calculations at P_Q' yielded conservative errors as high as 10%, the results varying as a function of a/W as shown in Figure 9. For a/W equivalent to 0.6 or greater, the disparity amounts to 4 or 5%. Merkle and Corten's expression for J, Eq. (4), appears to be more accurate, leading to critical J and converted K values that overestimate K_{IC} by an average of about 3% over the range of a/W from 0.45 to 0.70.

Elastic-plastic Fractures

A single test at 200 K did not yield a K_{IC} datum. The ASTM E-399-74 requirement that $P_{max}/P_Q \leq 1.10$ was not satisfied at this temperature. Nor could $K_{IC}(J)$ be obtained, since the J_{IC} measurement point could not be identified from the test record.

At room temperature one specimen was loaded to the point of fast fracture, while six others were unloaded at points along the P-δ diagram as shown in Figure 10. The corresponding values of J and Δa are listed in Table 7 and the J-resistance curve is shown in Figure 11.

There is some data scatter, but the resistance curve appears to rise steeply over the initial portion, becoming linear at crack extensions greater than 0.12 mm. Since methods of defining a discrete J_{IC} measurement point for such a curve have not been standardized, several plausible alternatives are considered here:

1. The trend at high Δa may be linearly extrapolated to $\Delta a = 0$, identifying J_{IC} as the intercept on the J axis [23]. The broken line in Figure 11 indicates in this case that $J_{IC} \simeq 88$ kJ/m^2.

2. As described elsewhere [9,24], the line $J/2\sigma_y$ may be constructed, its intersection with the resistance curve representing J_{IC}. Applied to Figure 11, this method yields $J_{IC} = 94$ kJ/m^2.

3. A significant amount of crack extension, Δa_c, may be defined as critical. Since good results for Ti-6Al-4V alloys were obtained by specifying $\Delta a_c = 1\%$ [11], the same criterion might be applied here. Then, the resistance curve at 1% crack extension yields $J_{IC} = 108$ kJ/m^2.

Summarizing, the J_{IC} value at room temperature lies in the range 98 ± 10 kJ/m^2, depending on the method applied to select the measurement point from the resistance curve of Figure 11. The corresponding values of $K_{IC}(J)$ given by Eq. (6) are in the range 110 ± 6 MN/m$^{3/2}$. This range of $K_{IC}(J)$ is in close agreement with valid room temperature ASTM E-399 test results for other ELI grade Ti-6Al-4V alloys; K_{IC} values from 102 to 121 MN/m$^{3/2}$ have been reported [25,26].

The J-integral specimen thickness criterion was amply satisfied. Using the $K_{IC}(J)$ value in Eq. (2), it is estimated that a 4.5 cm-thick specimen would be required to produce linear-elastic fractures in this material at room temperature. Thickness criteria calculations are summarized in Table 8.

Effect of Temperature

The specimen strength ratio, R_{Sc}, is listed for each temperature in Table 5. Defined according to ASTM E-399-74, R_{Sc} is the ratio of the maximum nominal net-section fracture stress to the tensile yield strength:

$$R_{Sc} = \frac{2P_{max}(2\ W + a)}{B(W-a)^2\sigma_y} \tag{9}$$

Referring to R_{Sc}, Section 4.1.3 of ASTM E-399-74 states that: "It is significant as a comparative measure of material toughness when results are compared from specimens of the same form and size, and when this size is sufficient that the limit load of the specimen is a consequence of pronounced crack extension prior to plastic instability ....".

As a qualitative parameter, R_{Sc} can be used here to rank the effect of temperature on toughness. The observed increase of R_{Sc} between 125 and 295 K implies that J_{IC} for this material at room temperature should exceed 82.5 kJ/m^2, the J_{IC} value at 125 K. Consequently, 82.5 kJ/m^2 could be taken as a lower bound for J_{IC} at room temperature. Critical values from 88 to 108 kJ/m^2 were obtained from Figure 11 and, although these values could vary

depending on how the resistance curve is drawn to account for scatter, it appears that the J-integral results at 295 K are consistent with the linear-elastic results at lower test temperatures.

The temperature dependence of K_{IC} is shown in Figure 12. The fracture toughness of the ELI alloy remains at a high shelf level as temperature is reduced from 295 to 125 K, but an abrupt decline of K_{IC} occurs in the range 125 to 76 K. Temperature reductions in this narrow interval decrease K_{IC} by 45%, while temperature reductions from 76 K to 4 K decrease K_{IC} slightly. The abrupt change in behavior between 125 and 76 K constitutes a ductile-to-brittle fracture transition, which, although commonly associated with beta titanium alloys and other bcc and hcp materials, has not previously been documented for a Ti-6Al-4V alloy.

The fracture mode and R_{Sc} parameters also indicate the ductile-to-brittle transition. Plotted as a function of temperature in Figure 13, the per cent slant fracture displays a trend similar to that of K_{IC} data. The R_{Sc} values also exhibit a step-like decrease between 125 and 110 K, but the effect is subtle. In contrast to the trends of K_{IC} and slant fracture mode, R_{Sc} does not exhibit a relatively constant "upper shelf" value.

Discussion

Valid K_{IC} data for a normal interstitial grade of Ti-6Al-4V were also shown in Figure 12. These results were obtained for 2.54 cm-thick compact specimens [16]. The normal grade had a microstructure similar to the ELI alloy, except that the average alpha grain diameter was 0.006 mm. In comparison:

1. the normal grade exhibits low toughness at each temperature, and

2. it does not exhibit a ductile-to-brittle fracture transition over the range of temperatures investigated.

Tests at higher temperatures than represented in this study might have revealed a transition in the normal grade. The transition temperature regime should vary with parameters such as grain size and composition. A finer grain size should tend to lower the transition temperature, whereas high impurity content tends to raise if [27-29]. Since the properties of titanium alloys are particularly sensitive to interstitial content [30,31], it seems possible that the normal grade of Ti-6Al-4V contained a level of embrittling elements sufficient to raise the transition temperature above 295 K.

A quantitative relationship between interstitial content and K_{IC} values has never been demonstrated, but the difference in toughness between normal and ELI Ti-6Al-4V grades is large. It may seem surprising that there is little difference in crack growth rates; but the data for other types of alloys have often led to the conclusion that rates of crack growth are not highly sensitive to compositional variations [32,33].

Wei and Ritter [20] found the crack growth rates of a normal grade of Ti-6Al-4V to be equivalent between 295 and 563 K, while Pittinato's data [2] for a normal grade appear temperature-independent between 145 and 295 K. The rates from these and other sources [21,22] compare quite closely with the data in Figure 5, supporting the conclusion that the rates for Ti-6Al-4V alloys are relatively constant over several hundred kelvins. The temperature effects at high ΔK values for the ELI grade may be related to the marked temperature dependence of K_{IC} for this material.

Cryogenic fracture data for ELI grades of Ti-6Al-4V are available from single-edge-notched or part-through-cracked specimens 0.162-0.325 cm-thick [3-5]. The part-through-cracked specimens simulate surface flaws that occur in service, but the results are considered directly applicable only where service conditions match the specifics of specimen design [34]. Some of these data at 77 K are nearly equivalent to our results for compact specimens while others are not. In any case, the values quoted for non-standard specimens

cannot be termed valid K_{IC} data until their independence of specimen geometry and flaw shape is proved.

The AMS 4930 specification requires a room temperature K_{IC} value of at least 60.4 $MN/m^{3/2}$, stating that the ELI alloy is useful at temperatures as low as 20 K. The present alloy amply exceeds this requirement, but the implied limitation to 20 K seems arbitrary. Other structural materials such as ferritic steels are seldom used below their ductile-to-brittle transition temperatures. If the ELI grade of Ti-6Al-4V is an exception, it should be considered useful at any cryogenic temperature; there is only a small change in toughness between 20 and 4 K.

If stable crack extension does not occur and J_{IC} is strictly defined as the value of J just prior to crack extension, it seems logical to choose the load point at the first noticeable pop-in, P_p, as the J_{IC} measurement point. For the tests described here at 76 and 4 K, P_p could be considered a possible measurement point. However, the appearance of load point discontinuities in test records is affected by material and experimental variables, and the identification of such a measurement point is also dependent on judgment in cases where pop-ins are faint and indistinct. The ASTM E-399-74 procedure obviates these problems by defining K_{IC} at P_Q, which corresponds to an effective crack extension of 2% [35]. Following the standard procedure in this study, P_p could not be taken as the K_{IC} measurement point for tests at 76 and 4 K. Similarly, the 2% point served as a basis for J_{IC} measurements in the linear-elastic case. Here, it was desirable to maintain consistency with ASTM E-399-74 results by measuring J_{IC} at P'_Q as described in the text.

Summary

1. The ELI grade of Ti-6Al-4V exhibits a ductile-to-brittle transition in the temperature interval 125 to 76 K; the fracture toughness significantly exceeds that of a normal grade at all temperatures between 295 and 4 K.

2. The fatigue crack growth rates of the ELI Ti-6Al-4V alloy were temperature independent for $\Delta K \leq 20$ $MN/m^{3/2}$; above 20 $MN/m^{3/2}$, the rates at 295 K were lower than at 76 and 4 K.

3. The J-integral fracture criterion provided meaningful results for a spectrum of load-deflection behaviors; J_{IC} data for the elastic-plastic case were in consistent agreement with valid K_{IC} data for this material.

4. Critical values of the J-integral calculated from the equation $J = 2A/Bb$ led to converted K_{IC} values that appeared to underestimate ASTM E-399-74 linear elastic fracture toughness values by 4 to 10%, depending on a/W; the equation $J = \lambda_J A/Bb$ led to modest overestimates of about 3%, independent of a/W.

Acknowledgment

The test material and room temperature tensile data were furnished by Beech Aircraft Division in Boulder, and the chemical analysis was performed by Titanium West, Reno, Nevada. The elastic properties at room temperature were measured by Dr. W. Weston of the NBS Cryogenics Division. Earl Balinger, Bea Crockett, and Steve Naranjo also aided in data reduction. All of this assistance is appreciated.

References

1. Handbook on Materials for Superconducting Machinery, MCIC-HB-04, Metals and Ceramics Information Center, Battelle Columbus Laboratories, Ohio, (1974).

2. G. F. Pittinato, Hydrogen-enhanced fatigue crack growth in Ti-6Al-4V ELI weldments, Met. Trans., 3, 235-243 (1972).

3. W. E. Witzell, Fracture data for materials at cryogenic temperatures, Tech. Report, AFML-TR-67-257, General Dynamics-Convair, AD 825264 (1967).

4. C. F. Tiffany and P. M. Lorenz, An investigation of low cycle fatigue failure using applied fracture mechanics, Tech. Doc. Report ML-TDR-64-53, Boeing (1964).

5. L. R. Hall, Plane-strain cycle flaw growth in 2014-T62 aluminum and 6Al-4V (ELI) titanium, N69-20265, NASA-CR-62396, Boeing (1968).

6. J. R. Rice, A path independent integral and the approximate analysis of strain concentration by notches and cracks, J. Appl. Mechs., Trans. ASME 35, 379-386 (1968).

7. J. A. Begley and J. D. Landes, The J-integral as a fracture criterion, in Fracture Toughness, Proc. 1971 Nat. Symp. on Frac. Mech., Part II, ASTM STP 514, pp 1-20 (Amer. Soc. Test. Mater., Philadelphia, PA, 1972).

8. J. D. Landes and J. A. Begley, The effect of specimen geometry on J_{IC}, in Fracture Toughness, Proc. 1971 Nat. Symp. on Frac. Mech., Part II, ASTM STP, pp 24-39 (Amer. Soc. Test. Mater., Philadelphia, PA, 1972).

9. J. D. Landes and J. A. Begley, Test results from J-integral studies: an attempt to establish a J_{IC} test procedure, in Fracture Analysis, ASTM STP, pp 560 (Amer. Soc. Test. Mater., Philadelphia, PA, 1974).

10. G. R. Yoder and C. A. Griffis, J-integral and the initiation of crack extension in a titanium alloy, NRL report 7662, Naval Res. Lab., Washington, D.C. (1974), 37pp.

11. G. R. Yoder and C. A. Griffis, Observations on the use of the J-integral to determine plane-strain fracture toughness from subsized specimens of a titanium-6Al-4V alloy, NRL report 7789, Naval Res. Lab., Washington, D.C. (1974), 17pp.

12. J. R. Rice, P. C. Paris, and J. G. Merkle, Some further results on J-integral and estimates, in Progress in Flaw Growth and Fracture Toughness Testing, ASTM STP 536, pp 231-244 (Amer. Soc. Test. Mater. Philadelphia, PA, 1973).

13. J. G. Merkle and H. T. Corten, A J-integral analysis for the compact specimen, considering axial force as well as bending effects, Trans. ASME, J. Pressure Vessel Tech., No. 6, 1-7 (1974).

14. R. J. Goode, Identification of fracture plane orientation, Mater. Res. Stand., 12, No. 9, 31-32 (1972).

15. E. R. Naimon, W. F. Weston, and H. M. Ledbetter, Elastic properties of two titanium alloys at low temperatures, Cryogenics, 14, 246-249 (1974).

16. C. W. Fowlkes and R. L. Tobler, Fracture testing and results for a Ti-6Al-4V alloy at liquid helium temperatures, submitted for publication.

17. E. Roberts, Jr., Elastic crack-edge displacements for the compact tension specimen, Mater. Res. Stand., MTRSA, 9, No. 2, 27 (1969).

18. P. C. Paris, The fracture mechanics approach to fatigue, in Fracture-An Interdisciplinary Approach, pp 107-133 (Syracuse Univ. Press, Syracuse, 1964).

19. P. C. Paris and F. Erdogan, A critical analysis of crack propagation laws, Jnl. Basic Eng., Trans. ASME, Series D, 85, No. 4, 528-534 (1963).

20. R. P. Wei and D. L. Ritter, The influence of temperature on fatigue-crack growth in a mill annealed Ti-6Al-4V alloy, NASA-CR-127042, Lehigh Univ. (1972).

21. R. J. Bucci, P. C. Paris, R. W. Hertzberg, R. A. Schmidt, and A. F. Anderson, Fatigue threshold crack propagation in air and dry argon for a Ti-6Al-4V alloy, in Stress Analysis and Growth of Cracks, ASTM STP 513, pp 125-14 (Amer. Soc. Test. Mater. Philadelphia, PA, 1972).

22. A. Yeun, S. W. Hopkins, G. R. Leverant, and C. A. Rau, Correlations between fracture surface appearance and fracture mechanics parameters for stage II fatigue crack propagation in Ti-6Al-4V, Met. Trans., 5, 1833-1844 (1974).

23. C. A. Griffis and G. R. Yoder, Application of the J-integral to crack initiation in a 2024-T351 aluminum alloy, NRL report 7676, Naval Res. Lab., Washington, D.C. (1974), 17pp.

24. G. A. Clarke, W. R. Andrews, P. C. Paris and D. Schmit, Single specimen tests for J_{IC} determination, presented at the Eighth National Symposium on Fracture Mechanics, Brown University (Aug. 1974).

25. H. I. McHenry and R. E. Key, Brazed titanium fail-safe structures, Welding Journal, 53, 432-439S (1974).

26. R. W. Judy, Jr., R. W. Huber and R. Goode, Fracture characteristics of Ti-6Al-1Mo and Ti-6Al-4V in 3-inch section, NRL Report MR 2156, Naval Res. Lab., Washington, D.C. (1970), AD 711-586, 22pp.

27. R. W. Armstrong, The influence of polycrystal grain size on mechanical properties, in Advances in Materials Research 4, Ed. H. Herman, pp 101-146 (Interscience, New York, 1970).

28. R. W. Armstrong, The polycrystal ductile-brittle transition, Paper 26 in Fracture 1969, pp 314-326, Ed. P. Pratt (Chapman and Hall, London 1969).

29. N. S. Stoloff, Effects of alloying on fracture characteristics, in Fracture-An Advanced Treatise, 6, Ed. H. Liebowitz, pp 1-81 (Academic Press, New York, 1969).

30. S. F. Frederick and W. D. Hanna, Fracture toughness and deformation of titanium alloys at low temperatures, Met. Trans., 1, 347-352 (1970).

31. J. L. Shannon, Jr., and W. F. Brown, Jr., A review of factors influencing the crack tolerance of titanium alloys, in Applications Related Phenomena in Titanium Alloys, ASTM STP 432, pp 33-63 (Amer. Soc. Test Mater., Philadelphia, PA, 1968).

32. J. M. Barsom, Fatigue-crack propagation in steels of various yield strengths, Trans. ASME J. Eng. Ind. 93, 1190-1196 (1971).

33. H. H. Johnson and P. C. Paris, Subcritical flaw growth, Eng. Fract. Mech. 1, 3-45 (1968).

34. R. M. Ehret, Assessment of fracture mechanics technology for space shuttle applications, SD-73-SH-0270, Rockwell International (1973), M 7302002.

35. J. E. Srawley, Plane strain fracture toughness, Chap. 2, in Fracture-An Advanced Treatise, Ed. H. Liebowitz, pp 45-68 (Academic Press, New York, 1969).

Table 1. Chemical analysis (wt. %).

Ti	Al	V	Fe	O	C	N	H
Balance	5.91	3.94	0.103	0.110	0.018	0.014	52 ppm

Table 2. Representative mechanical properties.

Temp. (K)	0.2% yield strength ($10^8 N/m^2$)	Ultimate strength ($10^8 N/m^2$)	Elongation (%)	RA (%)	E [15] ($10^{11} N/m^2$)	ν [15] (--)
295	8.3	8.9	14	53	1.11	.323
76	14.9	15.0	11	43	1.21	.310
4	16.6	17.1	4	32	1.22	.309

Table 3. Crack growth rate parameters.

Temp. (K)	C $(mm/cycle)/(MN/m^{3/2})^n$	n (-)	Range of ΔK $(MN/m^{3/2})$
$4 \leq T \leq 295$	1.1×10^{-13}	7.1	10-20
295	4.2×10^{-8}	2.8	20-70
76	2.8×10^{-9}	3.7	20-50
4	5.3×10^{-12}	5.8	20-30

Table 4. Summary of load-deflection behaviors.

Temperature (K)	ASTM E-399 classification	Category	Order of load points
295, 200	(no designation)	elastic-plastic	$P_Q < P_{max} < P_p$
125	type I	linear-elastic	$P_Q < P_{max} = P_p$
110	type III	linear-elastic	$P_Q = P_{max} = P_p$
76, 4	type II	linear-elastic	$P_p < P_Q \leq P_{max}$

Table 5. ASTM E-399-74 test results.

Specimen (#)	Temp. (K)	K_f ($MN/m^{3/2}$)	a (cm)	$\frac{a_e}{a}$[a] (%)	a/W (--)	P_{max}/P_Q (--)	K_Q ($MN/m^{3/2}$)	K_{Ic} ($MN/m^{3/2}$)	R_{Sc} (--)
6[b]	295	32.0	2.352	.95	.579	N/A	N/A	N/A	N/A
7[c]	295	32.0	2.364	.93	.582	N/A	77.5	invalid[d]	N/A
8	295	34.6	2.349	.93	.578	1.41	83.2	invalid	1.31
9[c]	295	35.0	2.337	.96	.575	N/A	78.9	invalid	N/A
10[c]	295	29.6	2.372	.92	.584	N/A	82.3	invalid	N/A
15[c]	295	29.5	2.320	.93	.570	N/A	85.9	invalid	N/A
17[c]	295	29.5	2.337	.94	.575	N/A	88.5	invalid	N/A
20	200	29.0	2.151	.90	.529	1.17	84.5	invalid[d]	.87
19	125	25.0	1.956	.96	.481	1.03	$K_Q=K_{Ic}$	100.2	.70
18	110	24.0	2.096	.92	.516	1.00	$K_Q=K_{Ic}$	78.0	.55
1	76	26.3	2.085	.93	.513	1.06	$K_Q=K_{Ic}$	61.7	.46
2	76	34.4	2.337	.91	.575	1.00	$K_Q=K_{Ic}$	61.0	.47
3	76	24.5	2.618	.95	.644	1.00	$K_Q=K_{Ic}$	61.6	.54
4	76	24.0	2.746	.97	.675	1.00	$K_Q=K_{Ic}$	59.9	.53
11	4	25.9	2.319	.95	.570	1.06	$K_Q=K_{Ic}$	54.0	.39
12	4	30.9	2.057	.97	.506	1.00	$K_Q=K_{Ic}$	53.7	.33
13	4	29.6	1.854	.95	.454	1.04	$K_Q=K_{Ic}$	54.6	.33

[a] a_e = crack length at specimen edge

[b] unloaded prior to P_Q

[c] unloaded prior to P_{max}

[d] $P_{max}/P_Q > 1.10$ and insufficient thickness

Table 6. J-integral results at cryogenic temperatures.

Spec. (#)	Temp. (K)	a/W (-)	λ_J (-)	$E/(1-\nu^2)$ (10^{11}N/m^2)	J_Q[a] (kJ/m^2)	$K_Q(J)/K_{Ic}$ (-)	J_{Ic}[b] (kJ/m^2)	$K_{Ic}(J)$ (MN/m$^{3/2}$)	$K_{Ic}(J)/K_{Ic}$ (-)
19	125	.481	2.45	1.32	95.4	1.12	82.5	104.3	1.04
18	110	.545	2.45	1.33	49.9	1.04	49.9	81.4	1.04
1	76	.573	2.45	1.34	31.7	1.06	28.8	62.1	1.01
2	76	.575	2.41	1.34	35.8	1.11	30.1	63.5	1.04
3	76	.644	2.34	1.34	33.3	1.08	30.1	63.5	1.03
4	76	.675	2.32	1.34	30.7	1.07	28.7	61.9	1.03
11	4	.570	2.41	1.35	25.2	1.08	23.6	56.4	1.04
12	4	.506	2.46	1.35	23.6	1.05	22.6	55.2	1.03
13	4	.454	2.48	1.35	23.4	1.03	22.3	54.9	1.00

[a] measured at P_Q

[b] measured at P_Q'

Table 7. J-integral test results, 295 K.

Specimen (#)	a/W (--)	λ_J (--)	$J = \frac{\lambda_J A}{Bb}$ (kJ/m^2)	Δa (avg) (mm)	Δa (max) (mm)
6	.579	2.40	52.8	0.02	0.02
7	.582	2.40	81.1	0.11	0.14
8	.578	2.40	240.3[a]	N/A	N/A
9	.575	2.41	106.6	0.14	0.23
10	.584	2.40	145.9	0.75	1.19
15	.575	2.41	99.7	0.28	0.55
17	.570	2.41	128.2	0.50	0.86

[a] J value at point of pop-in

Table 8. Specimen thickness criteria.

Temp. (K)	B (cm)	$2.5(K_{Ic}/\sigma_y)^2$ (cm)	$50(J_{Ic}/\sigma_y)$ (cm)
295	2.030	4.5[a]	0.59[a]
125	2.030	1.5	0.12
110	2.030	0.84	0.07
76	2.030	0.48	0.04
4	2.030	0.33	0.03

[a] assuming $J_{Ic} = 98\ kJ/m^2$ and $K_{Ic}(J) = 110\ MN/m^{3/2}$

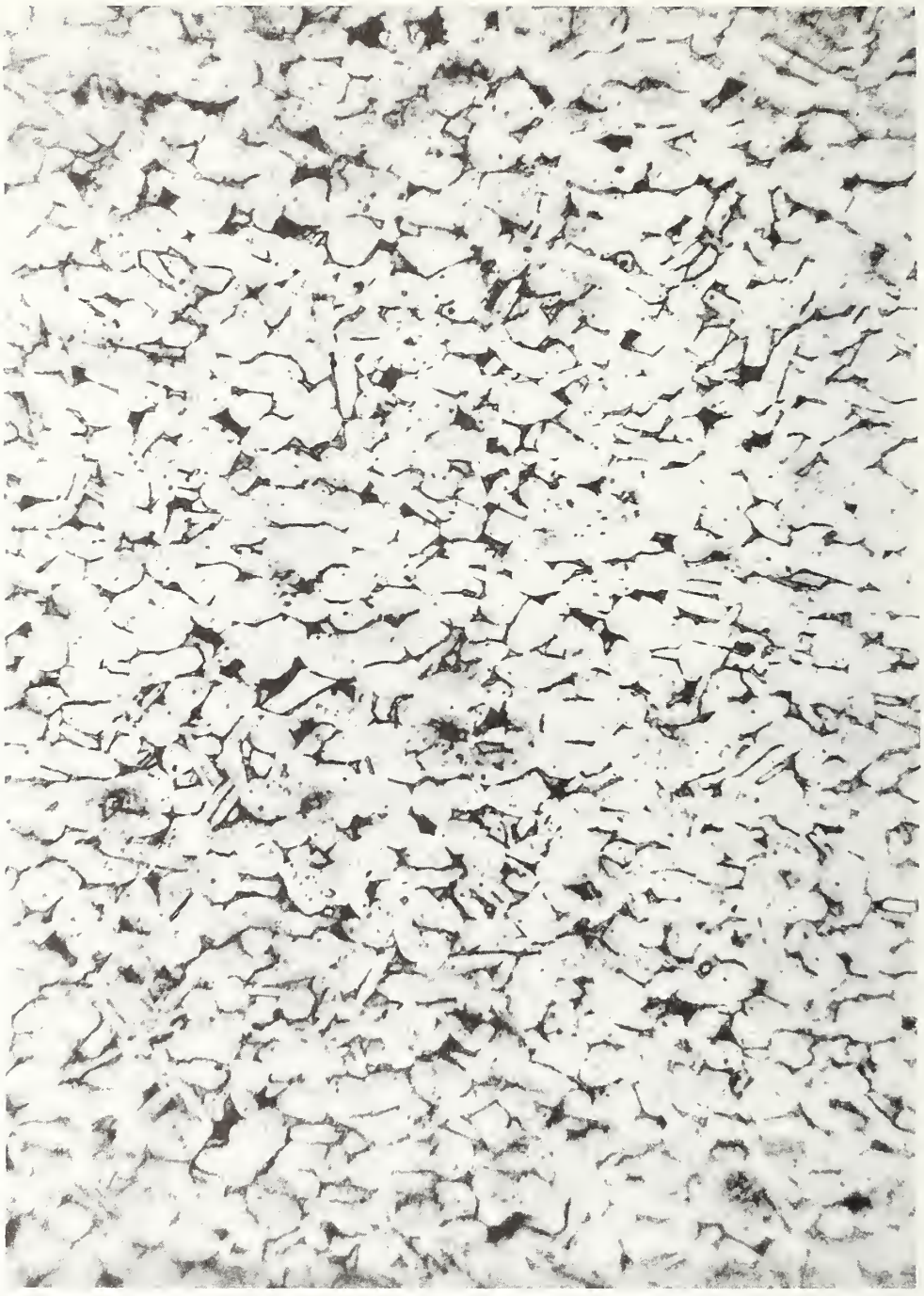

Figure 1. Microstructure of ELI Ti-6Al-4V alloy (etchant 10HF, $5HNO_3$, $85H_2O$) 250X

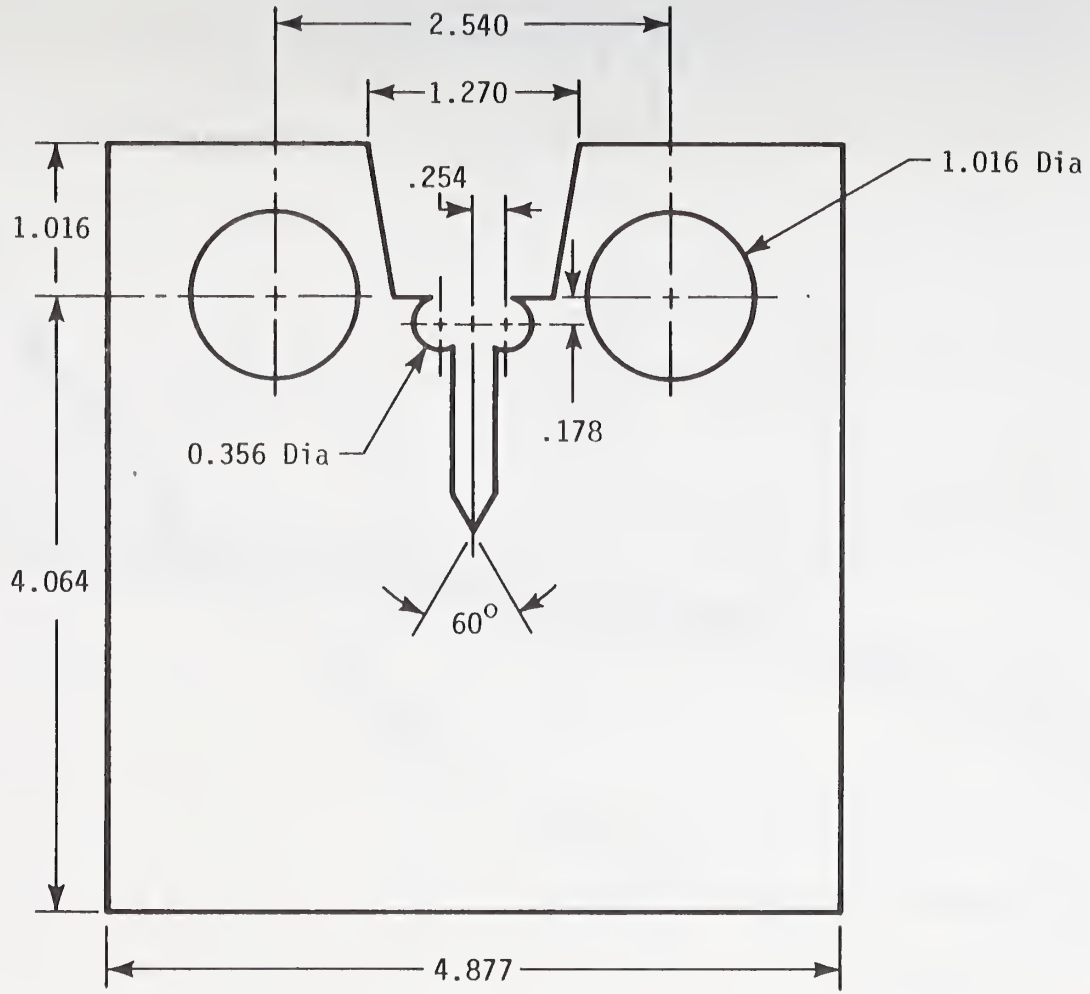

Figure 2. Compact specimen (cm).

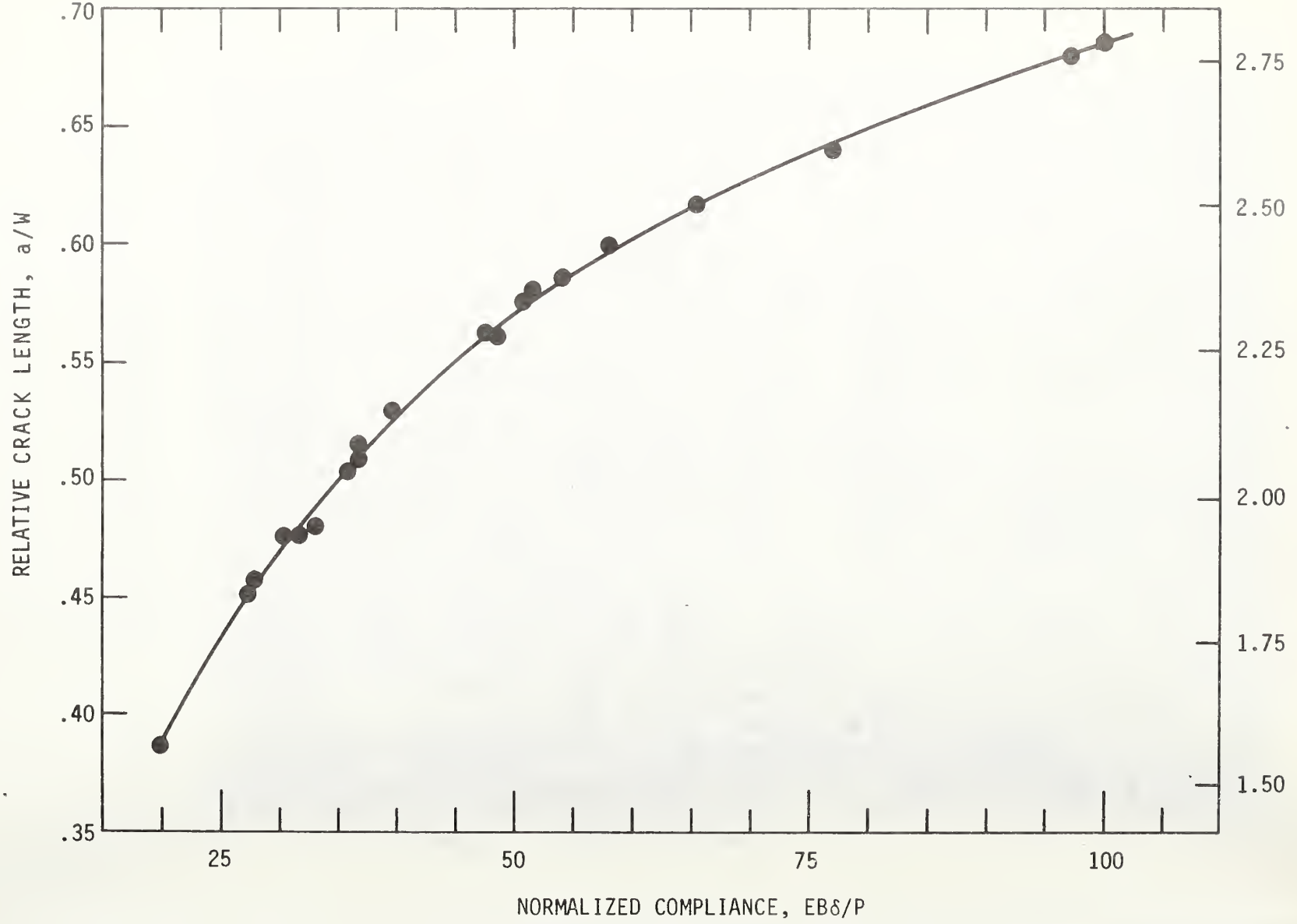
.70
.65
.60
.55
.50
.45
.40
.35
RELATIVE CRACK LENGTH, a/W
2.75
2.50
2.25
2.00
1.75
1.50
AVERAGE CRACK LENGTH, cm
25
50
75
100
NORMALIZED COMPLIANCE, EBδ/P

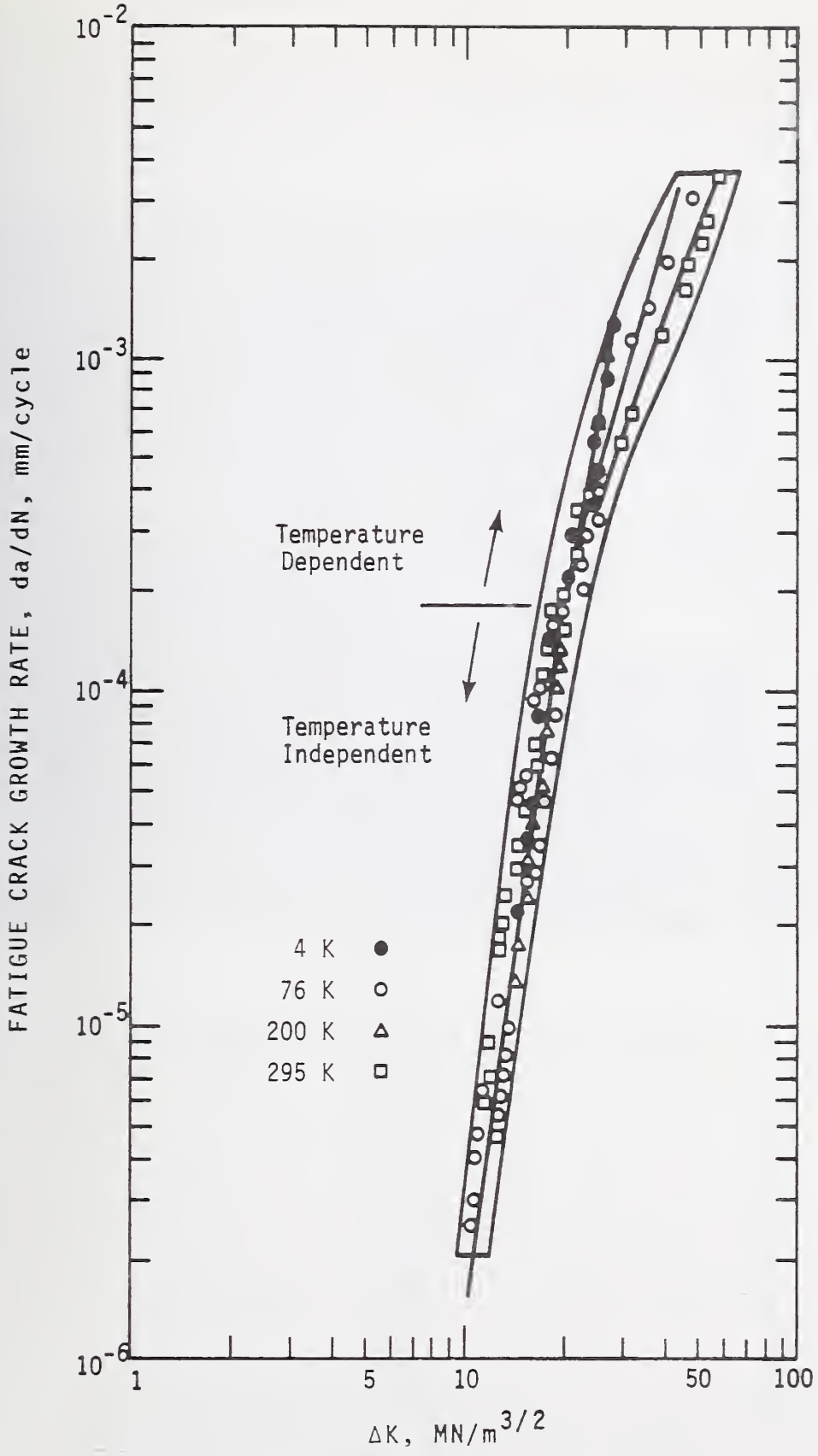

Figure 4 Growth rate data of ELI Ti-6Al-4V alloy.

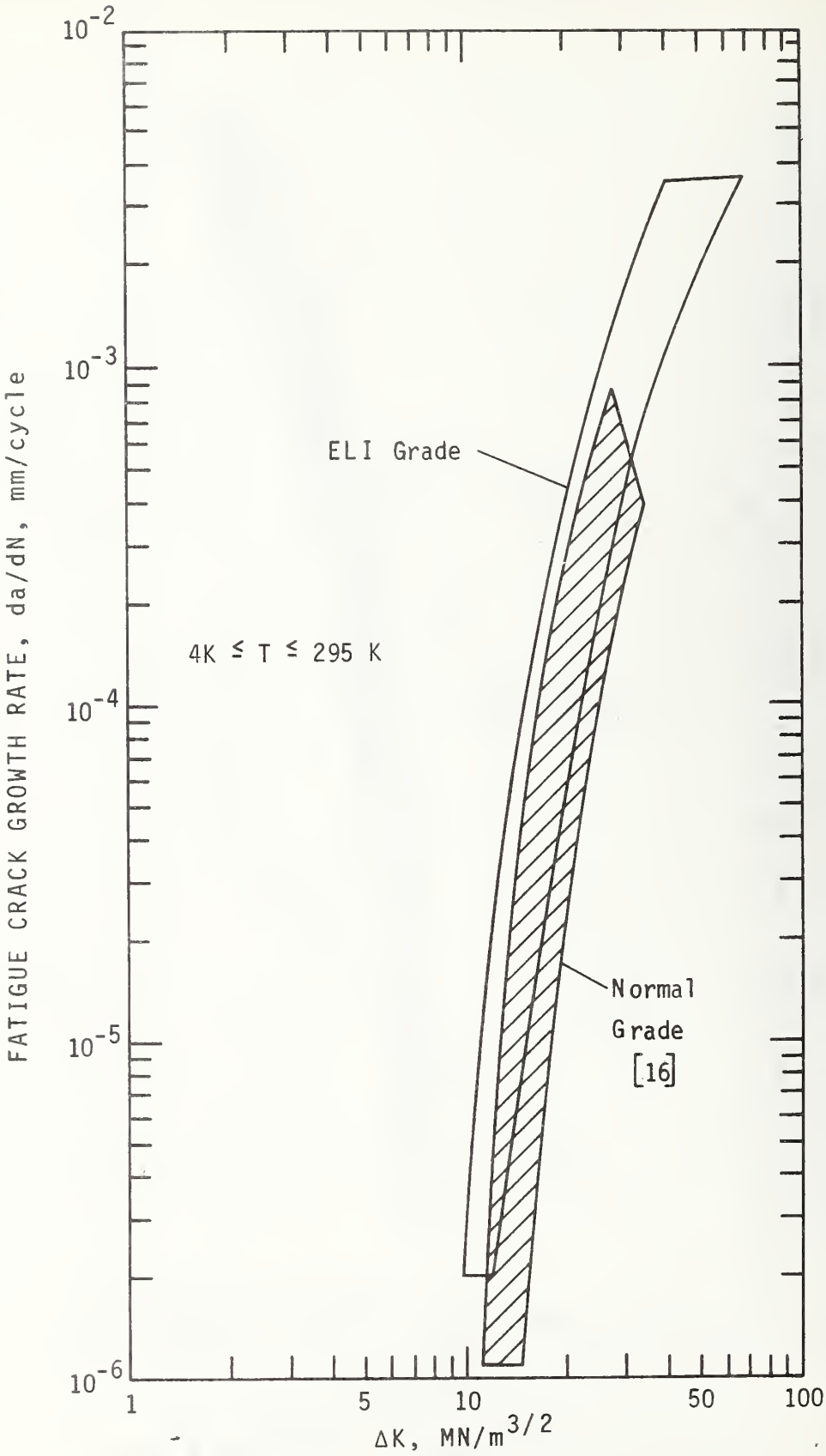

Figure 5. Growth rate data of Ti-6Al-4V alloys.

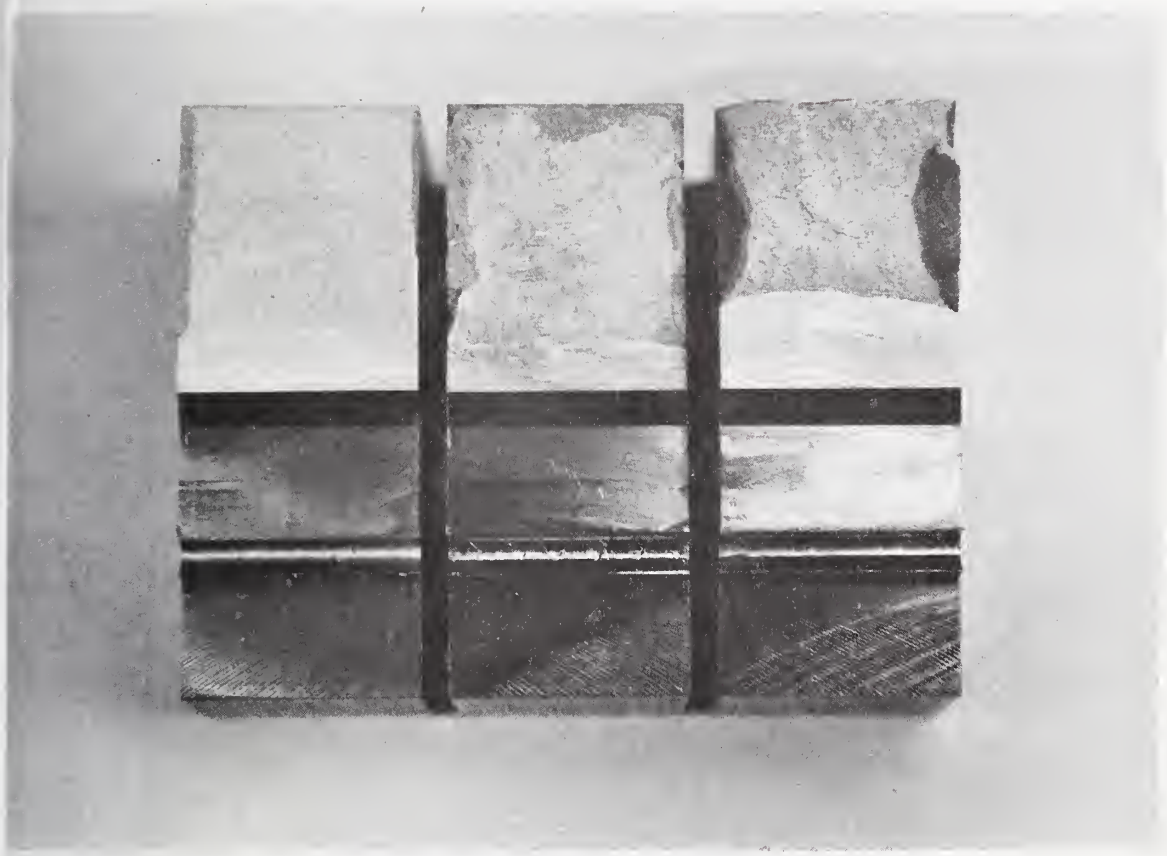

Figure 6. Surface appearances of 2.030 cm-thick ELI Ti-6Al-4V specimens fractured at (left to right) 4K, 110K, and 295K.

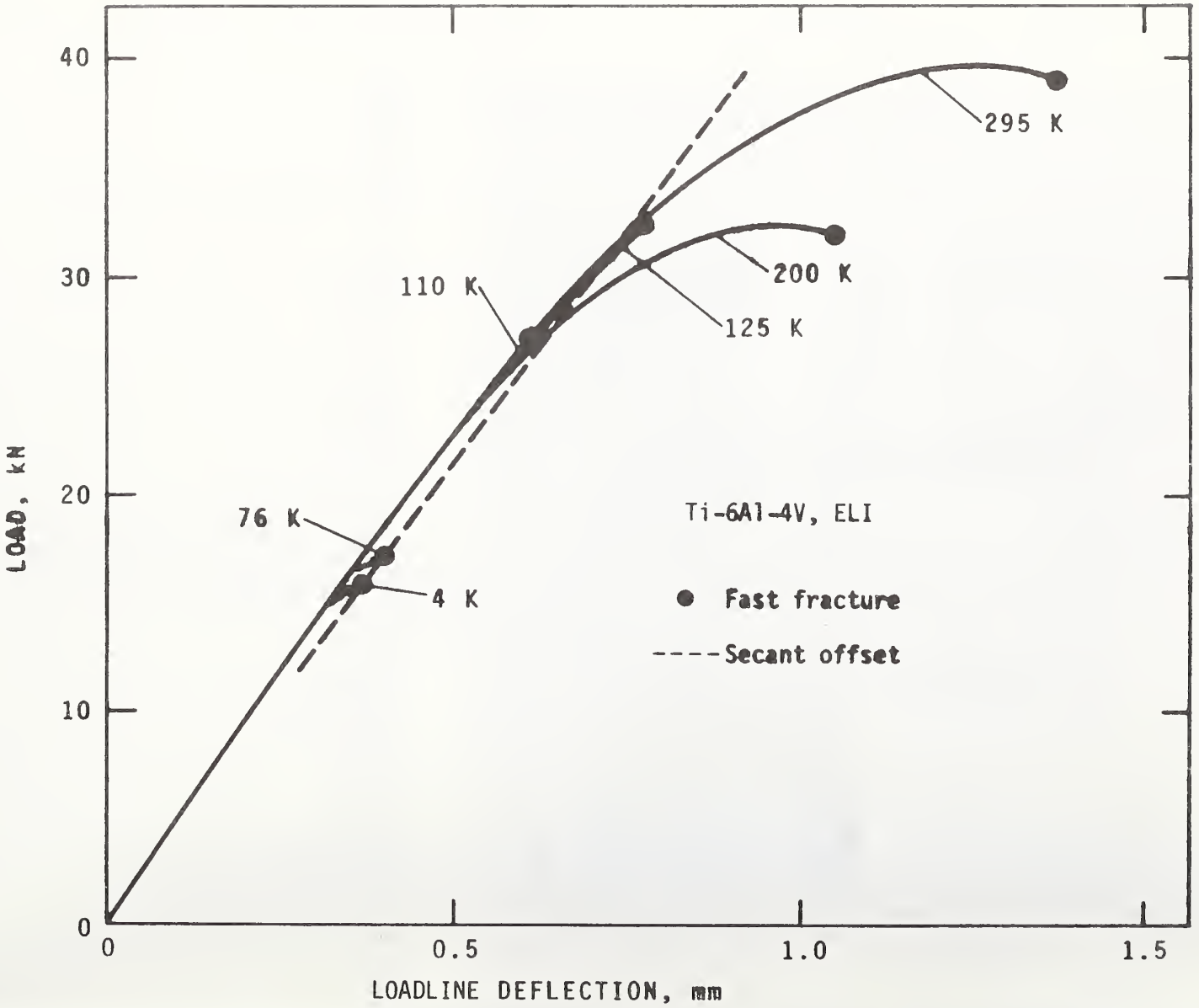

Figure 7. Load-deflection records of 2.030 cm-thick compact specimens normalized for a/W ≅ .58

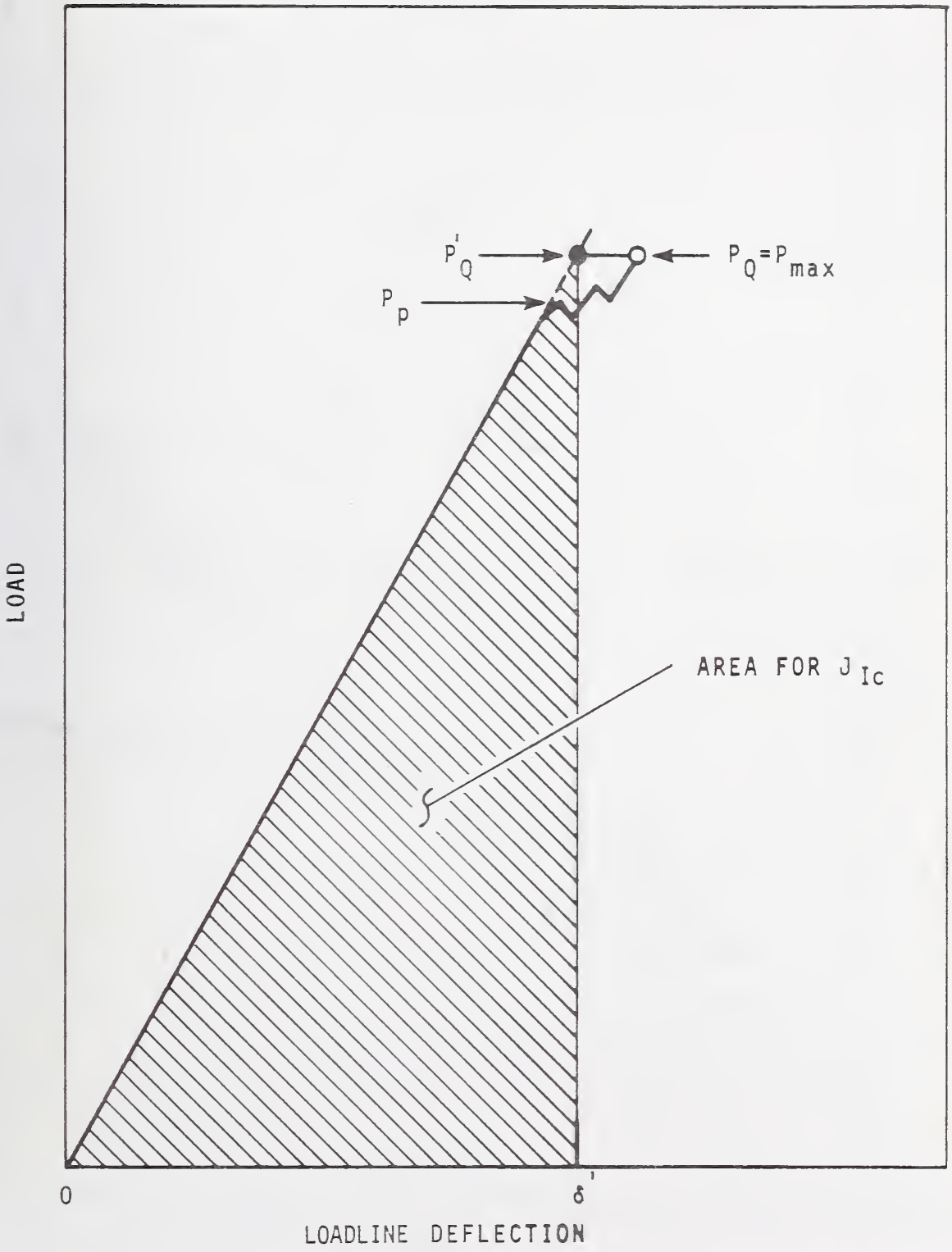

Figure 8. J_{Ic} calculation, adjusted for effects of pop-in (schematic).

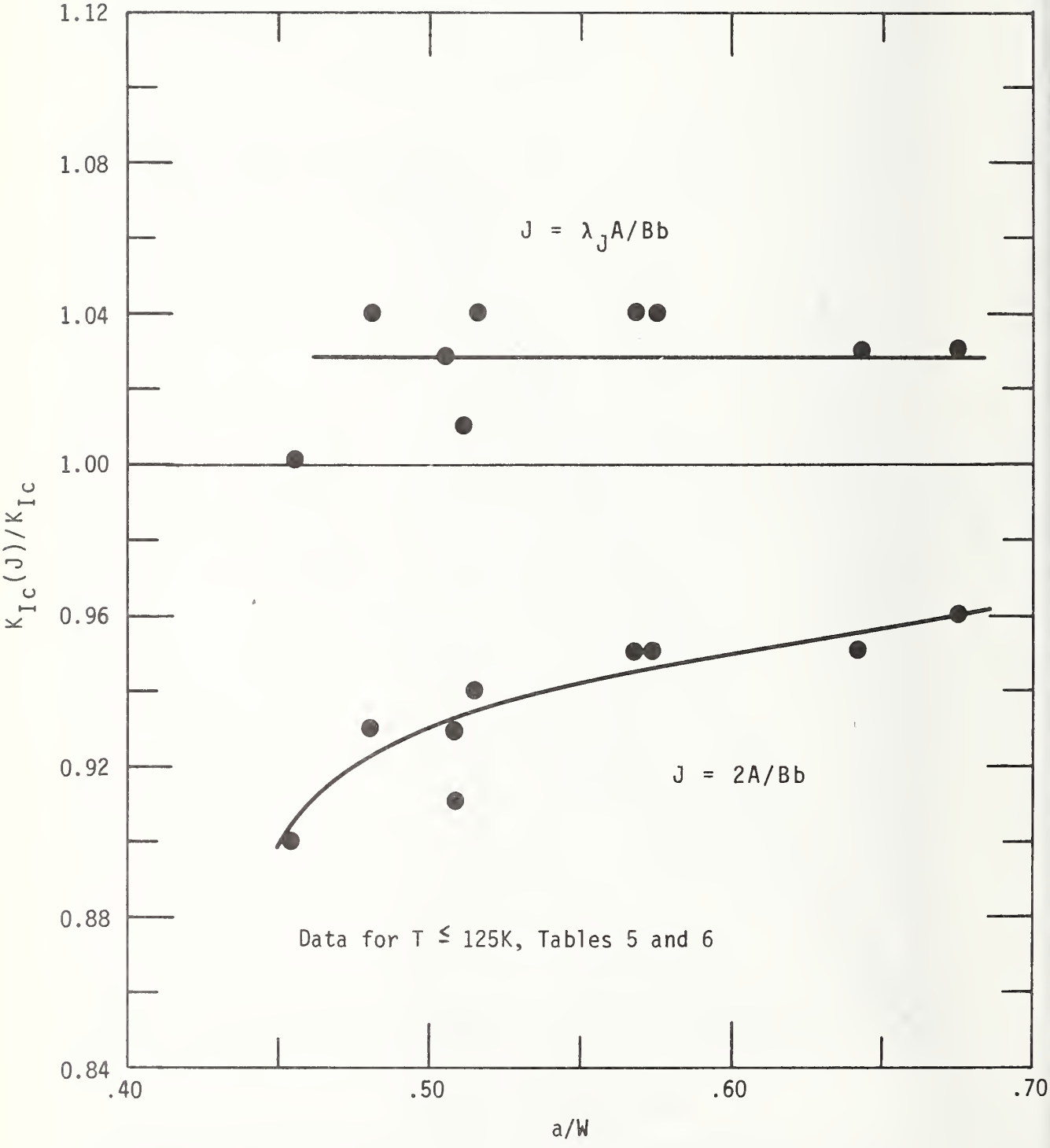

Figure 9 Agreement of K_{Ic} and J -integral results, as calculated from two equations.

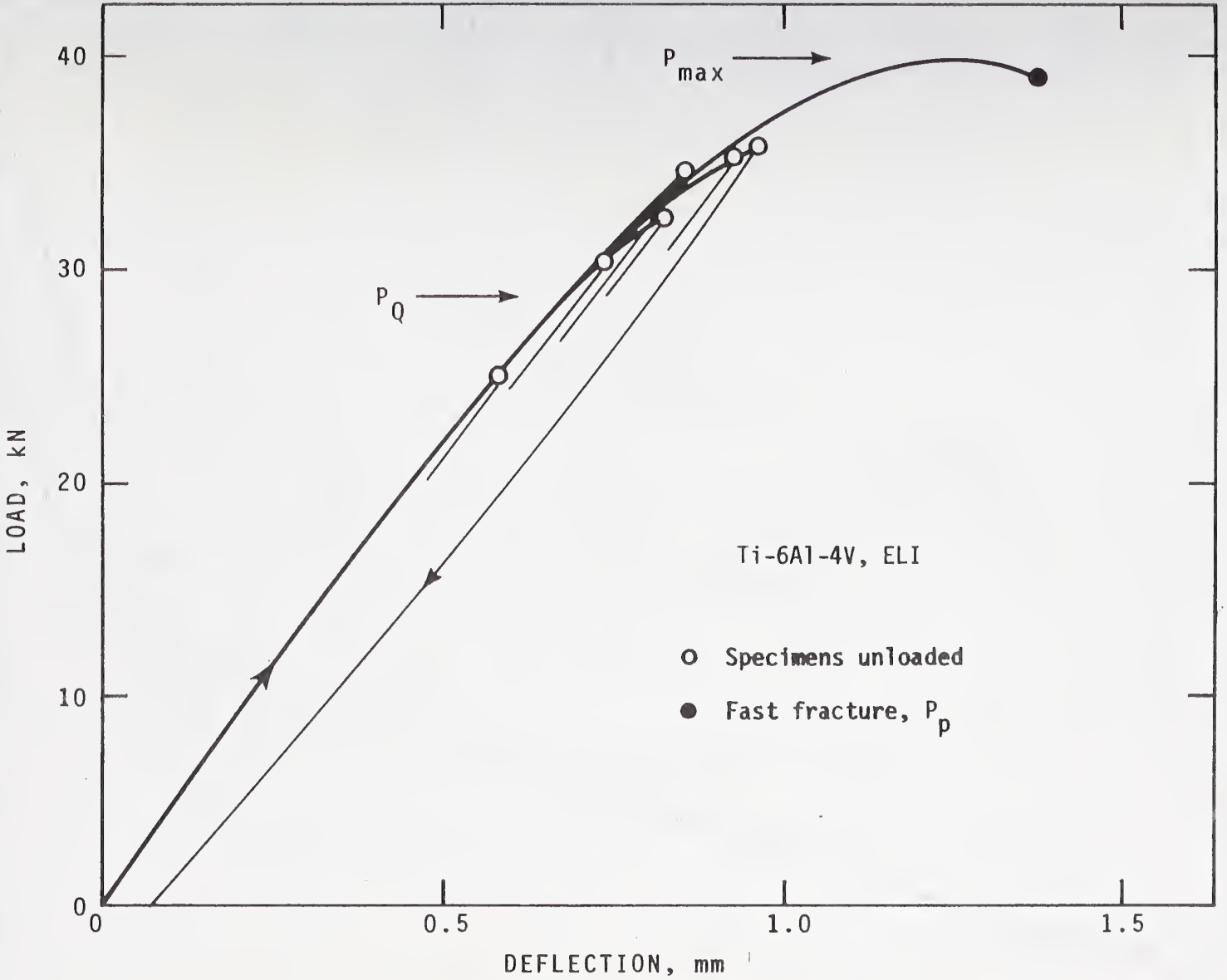

Figure 10. Room temperature P-δ records.

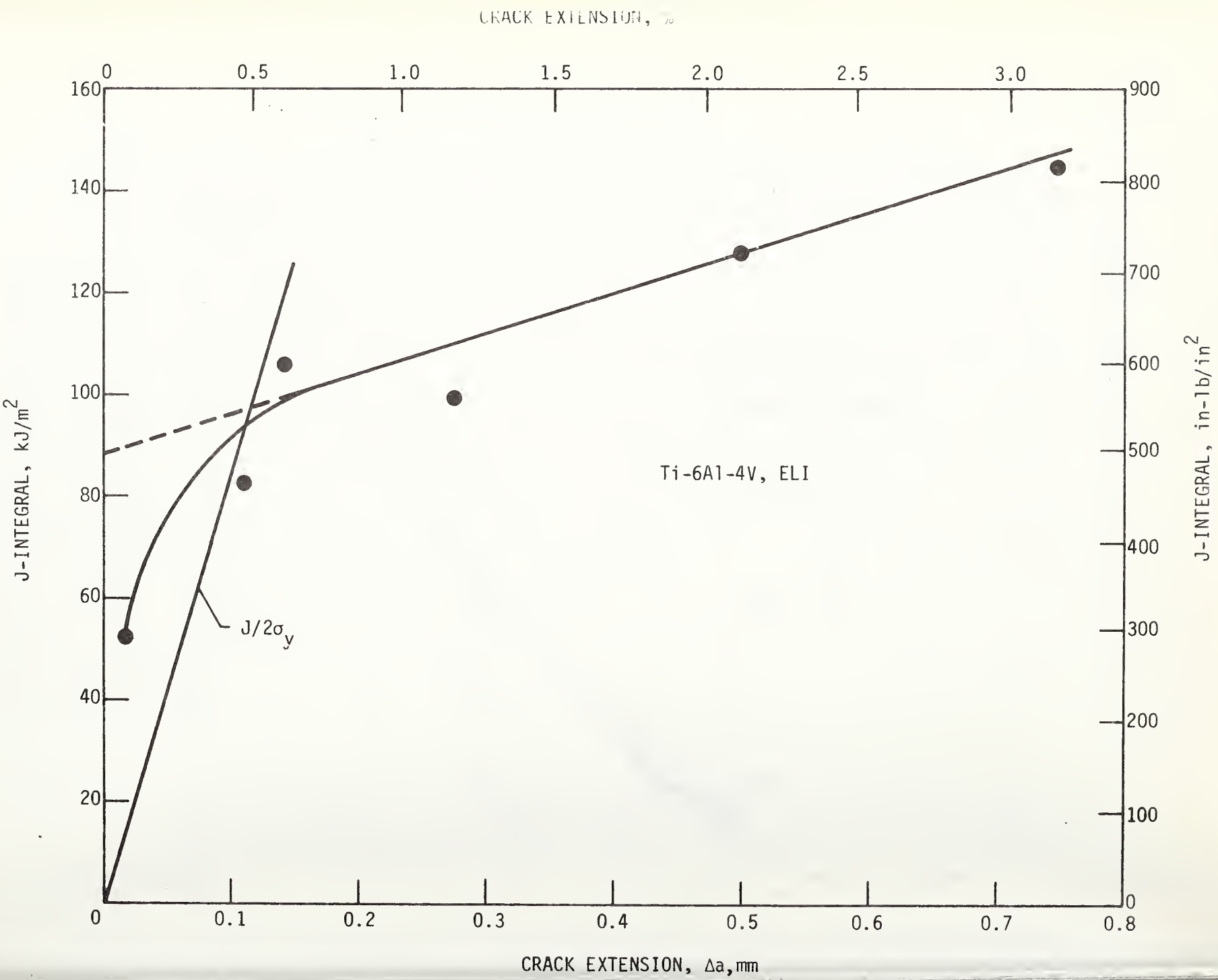
CRACK EXTENSION, %
0
0.5
1.0
1.5
2.0
2.5
3.0
160
140
120
100
80
60
40
20
0
900
800
700
600
500
400
300
200
100
0
J-INTEGRAL, kJ/m2
J-INTEGRAL, in-lb/in2
Ti-6Al-4V, ELI
J/2σy
0.1
0.2
0.3
0.4
0.5
0.6
0.7
0.8
CRACK EXTENSION, Δa,mm

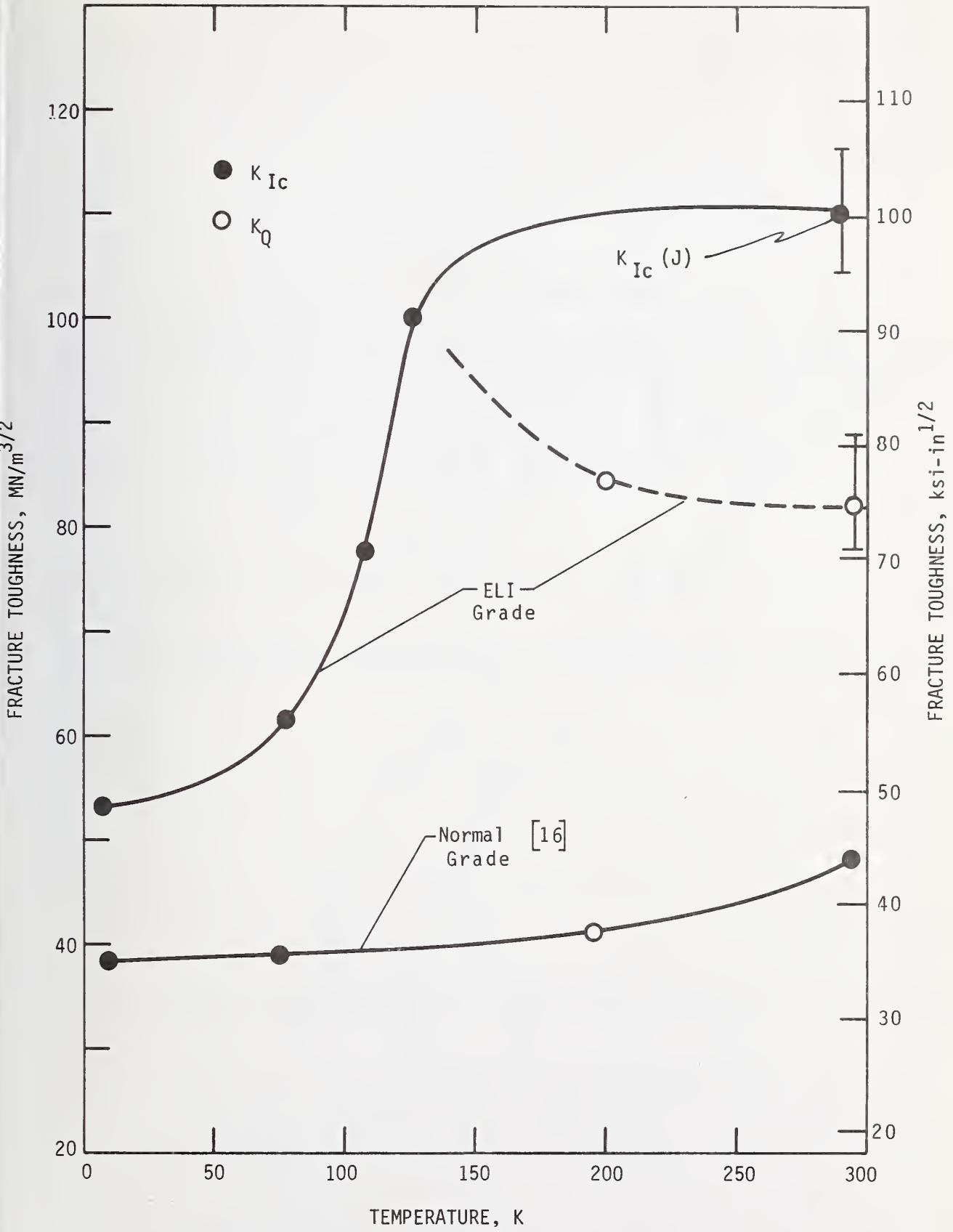

Figure 12. Temperature-dependence of K_{Ic} for Ti-6Al-4V alloys.

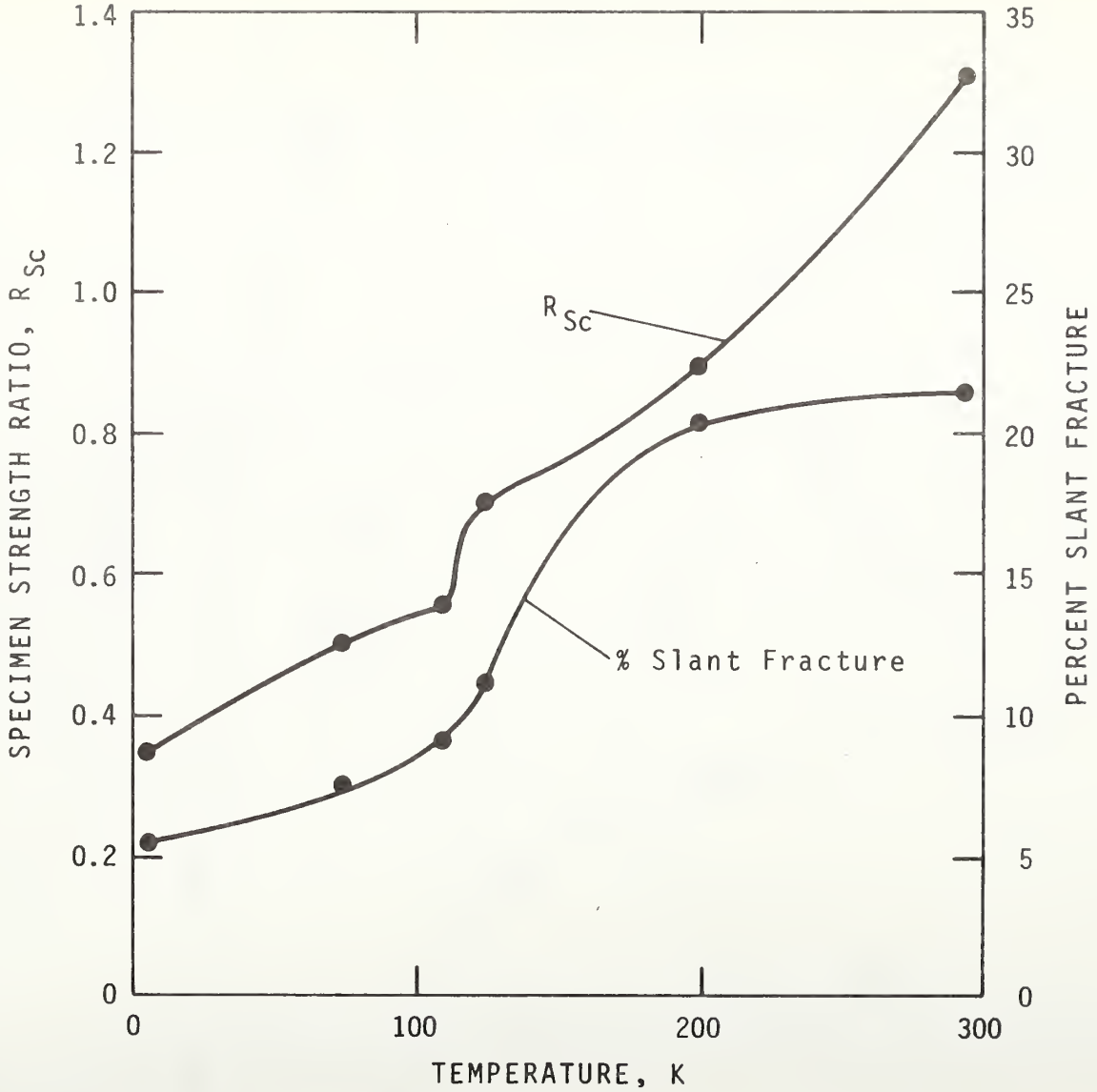

Figure 13. Temperature-dependence of qualitative fracture parameters for 2.030 cm-thick compact specimens of Ti-6Al-4V, ELI.

FATIGUE CRACK GROWTH RATES OF STRUCTURAL ALLOYS AT FOUR KELVIN*

R. L. Tobler and R. P. Reed

National Bureau of Standards
Boulder, Colorado

Abstract

The fatigue crack growth rates of nine structural alloys were tested at 4 K. Growth rates from 7×10^{-5} to 2×10^{-3} mm/cycle were measured for compact specimens 2.54 to 3.81 cm thick. The materials tested include: Ti-5Al-2.5Sn, Ti-6Al-4V, AISI 304, 310, and 316 stainless steels, 5083-0 aluminum, 9% nickel steel, and two Fe-Ni-Cr superalloys. Results showed that stable face-centered cubic alloys having high elastic moduli displayed superior crack growth resistance at 4 K, whereas materials with body-centered cubic, hexagonal-close-packed or martensitic phases exhibited relatively high growth rates at this temperature. When compared on the basis of the strain intensity factor, $\Delta K/E$, the growth rates of alloys having close-packed crystal structures were in close agreement. An equation describing the crack growth rates of four stable fcc alloys is:

$$\frac{da}{dN} = A \left(\frac{\Delta K}{E}\right)^{b},$$

where, depending on the range of $\Delta K/E$, the constants A and b have two distinct values.

Key words: Aluminum alloy; crack propagation; fatigue; iron alloys; liquid helium; stainless steels; steels; superalloys; titanium alloys.

* This work was sponsored by the Advanced Research Projects Agency and is a contribution of NBS, not subject to copyright.

Introduction

Recent developments in applied superconductivity have demonstrated the feasibility and practicality of constructing electrical machinery to operate at liquid helium temperature. A device such as a rotating superconducting generator contains structural members that are continually subjected to fatigue during operation at 4 K. The fatigue resistance of candidate structural materials in this environment is a vital design consideration, and fatigue studies at extreme cryogenic temperatures are currently of great practical importance.

Experiments at temperatures near absolute zero can provide basic information regarding the mechanical behavior of materials. At extreme cryogenic temperatures thermally activated deformation processes are suppressed and resistance to slip increases. Since fatigue is a process involving reversed slip, some early investigations [1-5] at temperatures of 4 K and below contributed to a basic understanding of fatigue in metals.

Fatigue design data at 4 K are not abundant. MacCrone, McCammon and Rosenberg reported S-N data for several commercially pure metals [1,2], while Nachtigall, Klima, and Freche [6] reported S-N data for structural alloys. Nachtigall also reported strain-cycling fatigue data for alloys [7]. The latter paper demonstrated that, with an accuracy equivalent to results at room temperature, the strain-cycling fatigue life of unnotched specimens at 4 K can be predicted by means of the Manson equation [8]:

$$\Delta\varepsilon_t = 3.5 \frac{\sigma_u}{E} (N_f)^{-0.12} + [\ln (\frac{100}{100-RA})]^{0.6} \cdot (N_f)^{0.6} \qquad (1)$$

where $\Delta\varepsilon_t$ is the total strain range, σ_u is the ultimate tensile strength, E is Young's modulus, N_f is the number of cycles to failure, and RA is the percent reduction in area from a uniaxial tensile test.

Although conventional S-N data provide valuable design information, the results in terms of total cycles to failure do not distinguish between the separate stages of crack initiation and crack growth. Specific knowledge of crack growth rates is needed to apply current techniques of fracture mechanics analysis. The fracture mechanics approach is based on the premise that cycle-life capability can be predicted, given the initial and critical crack sizes and the crack growth rate.

This paper provides crack growth rate data for nine structural alloys tested in a liquid helium environment. The alloys are familiar cryogenic materials that have potential applications at temperatures approaching absolute zero. These data can be used in a fracture mechanics evaluation of critical components, and the results lead to some generalizations regarding the selection of materials for maximum resistance to fatigue crack propagation at 4 K.

Materials and Specimens

A summary of the materials tested in this study is contained in Table 1; included are material condition, chemical analysis, grain size, hardness and tensile properties. Three alloys have more common designations: ASTM A 453 is A286*, ASTM A553 is Fe-9%Ni and ASTM A637 is Inconel 750*. All tensile data were obtained in our laboratory. Most of the alloys were tested in the as-received condition, but the ASTM A453 and A533 specimens were machined from stock and then heat treated prior to testing. Conventional heat treatments were applied. The A453 alloy was solution treated and aged:

1. 1172 K (1650 F), 2 hrs., oil quench
2. 1005 K (1350 F), 16 hrs., air cool

---

* The use of trade names is for the sake of clarity and does not imply a recommendation or endorsement by NBS.

and the A533 alloy was solution treated and double aged:

1. 1255 K (1800 F), 1 hr., air cool
2. 1144 K (1600 F), 24 hrs., air cool
3. 977 K (1300 F), 20 hrs., air cool.

Tests were performed on compact specimens, which are described in ASTM E-399-74 [9]. Specimens machined from plate stock (Ti-6Al-4V, AISI 304, 310 and 316, ASTM A553, and 5083-0Al) were tested in the TL orientation, whereas specimens from forged bar stock (Ti-5Al-2.5Sn, ASTM A453, and ASTM A637) were tested in the TS orientation [9]. Specimen thicknesses (B) ranged from 2.54 to 3.81 cm; specimen widths (W) were 7.62 cm except for a 5.08 cm width for Ti-6Al-4V. All width to thickness ratios (W/B) were 2.00 except for ASTM A553 (W/B = 2.5) and 5083-0 (W/B = 2.4). Titanium alloy specimens were provided with attachable knife edges and deflections were measured at the specimen edge as described in ASTM standard E-399-74. For other specimens, the notch was slightly modified [10], allowing deflections to be measured at the axis of loading.

Procedure

Fatigue tests were conducted using a 100 kN capacity servo-hydraulic mechanical testing machine. The machine was equipped with a 100 kN capacity cryostat for fatigue testing of specimens submerged in liquid helium. Conventional clip gages [9] were attached directly to the specimens. Calibrations at 4 K demonstrated that clip gage linearity satisfied ASTM E-399-74 requirements. Detailed descriptions of the low-temperature apparatus and test procedures are discussed by Fowlkes and Tobler [11].

All tests were performed using load control. Dynamic fatigue loads were measured and controlled to $\pm$ 2% by means of a digital peak-load recording device. The load cycle was sinusoidal at frequencies of 20-28 Hz, and the ratio, R, of minimum/maximum load was constant at 0.1.

Fatigue precracks were usually introduced at 4 or 76 K. Whenever precracking was performed at temperatures higher than 4 K, the subsequent growth rate data were discounted until the crack had propagated beyond the plastic zone created by precracking. Estimates of the plastic zone radius, r_p, were calculated using the relation [12]:

$$r_p = \frac{1}{2\pi} \left(\frac{K}{\sigma_y}\right)^2 \tag{2}$$

where K is the stress intensity factor defined by equation (3) and σ_y is the yield strength of the material at the temperature of precracking. Using this criterion, the data from several specimens of a given material were in good agreement, independent of precracking temperatures.

Crack length was monitored during the tests by means of elastic compliance measurements. A correlation between crack length and specimen compliance at 4 K was determined experimentally for each material, following techniques previously developed [10]. Striations were generated on the crack surfaces when fatigue loads were increased to obtain data at higher stress intensities. After the specimens were fractured subsequent to fatigue cracking, the distance separating striations was measured and correlated with compliance data obtained at the time the load changes were made. Crack length was measured as an average of three readings at 25, 50 and 75% of specimen thickness.

At least ten data points were used to define the crack length-compliance correlation for each material. The compliance correlation obtained for AISI 310 shown in Fig. 1, is typical, but the agreement between empirical and theoretical curves [13] varied for different materials.

To obtain crack growth rates, the crack length, a, was plotted versus the total number, N, of fatigue cycles. The crack growth rates, da/dN, were determined by graphical differentiation at points along the a-versus-N curves. Data were obtained from at least three specimens per material, except as noted.

The stress intensity factor, K, which governs the elastic stress distribution ahead of the crack tip, was calculated from the expression for compact specimens [9]:

$$K = \frac{P}{BW^{1/2}} \left[29.6 \left(\frac{a}{W}\right)^{1/2} - 185.5 \left(\frac{a}{W}\right)^{3/2} + 655.7 \left(\frac{a}{W}\right)^{5/2} - 1017.0 \left(\frac{a}{W}\right)^{7/2} + 638.9 \left(\frac{a}{W}\right)^{9/2}\right] \quad (3)$$

where P is the applied load, B is the specimen thickness, and W is the specimen width.

Stress intensity factor ranges, ΔK, corresponding to various crack growth rates, were calculated from the relation:

$$\Delta K = K_{max} - K_{min} \quad (4)$$

where K_{max} and K_{min} are the stress intensity factors at the maximum and minimum fatigue loads.

Results and Discussion

The crack growth rate data at 4 K for the Ti-5Al-2.5Sn alloy, as well as the results previously reported for a mill annealed Ti-6Al-4V alloy [11], are shown in Fig. 2. Metallographic examination indicated that the Ti-6Al-4V alloy had a two-phase microstructure consisting of primary alpha (hcp) and beta (bcc), whereas the Ti-5Al-2.5Sn alloy was almost 100% alpha. As Fig. 3 demonstrates, the rates of crack growth are higher for the two-phase alloy containing beta.

The results for three fcc alloys are shown in Fig. 3. Data for the nickel-base alloy ASTM A637 and the iron-base alloy ASTM A453 show little scatter and nearly equivalent behavior. Both alloys exhibit a high resistance to crack growth, as evidenced by the fact that ΔK values as high as 30 to 80 $Mn/m^{3/2}$ are required to produce growth rates from 5×10^{-7} to 7×10^{-7} mm/cycle. On the other hand, ΔK values of only 10 to 20 $Mn/m^{3/2}$ produce similar growth rates in 5083-0 aluminum. The fatigue crack growth resistance of the aluminum alloy is comparatively low, in proportion to its lower elastic modulus.

The data for several AISI 300-series stainless steels are compared in Fig. 4. The AISI 304 and 316 alloys exhibited similar growth rates at $\Delta K \simeq 40$ $Mn/m^{3/2}$. Above 40 $Mn/m^{3/2}$ the rates are only slightly higher for AISI 304, whereas below 40 $Mn/m^{3/2}$ the converse is true. Significantly, the behavior of AISI 310 is superior over the entire range of stress intensities investigated.

To varying degrees, depending primarily on alloy composition, the austenitic stainless steels are metastable. In response to plastic deformation or stress at low temperatures, the austenitic phase may transform to bcc and hcp martensitic structures. Several studies describe the effects of these transformations on low temperature tensile properties [14-19], but few discuss the effect of such transformations on fatigue crack growth rates [20].

The bcc martensite product is ferromagnetic while the austenite is paramagnetic. In this study, magnetic measurements [14,16] and metallographic examination confirmed that cyclic loading of AISI 304 and 316 caused martensite formation in crack-tip plastic zones. It can be assumed that the martensitic transformation preceded crack extension, and that the parameter measured in these tests was the rate of crack propagation through partially transformed austenite.

There was no evidence of transformation in the AISI 310 stainless steel. The data for this alloy represent crack propagation through stable austenite. A comparison shows that the rates for AISI 310 are similar to those shown in Fig. 3 for ASTM A637 and A453 alloys, two stable austenitic superalloys. These findings suggest that the martensitic transformation may have influenced the results for the metastable stainless steels, causing higher growth rates than observed for stable austenites.

The tests of a quenched and tempered 9% nickel steel (ASTM A553) revealed exceptionally high crack growth rates at 4 K, as shown in Fig. 5. The rates at 4 K are much higher than

the rates at 295 or 76 K, which are included in Fig. 5. To interpret the behavior at 4 K, it is essential to realize that the 9% nickel steel undergoes a ductile-to-brittle fracture toughness transition at temperatures below 76 K [10]. This transition is reflected in the crack growth rates, also.

Growth rates at ΔK below 30 $Mn/m^{3/2}$ were not obtained for A553 steel at 4 K, and the data in Fig. 5 cannot be extrapolated to lower ΔK without reservations. An A553 steel specimen subjected to 30,000 cycles at ΔK = 20 $Mn/m^{3/2}$ at 4 K exhibited no measureable crack growth, although an incremental advance of 3.5 mm was expected based on the trend in Fig. 5. McCammon and Rosenberg [2] reported that the S-N fatigue results of brittle metals at extreme cryogenic temperatures can be irregular. Their data for iron and zinc showed that only a narrow stress range existed in which fatigue was observed; moderate increases in stress levels resulted in immediate fracture, whereas moderate decreases led to inordinately long testing periods. The fatigue behavior of brittle materials, in particular the 4 K crack growth resistance of A553 steel at lower stress intensity ranges, deserves further investigation.

The data of Fig. 2-5 can be approximated by straight lines conforming to Paris' equation [21,22]:

$$\frac{da}{dN} = C(\Delta K)^n \tag{5}$$

where C and n are empirical constants. Such linear approximations are shown in Fig. 2-5, and the corresponding values of C and n are listed in Table 2. Over the range of ΔK investigated, a single straight line represents the data for each of the stainless steels and the A553 steel. However, the data for the other alloys extend to lower growth rates and are best approximated by two line segments. Such changes in the slope of crack growth data have been demonstrated by other authors [23-25].

The linear approximations in Fig. 6 represent the crack growth rate data plotted versus $\Delta K/E$. The values of Young's modulus at 4 K were taken from measurements by Ledbetter, Naimon, and Weston [26-29], and are listed in Table 1. For ideal elastic behavior, the stress, σ_n, normal to the crack plane is proportional to the strain, ε_n, and

$$\Delta K = \Delta\sigma_n \sqrt{2\pi a} \tag{6}$$

It follows that $\Delta K/E$ is proportional to $\Delta\varepsilon_n \sqrt{2\pi a}$ and, by analogy, $\Delta K/E$ may be termed the "strain intensity factor" [30,31].

When the present results are compared on the basis of $\Delta K/E$, the A553 steel, nearly 100% ferritic, clearly exhibits the highest growth rates. For growth rates from 2×10^{-4} to 3×10^{-3} mm/cycle the $\Delta K/E$ values are much lower for this alloy than for the stable fcc alloys having nearly equivalent Young's modulus. Since the titanium alloys and the metastable austenitic stainless steels also have higher crack growth rates than the stable austenitic alloys (AISI 310, ASTM A453 and A637, 5083-0), all observations are consistent with the conclusion that the presence of bcc and hcp phases are generally deleterious to crack growth resistance at 4 K. Note that the hcp Ti-5Al-2.5Sn alloy exhibits better resistance to fatigue crack propagation than do alloys containing bcc phases; its crack growth resistance is surpassed only by the stable fcc alloys. In sharp contrast, room temperature da/dN data versus $\Delta K/E$ show relatively good agreement among alloys regardless of crystal structure [32,33,34]. Therefore, it is reasonable to assume that the lower crack growth resistance of bcc and hcp materials at 4 K is another aspect of the low temperature embrittlement phenomenon that is characteristic of their fracture, tensile, and impact properties. These generalizations hold true for the alloys considered in this study, but exceptions may exist. For example, a few ferritic alloys retain high fracture toughness at 4 K [35]; it cannot be assumed that these alloys would exhibit poor resistance to fatigue crack propagation at liquid helium temperature.

The similar behavior observed for alloys having close-packed crystal structures is emphasized in Fig. 7. The shaded band represents the results obtained for the fcc alloys -- 5083-0 aluminum, AISI 310, ASTM 453 and ASTM A637. This band is relatively narrow, with a transition in slope occurring at about $\Delta K/E \simeq 1.6 \times 10^{-4}$ $m^{1/2}$. Two straight lines representing the data are described by the equation:

$$\frac{da}{dN} = A\left(\frac{\Delta K}{E}\right)^{b} \quad (7)$$

where $A = 6.7 \times 10^{25}$ and $b = 8$ for the upper range of $\Delta K/E$, and $A = 9.3 \times 10^{11}$ and $b = 4.3$ for the lower range of $\Delta K/E$. The units of A are $(mm/cycle)/(m^{b/2})$ and b is dimensionless. These equations approximate the growth rates of the four fcc alloys within a factor of about $\pm$ 2. Alternatively, a single equation:

$$\frac{da}{dN} = 8.6 \times 10^{15}\left(\frac{\Delta K}{E}\right)^{5.4} \quad (8)$$

may be used to approximate the data over the entire range of $\Delta K/E$ investigated, with some sacrifice of accuracy.

The alloys represented in Fig. 7 have widely varying tensile properties that were not taken into consideration in normalizing the crack growth data on the basis of $\Delta K/E$. This implies that properties such as yield and tensile strength are not particularly strong factors influencing crack growth rates at 4 K, as demonstrated for other alloys at ambient temperature [36,37]. The present results provide ample evidence that ΔK, Young's modulus, crystal structure, and phase stability are the primary factors governing fatigue crack growth at liquid helium temperature.

Summary

1. Stable fcc alloys having high elastic moduli offered maximum resistance to fatigue crack propagation at liquid helium temperature.
2. Several metastable austenitic alloys and alloys containing bcc and hcp phases displayed inferior crack growth resistance at 4 K.
3. The 4 K crack growth results for stable fcc alloys were a similar function of $\frac{\Delta K}{E}$. The results for an aluminum-base, a nickel-base, and two iron-base fcc alloys can be approximated within a factor of about $\pm$ 2 by a single equation:

$$da/dN = A(\Delta K/E)^{b}$$

where the constants A and b have values that depend on the range of $\Delta K/E$.

References

1. R. K. MacCrone, R. D. McCammon and H. M. Rosenberg, Phil. Mag., 4: 267 (1958).

2. R. D. McCammon and H. M. Rosenberg, Proc. Roy. Soc. A, 242: 203 (1957).

3. D. Hull, J. Inst. Met., 86: 425 (1957).

4. L. P. Andreev and N. V. Novikov, Problems of Strength, No. 11: 45 (1971).

5. I. A. Gindin, Ya. D. Starodubov and M. P. Starolat, Ukrainian J. Phys., 18: No. 11. 1899-1905 (1973).

6. A. J. Nachtigall, S. J. Klima and J. C. Freche, J. Mater. JMLSA 3: 425 (1968).

7. A. J. Nachtigall, NASA TN D-7532 National Aeronautics and Space Administration, Lewis Research Center, Cleveland, Ohio (1974).

8. S. S. Manson, Experimental Mech., 5: 193 (1965).

9. Standard method of test for plane strain fracture toughness of metallic materials, E-399-74. Annual book of ASTM Standards, Part 10, (ASTM, Philadelphia, Pa., 1974).

10. R. L. Tobler, R. P. Mikesell, R. L. Durcholz and R. P. Reed, "Properties of Materials for LNG Tankage," ASTM STP 579 (ASTM, Philadelphia, Pa., 1975).

11. C. W. Fowlkes and R. L. Tobler, submitted for publication to Engr. Mech. (1975).

12. G. Irwin, "Fracture," Handbuch der Physik, 6, (Springer-Verlag, Berlin, 1958) p. 551.

13. E. Roberts, Jr., Mater. Res. Stand., 9: 27 (1969).

14. C. J. Gunter and R. P. Reed, ASM Trans. Quart., 55: 399 (1962).

15. D. C. Larbalestier and H. W. King, Cryogenics, 13: 160 (1973).

16. R. P. Reed and C. J. Guntner, Trans. AIME, 230: 1713 (1964).

17. J. F. Watson and J. L. Christian, ASTM STP 287, (ASTM, Philadelphia, Pa., 1960), p. 170.

18. J. F. Watson and J. L. Christian, Trans. AIME, 224: 998 (1962).

19. D. Bhandarkar, V. F. Zackay and E. R. Parker, Met. Trans., 3: 2619 (1972).

20. A. G. Pineau and R. M. Pelloux, Met. Trans., 5: 1103 (1974).

21. P. C. Paris, "Fracture - An Interdisciplinary Approach," (Syracuse University Press, Syracuse, 1964), p. 107.

22. P. C. Paris and F. Erdogan, J. Basic Eng. Trans. ASME, D 85: 528 (1963).

23. T. W. Crooker, Report NRL Prog. 25 (Naval Research Laboratory, Washington, D.C., 1970).

24. J. A. Feeney, J. C. McMillan and R. P. Wei, Met. Trans., 1: 1741 (1970).

25. L. A. James and E. B. Schwenk, Jr., Met. Trans., 2: 491 (1971).

26. E. R. Naimon, W. F. Weston and H. M. Ledbetter, Cryogenics, 14: 274 (1974).

27. W. F. Weston, H. M. Ledbetter and E. R. Naimon, Mat. Sci. Engr., to be published (1975).

28. W. F. Weston, E. R. Naimon and H. M. Ledbetter, "Properties of Materials for LNG Tankage," ASTM STP 579 (ASTM, Philadelphia, Pa., 1975).

29. H. M. Ledbetter, W. F. Weston and E. R. Naimon, J. Appl. Phys., to be published (1975).

30. A. I. McEvily, Proc. Conf. on Fatigue and Fracture of Aircraft Structures and Materials, AFFDL-TR-70-144, Wright-Patterson Air Force Base, Ohio, AD 719756 (1973).

31. G. T. Hahn, A. R. Rosenfield and M. Sarrate, Tech. Report AFML-TR-67-143, Wright-Patterson Air Force Base, Ohio (1969).

32. R. C. Bates and W. G. Clark, Jr., Trans. ASM, 62: 380 (1969).

33. N. E. Frost, L. P. Pook and K. Denton, Eng. Frac. Mech., 3: 109 (1971).

34. "Materials Research for Superconducting Machinery", National Bureau of Standards, Boulder, CO., AD 780-596 and AD/A 004586, National Technical Information Service, Springfield, VA (1974).

35. S. Jin, J. W. Morris, Jr. and V. F. Zackay, Advances in Cryogenic Engineering 19, Ed. K. D. Timmerhaus, (Plenum Press, New York, 1972) p. 379.

36. J. M. Barsom, Trans. ASME J. Eng. Ind., 93: 1190 (1971).

37. H. H. Johnson and P. C. Paris, Eng. Fract. Mech., 1: 3 (1968).

List of Tables

1. Alloy conditions, chemical compositions, and selected properties.

2. Crack growth rate parameters for alloys at 4 K.

List of Figures

1. Crack length -- compliance curves for AISI 310 at 4 K.

2. Crack growth rates of titanium alloys at 4 K.

3. Crack growth rates of face-centered cubic alloys at 4 K.

4. Crack growth rates of austenitic stainless steels at 4 K.

5. Crack growth rates of ASTM A553 at 300, 76 and 4 K.

6. Comparison of crack growth rates, normalized to Young's modulus.

7. Normalized crack growth rate scatterband of stable face-centered cubic alloys.

Table 1. Alloy conditions, chemical compositions, and selected properties.

Alloy	Condition	Chemical Composition (wt. %)	Avg. Grain Dia. (mm)	Hardness	E 10^{11} Nm^{-2} 298K	E 10^{11} Nm^{-2} 4K	σ_y ($MN \cdot m^{-2}$) 298K	σ_t ($MN \cdot m^{-2}$) (298K)	Elongation (%) 298K
Ti-5Al-2.5Sn	annealed	bal. Ti, 5.28 Al, 0.327 Fe, 2.46 Sn, 0.01 C, 0.01 N, 0.174 O, 40 ppm H	0.01	R_c33	1.11	1.23	850	910	15
Ti-6Al-4V	annealed	bal. Ti, 6.24 Al, 4.18 V, 0.174 Fe, 0.035 C, 0.011 N, 0.155 O, 14 ppm H	0.01	R_c37	1.11	1.22	940	1010	16
AISI 304	annealed	bal. Fe, 18.33 Cr, 9.82 Ni, 1.60 Mn, 0.75 Si, 0.20 Mo, 0.13 Cu, 0.028 P, 0.015 S, 0.052 C	0.15	R_B80	1.90	2.04	260	610	80
AISI 310	annealed	bal. Fe, 24.65 Cr, 20.4 Ni, 1.41 Mn, 0.72 Si, 0.13 Mo, 0.14 Cu, 0.023 P, 0.016 S, 0.038 C	0.07	R_B80	1.84	1.99	230	560	57
AISI 316	annealed	bal. Fe, 17.8 Cr, 13.10 Ni, 1.72 Mn, 0.51 Si, 2.18 Mo, 0.019 P, 0.019 S, 0.04 C	0.10	R_B79	2.17	2.34	240	540	60
ASTM A453	solution treated and aged	bal. Fe, 24.97 Ni, 13.96 Cr, 2.23 Ti, 1.52 Mn, 1.30 Mo, 0.19 Al, 0.30 V, 0.004 B, 0.54 Si, 0.016 P, 0.007 S, 0.05 C	0.05	R_c31	1.93	2.12	610	1030	20
ASTM A553	quenched and tempered	bal. Fe, 8.99 Ni, 0.62 Mn, 0.19 Si, 0.010 P, 0.010 S, 0.08 C	0.05	R_c24	1.95	2.06			
ASTM A637	solution treated and aged	bal. Ni, 15.16 Cr, 6.58 Fe, 2.51 Ti, 0.04 C, 0.20 Mn, 0.007 S, 0.25 Si, 0.04 Cu, 0.78 Al, 0.89 Cb + Ta	0.04	R_c26	2.04	2.19	710	1180	19
5083-0 (Al)	annealed	bal. Al, 4.0-4.9 Mg, 0.3-1.0 Mn, 0.25 Zn, 0.05-0.25 Cr, 0.10 Cu, 0.15 Ti, 0.40 Si, 0.40 Fe, 0.15 others	0.02	R_B45	0.72	0.77	140	300	23

Table 2. Crack growth rate parameters for alloys at 4 K.

Alloy	n	C	Crack growth region, ΔK $MN \cdot m^{-3/2}$
Ti-5Al-2.5Sn	4.89	3.85×10^{-11}	$18 \leq \Delta K \leq 29$
	9.56	3.04×10^{-17}	$15 \leq \Delta K \leq 18$
Ti-6Al-4V	4.08	7.49×10^{-10}	$16 \leq \Delta K \leq 29$
	10.0	6.72×10^{-17}	$12 \leq \Delta K \leq 16$
AISI 304	3.78	2.04×10^{-10}	$23 \leq \Delta K \leq 71$
AISI 310	3.68	1.16×10^{-10}	$28 \leq \Delta K \leq 88$
AISI 316	2.92	5.36×10^{-9}	$18 \leq \Delta K \leq 77$
ASTM A453	3.84	5.34×10^{-11}	$38 \leq \Delta K \leq 88$
	8.87	3.33×10^{-19}	$33 \leq \Delta K \leq 38$
ASTM A553	5.31	1.72×10^{-13}	$21 \leq \Delta K \leq 33$
ASTM A637	4.16	1.77×10^{-11}	$34 \leq \Delta K \leq 93$
	7.43	1.06×10^{-16}	$29 \leq \Delta K \leq 34$
5083-0	4.5	6.76×10^{-10}	$13 \leq \Delta K \leq 28$
	8.1	4.59×10^{-14}	$9.8 \leq \Delta K \leq 13$

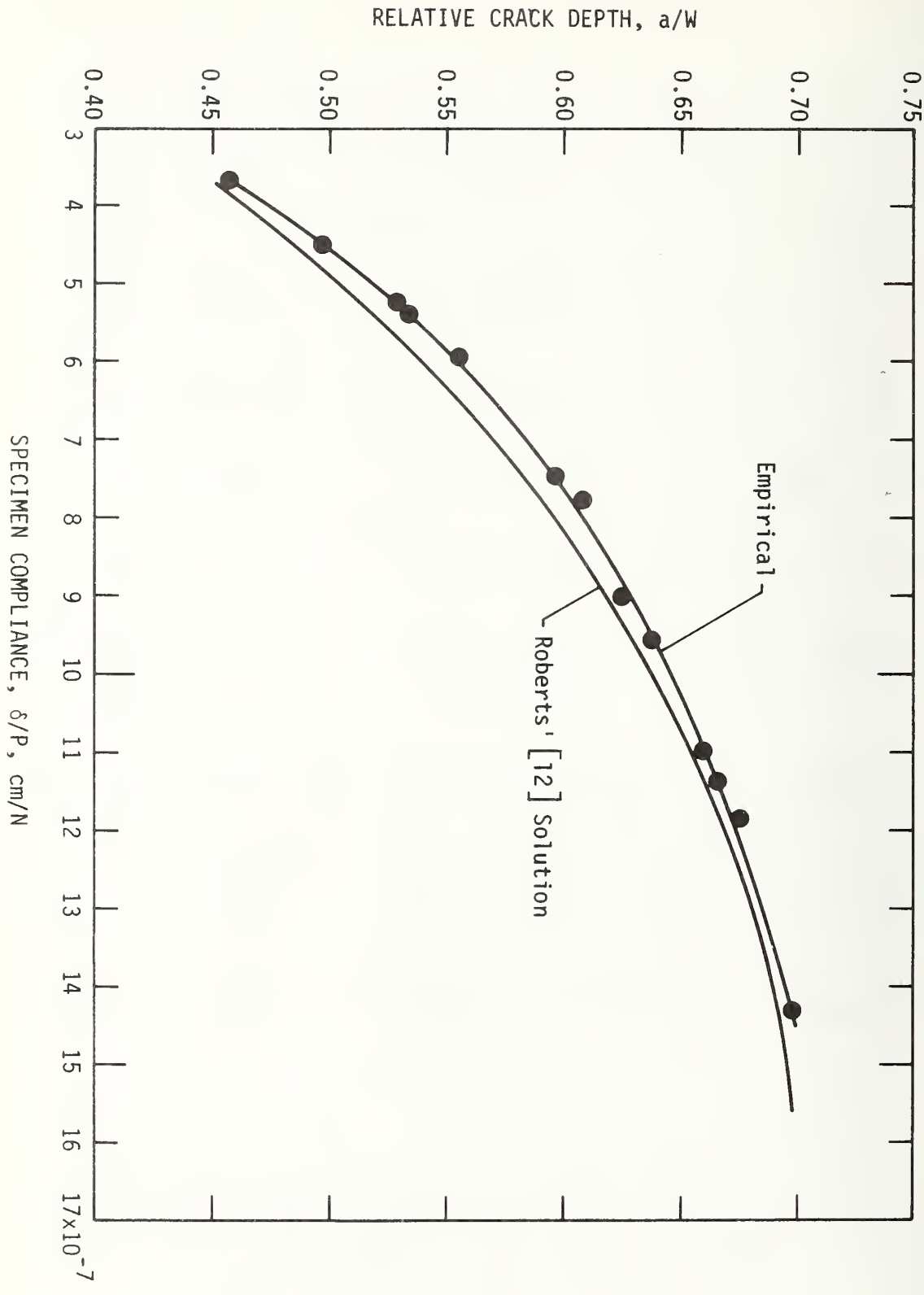

Fig. 1. Crack length -- compliance curves for AISI 310 at 4 K.

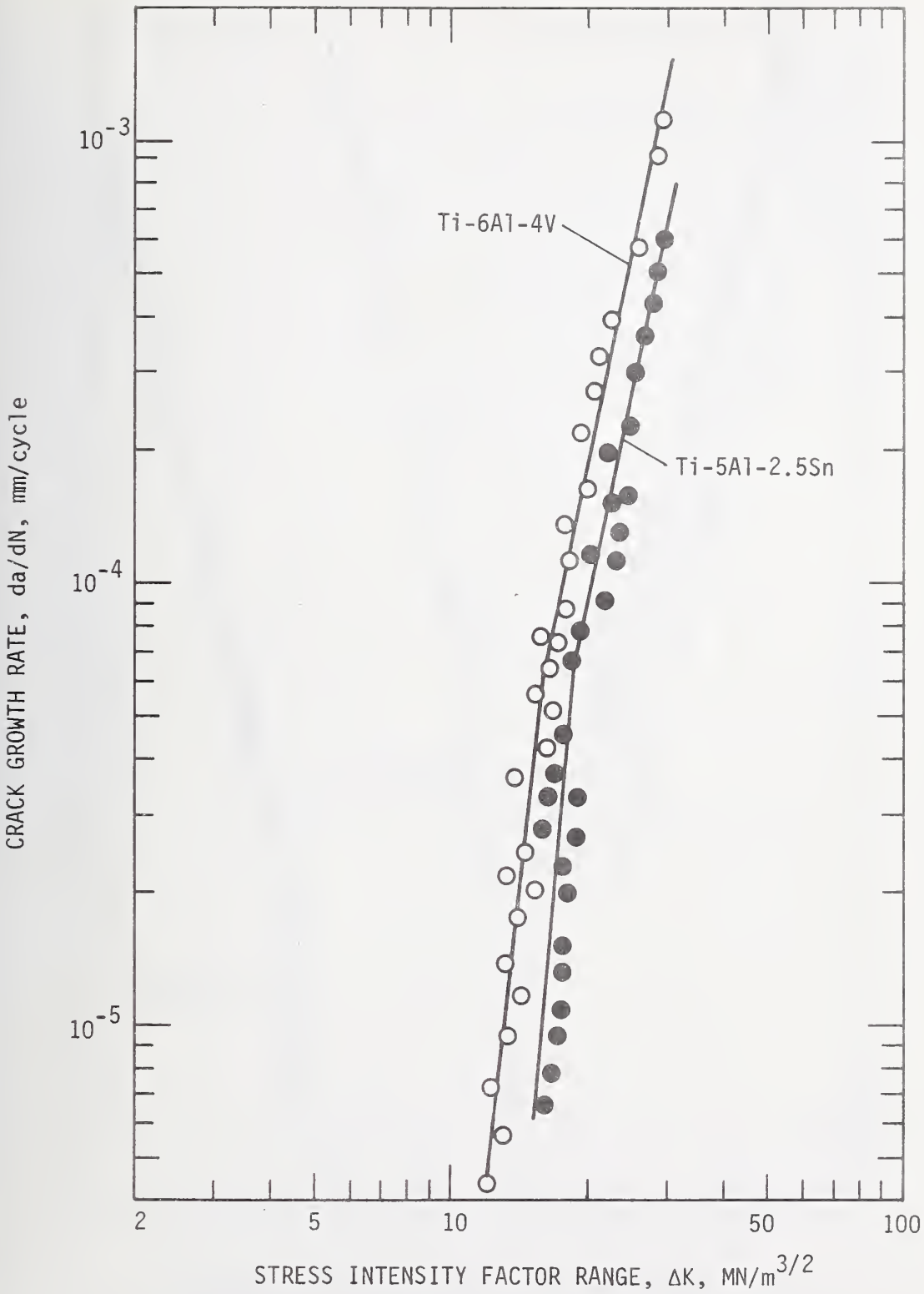

Fig. 2. Crack growth rates of titanium alloys at 4 K.

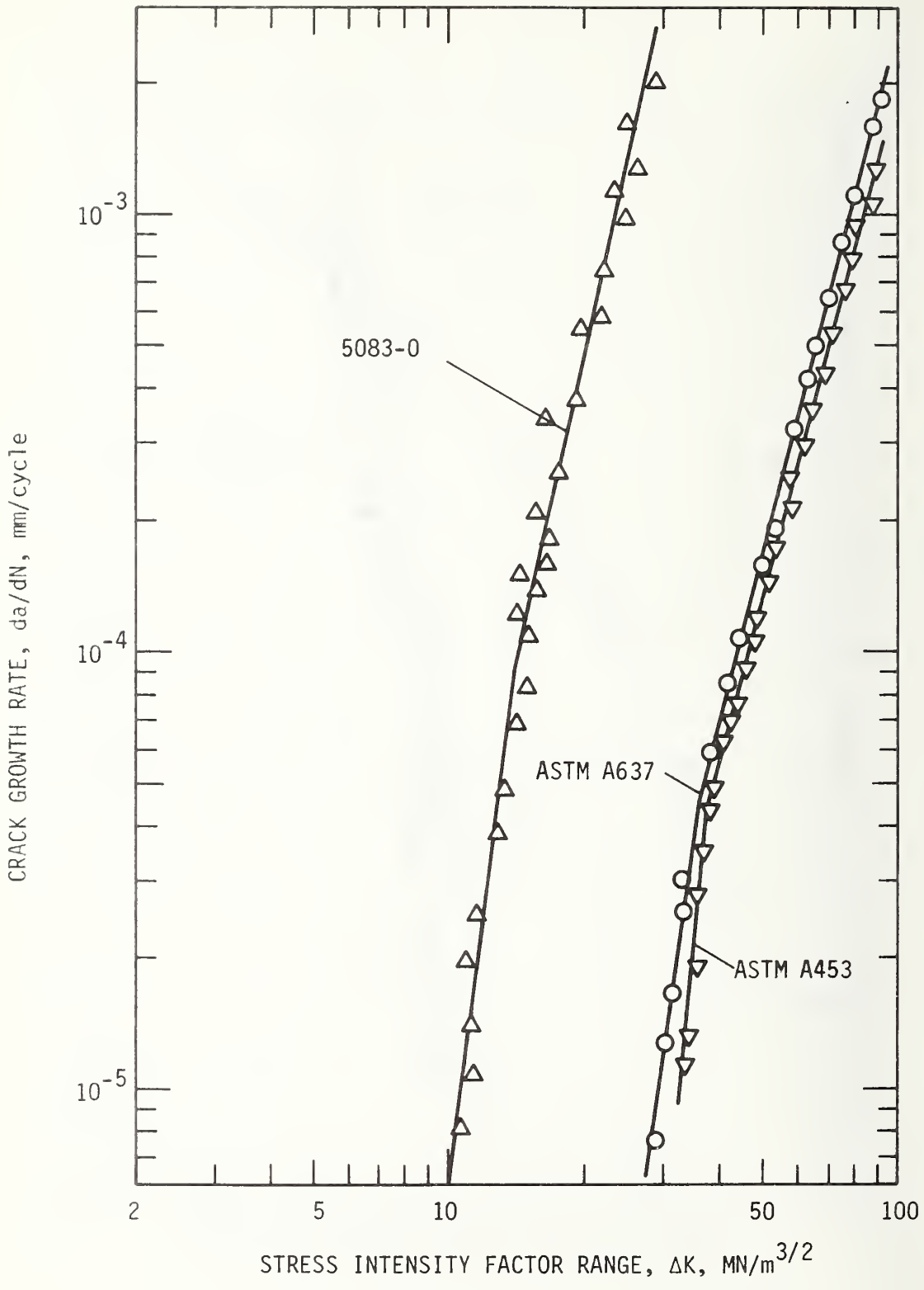

Fig. 3. Crack growth rates of face-centered cubic alloys at 4 K.

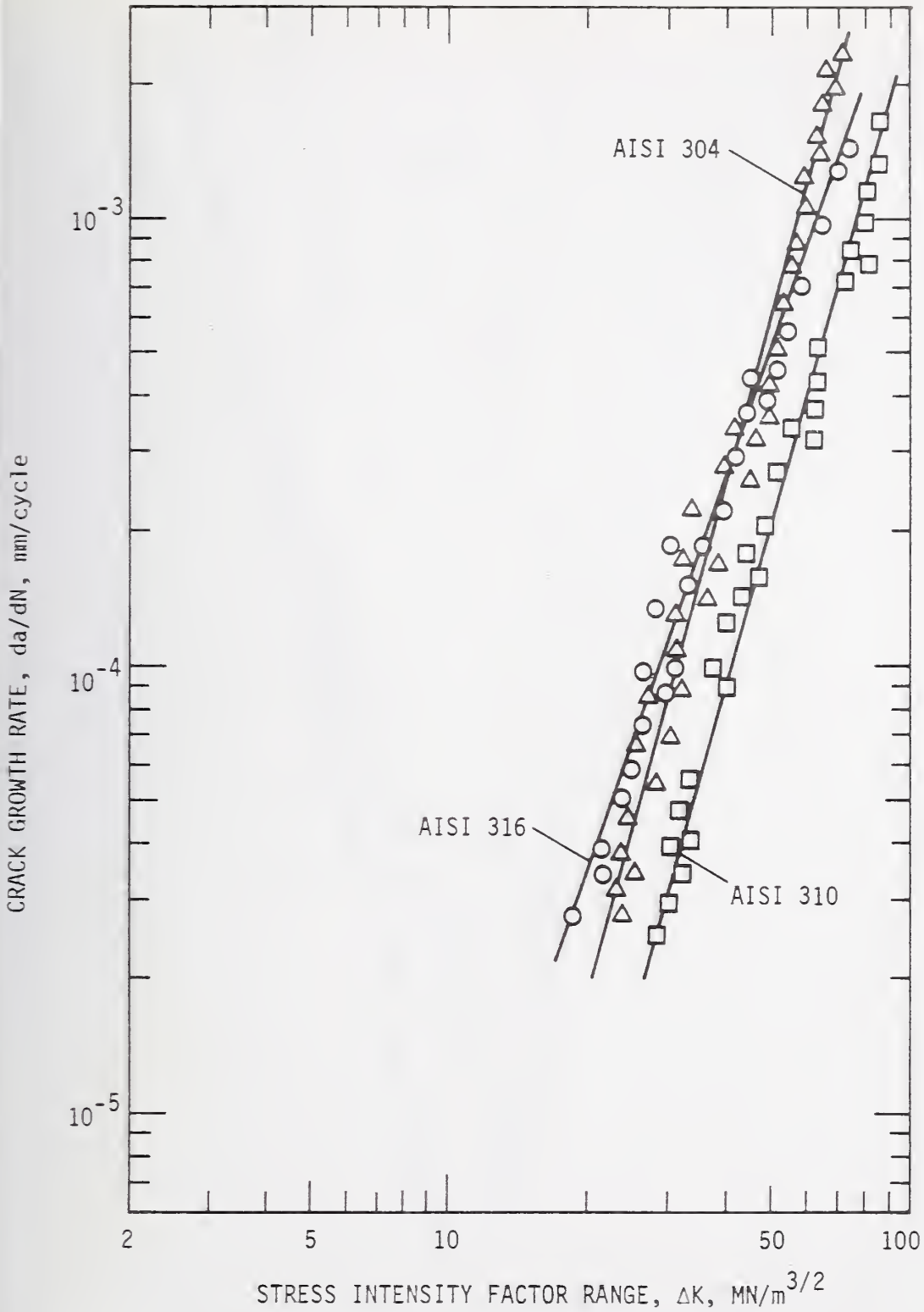

Fig. 4. Crack growth rates of austenitic stainless steels at 4 K.

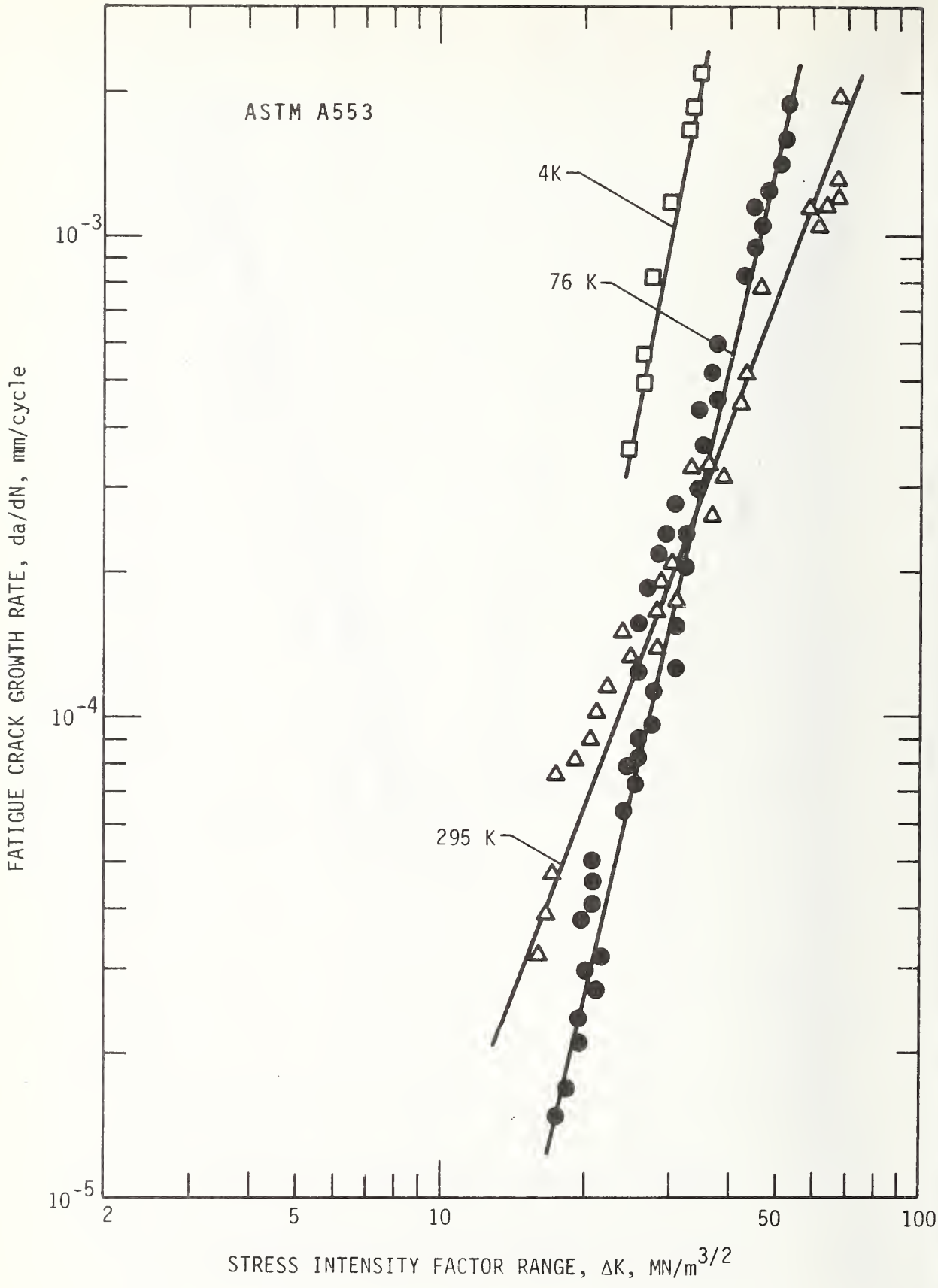

Fig. 5. Crack growth rates of ASTM A553 at 300, 76 and 4 K.

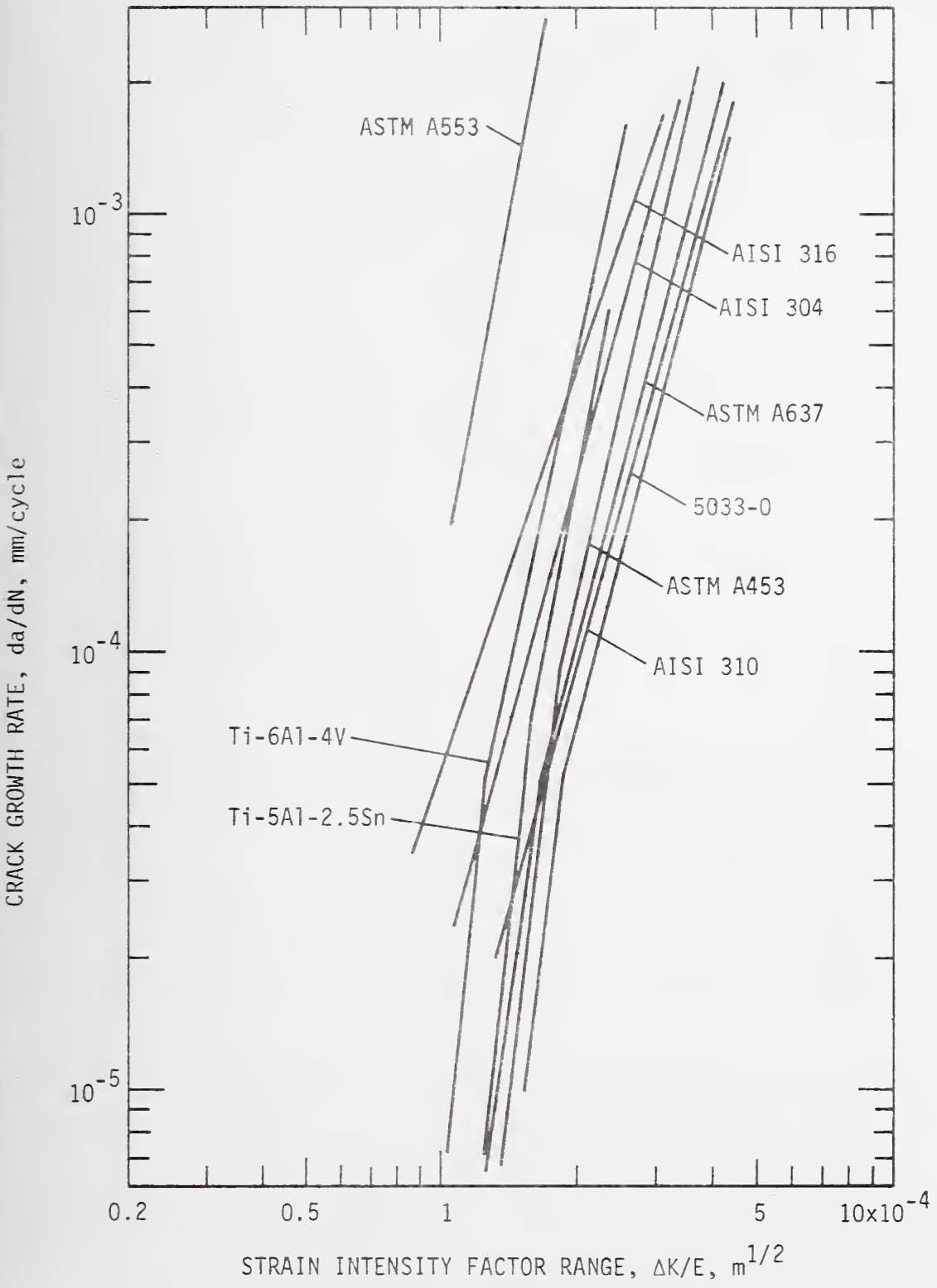

Fig. 6. Comparison of crack growth rates, normalized to Young's modulus.

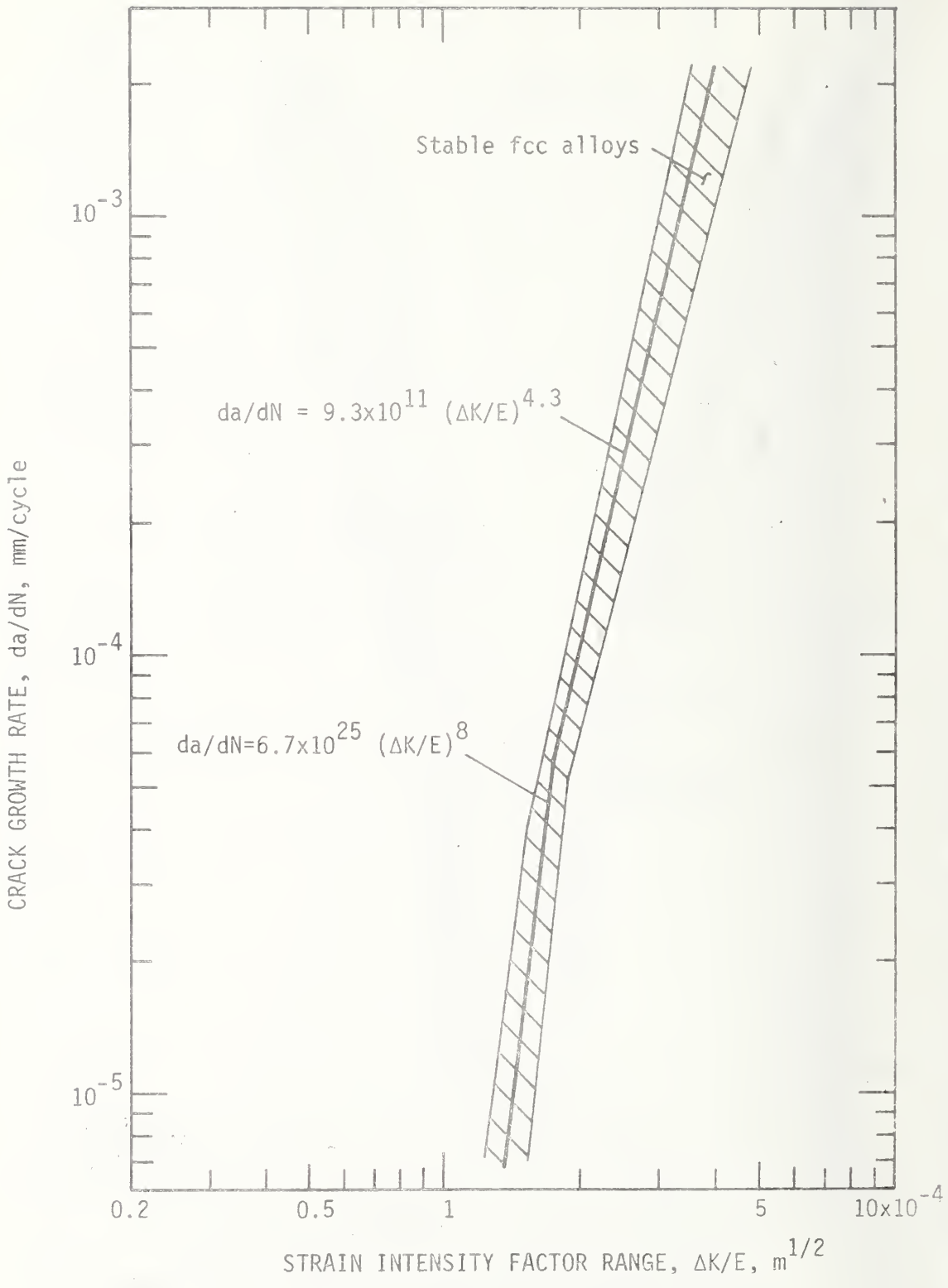

Fig. 7. Normalized crack growth rate scatterband of stable face-centered cubic alloys.

The Fracture Toughness and Fatigue Crack Growth Rate of an Fe-Ni-Cr Superalloy at 298, 76 and 4 K*

R. P. Reed, R. L. Tobler, and R. P. Mikesell

Cryogenics Division
Institute for Basic Standards
National Bureau of Standards
Boulder, Colorado 80302

ABSTRACT

Fatigue crack growth rate and fracture toughness data at 298, 76, and 4 K are presented for a precipitation hardenable, Fe-Ni-Cr superalloy, ASTM A 453. Linear-elastic plane strain and J-integral test techniques were applied using compact specimens. The crack growth rate was significantly lower at low temperatures than at room temperature. The toughness parameter, K_Q, and the critical value of the J-integral, J_{IC}, were determined. $K_{IC}(J)$, as converted from J_{IC}, decreased slightly with decreasing temperature. These results represent the first low temperature fatigue crack growth rate and fracture toughness data published for this alloy.

Key Words: Fatigue crack growth rate; J-integral; plane strain; stainless steel; tensile strength.

INTRODUCTION

Superconductivity is currently being exploited in prototype design and construction of motors and generators. Since superconducting components are cooled with liquid helium, a need exists for mechanical property data in this environment. One alloy that has exhibited high strength at low temperature is a precipitation hardenable, iron base (Fe-Ni-Cr) superalloy, designated ASTM A 453. Until this time, no fracture data for this alloy have been reported at 4 K. Therefore, this alloy was included in a program sponsored by the Advanced Research Projects Agency[1] to determine the fracture toughness and fatigue crack growth rate of structural materials at 298, 76, and 4 K. At all test temperatures, valid K_{IC} data were not obtained using standard compact specimen ASTM E-399-74 procedures and validity criteria. Therefore, it was necessary to employ J-integral test techniques to obtain useful fracture toughness data. These techniques and data are discussed in this paper.

The alloy A 453 is normally employed at elevated temperatures because it has excellent high temperature strength, creep resistance and oxidation resistance. Applications include fasteners, turbine wheels and blades, after burner parts for jet engines, and generator retaining rings. The alloy has been employed for cryogenic applications related to aerospace. Face-centered cubic metals are excellent low temperature materials, and this alloy contains sufficient Ni to stabilize the austenitic phase at cryogenic temperatures. As a result, the alloy has been considered for nuclear rocket structures requiring excellent mechanical properties in both the cryogenic and elevated temperature regimes. The alloy has potential applications at 4 K. The austenitic 300 series stainless steels are already in use in prototype superconducting machinery, and A 453 is a possible alternative to these materials where a higher yield strength, alloy is required.

Cryogenic mechanical property data for this Fe-Ni-Cr commercial alloy have been previously reported[1-7]. These references provide conventional uniaxial tensile properties to temperatures as low as 4 K and some Charpy impact data to 20 K. Fracture mechanics data have not been reported at cryogenic temperatures.

The mechanical properties of this alloy can be widely varied, depending on heat treatment and cold working. At room temperature, the yield strength of solution treated material may be as low as 50,000 psi[3]; for 40% cold worked and aged material, yield strengths as high as 183,000 psi are obtained[8]. At 20 K, the yield strength for these conditions increases to values of 92,000 and 240,000 psi, respectively. As expected, the ductility and impact energy decrease markedly for cold-worked material.

MATERIAL

The chemical composition of the Fe-Ni-Cr alloy, normally referred to as A-286* and designated AISI 660 and ASTM A 453, is 24.97 Ni, 13.96 Cr, 2.23 Ti, 1.52 Mn, 1.30 Mo, 0.30 V, 0.19 Al, 0.05 C, 0.54 Si, 0.016 P, 0.007 S, 0.004 B, and balance Fe. This alloy is paramagnetic, has an austenitic microstructure, and is strengthened by precipitation hardening. he austenitic structure has sufficient nickel to remain stable, with respect to martensite transformation, on cooling to 4 K. The aging process produces various intermetallic compounds, such as $Ni_3(Ti,Al)$, Ni_4Mo (Fe,Cr)Ti, and those containing trace impurities (e.g., Cr-Sn, Cr-Fe-C).

In fig. 1 the typical microstructure is shown. The austenitic grain size corresponds to ASTM grain size number 6 (average grain diameter = 0.0507 mm). The average hardness is R_c31, which is slightly less than the expected hardness[2] of R_c34 for the annealed and aged heat treatment.

The alloy was received as a forged 11.4 cm square bar, which had been mill solution treated at 1650°F for 2 hours and oil quenched. Subsequently, the individual tensile and compact tensile fracture specimens were annealed (1650°F, 2 hours, oil quenched) and aged (1350°F, 16 hours, air cooled).

EXPERIMENTAL PROCEDURES

Tensile Tests

All tensile specimens were machined according to ASTM specification E8-69[9]. Each specimen had a reduced section, 0.25-inch diameter (0.635 cm) by 1.5-inch long (3.81 cm). The axis of each specimen was transverse to the original forging direction.

Tests were performed with a 10,000 lb (44.5 kN) testing machine at a crosshead rate of 0.02 inch (5 cm) per minute, using a stainless steel cryostat as previously described by Reed[10]. Testing in liquid nitrogen (76 K) was accomplished by immersion of the specimen and cryostat in a single metal dewar containing the cryogen. Testing in liquid helium (4 K) was accomplished with a double glass dewar arrangement, the outer dewar containing liquid nitrogen. Load was monitored with a 10,000 lb (44.5 kN) commercial load cell. Specimen extension was measured with a standard clip-on, double beam extensometer.

Fatigue and Fracture Specimens

Standard 1.50-inch (3.8 cm) thick compact specimens were machined in the TS orientation with respect to the original forging axis. The geometry and dimensional tolerances were according to ASTM standard E 399-72[11], but the notch configuration was modified to enable measurement of deflections at the loadline. The depth of the machined notch was such that $a/W = 0.45$.

---

* Tradenames are used in this report for clarity and in no way imply endorsement or recommendation by NBS.

Low Temperature Fatigue Tests

Fatigue crack growth tests were conducted at 298, 76, and 4 K using a 20,000 lb (89 kN) servo-hydraulic test machine in the load control mode. The load was varied sinusoidally, and the ratio of minimum to maximum load was maintained at R = 0.1. Cycling was conducted at rates of 24 ± 4 Hz. No variation in crack growth rate was detected due to frequency change in this range. Loads were measured to within 1% during dynamic testing by means of a digital peak load recording device.

A fiberglass reinforced plastic dewar was used for testing at 76 K, and a double dewar arrangement was employed for tests at 4 K. The inner helium dewar was fabricated from vacuum insulated fiberglass reinforced plastic; the space between the walls contains thin layers of aluminized mylar to reduce heat transfer by radiation. The outer dewar was constructed of foam insulated fiberglass and epoxy. The load frame is composed of two tubular stand off compression members. To minimize heat transfer by conduction, the upper section of thermal gradient from 4 to 76 K was made of fiberglass reinforced plastic; AISI 304 stainless steel was used for the lower sections. The lower specimen grip of maraging steel is pinned into the center of the bridge. The upper specimen grip, also of maraging steel, is threaded and attached directly to a titanium alloy pull rod.

Specimens tested solely for fatigue crack growth rate data were subjected to a range of stress intensities approaching K_Q. The majority of specimens were intended for subsequent fracture tests. On these specimens, crack growth rates were obtained between a/W = 0.47 and a/W = 0.60, and the maximum fatigue stress intensity (K_f) was limited to 0.6 K_Q. During the final 3% of crack growth, the stress intensity factor was no greater than 0.36 K_Q, thus the fatigue precracking procedure should not have influenced the fracture data.

The change in crack length during crack growth rate tests was monitored by compliance measurements. Direct measurement of crack lengths was not possible since the specimens were inaccessible during cryogenic tests. The compliance method is advantageous for relatively thick specimens because it is sensitive to crack length variations through the thickness. Experimental crack length-compliance correlations were obtained at each temperature. The specimen compliance was determined experimentally and plotted for a variety of crack lengths. Fatigue load changes were used to generate striations so that several crack length-compliance observations could be obtained from each fractured specimen. Theoretical compliance curves, based on the solution given by Roberts[12], were not in complete agreement with experimental findings. For a given load and crack length, the compliance depends linearly on Young's modulus. Young's modulus and clip gage sensitivity are both temperature dependent. The change in clip gage sensitivity as a function of temperature was negligible, so that the shift in the compliance curve between 298 and 76 K can be attributed to a change in Young's modulus of 7%[13]. There was not a measurable change in the compliance curves between 76 and 4 K since the change in Young's modulus (0.3%) is negligible over this temperature interval.

Crack growth rates were measured by plotting compliance on an X-Y recorder at intervals during the fatigue test. At the same time, the total number, N, of fatigue cycles sustained by the specimen was noted. Using the experimental crack length compliance correlation, crack length (a) could then be obtained to ± 1.5%. The crack growth rate, da/dN, was determined by graphical differentiation of the "a" versus "N" curve. Since crack growth rates may be temporarily retarded in going from a higher to a lower applied load. Whenever such a change was made, the crack growth rate was allowed to stabilize before data were considered valid.

J-integral tests were performed using the procedure outlined by Landes and Begley[14]. Three or more nearly identical specimens (having equivalent average crack lengths) were tested at each temperature. The specimens were loaded to various increments of stable crack extension and the tests interrupted. Specimens were pulled apart for analysis after a heat tinting treatment oxidized the exposed crack surfaces. Each value of J, as derived

from the area under the load-displacement curve, was plotted as a function of the measured crack extension, Δa. The critical J integral, J_{IC}, was obtained by extrapolation of the J versus Δa plot to zero extension.

For the compact specimens described in this report, J was calculated from the relation:[14,15]

$$J = \frac{2A}{Bb} ,$$

where A is the area under the load-displacement curve to a particular value of extension, B is specimen thickness, and b is the ligament length, W-a. The area A was measured using a planimeter.

RESULTS AND DISCUSSION

Tensile

The yield and tensile strengths of this alloy and of other age-hardened[16-18] and annealed[3] conditions are shown in fig. 2 and Table 1. Notice that the strengths of the alloy reported in this paper are on the low side. This is substantiated by comparison of hardness and yield strength values with producer data[2]; for 1350°F-16 hour aging, a hardness of R_c 34 and a yield strength of 110 ksi are reported. However, the yield and tensile strengths meet the minimum AMS specifications[19,23] for the aged condition of bar stock, which lists a minimum yield strength of 85 ksi and a minimum tensile strength of 130 ksi for room temperature.

The data of fig. 2 are from five independent investigations, yet all conditions have a similar temperature dependence. This leads to the conclusion that for this alloy, within the limitations of conventional measurement accuracy, the temperature dependence of the yield and tensile strength is independent of heat treated condition. The low temperature yield and tensile strengths are predictable if the room temperature strength is known.

Fatigue

The fatigue crack growth rate results for the Fe-Ni-Cr alloy are presented in fig. 3. The crack growth rates are significantly lower at cryogenic temperatures than at room temperature. However, there is essentially no difference in the rates at 76 and 4 K. The crack growth rates at 4 K are relatively low, in comparison with other similar alloys[20]. The A 453 alloy has an equivalent rate to AISI 310 and slower rates than the metastable AISI 300 series austenitic steel grades. The reduced crack growth rates at low temperatures, compared to room temperature, seem to be typical of stable austenitic structures. Reduced crack growth rates might be expected to result from increased work hardening rates, yield strength, Young's modulus, and ductility, which these steels exhibit at lower temperatures[16]. Additional discussion on low temperature crack growth rate characteristics is found in the paper by Tobler and Reed[20].

Fracture

Figure 4 shows typical load-displacement curves at 298, 76, and 4 K. At 76 K, the first drop in load was accompanied by a barely audible "pop"; the load then continued at the same level until fracture occurred. The other two tests at 76 K were terminated before an audible pop occurred, although displacement did take place fairly rapidly once the maximum load of the curve was reached. At all the temperatures, the load-displacement curves were nonlinear. At 4 K, the load-displacement record was linear to about 0.8 P_Q, but then curved slightly before reaching the maximum load. As indicated by heat tinting, the nonlinearity was associated with stable crack growth.

The ASTM recommended criteria to establish the validity of potential K_{IC} data (K_Q data) is the relation of specimen thickness and crack length to the ratio $2.5(\frac{K_Q}{\sigma_{ys}})^2$; if this ratio is smaller than the dimensions B and a, then K_Q can be assumed to represent K_{IC}. As Table 2 illustrates, the ratio is larger than the dimensions at all temperatures, thus these tests cannot be used to obtain K_{IC}. Therefore, to obtain K_{IC} data for this alloy with the available thicknesses, it was necessary to use J-integral test procedures.

The J-integral at 298, 76, and 4 K, as a function of the crack extension, is shown in fig. 5. Each value of the crack extension represents an average of fifteen measurements with a traveling microscope, five measurements at the crack front center, and five measurements at each of the two points midway between the center and edge of the crack front. Macrophotographs of the three specimens used for measurements at 4 K are shown in fig. 6. Crack extension was measured on the heat tinted part of the fracture surface.

J_{IC}, the critical value of the J-integral just prior to crack extension, was calculated from a best fit of the data points. These limits were determined by drawing straight lines through the data points representing both maximum and minimum values at each temperature. It is obvious that for a more rigorous J_{IC} characterization, additional data points are needed. Unfortunately the quantity of material was limited, allowing for the manufacture of only 10 specimens.

Table 3 tabulates the values of J, Δa, J_{IC}, and $K_{IC}(J)$, as converted from the critical value of the J-integral. Conversion was made according to the relation[15,21]

$$K_{IC}(J) = \frac{E}{1-\nu} \cdot J_{IC} ,$$

where E is Young's modulus and ν is Poisson's ratio. The values of E and ν from 300 to 4 K were determined for the as-received material[13] and are summarized in Table 1. The limits of J_{IC} were derived according to the manner just described; the limits of $K_{IC}(J)$ were obtained from the J_{IC} limits.

The values of J_{IC} at each of the temperatures can be considered to be valid, according to a tentative criterion proposed by Begley and Landes[14,22]; if:

$$a,\ B,\ b \geq \alpha \frac{J_Q}{\sigma_{flow}} ,$$

where b is the ligament or uncracked length, α is between 25 and 50, and σ_{flow} is the average of the yield and tensile strengths. If J_Q, the parameter derived from the J-Δa curve, does meet the above requirements, then it represents a valid J_{IC}. Table 2 shows that the dimensional requirements are easily met.

Plots of K_Q and $K_{IC}(J)$, converted from J_{IC}, as a function of temperature are shown in fig. 7. The parameter K_Q increases with a temperature decrease to 76 K and then decreases between 76 and 4 K. $K_{IC}(J)$ changes little between 298 and 4 K. Note that the K_Q curve approaches the curve of $K_{IC}(J)$ as the temperature decreases from 76 to 4 K. This trend is noted in the two ASTM validity criteria, also, (Table 2) as these ratios ($\frac{P_{max}}{P_Q}$ and $2.5\ (\frac{K_Q}{\sigma_{ys}})^2$) approach acceptable values at 4 K.

SUMMARY

Fracture toughness and fatigue crack growth rate data have been obtained for A 453 Fe-Ni-Cr alloy. The results may be summarized as follows:

(1) The crack growth rate of A 453 is lower at 76 and 4 K than at 298 K and compares favorably with other austenitic stainless steel grades.

(2) The parameter $K_{IC}(J)$, obtained from J-integral tests, showed a toughness of about 110 ksi $\sqrt{in}$ at all temperatures, decreasing very slightly at lower temperatures.

ACKNOWLEDGEMENT

The authors wish to thank R. L. Durcholz who assisted in testing and cryostat construction and improvement for the fatigue and fracture tests at 4 K.

NOMENCLATURE

K_{IC}	Critical plane strain fracture toughness as defined in ASTM E 399-74.
P_Q	Load on load-displacement curve corresponding to the intercept of the 5% secant line, as defined in ASTM E 399-74.
K_Q	Stress intensity factor corresponding to P_Q.
J-integral	Parameter proportional to the amount of energy required to extend a crack.
Δa	Crack extension.
J_{IC}	Critical value of J meeting size requirements, derived from J vs. Δa curve.
J_Q	Candidate J_{IC} value subject to evaluation of size requirements.
α	Dimensionless factor used to evaluate J_Q.
B	Thickness of compact specimen.
a	Average value fatigue crack length of specimen measured from load line.
W	Width of specimen, measured from the load line, W = (a+b).
b	Uncracked ligament of specimen.
A	Area under load-displacement curve, to point where test was terminated.
N	Number of fatigue cycles.
da/dN	Crack growth rate in fatigue test.
ΔK	Stress intensity range in fatigue cycle.
σ_{ys}	0.2% offset yield strength in tensile test.
σ_{flow}	Tensile flow stress; the average of the 0.2% offset yield strength and the tensile strength.
E	Young's modulus.
ν	Poisson's ratio.

References

1. A. F. Clark, R. P. Reed, and E. C. van Reuth, "Materials Research for Superconducting Machinery, I and II," AD 780-596 National Technical Information System, Springfield, Va. (1974).

2. Armco Steel Corp., "Product Data - Armco A286", SA-1, Armco Steel Corp., Middletown, Ohio (1966).

3. R. D. Masteller, NASA CR-72638 (N70-27114) Martin Marietta Corp., Denver, Colo. (May, 1970).

4. C. J. Slunder, A. F. Hoenie, and A. M. Hall, NASA Tech. Memo TM-X-53578 (Feb. 20, 1967).

5. C. A. Schwanbeck, Topical Report to NASA by Lockheed Nuclear Products, Lockheed-Georgia Co. LAC ER-10008 (1968).

6. J. W. Montano, Report IN-P and VE-M64-1, Marshall Space Flight Center, Huntsville, Ala., (Feb. 25, 1964).

7. D. A. Roberts, D. B. Roach, and A. M. Hall, Defense Metals Information Center Report 112, Battelle Memorial Inst., Columbus, Ohio (May 1, 1959).

8. J. W. Montano, "An Evaluation of the Mechanical and Stress Corrosion Properties of Cold Worked A-286 Alloy," NASA-TM-X-64569, (Feb. 12, 1971).

9. "Tension Testing of Metallic Materials", E8-72, Annual Book of ASTM Standards, Part 31, (ASTM, Philadelphia, Pa. 1973).

10. R. P. Reed, Advances in Cryogenic Engineering, Vol. 7 (Plenum Press, Inc., New York, 1962, Edited by K. D. Timmerhaus) p. 448.

11. "Standard Method of Test for Plane-strain Fracture Toughness of Metallic Materials," E 399-74, Annual Book of ASTM Standards, Part 10 (ASTM, Philadelphia, Pa. 1974).

12. E. Roberts, Jr., Materials Res. and Standards, 9: 27 (1969).

13. E. R. Naimon, H. M. Ledbetter, and W. I. Weston, from Semi-Annual Report on Materials Research for Superconducting Machinery AD 780-596, National Technical Information Service, Springfield, Va (1974).

14. J. D. Landes, and J. A. Begley, Private Communication from J. A. Begley to R. P. Reed, Cryogenics Division, NBS, Boulder, Colorado (1973).

15. J. R. Rice, P. C. Paris, and J. G. Merkle, ASTM STP 536, (ASTM, Philadelphia, Pa., 1973) p. 231.

16. K. A. Warren, and R. P. Reed, "Tensile and Impact Properties of Selected Materials from 20 to 300 K", National Bureau of Standards Monograph 63, (June 28, 1963).

17. J. F. Watson, J. L. Christian, and A. Hurlich, AD 276-148, Convair Astronautics Rept. MRG-132-1, San Diego, Calif. (Feb., 1960).

18. Malin, C. O. as reported in NASA SP-5921 (01), Technology Utilization Office, NASA, Washington, D.C. (1970).

19. Aerospace Structural Metals Handbook, Vol. I., (Syracuse Univ. Press, March, 1963).

20. R. L. Tobler, and R. P. Reed, "Fatigue Crack Growth Rates of Structural Alloys at Four Kelvin" to be published in International Cryogenic Materials Conference Proceedings (Plenum Press, New York, 1976).

21. J. D. Landes, and J. A. Begley, Proc. of the 1971 National Symposium on Fracture Mechanics, Part II, ASTM STP 514, (ASTM, Philadelphia, Pa., 1972) p. 24.

22. J. A. Begley, and J. D. Landes, Fracture Toughness, Proc. of the 1971 National Symposium on Fracture Mechanics, Part II, ASTM STP 514, (ASTM, Philadelphia, Pa., 1972) p. 1.

23. R. F. Muraca and J. S. Whittick, "Materials Data Handbook. Stainless Steel Alloy A-286", N72-30463, Marshall Space Flight Center, Alabama (June, 1972).

Figure Captions

1. Microstructure of annealed and aged A 453 alloy. Magnification = 200 x.

2. Tensile and yield strength as function of temperature for a number of similar aged conditions for A 453 precipitation hardened alloy.

   Curves A - 1800°F, 1.5 hr, Oil Q; 1350°F, 16 hr. Air cool, bar, ref. 16.
   Curves B - 1800°F, 0.5 hr, Oil Q; 1325°F, 16 hr. Air cool, sheet, ref. 17.
   Curves C - 1800°F, 2.0 hr, Oil Q; 1350°F, 16 hr. Air cool, bar, this report.
   Curves D - 1800°F, 1.0 hr, Oil Q; 1350°F, 16 hr, Air cool, bar, ref. 18.
   Curves E - Solution treated, ref. 3.

3. Fatigue crack growth rate at 298, 76 and 4 K.

4. Load-displacement curves at 298, 76 and 4 K.

5. The J-integral as a function of crack extension at 298, 76 and 4 K.

6. Macrophotograph of the fracture surfaces of specimens tested at 4 K.

7. The toughness parameters, K_Q and $K_{IC}(J)$, plotted as a function of temperature.

List of Tables

1. Tensile properties of A 453 superalloy.

2. Dimensional criteria for valid K_{IC} and J_{IC} of A 453 superalloy.

3. J-integral and converted $K_{IC}(J)$ of A 453 superalloy.

Table 1. Tensile properties of A-453 superalloy.

Author	Condition	Temp. (K)	0.2% Yield Strength (ksi)	Tensile* Strength (ksi)	% E long (4D)	% R.A.	Young's Modulus	Poisson's Ratio (10^6 psi)
This report	1650°F-2hr,OQ 1350°F-16hr,AC	298	88.2	147.0	19.0		2.79	0.293
		76	108.4	195.0 (est)			2.99	0.280
		4	128,9	212.0 (est)			3.00	0.278
Warren & Reed (16)	1800°F-1-1/2 hr-OQ	298	111.1	160.0	25	49		
	Aged 1350°F-16hr-AC	195	120.3	175.8	29	52		
	R_c 30	76	135.4	209.4	36	49		
		20	150.2	235.3	36	43		

Note: 1 ksi = 6.895 Nm^{-2}

* Estimated from yield strength data and figure 1 temperature dependences.

Table 2. Dimensional criteria for valid K_{IC} and J_{IC} of A-453 superalloy.

Temp. (K)	a (in)	B (in)	b (in)	$2.5\left(\frac{K_Q}{\sigma_{ys}}\right)^2$ (in)	$50\frac{J_Q}{\sigma_{flow}}$ (in)
298	1.67	1.50	1.37	3.35	0.179
76	1.65	1.50	1.38	3.33	0.126
4	1.67	1.50	1.36	2.02	0.102

Note: 1 in = 2.54 cm

Table 3. J-integral and converted $K_{IC}(J)$ of A-453 superalloy.

Temp. (K)	Spec	b* (in)	J ($\frac{in\text{-}lb}{in^2}$)	Δa_{ave} (in)	J_{IC} ($\frac{in\text{-}lb}{in^2}$)	$K_{IC}(J)$ (ksi/in)
298	2	1.37	725	0.076	426 ± 25	114 ± 3.4
298	4	1.38	806	0.101		
298	5	1.39	507	0.015		
298	15	1.35	527	0.038		
76	6	1.40	396	0.005	385 ± 15	112 ± 2.4
76	8	1.35	658	0.056		
76	13	1.38	462	0.012		
76	9					
4	0	1.37	402	0.035	350 ± 20	107 ± 3
4	7	1.34	543	0.146		
4	10	1.37	373	0.022		

Notes:

1 in = 2.54 cm

$1 \frac{in\text{-}lb}{in^2} = 1.75 \times 10^2 \frac{N\text{-}m}{m^2}$

$1 \text{ ksi/in} = 1.09 \times 10^6 \frac{N}{m^2}/m$

B = 1.5 in (3.86 cm)
± 0.003 (0.008 cm)

*b = W-a

Figure 1. Microstructure of annealed and aged A 453 alloy. Magnification = 200 x.

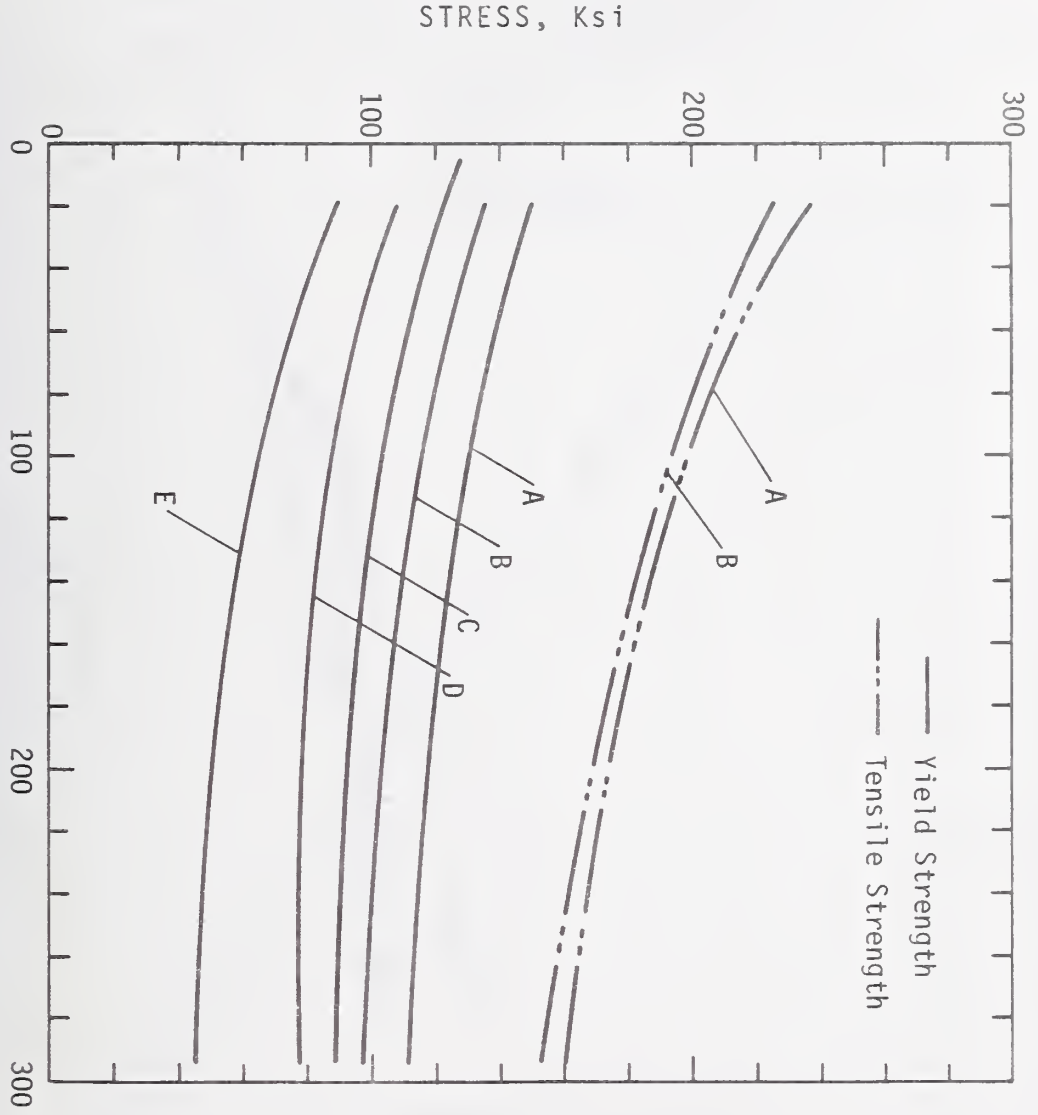

e 2. Tensile and yield strength as function of temperature for a number of similar aged conditions for A 453 precipitation hardened alloy.

Curves A - 1800°F, 1.5 hr, Oil Q; 1350°F, 16 hr. Air cool, bar, ref. 16.
Curves B - 1800°F, 0.5 hr, Oil Q; 1325°F, 16 hr. Air cool, sheet, ref. 17.
Curves C - 1800°F, 2.0 hr, Oil Q; 1350°F, 16 hr. Air cool, bar, this report.
Curves D - 1800°F, 1.0 hr, Oil Q; 1350°F, 16 hr, Air cool, bar, ref. 18.
Curves E - Solution treated, ref. 3.

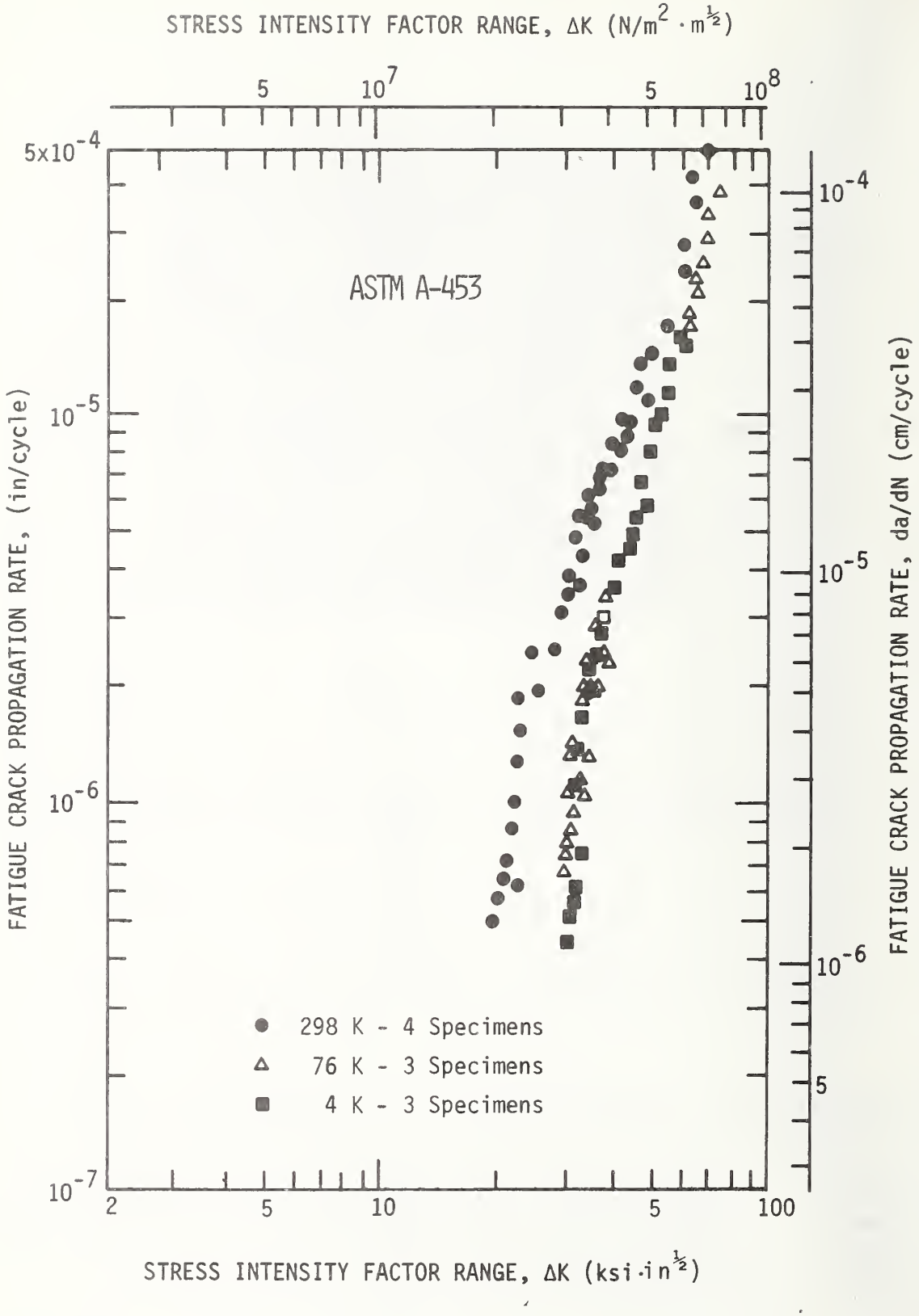

Figure 3. Fatigue crack growth rate at 298, 76 and 4 K.

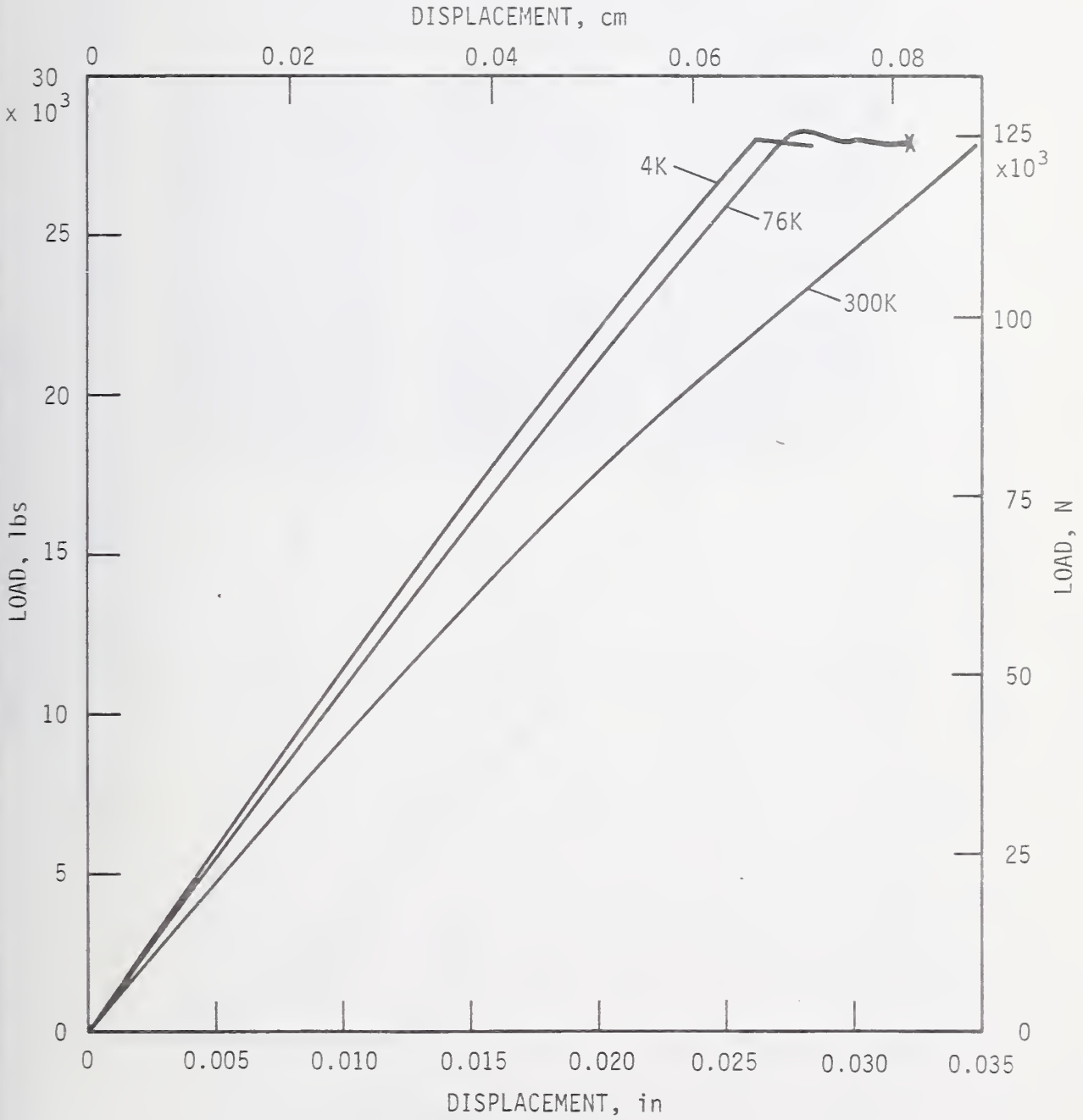

Figure 4. Load-displacement curves at 298, 76 and 4 K.

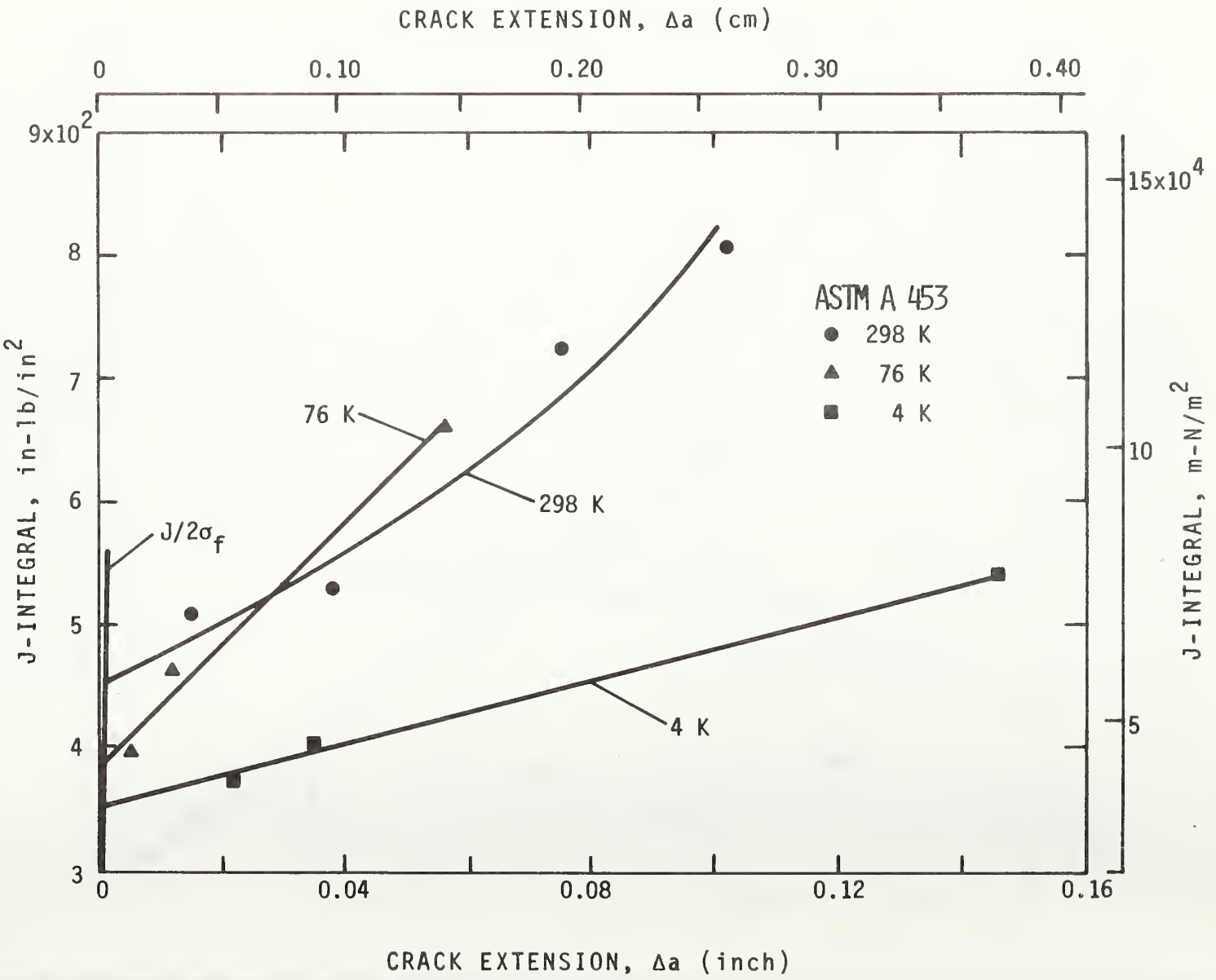
CRACK EXTENSION, Δa (cm)
0
0.10
0.20
0.30
0.40
9x10^2
8
7
6
5
4
3
J-INTEGRAL, in-lb/in^2
15x10^4
10
5
J-INTEGRAL, m-N/m^2
ASTM A 453
298 K
76 K
4 K
76 K
298 K
4 K
J/2σf
0
0.04
0.08
0.12
0.16
CRACK EXTENSION, Δa (inch)

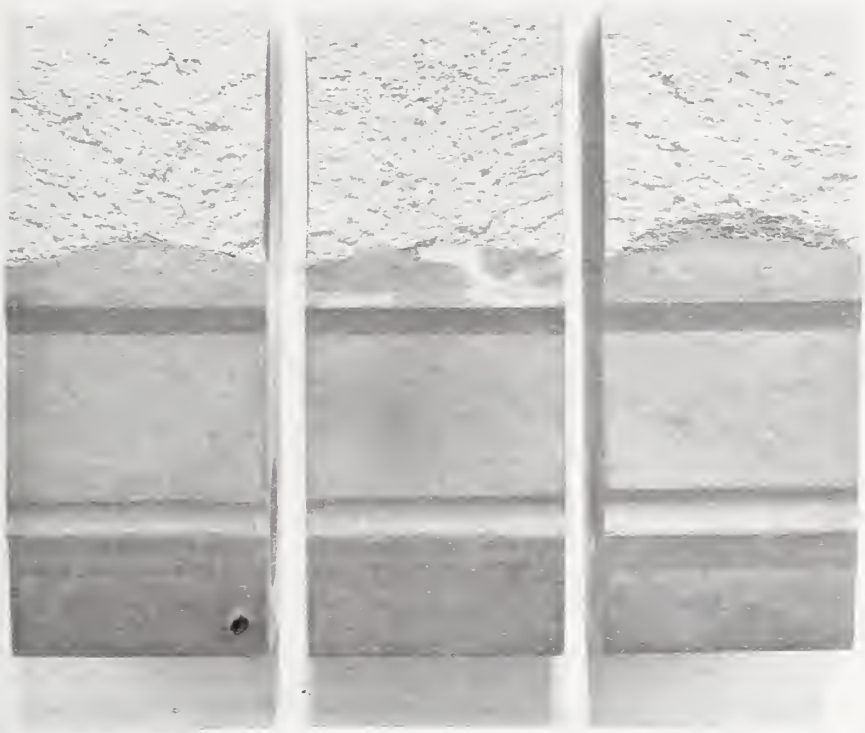

Figure 6. Macrophotograph of the fracture surfaces of specimens tested at 4 K.

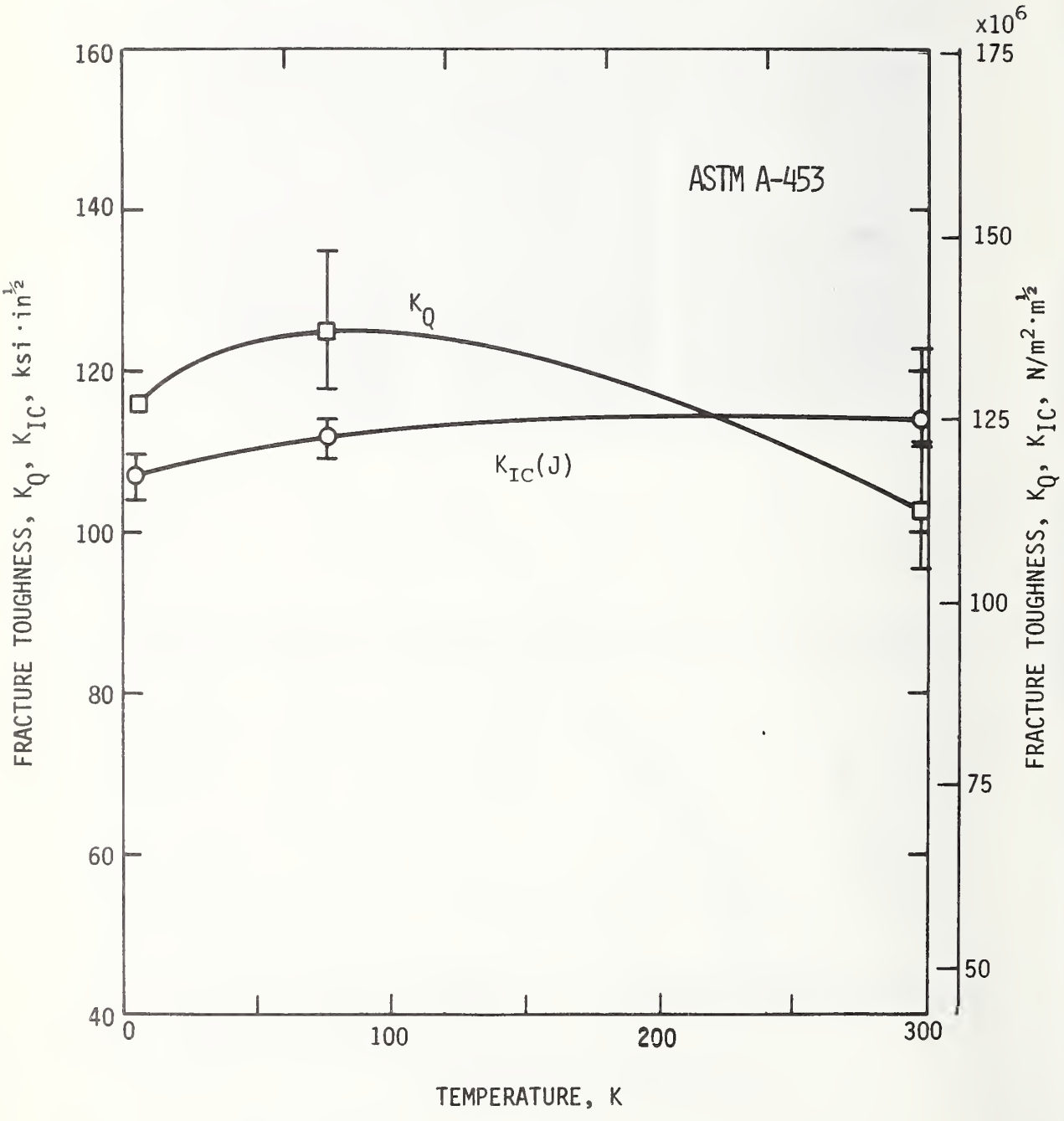

Figure 7. The toughness parameters, K_Q and $K_{IC}(J)$, plotted as a function of temperature

NBSIR

SEMI-ANNUAL REPORT ON MATERIALS RESEARCH IN SUPPORT OF SUPERCONDUCTING MACHINERY

ADVANCED COMPOSITES

R. E. Schramm and M. B. Kasen

Cryogenics Division
Institute for Basic Standards
National Bureau of Standards
Boulder, Colorado 80302

April, 1975

Contents: Advanced Composites

		Page
1.0	Review	126
2.0	Phase I: Preliminary Work	
	2.1 Materials	126
	2.2 Procedures	126
	2.3 Results	127
	2.4 Discussion	128
	2.5 Conclusions	129
3.0	Phase II: Characterization of the Mechanical Properties of Uniaxial Composites at Cryogenic Temperatures	
	3.1 Introduction	129
	3.2 Material	129
	3.3 Procedures	129
	3.4 Results	130
	3.5 Discussion	130
	3.6 Future Work	131
4.0	Appendix I: Symbols	131
5.0	Appendix II: Parameters Calculated from Test Results	131
6.0	References	132
7.0	List of Figures	133
8.0	List of Tables	140

Summary: Advanced Composites

The experimental work in this program is being conducted in two phases. Phase I was devoted to a check of the instrumentation and procedures to be used for tensile-mechanical property testing of uniaxial composites and included a preliminary evaluation of commercial, state-of-the-art boron-epoxy and graphite-epoxy composites. Phase I has now been completed.

In Phase II (now under way) we will measure basic tensile and compressive properties of five selected composites: boron-aluminum, boron-epoxy, and glass, graphite, and Kevlar-49* in a NASA Resin 2 matrix. These data will be determined at 4 K, 76 K, and 295 K and will be useful in the design of complex composite structures using macromechanical analytical methods. This report presents the detailed results of Phase I and includes some initial data obtained with a boron-aluminum composite in Phase II.

* The use of trade names in this paper in no way implies endorsement or approval by NBS and is included only to define the material.

1.0 Review

Comprehensive literature reviews in previous ARPA reports[1,2] have covered the mechanical and thermal properties of glass-filament- and advanced-fiber-reinforced structural composites at cryogenic temperatures. These reviews indicated there were few low temperature data - almost none at 4 K - but they did make it possible to select for our experimental program the most promising composites for cryogenic use. We arranged for commercial suppliers to fabricate the following composites:

5.6 mil Boron-6061 Aluminum

5.6 mil Boron-Epoxy

S-901 Glass-NASA Resin 2

Kevlar-49-NASA Resin 2

Type A Graphite-NASA Resin 2.

We will measure various mechanical properties (static tensile and compressive) for longitudinal (0°), transverse (90°), and crossply (± 45°) filament layups. Other investigators will measure dynamic mechanical and thermal properties. With these sorts of data, it will be possible to compute design values for complex structures using macromechanical analytical methods.

Phase I of the experimental program was preparatory in nature. After construction of the cryostat came the assembly and testing of the electronics. The development of a workable grip system and simple specimen configuration was essential to allow us to perform a large number of tests within our time and money restrictions. The tensile testing system that evolved consists of a straight-sided coupon with the ends wrapped in stainless steel screen and sandwiched between serrated titanium grip plates; pressure plates hold the assembly together. Two commercial producers supplied us with some material so we could both test the apparatus and obtain some preliminary values while awaiting the arrival of the composites listed above. The last report[2] included the results of the first few tests.

2.0 Phase I: Preliminary Work

2.1 Materials

The graphite- and boron-epoxy composites evaluated in Phase I were state-of-the-art products, not optimized for cryogenic service. They were obtained as uniaxial panels from commercial suppliers, and radiography indicated they were of excellent quality. The nominal fiber volume fractions were reported by the manufacturers to be 50% for the boron-epoxy and 60% for the graphite-epoxy. The void content is less than 2%, typical of good commercial production.

Material	Supplier	Plies	Test Orientation
5.6 mil Boron-Epoxy	A	4	longitudinal (0°)
5.6 mil Boron-Epoxy	A	11	transverse (90°)
4.0 mil Boron-Epoxy	B	6	longitudinal (0°)
Graphite-Epoxy	A	6	longitudinal (0°)
Graphite-Epoxy	A	15	transverse (90°)

2.2 Procedures

All tensile specimens were straight-sided coupons cut by a diamond circular saw, lubricated and cooled by a stream of water-soluble oil. Although the as-cut edges were already very smooth, light hand buffing with emery paper was added to further minimize edge imperfections that might cause premature failure. The longitudinal (0°) specimens were 27.9 cm (11 in.) long by 1.3 cm (0.5 in.) wide by a nominal 0.076 cm (0.030 in.) thick; the transverse (90°) specimens were about 15.2 cm (6 in.) long by 2.5 cm (1 in.) wide by a nominal 0.203 cm (0.080 in.) thick. No end tabs were used.

Resistance strain gages monitored longitudinal and transverse strains. Before mounting the gages, the specimen surface was lightly sanded and carefully degreased. After application of a commercial cement recommended for cryogenic use, the strain gages were aligned with the center line of the specimen, clamped between pressure pads, and cured overnight at about 345 K, well below the temperature at which the epoxy matrices had been cured. A second gage, perpendicular to the first, was added whenever Poisson's ratio was to be determined. For these preliminary tests, the atmospheric conditioning specified by ASTM D3039-71T, Method of Test of Tensile Properties of Oriented-Fiber Composites, was not strictly observed; however, all materials were exposed to 293-296 K at 30-40% relative humidity for at least two days between the strain-gage cement cure and the tensile testing.

Just prior to the test, the grips were attached to each specimen in a separate alignment fixture. The resulting gage length was 15.2 cm (6 in.) for the longitudinal (0°) specimens and 5.0 cm (2 in.) for the transverse (90°) specimens. This assembly was then suspended in the test fixture by a pin and clevis at the upper and lower pull rods, and the cryostat support system was enclosed by a dewar containing either liquid nitrogen (76 K) or liquid helium (4 K), the latter being shielded by an outer liquid nitrogen dewar. Three different crosshead speeds produced strain rates of 0.01-0.03 min^{-1} in the longitudinal (0°) specimens and 0.02-0.04 min^{-1} in the transverse (90°) specimens. Within this small range and limited number of tests, no strain rate sensitivity was noted in either composite type. For this set of measurements, the specimens were initially stress cycled in tension to about 25-75% of their anticipated ultimate loads several times before loading to fracture. In this way we could determine the repeatability of the elastic portion of the stress-strain curve for each material.

2.3 Results

The results of each test and their group averages are presented in Tables 1-4. The elastic moduli for both boron- and graphite-epoxy materials indicate a tendency to increase as the temperature decreases; however, the data scatter is sufficiently large as to render this effect uncertain. The highest modulus was obtained with the longitudinal (0°) 5.6 mil boron-epoxy, while the 4 mil boron-fiber composite had a modulus almost 19% lower at both 76 K and 4 K. The modulus of the longitudinal (0°) graphite-epoxy material was about 60% of the boron-epoxy of similar orientation.

The Poisson's ratios are significantly higher in the graphite-epoxy than in either of the boron composites. Of the two sizes of boron fiber, specimens fabricated with the larger 5.6 mil fiber produced slightly higher ratios.

The ultimate tensile strength data illustrate the large anisotropy of these materials. Rotating the tensile axis of the composite from longitudinal (0°) to transverse (90°) changes the ultimate strength by more than a factor of 20. Longitudinal (0°) properties primarily reflect the properties of the fiber reinforcement, while the transverse (90°) properties are mainly a function of the matrix and the fiber-matrix interface. Tensile strengths in the fiber direction are very high, approximately 17.4 x 10^8 N/m^2 (253 ksi) for the boron-epoxy and approximately 13.1 x 10^8 N/m^2 (190 ksi) for the graphite-epoxy materials at 76 K and 4 K. Slightly higher strength values were obtained with the 5.6 mil boron-epoxy than for the 4.0 mil fiber. Room temperature tests were not taken to fracture in Phase I; however, the typical room temperature strength of the 4.0 mil boron-epoxy is about 13.0 x 10^8 N/m^2 (188 ksi)[4] and about 14.5 x 10^8 N/m^2 (210 ksi) for the 5.6 mill product (manufacturer's data), suggesting a significant strength increase in this material on cooling. The latter result was unexpected, since the results of the earlier survey[2] indicated little temperature sensitivity of strength properties for boron-epoxy in the cryogenic range. Further testing of this material in Phase II will clarify the temperature dependence question. The manufacturer reports typical room temperature tensile strengths of about 14.7 x 10^8 N/m^2 (213 ksi) for the graphite-epoxy materials used in Phase I, suggesting that this material decreases in strength somewhat upon cooling. The latter is consistent with the results published in the literature survey.[2]

The elongation at fracture is very small (< 1%) for both materials. Again it was substantially less in the transverse (90°) than in the longitudinal (0°) direction.

2.4 Discussion

As frequently is observed with composites, a small hysteresis loop appeared on the initial loading cycle and disappeared on subsequent cycling in tension. This initial hysteresis is usually attributed to isolated failure of some of the filaments, perhaps at filament kinks. Except for the small hysteresis, these tests indicated complete elasticity (no evidence of plasticity).

Figure 1 presents a schematic of the stress-strain characteristics of the two composite types included in this program. With one exception, both materials and all configurations displayed a simple straight line, as exemplified by the longitudinal (0°) boron-epoxy in Figure 1. However, the longitudinal (0°) graphite-epoxy produced an initial slope, followed by a second and higher slope. There is not a large difference between these slopes, but they are distinct and reproducible. The change of slope occurs at about 20-30% of the ultimate stress. This does not represent plastic yielding, as unloading of the specimens at any point on the curve resulted in retracing of the curves back to the origin. The authors do not presently understand the mechanism reflected by these two slopes. Primary and secondary moduli have been noted previously in crossplied glass-polymeric composites where the knee between the two slopes is attributed to cracking of the epoxy matrix.[3] However, we know of no previous reports of double moduli in longitudinal (0°) composites. Furthermore, when observed in glass-reinforced composites, the second slope is always lower than the first, contrary to the present results. Clearly, the present phenomenon is of different origin. One possibility is that the increase in slope (increased stiffness) reflects the straightening out of graphite filaments in the yarn bundles. Additional information on this phenomenon will be obtained during further testing of graphite-epoxy specimens during Phase II of the current program.

Tensile testing of uniaxial longitudinal (0°) composites is complicated by the necessity of gradually transferring the tensile load from the grips into the fiber reinforcement, thus minimizing localized stress concentrations that cause premature failure of the specimen outside the gage length. An "acceptable" fracture is defined as one in which the tensile break initiates at least one specimen thickness away from the grips (ASTM D3039-71T). Using this criterion, there was only one unacceptable fracture among the thirty tests conducted in Phase I. These results were very rewarding, as available information had suggested that a 50-70% acceptable fracture rate might be expected, and this would have been prohibitively expensive at cryogenic temperatures. One other fracture was not included in the averages, as noted on Table 3. The latter specimen inexplicably failed within the gage length during the third cycle of the preliminary test sequence, failure occurring at a lower load than the specimen had sustained in the two previous cycles.

The "good break" criterion was difficult to apply to the longitudinal (0°) graphite-epoxy specimens. This material failed catastrophically over the entire gage length, making it impossible to accurately determine the location of the initial point of failure. Conversely, the longitudinal (0°) boron-epoxy fractures were irregular, but well defined. In all boron-epoxy specimens, one or more splits along the length of the specimen propagated from the fracture site toward the specimen grips, frequently stopping before reaching the grip. In these tests, no spurious transverse fractures branched from the longitudinal splits. All transverse (90°) fractures were straight and sharp, indicating brittle fracture of the epoxy matrix.

The experimental data of Tables 1-4 are reported as recommended by ASTM D3039-71T. The coefficient of variation (CV) is the standard deviation stated as a percentage of the average value. These values for the elastic properties in Tables 1 and 3 indicate both a very good instrumental precision and good material consistency after a few mechanical cycles, i.e., the results indicate that the fiber-matrix bond had not degraded and that very few, if any, of the fibers had broken. The spread in values from the separate tests itemized in Tables 2 and 4 are reasonably consistent with that expected during tensile testing of other structural materials.

2.5 Conclusions

This series of tests has shown that tensile tests can be performed on composites at cryogenic temperatures with a high rate of success. The simple, straight-edged specimen without tabs in the grip system is acceptable. The mechanical and electronic instrumentation have been debugged and have proven to have sufficient reliability and more than adequate sensitivity. The data of Phase I will aid in planning the Phase II tests and have pointed to the interesting phenomenon of two elastic regions in graphite-epoxy.

3.0 Phase II: Characterization of the Mechanical Properties of Uniaxial Composites at Cryogenic Temperatures

3.1 Introduction

The five composites selected for the main body of this work are being fabricated by two commercial companies so that they will be representative of the best production techniques. Table 5 itemizes the final test materials for this program. This list is essentially that reported in the last report,[2] modified at the request of the producing company for their convenience in supplying the materials. The test matrix presented in the last report remains essentially the same, altered only by a reduction from five to three in the number of specimens to be run for each combination of composite type, test type, and temperatures. The latter is necessitated by delay in delivery of some composite materials due to fabricating problems. If time permits, additional tests will be performed at 4 K.

The fabricator of the three composites using the NASA Resin 2 matrix found extremely low interlaminate integrity in the first set of composites produced, eventually tracing the problem to incorrect preparation of the resin. This necessitated a complete remanufacture of the three sets of composite samples and inadvertently delayed the program. However, no problems were encountered with the boron-aluminum, which has been delivered and has now been extensively tensile tested. The boron-epoxy material has also arrived and work has begun on this material. The fabricator indicates all material will be delivered by the end of April.

The Phase II mechanical characterization data reported here are restricted to the boron-aluminum composite.

3.2 Material

Boron-aluminum is a high strength, high modulus composite. However, unlike polymer-matrix composites, boron-aluminum has high thermal and electrical conductivities. Consequently, application of this composite in superconducting machinery will be very specialized; possibly this composite may be used for the eddy current shield.

The boron-aluminum material was supplied in an F temper (as fabricated). Nominal thickness of the three orientations selected for tensile testing are noted below. The nominal fiber volume fraction is 50%. The manufacturer will measure the volume fraction and provide fabrication details later. Radiography did not reveal any voids.

Orientation	Plies	Nominal Thickness (cm)	Nominal Thickness (in)
Longitudinal (0°)	6	0.109	0.043
Transverse (90°)	15	0.246	0.097
Crossply (± 45°)	10	0.178	0.070

3.3 Procedures

As in the Phase I work, all test specimens were straight-sided coupons; however, the overall length of the boron-aluminum was reduced to 15.2 cm (6 in.) with the gage length reduced to 5.0 cm (2 in.) for all configurations. These reductions are acceptable in view of the higher strength and ductility of the aluminum matrix as compared to epoxy. Specimen width was 1.3 cm (0.5 in.) for the longitudinal (0°) tests and 2.5 cm (1 in.) for the

transverse (90°) and crossply (± 45°) tests. The edge preparation and gage mounting were as previously described. The aluminum matrix required no humidity or temperature conditioning before testing. A constant strain rate of 0.01 min^{-1} was used for all boron-aluminum tests.

3.4 Results

The results of the individual tests and the group averages are presented in Tables 6 and 7. The Poisson's ratios and intralaminar (in-plane) shear moduli, calculated from the test results, are presented in Table 8. Figures 2-4 are representative tensile stress-strain diagrams of the three orientations of boron-aluminum tested in this program. There was insufficient yielding in the longitudinal (0°) specimens to permit determination of a meaningful proportional limit.

A particularly intriguing phenomenon is the repeated appearance of serrations as evidence of discontinuous yielding during testing of the transverse (90°) and crossply (± 45°) specimens at room temperature and at 4 K, and the complete absence of serrations at 76 K. An additional peculiarity of this phenomenon is that the serrations are caused by sudden elongation without appreciable load drop, in direct contrast to the serrated yielding phenomenon in metals and alloys where the primary characteristic is the load drop. The serrated yielding phenomenon will be investigated further.

The variations in elastic properties with temperature are illustrated in Figures 5-7. Statistically there appear to be no differences between the 295 K and 4 K values. However, at 76 K there does appear to be a rather consistent minimum in all of the elastic parameters. The ν_{21} and G values have been calculated from tensile data obtained from the crossply (± 45°) specimens using the method of Petit[5] (see Appendix 2).

The temperature dependences of the proportional limit, 0.2% offset yield strength, ultimate tensile strength, and fracture strain for the boron-aluminum are presented in Figures 8-11, respectively. The large scatter in the proportional limit data reflects the difficulty in determining the point at which the stress-strain curves first deviate from linearity. The 0.2% offset yield strength is much better defined.

In general, the ultimate and yield strength increase with a decrease in temperature. The ultimate elongation of the crossply (± 45°) shows a significant decrease as temperature is lowered; however, the longitudinal (0°) and transverse (90°) orientations displayed a small increase in fracture strain on cooling.

3.5 Discussion

Reflecting the ductility of aluminum, this composite developed a distinct yield point, followed by plastic deformation in all but the longitudinal (0°) orientation. Because of this, each test consisted of only one loading, to fracture. The crossply specimens displayed considerable necking at all temperatures. Since the strain gages failed at about 1% strain, to continue observing the stress-strain behavior and to determine elongation at fracture, the load-cell output fed a constant-speed strip-chart recorder and a two-pen strain-gage recorder in parallel. Knowledge of chart speed, crosshead speed, and gage length allowed estimation of strain over the entire stress range. The ultimate elongation was also checked by displacement of lightly scribed gage marks on the specimen surface.

The gripping method described earlier worked well for all specimens, but a slight modification was required for the longitudinal (0°) tests at room temperature. Here, the specimen began to slip from the grips just before reaching the ultimate load. This problem was solved by removing the stainless steel screen so the specimen was in direct contact with the serrated titanium grip plates. Table 7 shows that the tensile coupon broke immediately adjacent to the specimen grip in three of the four longitudinal (0°) room temperature tests and in one 76 K test; however, values obtained from the latter were equal or in excess of values obtained with "acceptable" fractures away from the grips. Conversely, the one transverse (90°) fracture immediately at the grip did appear to result in a low tensile value. No failures at the grips were observed at 4 K.

3.6 Future Work

All of the material required for the mechanical property testing of boron-epoxy composite has been received, the test coupons have been cut, and the strain gages mounted. Testing of this material has begun. Shipment of the remainder of the boron-epoxy required for thermal characterization and the three NASA Resin 2 matrix composites has been promised by the end of April.

A fixture for compression tests is now completed, but has not yet been tested. Some additional work will be required to determine the best specimen configuration and the best gripping method.

4.0 Appendix I: Symbols

E_{11}	=	longitudinal (0°) elastic modulus
E_{22}	=	transverse (90°) elastic modulus
E_x	=	crossply ($\pm$ 45°) elastic modulus
ν_{12}	=	longitudinal (0°) Poisson's ratio
ν_{21}	=	transverse (90°) Poisson's ratio
ν_x	=	crossply ($\pm$ 45°) Poisson's ratio
G	=	intralaminar shear modulus
σ^{pl}	=	proportional limit; stress at which a stress-strain curve deviates from elasticity, i.e., is no longer a straight line
σ^{ty}	=	0.2% tensile yield strength; stress at the intersection of the stress-strain curve with a straight line having the same slope as the elastic modulus and offset by 0.2% along the strain scale
σ^{tu}	=	ultimate strength; highest stress attained on the stress-strain curve
ε^{tu}	=	ultimate elongation; highest strain attained on the stress-strain curve

Superscript 1 and 2 on E and ν indicate the primary and secondary values calculated from the first and second parts of the stress-strain curve for those materials that exhibit a two-part elastic zone.

5.0 Appendix II: Parameters Calculated from Test Results

By combining the parameters measured for the three configurations (0°, 90° $\pm$ 45°), it is possible to calculate the transverse Poisson's ratio and the intralaminar (in-plane) shear modulus.[5]

$$\nu_{21} = \nu_{12} \frac{E_{22}}{E_{11}}$$

and

$$G = \frac{2UE_x}{8U - E_x}$$

where

$$U = \frac{E_{11} + E_{22} + 2\nu_{21}E_{11}}{8(1-\nu_{12}\nu_{21})} \quad .$$

6.0 References

1) Kasen, M. B., "Advanced Composites," Semi-Annual Technical Reports on Materials Research in Support of Superconducting Machinery, (1 Sept., 1973 to 1 March, 1974) National Bureau of Standards - Advanced Research Projects Agency.

2) Kasen, M. B. and Schramm, R. E., "Advanced Composites," Semi-Annual Technical Reports on Materials Research in Support of Superconducting Machinery - II, (1 March, 1974 to 1 Sept., 1974) National Bureau of Standards - Advanced Research Projects Agency.

3) Broutman, L. J. and Krock, R. H., Modern Composite Materials, Addison-Wesley, Reading, Mass., 1967, p. 375.

4) Advanced Composites Design Guide, 3rd Edition, Vol IV, Materials, Air Force Materials Laboratory, Wright-Patterson Air Force Base, Ohio, January, 1973.

5) Petit, P. H., "A Simplified Method of Determining the In-plane Shear Stress-Strain Response of Unidirectional Composites," ASTM STP 460, Composite Materials: Testing and Design, American Society for Testing and Materials, 1969, pp. 83-93.

7.0 List of Figures

1. Typical stress-strain curves for boron-epoxy and graphite-epoxy composites. Note deviations from linearity in the graphite-epoxy.

2. Typical stress-strain curves for longitudinal (0°) boron-aluminum at various temperatures.

3. Typical stress-strain curves for transverse (90°) boron-aluminum at various temperatures.

4. Typical stress-strain curves for crossply (± 45°) boron-aluminum at various temperatures.

5. Elastic moduli of boron-aluminum. Error bars reflect ± one standard deviation.

6. Poisson's ratio of boron-aluminum. Error bars reflect ± one standard deviation.

7. Intralaminar (in-plane) shear modulus of boron-aluminum calculated from the crossply (± 45°) stress-strain curve. Error bars reflect ± one standard deviation.

8. Proportional limit of boron-aluminum. Error bars reflect ± one standard deviation.

9. Yield strength (0.2% offset) of boron-aluminum. Error bars reflect ± one standard deviation.

10. Ultimate tensile strength of boron-aluminum. Error bars reflect ± one standard deviation.

11. Ultimate elongation of boron-aluminum. Error bars reflect ± one standard deviation.

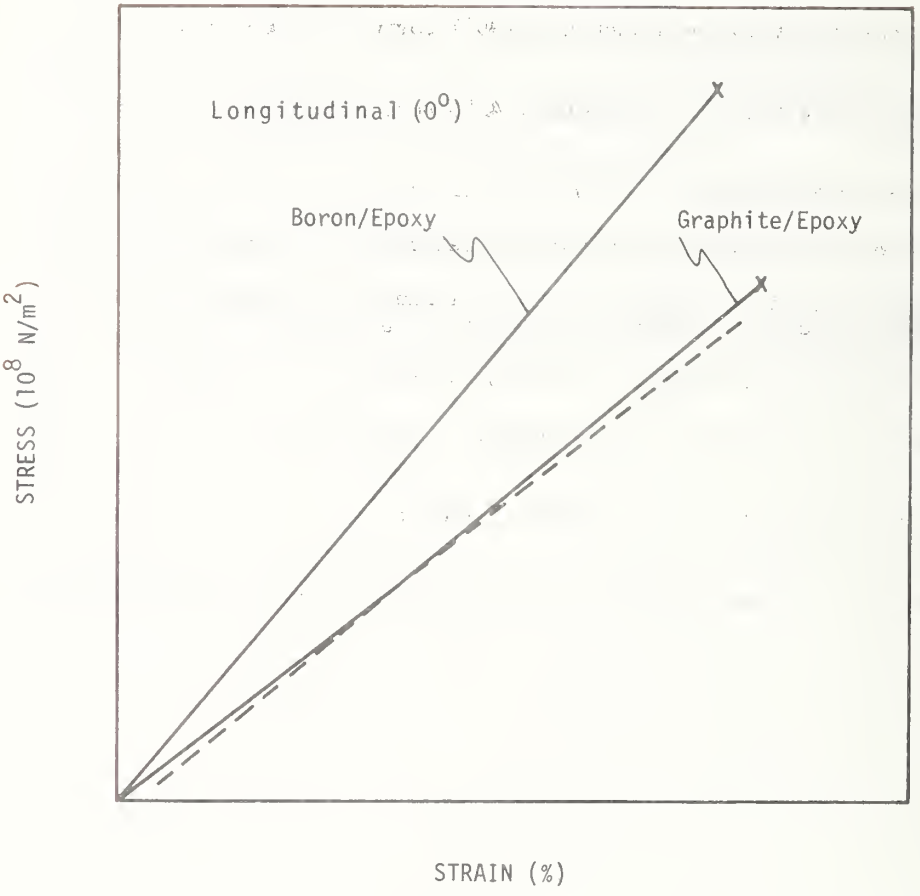

Figure 1. Typical stress-strain curves for boron-epoxy and graphite-epoxy composites. Note deviations from linearity in the graphite-epoxy.

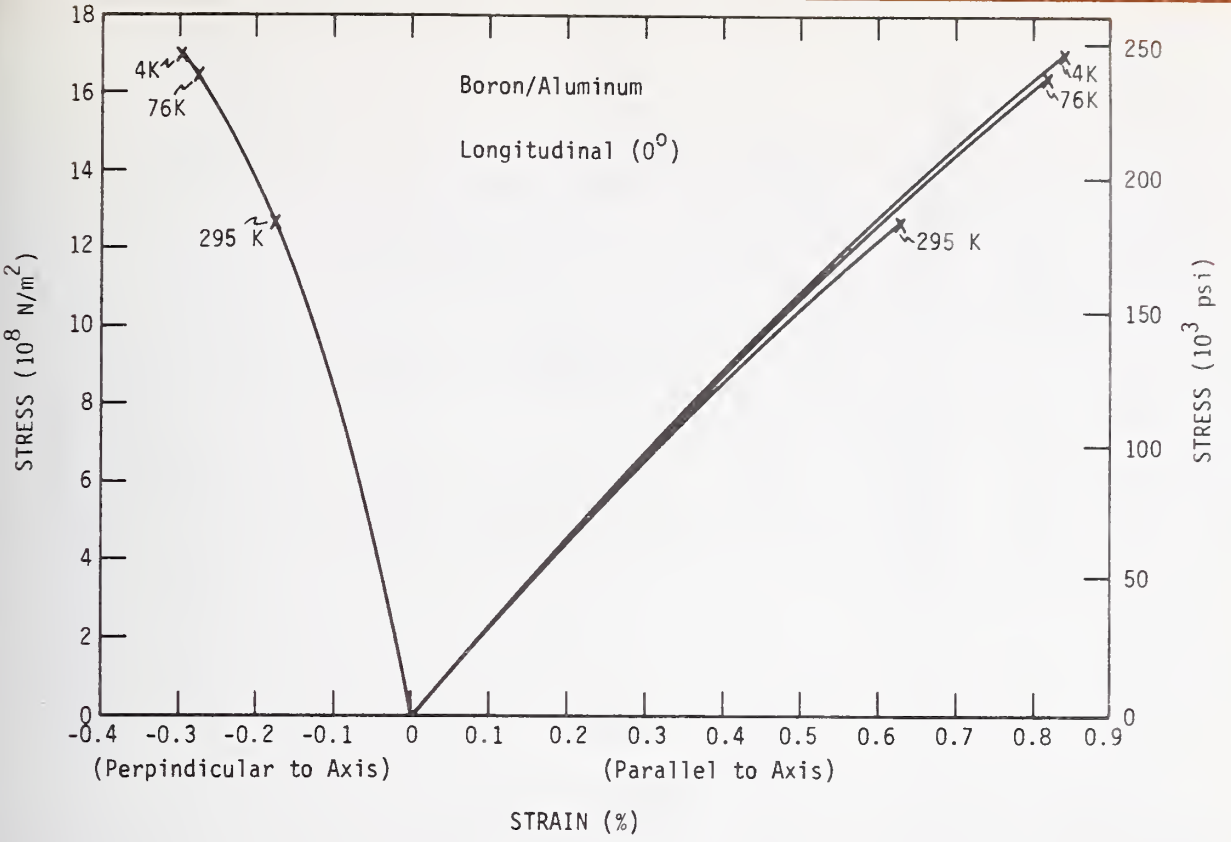

Figure 2. Typical stress-strain curves for longitudinal (0°) boron-aluminum at various temperatures.

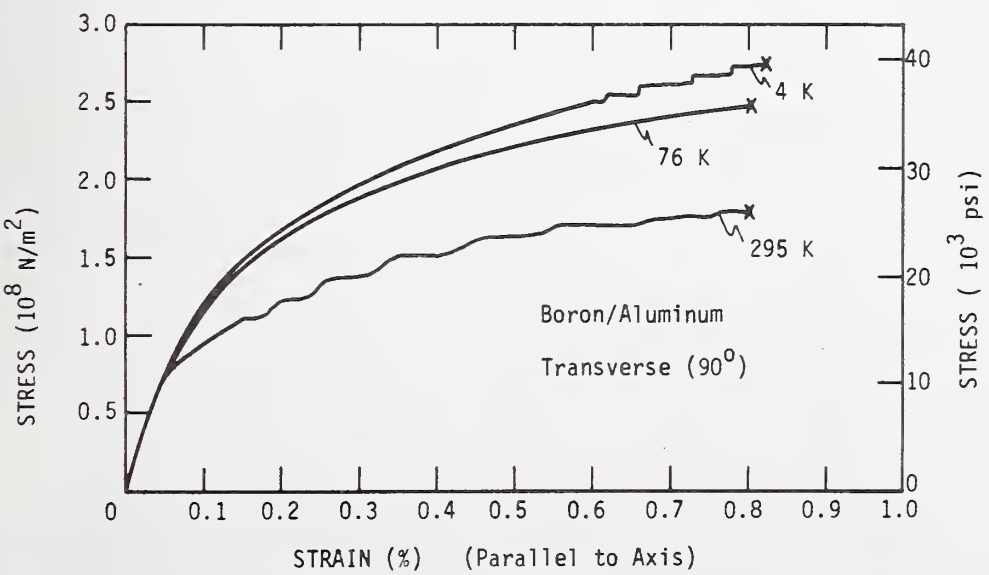

Figure 3. Typical stress-strain curves for transverse (90°) boron-aluminum at various temperatures.

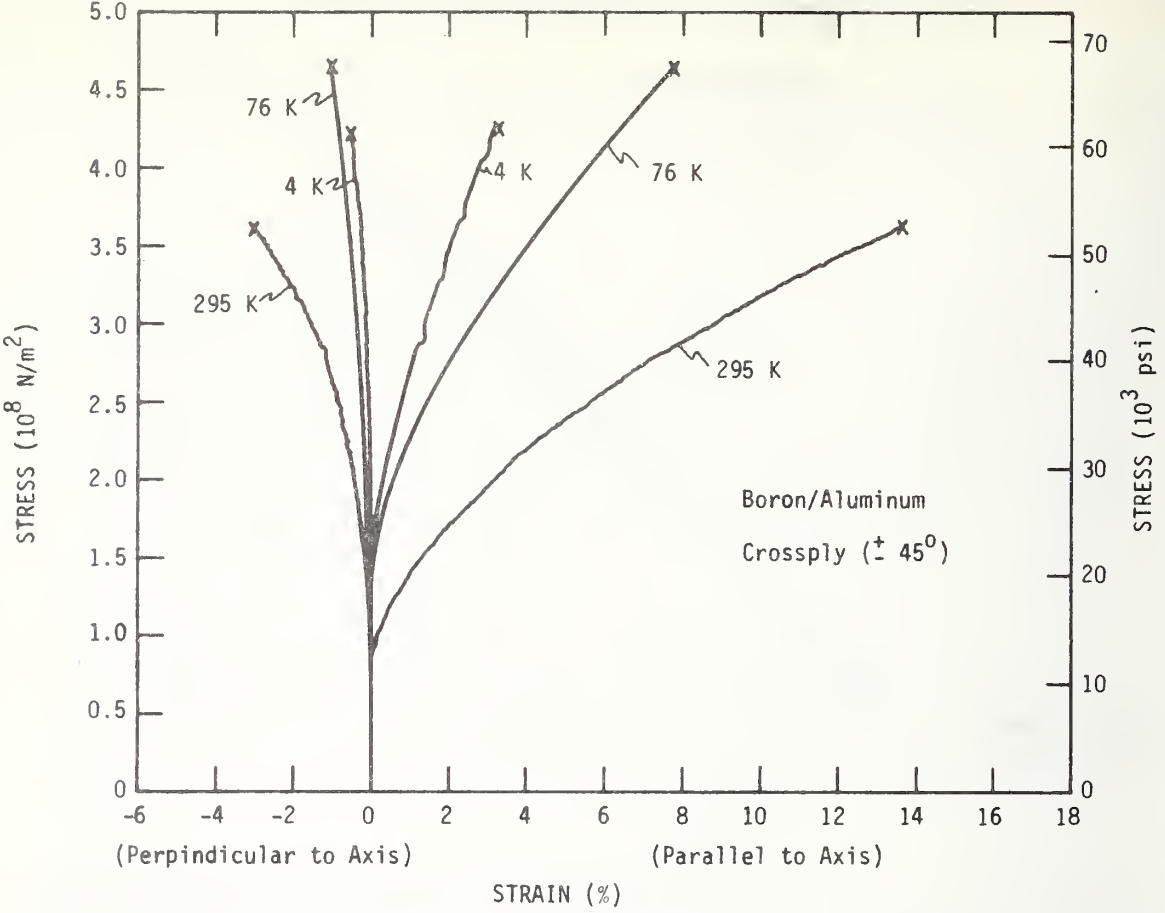

Figure 4. Typical stress-strain curves for crossply (± 45°) boron-aluminum at various temperatures.

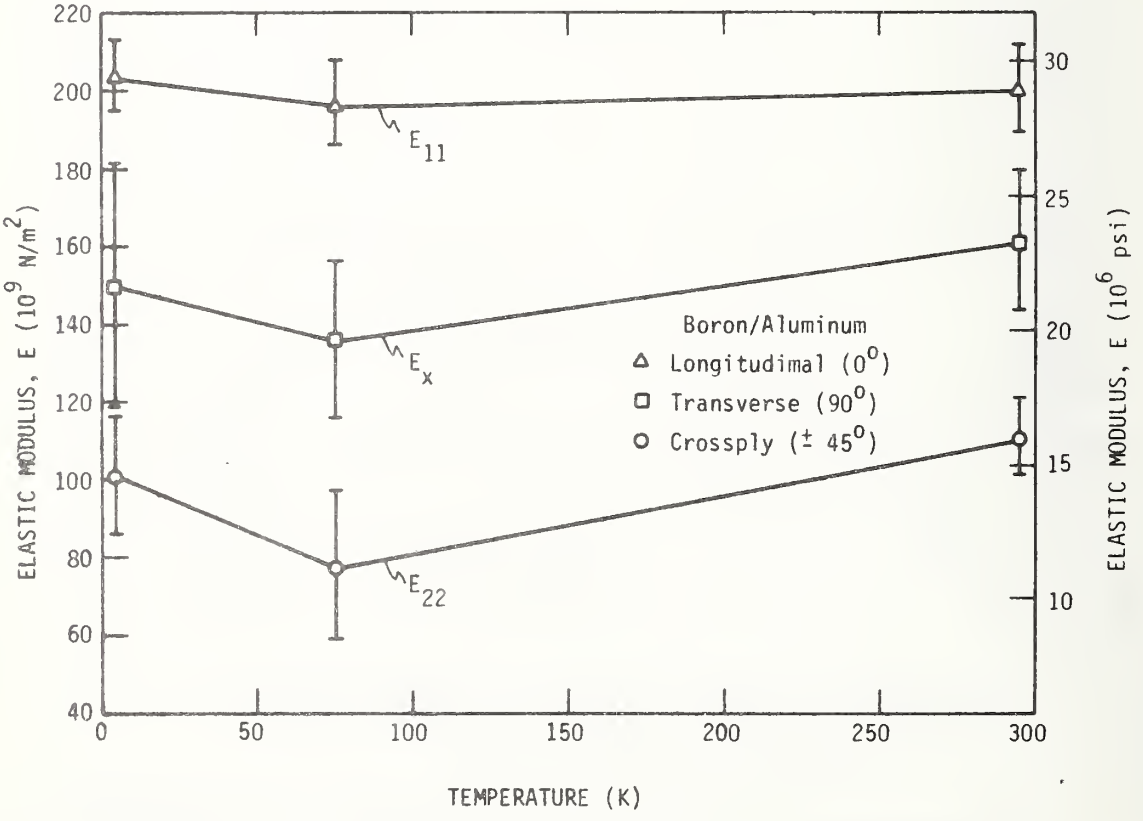

Figure 5. Elastic moduli of boron-aluminum. Error bars reflect ± one standard deviation.

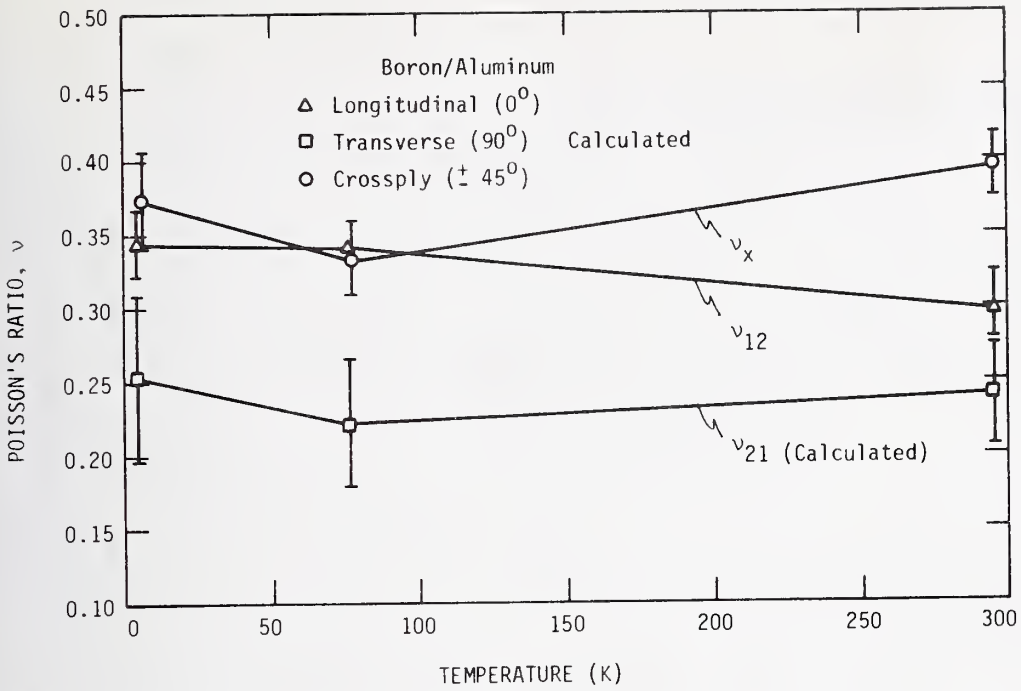

Figure 6. Poisson's ratio of boron-aluminum. Error bars reflect ± one standard deviation.

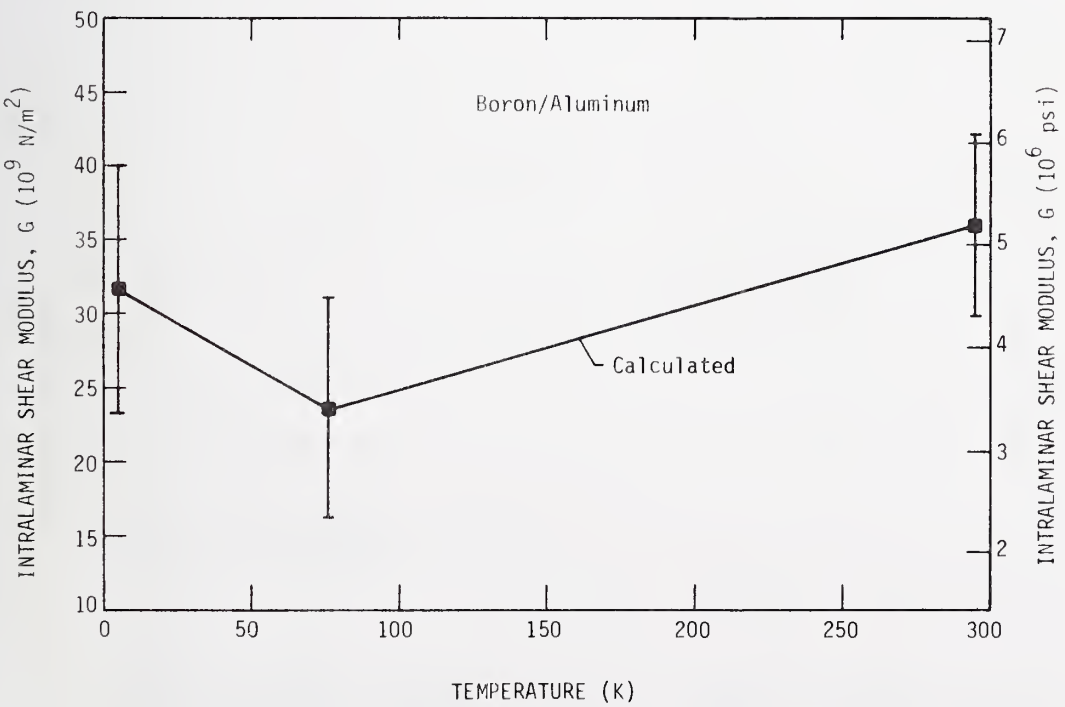

Figure 7. Intralaminar (in-plane) shear modulus of boron-aluminum calculated from the crossply (± 45°) stress-strain curve. Error bars reflect ± one standard deviation.

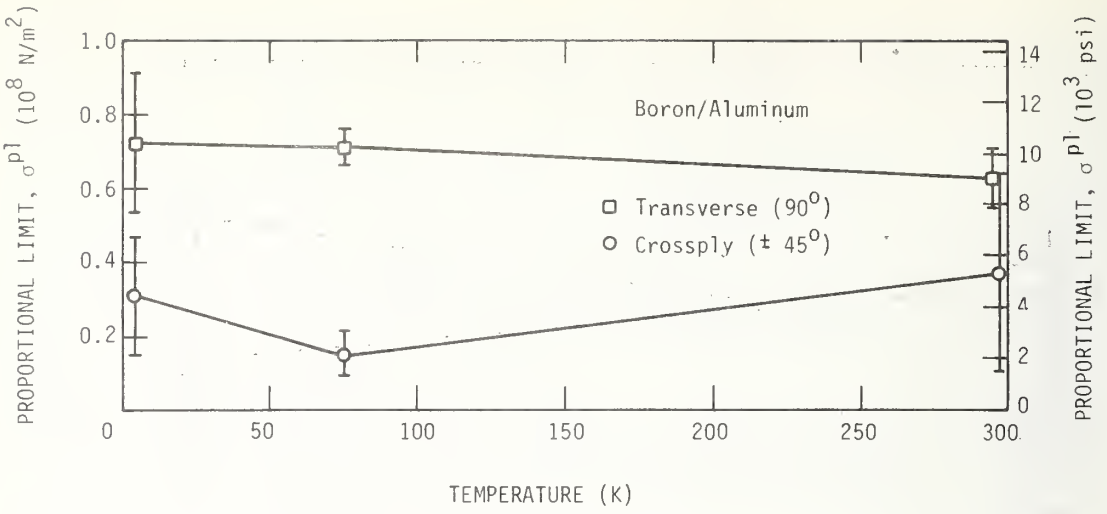

Figure 8. Proportional limit of boron-aluminum. Error bars reflect ± one standard deviation.

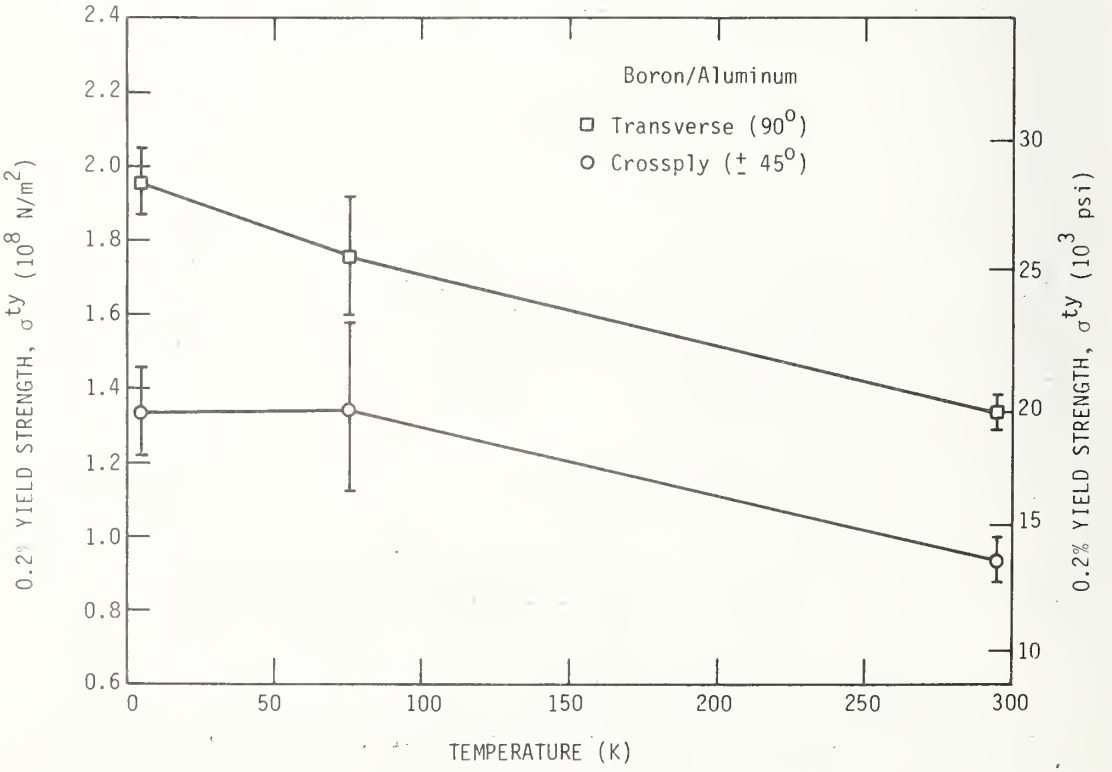

Figure 9. Yield strength (0.2% offset) of boron-aluminum. Error bars reflect ± one standard deviation.

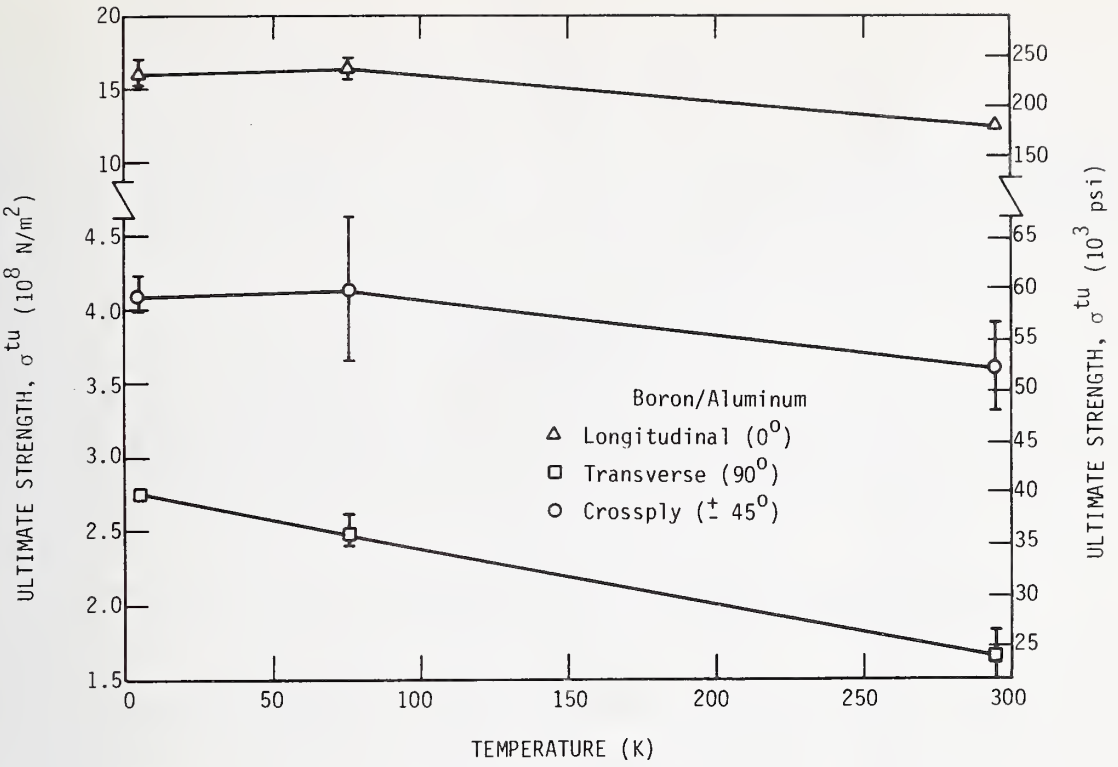

Figure 10. Ultimate tensile strength of boron-aluminum. Error bars reflect ± one standard deviation.

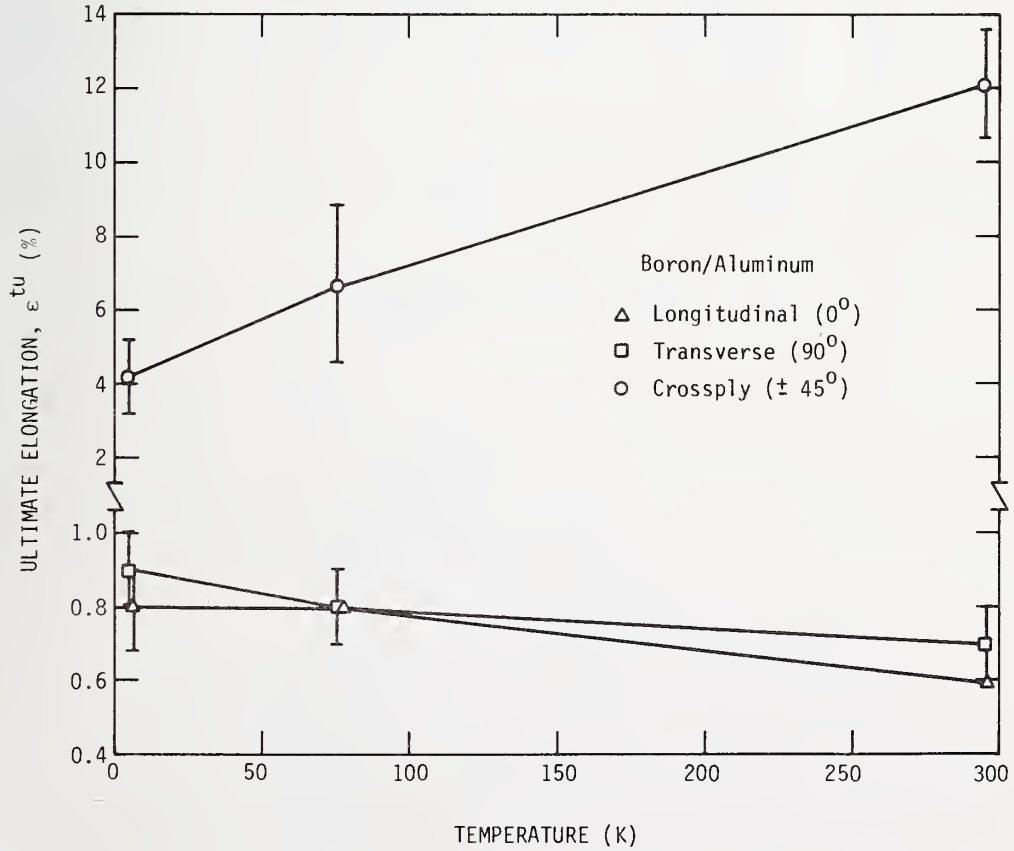

Figure 11. Ultimate elongation of boron-aluminum. Error bars reflect ± one standard deviation.

8.0 List of Tables

1. Tensile properties of boron-epoxy composites (individual specimens).
2. Tensile properties of boron-epoxy composites (averages of all tested specimens).
3. Tensile properties of graphite-epoxy composite, Supplier A (individual specimens).
4. Tensile properties of graphite-epoxy composite, Supplier A (average of all tested specimens).
5. Selected composite test materials.
6. Tensile properties of boron-aluminum composites (individual specimens).
7. Tensile properties of boron-aluminum composites (averages of specimens tested).
8. Poisson's ratios and intralaminar shear moduli calculated from tensile property data.

Table 1

Tensile Properties of Boron-Epoxy Composites

(Individual Specimens[a])

Temp (K)	Elastic Modulus, E (10^9 N/m^2)	(10^6 psi)	CV(%)	Poisson's Ratio, ν	CV(%)	Ultimate Strength, σ^{tu} (10^8 N/m^2)	(10^3 psi)	Ultimate Elongation ϵ^{tu} (%)
				Longitudinal (0°) Supplier A (5.6 mil fibers)				
295	238(0.5)	34.5(0.06)	0.2	0.236 (0.001)	0.5	[b]		
76	249(0.4)[c]	36.2(0.07)	0.2	0.256 (0.010)	4.1	[b]		
76	229(0.6)	33.2(0.10)	0.3	0.249 (0.002)	0.7	17.7	256	0.78
76	228(0.6)	33.1(0.09)	0.3	0.250 (0.001)	0.4	18.0	261	0.79
76	237(0.0)	34.2(0.00)	0.0	0.261 (0.006)	2.2	16.9[d]	245	0.73
4	252(0.6)[e]	36.6(0.10)	0.3	[f]		18.8	273	0.74
4	243(0.6)	35.2(0.10)	0.3	0.248 (0.002)	0.6	17.8	258	0.74
4	237(0.7)	34.3(0.10)	0.3	0.255 (0.004)	1.6	17.9	259	0.76
				Longitudinal (0°) Supplier B (4.0 mil fibers)				
76	222(0.6)	32.2(0.08)	0.2	0.243 (0.001)	0.2	17.6	255	0.81
76	219(0.5)	31.7(0.08)	0.3	0.254 (0.001)	0.4	16.4	237	0.75
76	220(0.6)	31.9(0.08)	0.3	0.239 (0.002)	0.7	15.6	227	0.84
4	226(0.7)	32.8(0.09)	0.3	0.231 (0.001)	0.5	18.7	270	0.83
4	224(1.8)	32.5(0.25)	0.8	0.230 (0.008)	3.5	17.4	253	0.78
4	216(0.8)	31.4(0.11)	0.4	0.238 (0.001)	0.5	17.2	250	0.80
				Transverse (90°) Supplier A (5.6 mil fibers)				
76	39(1.0)	5.6(0.10)	1.7			0.82[d]	12.0	0.19
76	41(1.0)	5.9(0.08)	1.4			0.72	10.4	0.15
76	39(1.2)	5.6(0.17)	3.0			0.78	11.2	0.19
4	46	6.7				0.52[d, g]	7.5	0.12
4	43	6.2				0.43	6.2	0.14
4	46(0.3)	6.7(0.05)	0.7			0.65	9.5	0.14

[a] Standard deviations (in parentheses) and coefficients of variation (CV) given for data from three or more loading-unloading cycles

[b] Specimen not fractured

[c] Previously cycled at 295 K

[d] Fractured in grip

[e] Previously cycled at 295 K, then at 76 K

[f] Transverse strain gage malfunctioned

[g] Fractured during first loading

Table 2

Tensile Properties of Boron-Epoxy Composites

(Averages of All Tested Specimens[a])

Temperature (K)	Elastic Modulus, E (10^9 N/m^2)	(10^6 psi)	CV(%)	Poisson's Ratio, ν	CV(%)	Ultimate Strength, σ^{tu} (10^8 N/m^2)	(10^3 psi)	CV(%)	Ultimate Elongation, ε^{tu} (%)	CV(%)
				Longitudinal (0°) Supplier A		(5.6 mil fibers)				
295	238	34.5		0.236						
76	236 (10)	34.2 (1.4)	4.2	0.254 (0.006)	2.2	17.5 (0.6)	254 (8)	3.2	0.77 (0.03)	4.2
4	244 (8)	35.4 (1.2)	3.2	0.252 (0.005)	2.0	18.2 (0.6)	263 (8)	3.1	0.75 (0.01)	1.5
				Longitudinal (0°) Supplier B		(4.0 mil fibers)				
76	220 (2)	31.9 (0.3)	0.7	0.245 (0.008)	3.2	16.5 (1.0)	240 (14)	6.0	0.80 (0.05)	5.7
4	222 (5)	32.2 (0.7)	2.3	0.233 (0.004)	1.9	17.8 (0.8)	258 (11)	4.4	0.80 (0.03)	3.1
				Transverse (90°) Supplier A		(5.6 mil fibers)				
76	40 (1)	5.7 (0.2)	3.0			0.77 (0.05)	11.2 (0.8)	6.8	0.18 (0.02)	12.8
4	45 (2)	6.5 (0.3)	4.1			0.53 (0.11)	7.7 (1.6)	21.2	0.13 (0.01)	8.9

[a] Standard deviations (in parentheses) and coefficients of variation (CV) for three specimens

Table 3

Tensile Properties of a Graphite-Epoxy Composite, Supplier A

(Individual Specimens[a])

Temperature (K)	Primary Elastic Modulus, E_1 (10^9 N/m^2)	(10^6 psi)	CV(%)	Secondary Elastic Modulus, E_2 (10^9 N/m^2)	(10^6 psi)	CV(%)	Primary Poisson's Ratio, ν_1	CV(%)	Secondary Poisson's Ratio, ν_2	CV(%)	Ultimate Strength, σ_{tu} (10^8 N/m^2)	(10^3 psi)	Ultimate Elongation, ϵ_{tu} (%)
							Longitudinal (0°)						
295	135 (0.0)	19.6 (0.00)	0.0	148 (1.3)	21.4 (0.18)	0.8	0.294 (0.008)	2.8	0.297 (0.006)	1.9	[b]		
76	136 (1.0)[c]	19.7 (0.15)	0.8	150 (1.3)	21.7 (0.18)	0.9	0.317 (0.002)	0.7	0.321 (0.003)	0.9	[b]		
76	135 (1.9)	19.6 (0.27)	1.4	146 (1.2)	21.2 (0.18)	0.9	0.297 (0.005)	1.5	0.310 (0.002)	0.7	12.7	184	0.87
76	159 (2.8)	23.1 (0.40)	1.7	154 (0.0)	22.3 (0.0)	0.0	0.386 (0.016)	4.1	0.324 (0.000)	0.0	12.9	188	0.82
76	138 (0.8)	20.0 (0.12)	0.6	147 (0.6)	21.3 (0.1)	0.4	0.351 (0.007)	2.0	0.334 (0.002)	0.5	13.8	200	0.93
4	133 (1.0)[d]	19.2 (0.16)	0.8	145 (1.3)	20.9 (0.18)	0.9	0.310 (0.002)	0.7	0.308 (0.002)	0.8	13.1	191	0.86
4	143 (1.2)	20.6 (0.17)	0.8	157 (1.4)	22.7 (0.20)	0.9	0.311 (0.002)	0.7	0.342 (0.003)	1.0	13.5	195	0.90
4	143 (1.4)	20.7 (0.20)	0.9	160 (2.9)	23.2 (0.42)	1.8	0.307 (0.002)	0.7	0.329 (0.004)	1.2	12.5	182	0.79
							Transverse (90°)						
76	13 (0.2)	1.8 (0.2)	1.8								0.44	6.4	0.36
76	14 (0.2)	2.0 (0.0)	1.7								0.44	6.4	0.30
76	13 (0.1)	1.9 (0.0)	0.7								0.40	5.7	0.31
4	14 (0.0)	2.0 (0.0)	0.3								0.52[e]	7.6	0.39
4	10 (0.4)	1.5 (0.1)	3.7								0.20[e]	2.9	0.18
4	12 (0.1)	1.8 (0.0)	0.5								0.45	6.5	0.35

[a] Standard deviations (in parentheses) and coefficients of variation (CV) given for data from three or more loading-unloading cycles

[b] Specimen not fractured

[c] Previously cycled at 295 K

[d] Previously cycled at 295 K, then at 76 K

[e] This specimen fractured on the third loading cycle under a lower load than it had sustained in the two previous cycles. These fracture data are not included in the averages calculated.

Table 4

Tensile Properties of Graphite-Epoxy Composite Supplier A

(Average of All Tested Specimens[a])

Temperature (K)	Primary Elastic Modulus, E^1 (10^9 N/m^2)	(10^6 psi)	CV(%)	Secondary Elastic Modulus, E^2 (10^9 N/m^2)	(10^6 psi)	CV(%)	Primary Poisson's Ratio, ν^1	CV(%)	Secondary Poisson's Ratio, ν^2	CV(%)	Ultimate Strength σ^{tu} (10^8 N/m^2)	(10^3 psi)	CV(%)	Ultimate Elongation, ϵ^{tu}	CV(%)
							Longitudinal (0°)								
295	135	19.6		148	21.4		0.294		0.297						
76	142 (11)	20.6 (1.7)	8.1	149(4)	21.6(0.5)	2.4	0.338(0.039)	11.5	0.322(0.010)	3.1	13.1(0.6)	191(8)	4.4	0.87 (0.06)	6.3
4	140 (6)	20.2 (0.8)	4.1	154(8)	22.3(1.2)	5.3	0.309(0.002)	0.7	0.326(0.017)	5.3	13.0(0.5)	189(7)	3.7	0.85 (0.06)	6.6
							Transverse (90°)								
76	13 (0.6)	1.9 (0.1)	4.9								0.43(0.02)	6.2(0.4)	5.9	0.32 (0.03)	10.0
4	12 (2.0)	1.8 (0.3)	15.3								0.49(0.05)[b]	7.1(0.8)[b]	10.5	0.37 (0.03)[b]	7.6

[a] Standard deviations (in parentheses) and coefficients of variation (CV) for three specimens except as noted.

[b] These ultimate strength and elongation averages are for two specimens only; they do not include the value from a premature fracture.

TABLE 5

SELECTED COMPOSITE TEST MATERIALS

Composite Type	Number of Panels	Size (in.)	Thickness	Filament Orientation	Use
	1	11 x 11	6 ply	Uniaxial	(1)
S-901 glass/Resin 2	2	11 x 11	15 ply	Uniaxial	(2)
Kevlar 49/Resin 2	2	11 x 11	10 ply	±45°	(3)
Type A Graphite/Resin 2	1	4 x 4	0.150 in.	Uniaxial	(4)
5.6 mil Boron/Epoxy	1	1 x 1 x 2	----	Uniaxial to 2"	(5)
	1	1 x 1 x 2	----	Transverse to 2"	(6)
	1	22 x 6	6 ply	Uniaxial to 6"	(1)
	1	22 x 6	15 ply	Uniaxial to 6"	(2)
5.6 mil Boron/6061	1	22 x 6	10 ply	±45°	(3)
Aluminum	1	4 x 4	0.150 in.	Uniaxial	(4)
	2	4 x 4	0.5	Uniaxial to 4"	(5)

Use:

(1) Uniaxial longitudinal tensile
(2) Uniaxial transverse tensile and transverse compression
(3) In-plane (intralaminar) shear
(4) Longitudinal compression, longitudinal and transverse dynamic modulus (resonance method)
(5) Longitudinal thermal conductivity and longitudinal dynamic modulus (pulse-echo method)
(6) Transverse thermal conductivity and transverse dynamic modulus (pulse-echo method)

Table 6

Tensile Properties of Boron-Aluminum Composites

(Individual Specimens)

Temperature (K)	Elastic Modulus, E (10^9 N/m^2)	Elastic Modulus, E (10^6 psi)	Poisson's Ratio, ν	Proportional Limit, σ^{pl} (10^8 N/m^2)	Proportional Limit, σ^{pl} (10^3 psi)	0.2% Yield Strength, σ^{ty} (10^8 N/m^2)	0.2% Yield Strength, σ^{ty} (10^3 psi)	Ultimate Strength, σ^{tu} (10^8 N/m^2)	Ultimate Strength, σ^{tu} (10^3 psi)	Ultimate Elongation, ε^{tu} (%)
				Longitudinal (0°)						
295[a]	195	28.3	0.320					12.4	180	0.6
295	194	28.1	0.280					12.7	184	0.6
295[a]	194	28.2	0.275					13.2	191	0.6
295[a]	217	31.4	0.320					12.5	175	0.6
76	186	27.0	0.345					16.9	245	0.8
76	196	28.4	0.344					15.8	230	0.7
76	208	30.1	0.335					16.5	239	0.8
76[a]	196	28.4	0.351					16.0	233	0.8
4	211	30.6	0.313					14.9	217	0.7
4	207	30.0	0.358					16.9	245	0.8
4	191	27.7	0.343					16.0	231	0.8
4	206	29.9	0.360					16.4	238	0.8
				Transverse (90°)						
295	165	24.0		0.67	9.7	1.38	20.1	1.74	25.3	0.8
295	177	25.7		0.54	7.8	-	-	1.80	26.1	-
295	142	20.6		0.67	9.7	1.29	18.7	1.46	21.1	0.6
76[a]	101	14.6		0.92	13.3	1.86	27.0	2.29	33.2	0.8
76	155	22.5		0.75	10.9	1.67	24.3	2.57	37.3	0.8
76	138	20.1		0.65	9.4	1.94	28.2	2.47	35.9	0.8
76	116	16.8		0.72	10.5	1.66	24.1	2.42	35.1	0.9
4	180	26.2		0.50	7.3	1.97	28.6	2.79	40.5	0.9
4	152	22.1		0.80	11.6	2.05	29.7	2.73	39.6	0.8
4	118	17.1		0.86	12.5	1.87	27.1	2.76	40.0	0.9
				Crossply (±45°)						
295	112	16.2	-	0.27	3.9	0.90	13.0	3.62	52.4	13.6
295	100	14.5	0.417	0.68	9.9	1.01	14.6	3.92	56.9	-
295	120	17.3	0.375	0.17	2.4	0.92	13.3	3.32	48.2	10.6
76	61.8	9.0	0.313	0.08	1.2	1.52	22.0	4.11	59.6	4.6
76	71.8	10.5	0.361	0.20	2.8	1.44	20.9	4.64	67.2	8.8
75	99.0	14.4	0.325	0.16	2.3	1.09	15.8	3.66	53.1	-
4	109	15.9	0.405	0.48	6.9	1.40	20.3	4.25	61.7	3.2
4	111	16.0	0.378	0.26	3.7	1.20	17.4	4.06	58.9	4.1
4	84	12.1	0.337	0.18	2.7	1.41	20.5	4.02	58.4	5.2

[a]Fractured at or in grip

Tensile Properties of Boron-Aluminum Composites

(Averages of Specimens Tested[a])

Temperature	Elastic Modulus, E			Poisson's Ratio, ν		Proportional Limit, σ^{pl}			0.2% Yield Strength, σ^{ty}			Ultimate Strength, σ^{tu}			Ultimate Elongation, ϵ^{tu}	
(K)	(10^9 N/m^2)	(10^6 psi)	CV(%)		CV(%)	(10^8 N/m^2)	(10^3 psi)	CV(%)	(10^8 N/m^2)	(10^3 psi)	CV(%)	(10^8 N/m^2)	(10^3 psi)	CV(%)	(%)	CV(%)
							Longitudinal (0°)									
295	200(11)	29.0(1.6)	5.7	0.299(0.024)	8.2											
76	197(11)	28.5(1.6)	5.6	0.341(0.005)	1.6							12.7	184	-	0.6	-
4	204(9)	29.6(1.3)	4.3	0.344(0.022)	6.3							16.4(0.6)	238(8)	3.4	0.8(0.0)	3.1
												16.1(0.9)	233(12)	5.3	0.8(0.1)	7.7
							Transverse(90°)									
295	161(18)	23.4(2.6)	11.0			0.63(0.08)	9.1(1.1)	11.9	1.34(0.05)	19.4(0.7)	3.6	1.67(0.18)	24.2(2.7)	10.9	0.7(0.1)	14.3
76	128(24)	18.5(3.5)	18.7			0.76(0.11)	11.0(1.6)	15.1	1.78(0.14)	25.9(2.0)	7.8	2.49(0.08)	36.1(1.1)	3.1	0.8(0.1)	7.2
4	150(31)	21.8(4.6)	20.8			0.72(0.19)	10.5(2.8)	26.8	1.96(0.09)	28.5(1.3)	4.6	2.76(0.03)	40.0(0.5)	1.1	0.9(0.1)	6.4
							Crossply (± 45°)									
295	111(10)	16.0(1.4)	9.0	0.396(0.021)	5.3	0.37(0.27)	5.4(4.0)	73.0	0.94(0.06)	13.6(0.9)	6.2	3.62(0.30)	52.5(4.4)	8.3	12.1(1.5)	12.4
76	78(19)	11.3(2.8)	24.8	0.333(0.025)	7.5	0.15(0.06)	2.1(0.8)	40.7	1.35(0.23)	19.6(3.3)	16.9	4.14(0.49)	60.0(7.1)	11.8	6.7(2.1)	31.3
4	101(15)	14.7(2.2)	14.9	0.373(0.034)	9.2	0.31(0.16)	4.4(2.2)	50.1	1.34(0.12)	19.4(1.7)	8.8	4.11(0.12)	59.7(1.8)	3.0	4.2(1.0)	23.8

[a]Standard deviations are in parentheses. CV is coefficient of variation. Data from the specimens that broke at or in the grips are not included in the calculations of ultimate strength or elongation.

Table 8

Poisson's Ratios and Intralaminar Shear Moduli of Boron-Aluminum Composite Calculated from Tensile Property Data

Temperature	Poisson's Ratio, ν_{21}		Intralaminar Shear Modulus, G		
		CV(%)	$10^9 N/m^2$	10^6 psi	CV(%)
295	0.241	14.9	35.8	5.15	17.4
76	0.222	19.6	23.6	3.43	31.6
4	0.253	22.2	31.6	4.61	26.6

NBSIR

SEMI-ANNUAL REPORT ON MATERIALS RESEARCH IN SUPPORT OF SUPERCONDUCTING MACHINERY

ELASTIC PROPERTIES OF ENGINEERING MATERIALS AT CRYOGENIC TEMPERATURES

H. M. Ledbetter and W. F. Weston

Cryogenics Division
Institute for Basic Standards
National Bureau of Standards
Boulder, Colorado 80302

April 1975

Summary: Elastic Properties

During the current year, the elastic properties of a variety of materials are being studied between room temperature and liquid-helium temperature. Studies on some materials are now complete; others are in progress. Two accompanying manuscripts describe some of the completed studies. The status of all current studies is briefly as follows:

(1) Oxygen-free copper. Experimental work and data analysis are complete. Present results agree well with those of previous studies. This data is essential for analyzing the behavior of copper-base alloys; two alloy systems are discussed below -- copper-nickel and copper-tin -- and the results for oxygen-free copper will be included in the reports on these alloy systems.

(2) Composite materials. Because composite materials are candidates for components in superconducting machinery, a study of the elastic properties of composite materials is needed. Because of the conspicuous lack of elastic data on composite materials, the goal this year was to determine the feasibility of measuring the elastic properties of a composite material using a resonance method. Because of acoustic attenuation and dispersion, pulse-echo methods are unusable. Conventional static tests have the disadvantages of large specimen sizes, high refrigeration costs, and less accurate results. The material selected for this first study was a copper-stabilized niobium-titanium wire embedded in a fiberglass-epoxy matrix. This material has five independent elastic constants. (Polycrystalline aggregates have only two independent elastic constants.) This attempt succeeded, and the results are described in the accompanying manuscript: "Elastic constants of a superconducting-coil composite material." This study represents one of the few determinations of the elastic constants of a composite material by a resonance method. It is the first determination of the complete set of elastic constants of such a material at liquid-helium temperature.

(3) Inconel 718. All work on this material is complete. Results are described in the accompanying manuscript: "Low-temperature elastic properties of a nickel-chromium-iron-molybdenum alloy." This material is similar elastically to Inconel X-750, which was described in a previous report in this series. It is slightly softer elastically than Inconel X-750. At least above liquid-nitrogen temperature, it does not undergo a magnetic transition like those that occur in both Inconel 600 and Inconel X-750.

(4) Copper-nickel alloys. Most of the experimental work on these alloys -- commercial-grade copper-10 nickel and copper-30 nickel -- is complete. Most results were obtained by a resonance method, although some pulse-echo results were also obtained. Surprisingly, both materials are magnetic, due presumably to trace impurities of iron. Basically, both materials are regularly behaved elastically, but they do show some peculiarities.

(5) Titanium-niobium alloys. These alloys were supplied by F. Jelenik at Battelle; they have compositions of 5, 10, 20, 22, and 25 at. pct. niobium. While the experimental results are still preliminary, these alloys show abnormal elastic behavior. The Young's modulus varies strongly with composition in the low-niobium region. The change in elastic constants between room-temperature and liquid-helium temperature is unusually large.

(6) Copper-tin alloys. Experimental studies have not yet begun on this system.

(7) Invar. Invar was studied in last year's program using a pulse-echo technique, and the results were given in a previous report in this series. To better understand the very unusual elastic behavior of this material, some additional studies were made -- resonance measurements between room temperature and liquid-helium temperature. A manuscript describing these results and reviewing previous elastic studies on invar is in progress and should appear in the next report in this series. Note: Because of a wrong mass density, the values of C_ℓ, E, G, and B reported previously for Invar are all too high by a factor of 1.1045. The values of ν reported are correct since they do not depend on the mass density.

Low-Temperature Elastic Constants of a Superconducting Coil Composite*

W. F. Weston**

Cryogenics Division
Institute for Basic Standards
National Bureau of Standards
Boulder, Colorado 80302

Abstract

A resonant piezoelectric oscillator method for measuring elastic moduli was applied to composite materials. The complete set of elastic compliances of a superconducting coil composite was determined semi-continously between 4 and 300 K. Also, two moduli of a layered fiber-glass-epoxy composite were determined; this composite is essentially the matrix material of the coil composite. The Young's moduli, shear moduli, Poisson ratios, and elastic stiffness coefficients are also reported. Results agree closely with elastic data obtained by conventional testing methods.

Key Words: Bulk modulus; composite; compressibility; elastic compliance; elastic stiffness; piezoelectric oscillator; Poisson's ratio; shear modulus; Young's modulus.

**NRC-NBS Postdoctoral Research Associate, 1974-5.

Low-Temperature Elastic Constants of a Superconducting Coil Composite

I. Introduction

The elastic properties of composite materials are currently of considerable interest. Many composites, because they have high mechanical strength and a high modulus-to-density ratio, are useful as strong, lightweight structural materials. Some composites have been designed for use at low temperatures, for example as superconducting coils for high-field magnets. However, few elastic data are available for composite materials, particularly at low temperatures. To the author's knowledge, no complete sets of elastic data are available for composite materials at 4 K. Such data are useful as design parameters, and elastic constants are among the most accurately known fundamental physical properties of solids.

Because composite materials are usually highly anisotropic, the determination of their elastic constants is much more difficult than for the more usual quasi-isotropic engineering materials. Conventional methods of measuring the elastic properties of solids have been applied to composites with only limited success. These methods usually require relatively large specimens and considerable time and effort, especially if a complete set of elastic constants is required.[1] These methods, as applied to composites, include vibrating[2,3] or resonant-beam[4,5,6] tests, tensile or compressive tests,[1,7,8] torsion tests,[1,9] bending tests,[1,10] and pressure tests[11,12,13]. Generally, the elastic constants measured by these methods are less accurate than those acquired by ultrasonic tests.

Ultrasonic pulse techniques are limited by the necessity of using wave-lengths that are large compared with fiber diameters and at the same time sufficiently small compared with the dimensions of the specimen so that true plane-wave conditions can exist. Since ultrasonic pulse methods are typically performed at megahertz frequencies, this condition cannot be met for many composites. If the wavelength is not larger than the fiber diameter, the wave is attenuated and scattered. Ultrasonic pulse-echo methods have been applied to some metal-matrix composites with extremely small fibers.[14,15,16] Even in these cases the pulse-echo trains are poor because of high attenuation and dispersion[15]. In fact, Achenbach and Herrman[17] predicted large dispersive effects for shear waves propagated in the fiber direction, even when the wavelength is much larger than fiber diameters. Zimmer and Cost[18] verified this prediction by measuring sound velocities in a unidirectional glass-reinforced epoxy-fiber composite. For wavelength-to-fiber diameter ratios of roughly 50, dispersion increased some phase velocities by a factor of 2. Elastic constants of some carbon-fiber-reinforced plastics have also been measured by ultrasonic pulse-echo techniques.[19,20,21]

Attempts to use 10 MHz pulse echo techniques on the composite studied herein were unsuccessful. Both longitudinal and shear waves were propagated along all orientations and produced no detectable echoes. This is understandable since the filament sizes for this composite, as described in the text, are larger than the sound wavelength. Larger specimens than are currently available would be needed for 1-5 MHz pulses, although it is doubtful that even these frequencies would produce useable echo patterns for this material.

The ultrasonic immersion technique, as described by Markham,[22] is fast and accurate and offers the possibility of measuring all the elastic properties on one specimen. However, this technique is also limited by fiber size and by sample dimensions.[23,24] The choice of ultrasonic modes that can be propagated in a given direction in a specimen is also limited, and the technique is inapplicable to low-temperature measurements.

Zecca and Hay[25] avoided the problems encountered with megahertz frequencies by using electrostatic transducers to generate and to detect resonant kilohertz frequencies of a metal-matrix composite. Electrostatic transducers, however, cannot be used with non-metallic materials.

The most widely used ultrasonic technique, using kilohertz frequencies, is the resonant piezoelectric oscillator. This method is due principally to Quimby and associates.[26] Quimby thoroughly analyzed the vibrations of solid rods driven by a piezoelectric crystal, and Balamuth[27] first employed drivers and specimens of matching fundamental frequencies. Rose[28] extended this method to torsional oscillators. Basically, the piezoelectric properties of quartz are used to generate and to detect resonant frequencies of an oscillator consisting of one or two quartz crystals, a specimen, and perhaps a dummy rod, all cemented together. This method has been used to measure elastic moduli at both high[29,30] and low [27,28,30,31] temperatures, and has worked well with both metals[32,33] and non-metals.[27-31] Thus, this technique is well understood both theoretically and practically, and it would seem to be well suited for testing composites. The long wavelengths used (typically on the order of centimeters in the kilohertz region) are much larger than fiber diameters, and, since the technique employs standing waves rather than traveling waves, specimen sizes can still be kept small.

In the present paper it is described how this resonance technique was used to measure the complete set of elastic compliances of a superconducting coil composite, which was essentially composed of an epoxy matrix and unidirectional copper-niobium-titanium fibers. The compliances were measured semi-continuously from 300 to 4 K. Results are given also for an epoxy-fiberglass layered composite. The results generally agreed closely with the few existing static measurements on the same composite.

2. Experimental Procedure

A. Resonant Piezoelectric Oscillator

The three-component resonant piezoelectric oscillator technique was originally described by Marx[34], and was discussed in detail by Fine[35]. The technique consists of bonding quartz-driver and quartz-gauge piezoelectric crystals to a specimen to produce and to detect a standing longitudinal (or torsional) resonant wave. Each component's length is adjusted so that its resonant frequency is closely matched to that of the other components. The system is then driven by the driver transducer at its resonant frequency, which is monitored by the gauge crystal.

Longitudinal waves are excited by α-quartz bars of square cross section, excited into longitudinal vibration by an ac signal applied to full-length, adherent electrodes (see Fig. 1). The driver quartz was fully gold plated on two parallel sides (z-faces) with a shallow notch cut in the center of each electrode. Fine, gold-plated tungsten wires, seated in these notches, served to suspend the resonator assembly at displacement nodes and provided the necessary electrical contact. The gauge quartz was gold-plated only over the center third of the two parallel faces and electrical contact was made through fine wires adhered into the notches with silver conducting paint. The electric axes of the driver and the gauge crystals were perpendicular to reduce electrical pickup.

The longitudinal oscillator apparatus is illustrated in Figure 1. The driver-quartz crystal was suspended by 0.003 in gold-plated tungsten wires. The driver mounts, which were aluminum, were removed during the torsional measurements, since the torsional driver crystal was suspended between the bakelite posts by nylon threads. The specimens were cylindrical for all measurements. The chromel-constantan thermocouple was placed near, but not touching, the specimen. The entire apparatus was sealed in a thin-walled stainless-steel can. The can was partially evacuated, placed in the ullage of a helium dewar and lowered stepwise to achieve cooling.

The torsional quartz crystals were circular cylinders with their length in the x-direction and with four gold-plated electrodes running the length of the crystal.[36] Opposite pairs of electrodes were electrically connected. The driver quartz was suspended vertically by means of fine nylon treads attached with varnish to opposite sides of the quartz near a displacement node of vibratio

The quartz crystals were bonded together with a semi-permanent adhesive, Eastman 910.[37] The specimens were right-circular cylinders and were also bonded to the gauge quartz with the same adhesive. For some torsional experiments, this cement occasionally failed at low temperatures; such experiments were repeated until successful. Other materials such as vacuum grease and epoxy resin have been used as low-temperature bonding agents.[38]

The quartz crystals used had resonant frequencies of 60 and 100 kHz. Most of the measurements were done with the 60 kHz quartz crystals (3/16 in square cross for longitudinal, and 3/16 in diameter for torsional), but some were done with the 100 kHz crystals (1/8 in diameter). The mass of each driver-gauge combination was noted and the resonant frequencies were monitored from 300 to 4 K. The length of each specimen was determined such that its resonant frequency for the entire temperature range was within approximately 5% of the oscillator assembly although in some cases the specimen frequency differed by as much as 10%. The mass, length, and diameter of each specimen were noted and its mass density was determined by Archimedes' method using distilled water as a standard. The specimen was then cemented to the quartz crystals and the resonant frequency of the oscillator was monitored from 300 to 4 K. No thermal contraction corrections were made; for the coil composite described below this introduces a maximum error (over a 300 K range) of about 0.5%.[39] Maximum uncertainties in the frequency measurements are estimated to be about one part in 10^5.

B. Electronics

Most workers who have used the piezoelectric oscillator technique have employed electronics similar to those described by Marx.[34] This system requires manual adjustment of the input frequency to the driver crystal to keep the oscillator at resonance. A less time-consuming and more accurate system is the regenerative system designed by Gerk[40] and slightly modified by Johnson.[41]

Gerk's system consists primarily of a closed loop containing an amplifier and the driver-gauge combination of piezoelectric crystals, which act as a resonant element, with a feedback circuit to control the gain of the amplifier. This system is based on the principles of an oscillator; that is, the output of an amplifier is fed into the input through a frequency-selective network (the quartz crystals). The phase shifts are corrected with a variable phase shifter. A more complete description of the system was given by Gerk.[40] This system locks onto the resonant frequency and automatically stays at the resonant frequency if this frequency changes, due to a change of the specimen's environment, for example.

C. Specimens

The superconducting coil composite is fully described in reference 39. Basically, the coil is composed of a copper-stabilized niobium-titanium wire (0.56 mm by 0.72 mm cross section) coil impregnated with epoxy. The wire layers are separated by layers of dry fiberglass cloth (0.1 mm thick). The copper-to-superconductor volume ratio of the wire is 1.8 to 1. The wire-to-epoxy cross-sectional area fraction is about 3 to 1. The coil dimensions were approximately 19 cm I.D., 24 cm O.D., and 10 cm long.

Coordinate axes were chosen to coincide with the specimen axes. The longitudinal axis (3-axis) coincides with the axis of the wire, which was assumed to have zero helix angle. The 1- and 2-axes lie along the radius and coil axes, respectively, and form an orthogonal set with the 3-axis. The symmetry of the coil (orthorhombic) requires nine elastic constants to characterize the material. By assuming the material to be transversely isotropic, by neglecting the effects of curvature, the number of independent elastic constants is reduced to five. An orthotropic body with transverse isotropy has the same symmetry as close-packed hexagonal crystals such as magnesium and zinc. Justification for equating the 1- and 2-axes is given in reference 39, and further experimental data show that the effect of curvature on the moduli is minor[42].

The masses, lengths, and angles between the specimen axis and the 3-axis are given in Table I. The density of the coil composite was found to be 6.000 gm/cm^3.

Besides the superconducting coil, some specimens composed only of fiberglass cloth and epoxy were made available. The fiberglass-to-epoxy volume ratio in

these samples was approximately the same as in the coil composite. Measurements were made on two specimens of this material. Dimensions and orientations of these specimens are also reported in Table I, with the angle θ corresponding to the angle between the specimen axis and the direction parallel to the layers of fiberglass cloth. The density of this material was found to be 1.931 gm/cm^3. This material can also be considered transversely isotropic, if the fiberglass is considered transversely isotropic. Thus, five constants are again needed to completely characterize the material elastically. Cylindrical specimens of only one orientation were available; thus, only two elastic constants of the fiberglass-epoxy matrix material were determined.

3. Results

The directly measured quantity in these measurements is f_o, the frequency of the three-component piezoelectric resonator. For longitudinal resonance the frequency of the specimen (f_s) can be found from f_o, the frequency of the driver-gauge quartz assembly (f_q), the mass of the specimen (m_s), and the mass of the quartz (m_q)[43]:

$$f_s^2 = f_o^2 + (f_o^2 - f_q^2)m_q/m_s. \qquad (1)$$

This formula is more exact than the approximation

$$f_s = f_o + (f_o - f_q)m_q/m_s, \qquad (2)$$

which is usually quoted and used for resonant oscillators[34].

The formula for the torsional oscillator is somewhat more complicated since the moments of inertia (rather than the masses) of the components are involved:[36]

$$f_s^2 = f_o^2 + (f_o^2 - f_q^2) m_q r_q / (m_s r_s^2). \quad (3)$$

Here, r_q is the radius of the quartz and r_s is the radius of the specimen.

The Young's modulus, E, or shear modulus, G, for the particular orientation of the specimen is given by:

$$E \text{ or } G = 4 L^2 f_s^2 \rho. \quad (4)$$

E is found from the longitudinal-mode fundamental frequency and G is found from the torsional-mode fundamental frequency. In Eq. 4, L is the specimen length and ρ is the mass density.

Thus, the measured quantities are the Young's and shear moduli, which are directly related to the elastic compliances, S_{ij}. However, if the wavelength is not much larger than the sample dimensions, a correction for the Poisson contraction (or lateral motion) must be applied to Young's modulus.[35] When the length-to-diameter ratio is 10 to 1, this correction amounts to about one part in a thousand.

The value of Young's modulus for an arbitrary direction in a specimen with transverse isotropy is given in terms of the elastic compliances by[44]

$$\frac{1}{E} = S_{11}\sin^4\theta + S_{33}\cos^4\theta + (2\,S_{13} + S_{44})\sin^2\theta\,\cos^2\theta, \qquad (5)$$

where θ is the angle between the specimen axis and the unique axis. Similarly, the shear modulus is

$$\frac{1}{G} = S_{44} + (S_{11}-S_{12}-\tfrac{1}{2}S_{44})\sin^2\theta + 2(S_{11}+S_{33}-2S_{13}-S_{44})\sin^2\theta\,\cos^2\theta. \qquad (6)$$

Most measurements were made during cooling. All experiments were performed at least twice, and any unusual behavior was examined on heating as well as cooling, for reversibility.

A. Superconducting Coil Composite

Measurements made on the coil composite are listed in Table II. Again, θ is the angle between the specimen axis and the 3-axis (longitudinal axis). The mode specifies either longitudinal or torsional oscillations. The subscripts on E and G designate the direction of the force and the plane on which the force is applied, respectively. The compliances S_{11}, S_{33}, and S_{44} are found directly from experiments 1, 2, and 3, respectively. From experiment 4, S_{12} is found using the relation $2(S_{11} - S_{12}) = S_{66}$, and the value of S_{44} from experiment 3. Either specimen 5 or 6 can be used to determine S_{13}. This compliance must be determined from a measurement on a specimen with its axis at an angle to the longitudinal direction. As can be seen from Table 2, however, the Young's or shear modulus measured on specimens with $0^\circ < \theta < 90^\circ$, is only partly dependent on S_{13}. Thus, S_{13} will be the least accurately determined compliance. The measurement of this compliance corresponds to the measurement of the elastic stiffness C_{13} by megahertz ultrasonic techniques. Zimmer and Cost[17] encountered difficulty in measuring C_{13} for a composite material and their estimated uncertainty is this elastic constant (100%) was ascribed to dispersion as well as to the relatively high inaccuracy.

The experimental data are presented in Figures 2-7. The smooth curves represent regular temperature behavior as given by a theoretical relationship suggested by Varshni,[45] that has been used successfully to represent the temperature dependences of metals,[45] ionic solids,[45] and several alloys.[46] The overall fit of this function to these data is not nearly as good as for other materials, and the data for E_{33}, could not be fitted to the Varshni function because of its concave-upwards curvature. A smooth curve was drawn through the data points and the actual point values were used in calculations. This modulus was measured several times to check its behavior and the data from the different measurements were in excellent agreement. This data is completely reversible.

The shear modulus corresponding to shearing the axial planes in the radial direction G_{12}, or vice-versa is shown in Figure 8. This modulus was calculated from the curve values of G_{13} and G', since $G_{12} = 1/S_{66}$.

Because of the difficulty in machining the specimens to small radii, the ratios of lengths to diameters were in some cases on the order of four or five to one. The estimated correction to the Young's moduli in these cases is still only about one percent.

The elastic compliances as functions of temperature are given in Table III. The compliances S_{11}, S_{33}, and S_{44} are just reciprocals of E_{11}, E_{33}, and G_{13}, as mentioned previously. The error in the directly measured moduli is estimated to be about 1%, thus these compliances should be accurate to 1%, also. The compliance S_{12} is found from combining the results of three measurements. Thus, S_{12} may be less accurately known. It was found that in solving for S_{13} from either Eq. 5 or 6, a 1% error in the measured modulus led to a 10-20% error in S_{13}. Thus, the error associated with S_{13} is considerable, perhaps as much as 100%. The values reported for S_{13} are the average of the values

found from experiments 5 and 6, which are -0.110 and -0.058, respectively. From the material available, it was not possible to machine specimens with $\theta < 60^{o}$ for other determinations of S_{13}. As expected, the material was found to be highly anisotropic with $s_{11} \approx 2s_{33}$.

It is emphasized that the data reported here are dynamic (adiabatic) rather than static (isothermal) and apply to rapid, rather than slow, loading. Conversion formulas are given in Landau and Litschitz[47], for example, and in most cases the differences between adiabatic and isothermal elastic constants are small. These formulas involve the thermal expansion coefficients and the specific heat. The thermal expansion coefficients are known for this composite[39], but the specific heat has not yet been determined. If an estimate of the specific heat of the composite is made from the specific heats of the components, the difference between the adiabatic and isothermal Young's moduli is at most 0.5%. The adiabatic and isothermal shear moduli are, of course, equal.

B. Epoxy-Fiberlgass Composite

Measurements were also made on the epoxy-fiberglass specimens listed in Table I. These specimens were oriented with the layers of fiberglass cloth running the length of the specimen; these were the only orientations available. The Young's modulus and shear modulus are shown in Figures 9 and 10. The shear modulus is well represented by the Varshni function, and is seen to have normal temperature behavior. A smooth curve was drawn through the Young's modulus data, which could not be fitted to the Varshni function because of the low-temperature maximum.

4. Discussion

Some elastic data, taken by conventional static methods, were available for the superconducting coil composite and the epoxy-fiberglass composite.[40,48] These data generally compared very favorably with the resonance data. For example, resonance values of E_{11} at room temperature and 4 K are 12% and 1% larger than the static data taken at these temperatures. The inaccuracy of the static values is given as about 10%. Also, resonance values of E_{33} compare to within 5 - 7% of the static data, and resonance values of G_{13} agree within 6 - 11% of the static values.

Other elastic constants of interest include the Poisson ratios:

$$\nu_{12} = -S_{12}/S_{11}, \tag{7}$$

and

$$\nu_{13} = -S_{13}/S_{33}, \tag{8}$$

where ν_{ij} represents the negative ratio of strain in the j-direction to strain in the i-direction.

The value of ν_{12} at room temperature is 0.304. The reported [39] static value is 0.335, with the inaccuracy again believed to be about 10%. Thus, this result gives added confidence to the resonance value of S_{12}. However, the Poisson ratio ν_{13}, involves the compliance S_{13}, which has already been noted to be much more inaccurate than the other four compliances. In fact, if the room-temperature values of S_{13} and S_{33} are used, $\nu_{13} = 0.683$, whereas the static value is 0.333.[39] Since the other elastic constants are all in relatively good agreement with the static values, it is reasonable to expect that ν_{13} should be also. Thus, the value of S_{13} is highly suspect, especially since a value near 1/3 seems more realistic for Poisson's ratio.

It is also of interest to consider the compressibilities. For a material with transverse isotropy, the linear compressibilities are

$$k_1 = S_{11} + S_{12} + S_{13},$$

and (9)

$$k_3 = 2S_{13} + S_{33},$$

where the subscripts designate the axis. Also, the volume compressibility is

$$K = 2k_1 + k_3. \tag{10}$$

If the room temperature values of the compliances, as given in Table III, are used, then $k_1 = 0.136 \times 10^{-10}$ m^2/N, $k_3 = -0.045 \times 10^{-10}$ m^2/N and $K = 0.027 \times 10^{-10}$ m^2/N. However, if the Poisson ratio ν_{13} is taken as 1/3, then $S_{13} = -0.041 \times 10^{-10}$ m^2/N at room temperature, and $k_1 = 0.179 \times 10^{-10}$ m^2/N $k_3 = 0.041 \times 10^{-10}$ m^2/N, and the volume compressibility $K = 0.399 \times 10^{-10}$ m^2/N. The relatively large value for ν_{13} and the negative k_3 which result from the resonance S_{13}, may not be unreasonable, considering the multi-component material. The elastic stiffness coefficients, however, can be calculated from the compliances, and indicate that the resonance value of S_{13} is in error.

The elastic stiffnesses (C_{ij}) can be directly calculated by inverting the S_{ij} matrix if all the compliances are known. The explicit relationships are[49]:

$$C_{11} = \frac{S_{11}S_{33} - S_{13}^2}{(S_{11} - S_{12})\tilde{S}},$$

$$C_{12} = \frac{S_{13}^2 - S_{12}S_{33}}{(S_{11} - S_{12})\tilde{S}},$$

$$C_{13} = \frac{-S_{13}}{\tilde{S}}, \qquad (12)$$

$$C_{33} = \frac{S_{11} + S_{12}}{\tilde{S}},$$

$$C_{44} = 1/S_{44},$$

and

$$C_{66} = 1/S_{66},$$

where $\tilde{S} = S_{33}(S_{11} + S_{12}) - 2S_{13}^2$. Except for C_{44} and C_{66}, these relationships depend strongly on S_{13}. Using the resonance value of S_{13}, the elastic stiffnesses which depend on S_{13} are found to increase with increasing temperature, which is contrary to normal behavior. Since the Young's moduli and shear moduli all behave fairly regularly with temperature, the resonance value of S_{13} seems unreasonable. In calculating the elastic stiffnesses, then, a value of 1/3 for ν_{13} was used, and this Poisson's ratio was taken as constant with temperature.[39] It is believed that the eleastic stiffnesses obtained this way are more accurate than those obtained using the resonance value of S_{13}. The elastic stiffnesses are given in Table IV.

As expected, the elastic properties of this composite are highly anisotropic. The anisotropy is best described by considering the percent elastic anistropy as discussed by Chung and Buessem.[50] For transversely isotropic symmetry, this scheme involves using the conventional anisotropy ratios (the linear compressibility ratio $A_c = k_3/k_1$, and the shear anisotropy $A_s = C_{44}/C_{66}$) to calculate anisotropy parameters A_c^* and A_s^* with the following properties:

A^* is zero for materials that are elastically isotropic, i.e., $A = 1$; A^* is always positive and a single valued measure of the elastic anisotropy of a material regardless of whether $A < 1$ or $A > 1$; and A^* gives the relative magnitude of the elastic anisotropy present in the material. For this composite $A_c \simeq 0.23$, $A_c^* \simeq 8.4\%$, $A_s \simeq 0.61$, and $A_s^* \simeq 12.3\%$. For comparison, $A_c^* \simeq 9.9\%$ and $A_s^* \simeq 13.7\%$ for zinc,[49] which is one of the most anisotropic hexagonal metals.

The static value of Young's modulus of the fiberglass-epoxy is also available.[40] This Young's modulus was measured on a specimen oriented like the one used for the resonance measurements. The resonance and static values differ by 4 - 10%. There was no evidence of a maximum in the static data, but it is believed that the maximum is real. This maximum was observed during several measurements and was completely reversible. No explanation for this behavior can be given at this time.

5. Conclusions

The resonant piezoelectric oscillator method used in this work is generally suitable for measuring the elastic properties of composite materials. This method is accurate, fast, and requires only small specimens. It is suitable for measurements at all temperatures from 0 K to greater than 1000°C.[29,30] The general techniques and theory of this method are well understood. This method does not appear to have the limitations of static and ultrasonic techniques.

The elastic compliance data presented in this work agree well with existing data taken by conventional static methods. These data can be used to calculate other elastic properties, such as the elastic stiffness coefficients and compressibilities.

The superconducting coil composite was highly anisotropic, with elastic anisotropies similar to those of zinc. This high anisotropy, characteristic of many composite materials, necessitates careful measurements of elastic properties of these materials.

The measured elastic moduli of the composite are not as well represented by the Varshni function as they are for most metals and alloys; i.e., the elastic moduli of the superconducting coil composite are less regularly behaved with respect to temperature.

6. Acknowledgments

The author would like to express his graditude to D. L. Johnson for his considerable assistance with the piezoelectric oscillator techniques. He would also like to thank A. F. Clark for supplying the specimens and the static data on the coil composite, and H. Dickinson, who aided in the experiments.

The author is also indebted to H. M. Ledbetter for many helpful discussions on elastic properties in general and for a critical reading of the manuscript.

References

1. P. R. Goggin, J. Mater. Sci. 8, 233 (1973).
2. T. J. Dudek, J. Compos. Mater. 4, 232 (1970).
3. T. Hirai and D. E. Kline, J. Compos. Mater. 7, 160 (1973).
4. Albert B. Schultz and Stephen W. Tsai, J. Compos. Mater. 2, 368 (1968).
5. R. C. Rossi, J. R. Cost, and K. R. Janowski, J. Amer. Ceramic Soc. 55, 234 (1972).
6. G. C. Wright, J. Sound Vibr. 21, 205 (1972).
7. R. E. Allred and W. R. Hoover, J. Compos. Mater. 8, 15 (1974).
8. L. J. Cohen and O. Ishai, J. Compos. Mater. 1, 1030 (1967).
9. N. L. Hancox, J. Mater. Sci. 7, 1030 (1972).
10. T. R. Tauchert, J. Compos. Mater. 5, 456 (1971).
11. A. Smith, J. Phys. E. Sci. Instrum. 5, 274 (1972).
12. A. Smith, W. N. Reynolds, and N. L. Hancox, J. Compos. Mater. 7, 138 (1973).
13. A. Smith, S. J. Wilkinson, and W. N. Reynolds, J. Mater. Sci. 9, 547 (1974).
14. J. V. Grabel and J. R. Cost, Metall. Trans. 3, 1973 (1972).
15. A. E. Lord and D. Robert Hay, J. Compos. Mater. 6, 278 (1972).
16. W. Sachse, J. Compos. Mater. 8, 378 (1974).
17. J. O. Achenbach and G. Hermann, AIAA J. 6, 1832 (1968).
18. J. E. Zimmer and J. R. Cost, J. Acoust. Soc. Amer. 47, 795 (1970).
19. W. N. Reynolds and S. J. Wilkinson, Ultrasonics 12, 109 (1974).
20. S. J. Wilkinson and W. N. Reynolds, J. Phys. D: Appl. Phys. 7, 50 (1974).
21. T. R. Tauchert and A. N. Guzelsu, J. Appl. Mech., Trans. ASME 39, 98 (1972).
22. M. F. Markham, Composites 1, 145 (1970).
23. G. D. Dean and P. Turner, Composites, July 174 (1973).

24. Robert S. Smith, J. Appl. Phys. 43, 2555 (1972).

25. A. R. Zecca and D. R. Hay, J. Compos. Mater. 4, 556 (1970).

26. S.L. Quimby, Phys. Rev. 25, 558 (1925).

27. L. Balamuth, Phys. Rev. 45,715 (1934).

28. F. C. Rose, Phys. Rev. 49, 50 (1936).

29. L. Hunter and S. Siegel, Phys. Rev. 61, 84 (1942).

30. J. W. Marx and J. M. Silvertsen, J. Appl. Phys. 24, 81 (1953).

31. M. E. Fine, Rev. Sci. Instrum. 25, 1188 (1954).

32. S. Siegel and S. L. Quimby, Phys. Rev. 49, 663 (1936).

33. J. Zacarias, Phys. Rev. 44, 116 (1933).

34. J. Marx, Rev. Sci. Instrum. 22, 503 (1951).

35. M. E. Fine, ASTM Special Tech. Publ. No. 129, 48 (1952).

36. W. H. Robinson, S. H. Carpenter and J. L. Tallon, J. Appl. Phys. 45, 1975 (1974).

37. The use in this paper of trade names of specific products is essential to a proper understanding of the work presented. Their use in no way implies any approval, endorsement, on recommendation by NBS.

38. A. J. Matheson, J. Phys. E. (Sci. Instru.) 4, 796 (1971).

39. C. W. Fowles, P. E. Angerhofer, R. N. Newton, and A. F. Clark, NBSIR 73-349 (1973).

40. A. P. Gerk, Rev. Sci. Instrum. 43, 1786 (1972).

41. D. L. Johnson, University of Illinois, private communication.

42. A. F. Clark, National Bureau of Standards, private communication.

43. W. N. Robinson and A. Edgar, IEEE Trans. Sonics and Ultrasonics 21, 98 (1974).

44. W. Voigt, Lehrbuch der Kristallphysik, (Teubner, Berlin, 1928), p. 746-7.

45. Y. P. Varshni, Phys. Rev. B2, 3952 (1970).

46. E. R. Naimon, W. F. Weston, and H. M. Ledbetter, Cryogenics 14, 721 (1973).

47. L. D. Landau and E. M. Lifshitz, Theory of Elasticity (Pergamon, London 1959) p. 17.

48. M. B. Kasen, National Bureau of Standards, private communication.

49. R. F. S. Hearmon, Rev. Mod. Phys. 18, 409 (1946).

50. D. H. Chung and W. R. Buessem, Anisotropy in Single-Crystal Compounds (Edited by F. W. Vahldiek and S. A. Mersol, Plenum, N. Y., Vol. 2, p. 217, 1968).

Table I. Dimensions and orientations of specimens

Specimen Number	Diameter (inches)	Mass (gm)	Length (cm)	θ (degrees)
	Superconducting Coil Composite Specimens			
1	0.1250	0.540	1.1128	90
2	0.1250	0.925	1.9439	0
3	0.1863	1.081	1.0818	0
4	0.1890	1.248	1.1481	90
5	0.1875	1.874	1.7600	60
6	0.1851	1.327	1.2555	60
	Epoxy-Fiberglass Composite Specimens			
1	0.1875	0.885	2.5387	0
2	0.1878	0.520	1.4862	0

Table II. Experiments performed on Superconducting coil composite

Exp. No.	Spec. No.	Mode	θ	Measured Quantity
1	1	L	90	$E_{11} = \frac{1}{S_{11}}$
2	2	L	0	$E_{33} = \frac{1}{S_{33}}$
3	3	T	0	$G_{13} = \frac{1}{S_{44}}$
4	4	T	90	$G' = \frac{2}{S_{44} + S_{66}}$
5	5	L	60	$E_{\theta=60^o} = \frac{16}{9S_{11} + S_{33} + 6S_{13} + 3S_{44}}$
6	6	T	60	$G_{\theta=60^o} = \frac{8}{3S_{11} + 3S_{33} - 6S_{13} + 2S_{44} + 3S_{66}}$

Table III. Elastic compliances of the superconducting coil composite at selected temperatures (10^{-10} m^2/N)

T(K)	S_{11}	S_{12}	S_{13}	S_{33}	S_{44}	S_{66}
0	0.242	-0.074	-0.061	0.112	0.910	0.631
50	0.242	-0.074	-0.061	0.113	0.910	0.632
100	0.248	-0.076	-0.066	0.115	0.920	0.648
150	0.260	-0.083	-0.073	0.118	0.964	0.684
200	0.275	-0.089	-0.079	0.119	1.046	0.728
250	0.294	-0.094	-0.082	0.121	1.170	0.776
300	0.316	-0.096	-0.084	0.123	1.350	0.823

Table IV. Elastic stiffnesses of the superconducting coil composite at selected temperatures (10^{10} N/m^2)

T(K)	C_{11}	C_{12}	C_{13}	C_{33}	C_{44}	C_{66}
0	5.10	1.94	2.39	10.59	1.10	1.58
50	5.10	1.93	2.39	10.46	1.10	1.58
100	4.99	1.90	2.34	10.27	1.09	1.54
150	4.80	1.87	2.27	10.05	1.04	1.46
200	4.54	1.79	2.15	9.86	0.96	1.37
250	4.21	1.63	1.99	9.64	0.85	1.29
300	3.82	1.39	1.77	9.35	0.74	1.22

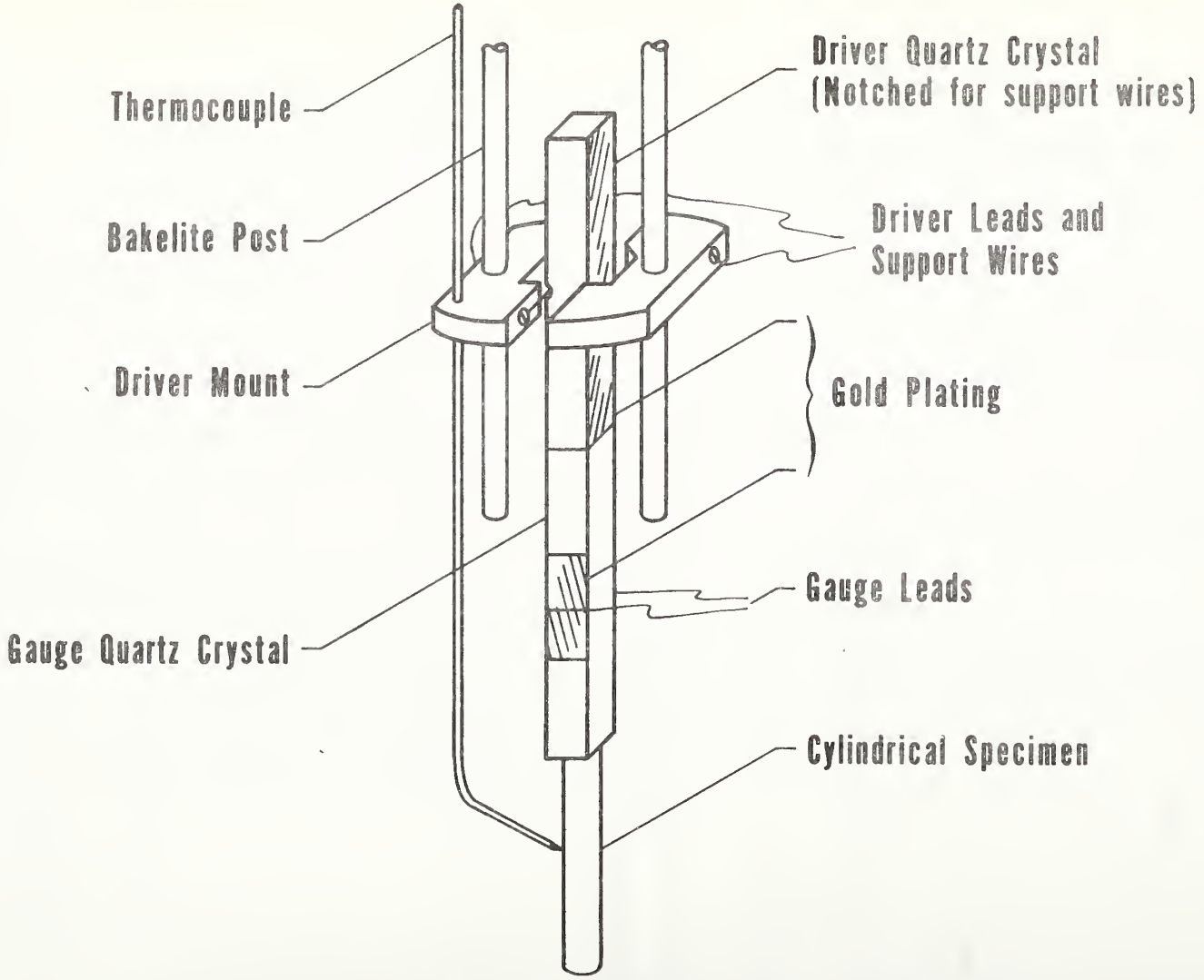

75X 3735

Fig. 1. Resonant piezoelectric oscillator apparatus.

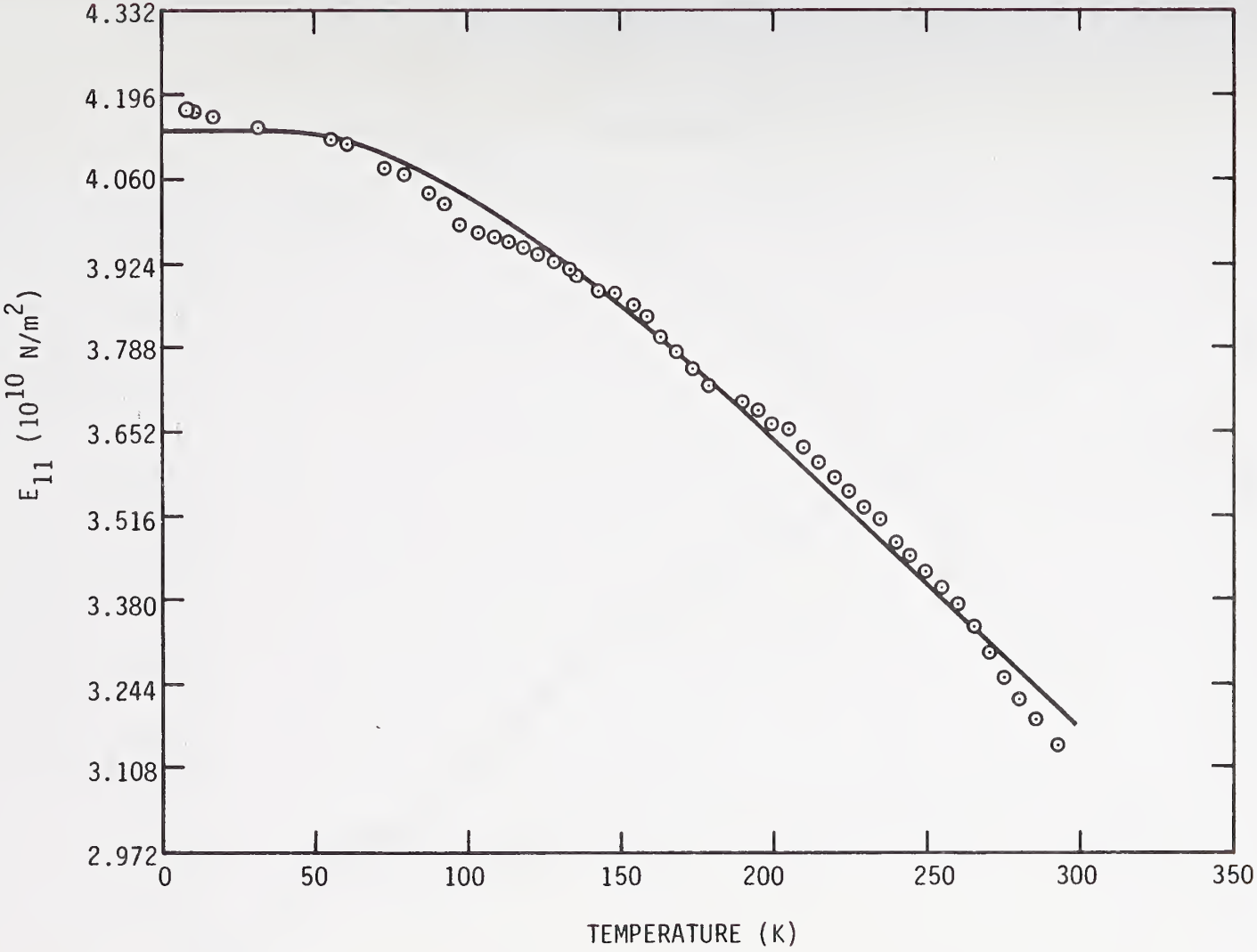

Fig. 2. Young's modulus of the superconducting coil composite, $\theta = 90^{o}$.

75X5747

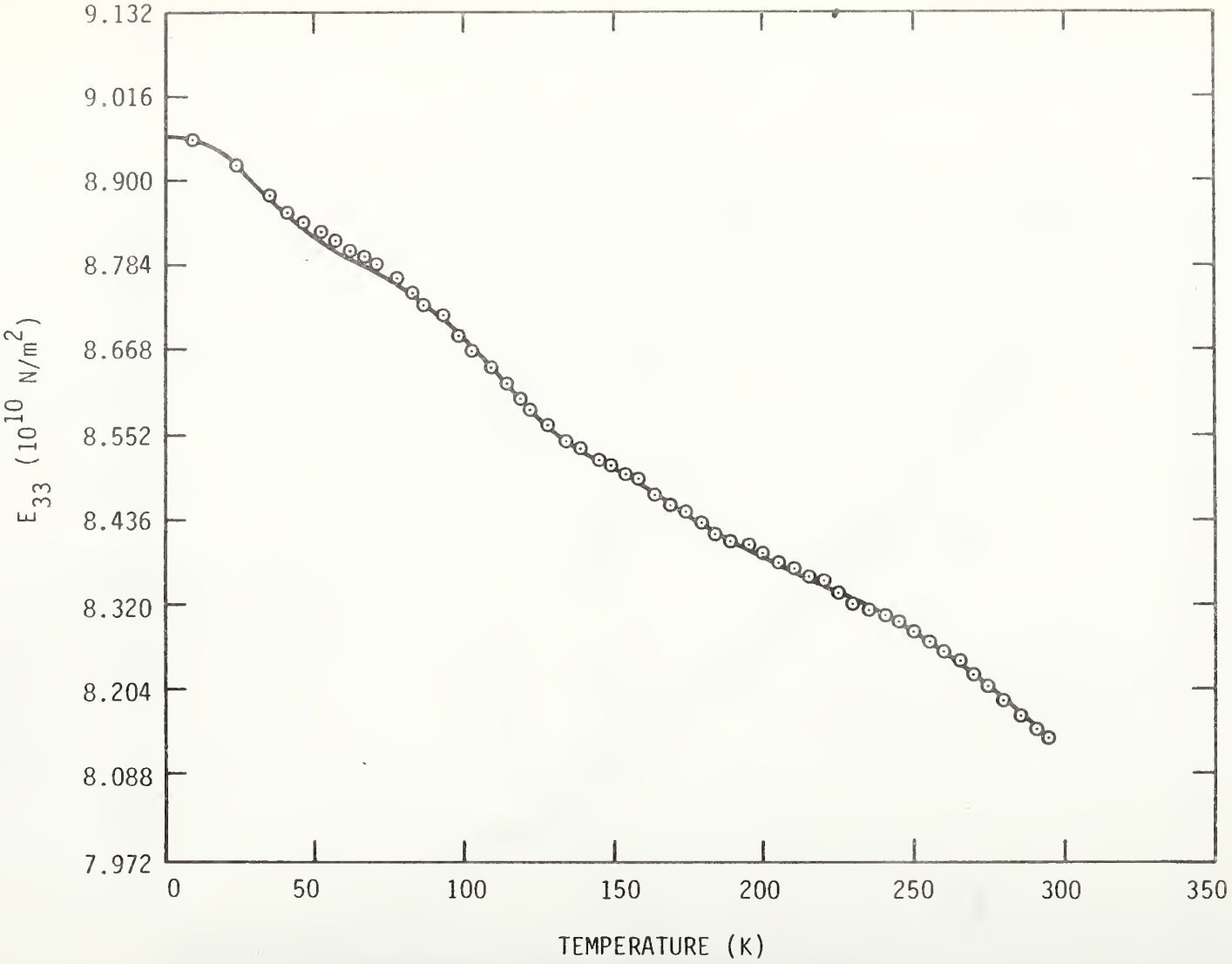

Fig. 3. Young's modulus of the superconducting coil composite, $\theta = 0^{o}$.

75x 5748

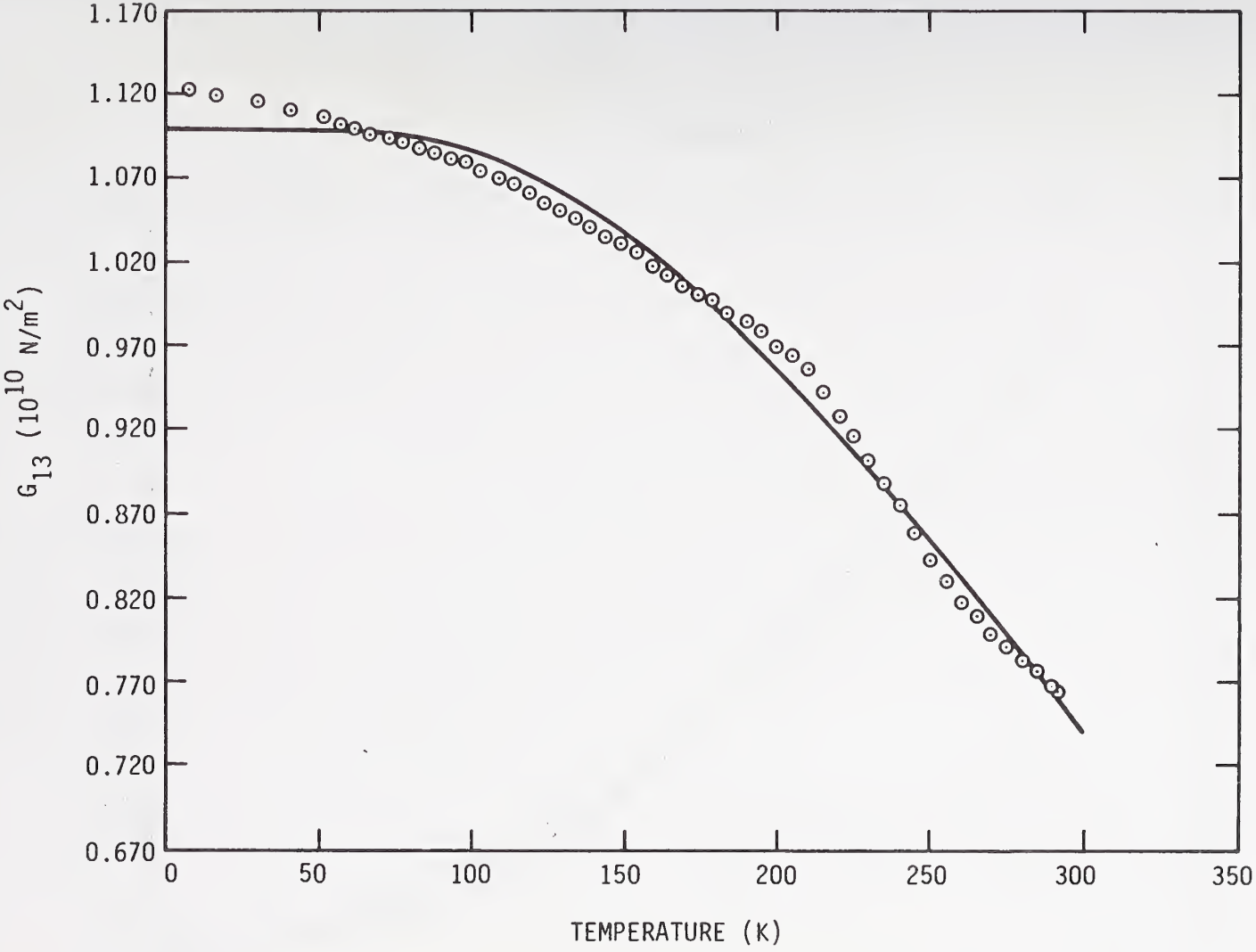

Fig. 4. Shear modulus of the superconducting coil composite, $\theta = 0^{o}$.

75X 5749

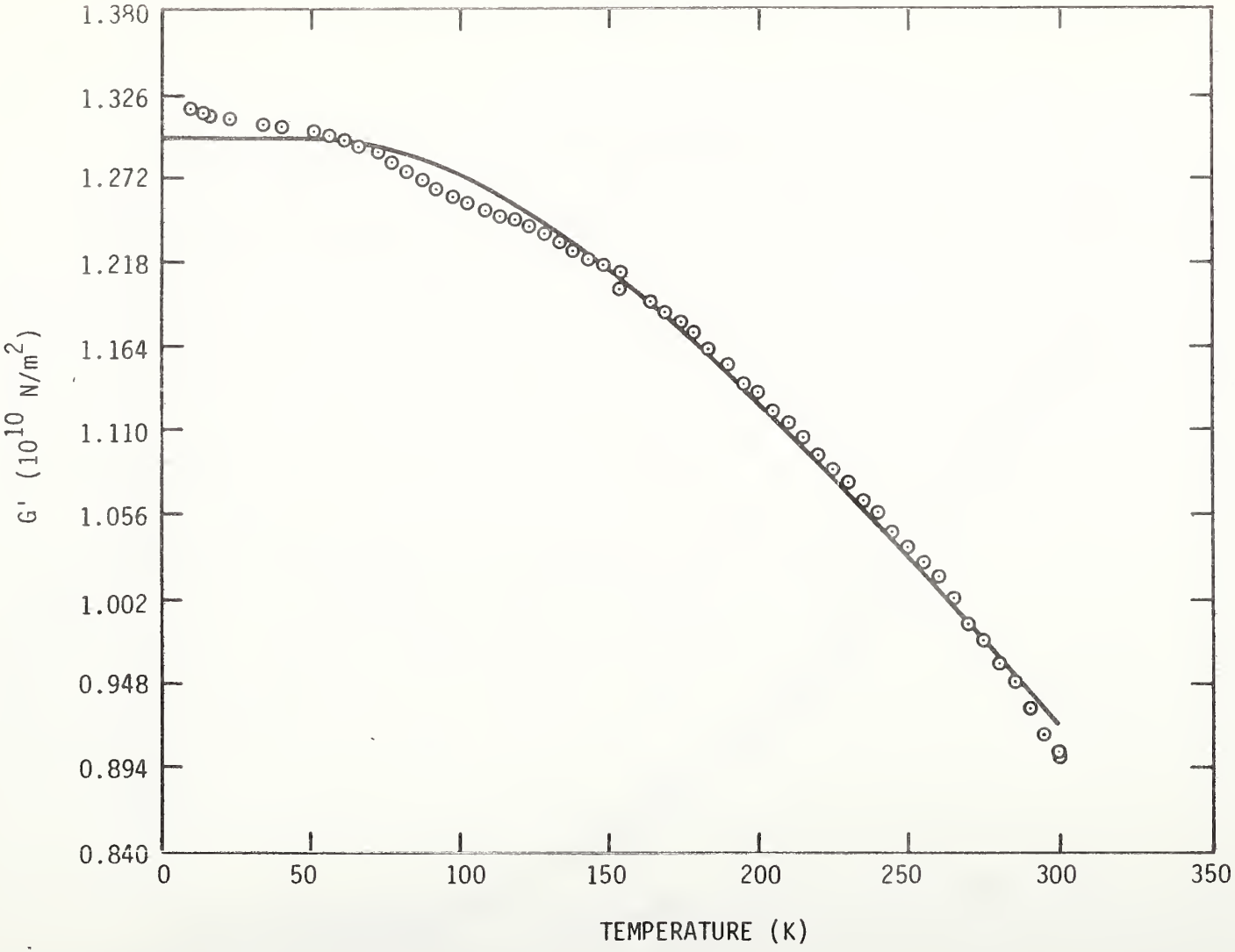

Fig. 5. Shear modulus of the superconducting coil composite, $\theta = 90^{\circ}$. 75X 5750

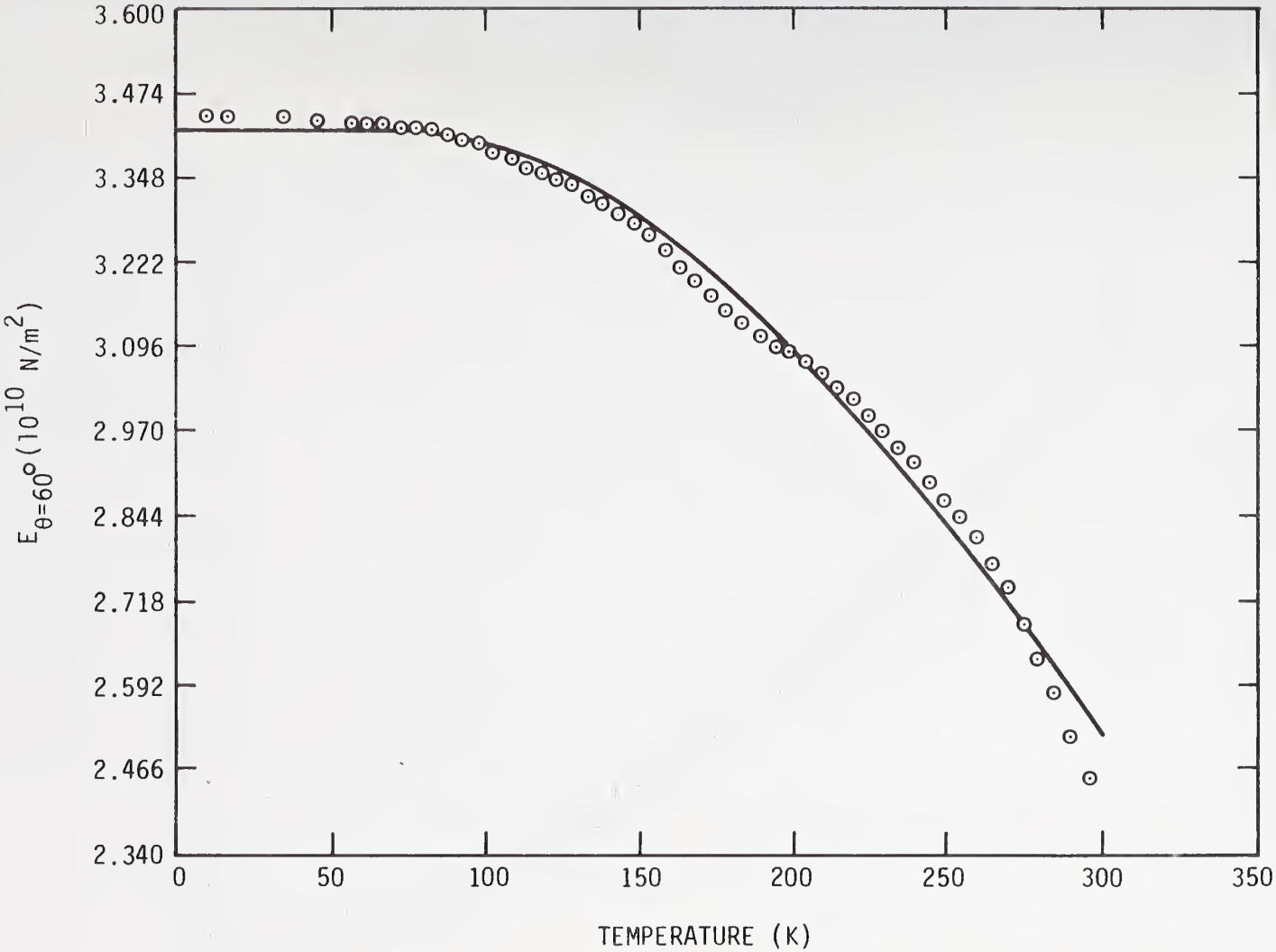

Fig. 6. Young's modulus of the superconducting coil composite, $\theta = 60^o$.

75X 5751

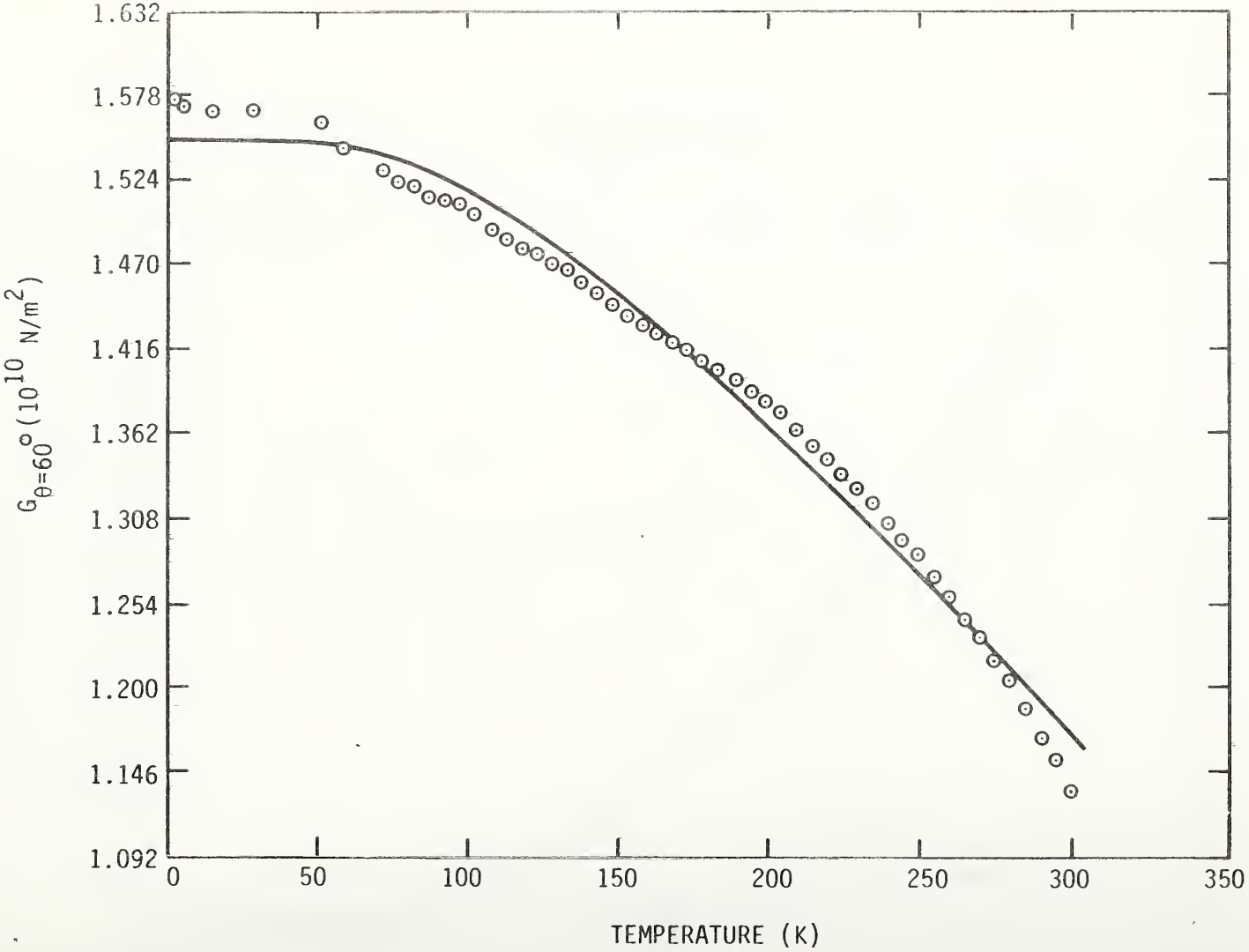

Fig. 7. Shear modulus of the superconducting coil composite, $\theta = 60^o$.

75X5752

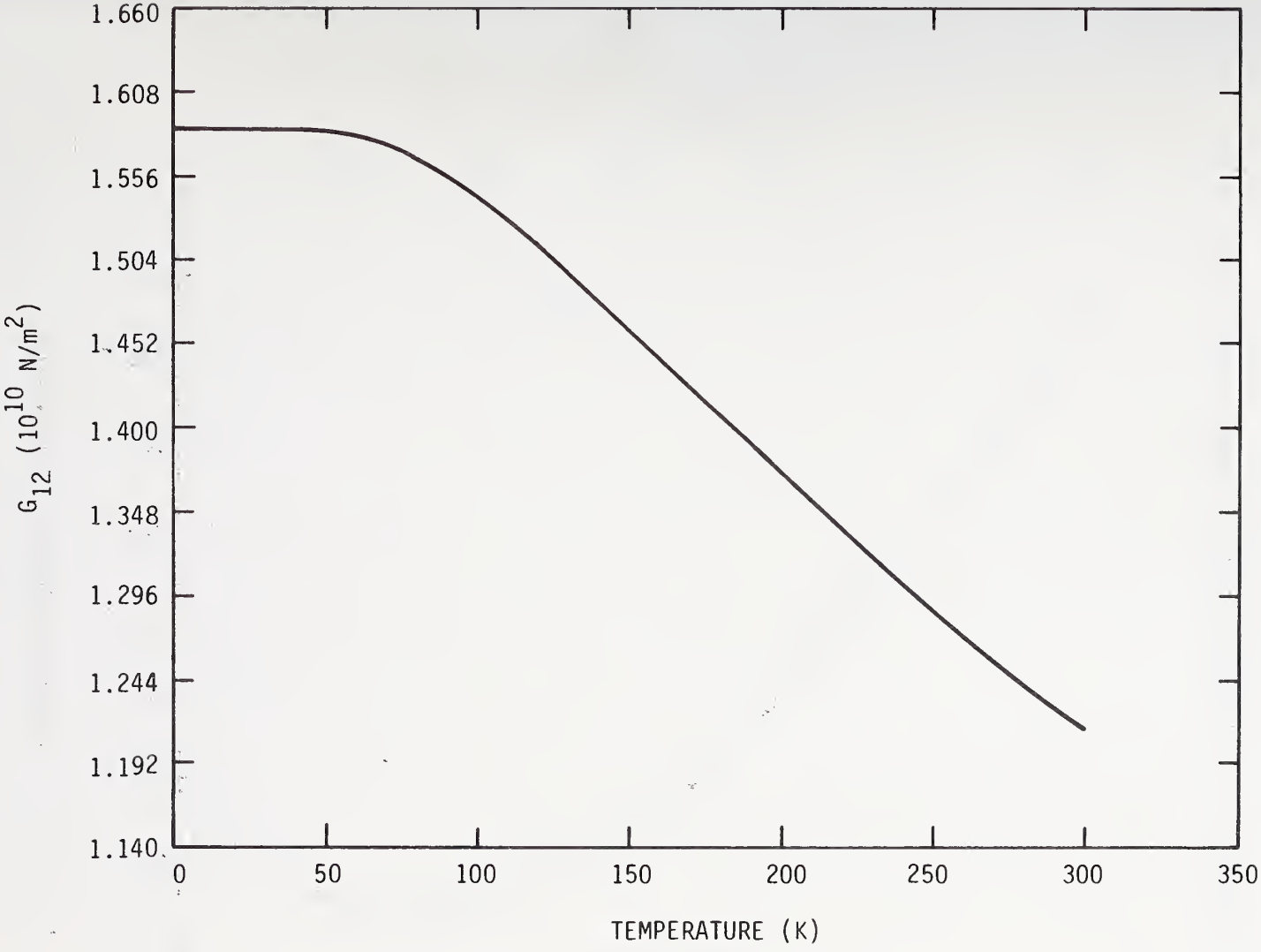

Fig. 8. Shear modulus G_{12} of the superconducting coil composite.

75x 5753

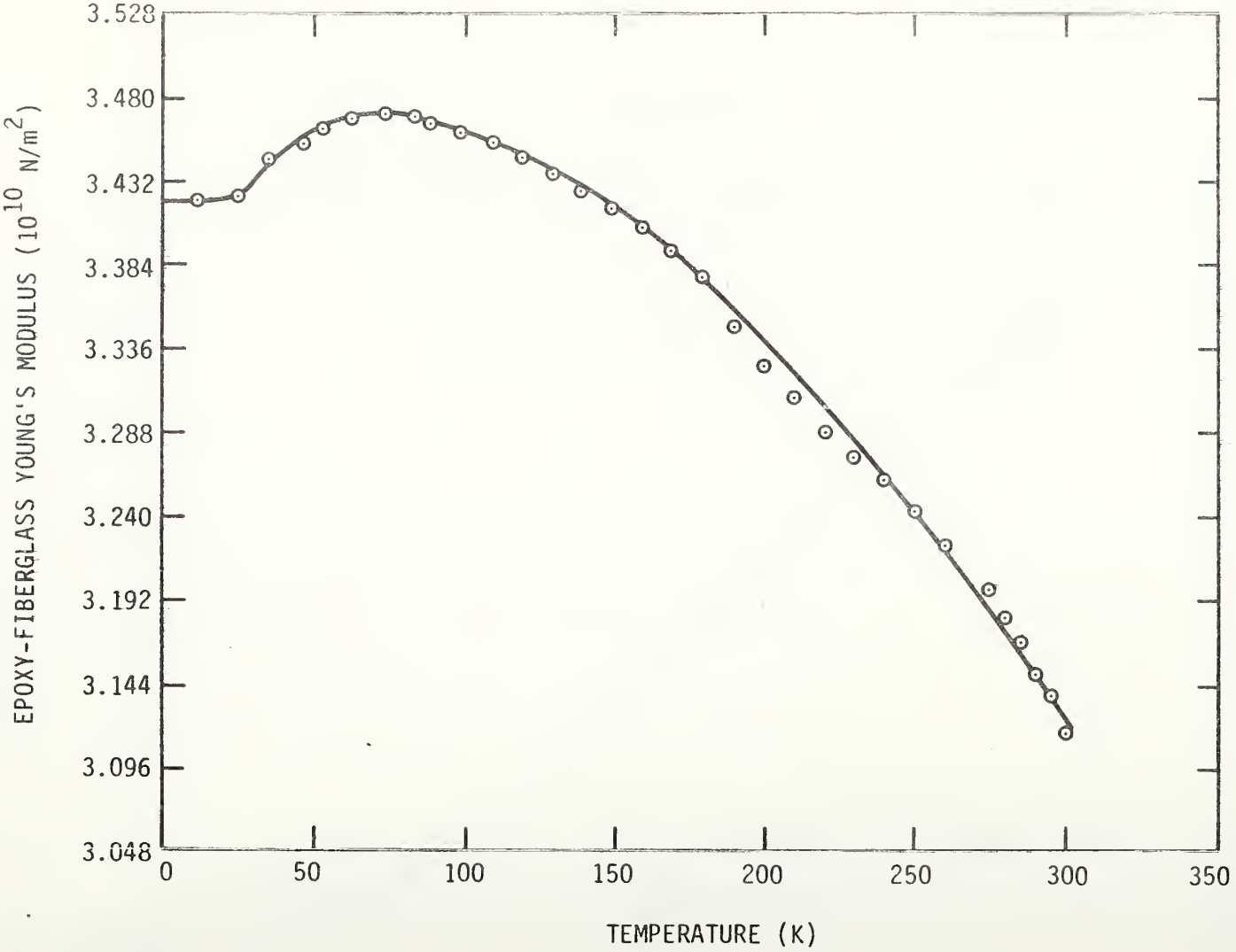

Fig. 9. Young's modulus of epoxy-fiberglass, $\theta = 0^{\circ}$.

75X 5754

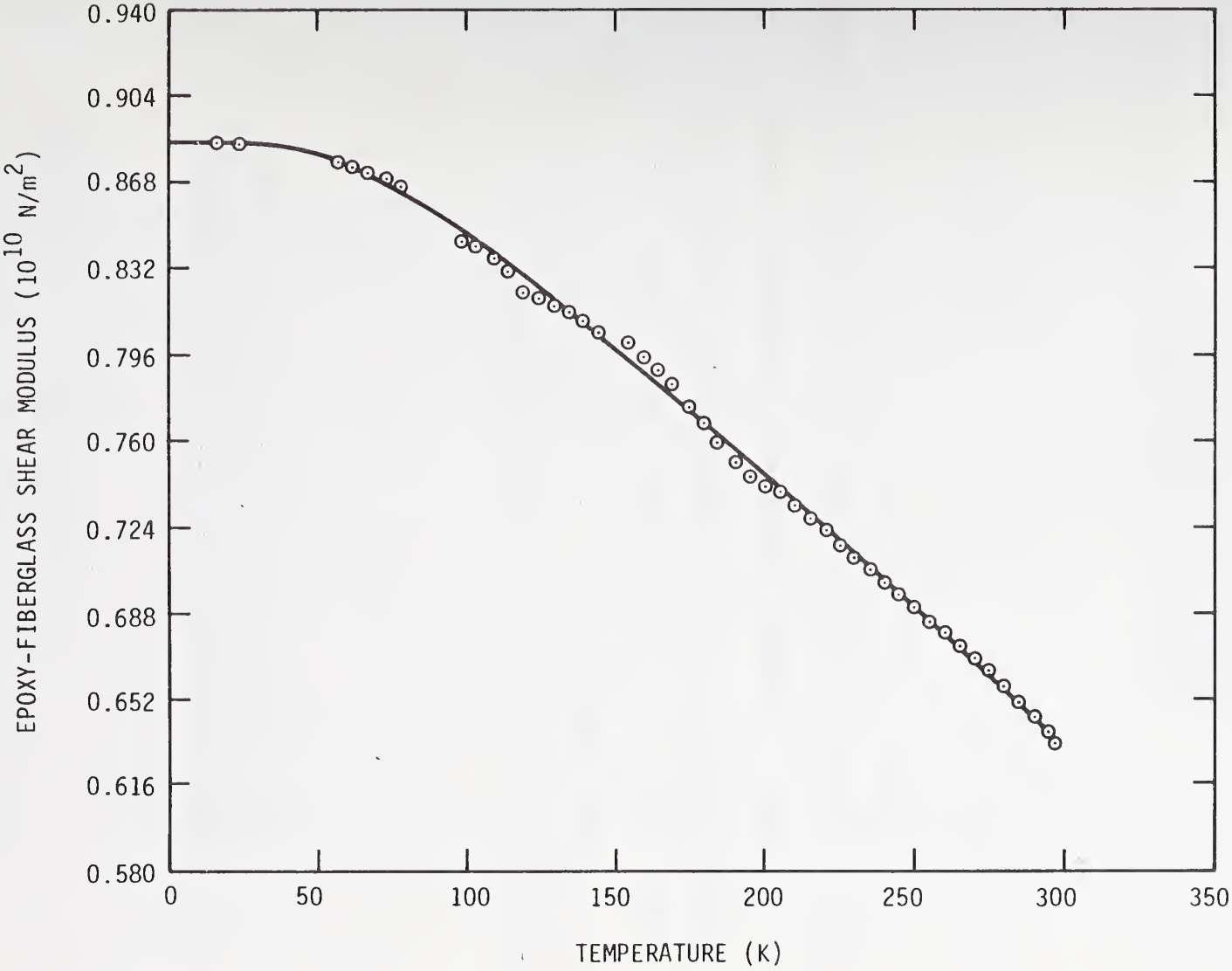

Fig. 10. Shear modulus of epoxy-fiberglass, $\theta = 0^{o}$.

75X 5755

LOW-TEMPERATURE ELASTIC PROPERTIES OF A NICKEL-CHROMIUM-IRON-MOLYBDENUM ALLOY

W. F. Weston and H. M. Ledbetter

Cryogenics Division
Institute for Basic Standards
National Bureau of Standards
Boulder, Colorado 80302

Abstract

The elastic properties of a nickel-chromium-iron-molybdenum alloy were determined between room temperature and liquid-helium temperature by measuring both the longitudinal and transverse sound-wave velocities in a polycrystalline material. These properties include: the longitudinal modulus, Young's modulus, the shear modulus, the bulk modulus (reciprocal compressibility), and Poisson's ratio. Except for a small anomaly in the bulk modulus, this material exhibits regular elastic-constant/temperature behavior.

Key words: Bulk modulus; compressibility; Debye temperature; elastic constants; nickel-base alloys; Poisson's ratio; shear modulus; sound velocity; Young's modulus.

Low-temperature Elastic Properties of a Nickel-Chromium-Iron-Molybdenum Alloy*

W. F. Weston+ and H. M. Ledbetter

Cryogenics Division
Institute for Basic Standards
National Bureau of Standards
Boulder, Colorado 80302

The low-temperature elastic properties of two nickel-chromium-iron alloys, Inconel 600** and Inconel X-750, were reported recently.[1] The same properties--the longitudinal modulus, Young's modulus, the shear modulus, the bulk modulus (reciprocal compressibility), and Poisson's ratio--are reported here for a nickel-chromium-iron-molybdenum alloy, Inconel 718. Except for being slightly softer elastically, it resembles Inconel X-750.

The low-temperature elastic properties of Inconel 718 are of interest mainly because it is a candidate material for cryogenic structural applications.[2] The elastic properties are important both for the design of structural components and for understanding the basic physical properties of a material. From the temperature-dependent elastic constants, deflections can be predicted for any combination of stress and temperature. Also, the Debye characteristic temperature can be calculated from the

---

+ NRC-NBS Postdoctoral Research Associate, 1973-74.

** Tradenames are used to identify the materials tested; they are not NBS endorsements of particular products.

elastic constants. The Debye temperature relates in turn to a wide variety of solid-state phenomena.[3]

Inconel 718 is made precipitation hardenable by its niobium-plus-tantalum content. (Inconel X-750 is made precipitation hardenable by its aluminum-plus-titanium content.) It differs from the nickel-chromium-iron alloys in having superior mechanical properties such as yield, creep, rupture, and fatigue strengths.[2] Its sluggish response to precipitation hardening permits annealing and welding without significant property changes.

Experimental Methods

Ultrasonic (10 MHz) longitudinal and transverse sound-wave velocities were measured between room temperature and liquid-helium temperature (4 K) using a pulse-echo-superposition method.[4] Experimental procedures were identical to those reported previously[1] except that the material was obtained from a commercial source in the form of 3/4-inch (1.9 -cm) rods. Chemical and physical data on the material are given in Table 1.

Results

The longitudinal modulus

$$C_\ell = \rho v_\ell^2 \tag{1}$$

versus temperature is shown in Fig. 1, where ρ is the mass density and v_ℓ is the longitudinal sound-wave velocity. The transverse modulus

$$C_t = \rho v_t^2 = G \tag{2}$$

is shown versus temperature in Fig. 2, where v_t is the transverse sound-wave velocity and G is the shear modulus. Young's modulus E, the bulk modulus B, and Poisson's ratio ν were calculated from the formulas[5]:

$$E = 3C_t(C_\ell - \tfrac{4}{3}C_t)/(C_\ell - C_t), \tag{3}$$

$$B = C_\ell - \tfrac{4}{3}C_t, \tag{4}$$

$$\nu = (1/2)(C_\ell - 2C_t)/(C_\ell - C_t); \tag{5}$$

and these elastic constants are shown versus temperature in Figs. 3-5. For comparison, Figs. 1-5 also show as dashed lines the elastic constants of Inconel X-750, which were reported previously.[1]

The temperature dependences of both C_ℓ and C_t were fitted to a theoretical relationship suggested by Varshni:[6]

$$C = C^o - s/(e^{t/T} - 1) \tag{6}$$

where C^o, s, and t are adjustable parameters and T is temperature. The average difference between curve values and measured values was 0.06 and 0.05 pct. for the transverse and the longitudinal modes, respectively.

The elastic Debye temperature was calculated from C_ℓ and C_t using standard formulas[1] and was found to be Θ = 446 K at absolute zero. For comparison, Θ (nickel) = 476 K and Θ (Inconel X-750) = 474 K.

Discussion

Basically, the low-temperature elastic properties of Inconel 718 are very similar to those of Inconel X-750. The higher-iron, lower-nickel content of Inconel 718 accounts for its slightly lower elastic

Debye temperature. Inconel 718 is also similar to Inconel X-750 in the temperature dependences of its elastic constants for the cases of E, G, and C_ℓ, which show regular behavior. By regular behavior is meant: continuously decreasing with increasing temperature, linear behavior at higher temperatures, relative flatness at low temperatures, and zero slope at T = 0 K. Both materials show slight anomalies in the temperature dependence of the bulk modulus. While Inconel X-750 shows a concavity upwards in the B(T) curve, Inconel 718, as shown in Fig. 4, shows a maximum near 100 K in its B(T) curve. Based on the previous experience of this laboratory, it is believed in this case that the imprecisions in both C_ℓ and C_t are a few parts in 10^4. Thus, this anomaly (though small) is believed to be real and not a measurement-computational artifact.

The interpretation of the maximum in the B(T) curve of Inconel 718 can only be speculative. Unlike Inconel X-750, it was verified during the present study that Inconel 718 is non-magnetic between room temperature and liquid-nitrogen temperature (77 K). In some respects, the low-temperature behavior of the bulk modulus of Inconel 718 resembles that of stainless steels AISI 304, 310, and 316 reported previously.[7] In those cases, the anomalous behavior was interpreted in terms of the Döring effect that results from a large volume magnetostriction accompanying a paramagnetic-to-antiferromagnetic transition. However, no evidence of a low-temperature magnetic transition in Inconel 718 seems to exist; and neither the longitudinal modulus nor Young's modulus show any evidence of a dilatational anomaly. Thus, the nature of this anomaly, its magnitude, and perhaps even the question of its existence deserve further study.

Comparisons with some previous results[8] show reasonable agreement for both the room-temperature elastic constants and the temperature derivatives of E and G. It is easy to verify that the temperature derivative of ν reported here is more reasonable than that obtained from data in ref. 8. Differentiation of the standard relationship

$$\nu = \frac{E}{2G} - 1 \tag{7}$$

gives

$$\frac{1}{\nu}\frac{d\nu}{dT} = \frac{E}{E-2G}\left(\frac{1}{E}\frac{dE}{dT} - \frac{1}{G}\frac{dG}{dT}\right) . \tag{8}$$

The present data satisfy eqn. (8) exactly, while the data from ref. 8 give a L. H. S. /R. H. S. ratio of 2. 6. Temperature derivatives of B have apparently not been reported previously. The only previously reported elastic constant at 4 K is Young's modulus;[2] this value, $2.11 \times 10^{11} N/m^2$, is identical to the present value.

This work was supported in part by the Advanced Research Projects Agency of the U. S. Department of Defense. Dr. E. R. Naimon of Dow Chemical (Rocky Flats Division) commented on the manuscript.

References

1. W. F. Weston, H. M. Ledbetter, and E. R. Naimon, Mater. Sci. Engg., forthcoming.

2. Handbook on Materials for Superconducting Machinery, Battelle Metals and Ceramics Information Center, Columbus, Ohio, 1974.

3. F. H. Herbstein, Adv. Phys. 10(1961) 313.

4. H. J. McSkimin, J. Acoust. Soc. Amer. 33 (1961) 12.

5. H. M. Ledbetter and R. P. Reed, J. Phys. Chem. Ref. Data, 2 (1974) 531.

6. Y. P. Varshni, Phys. Rev. B2 (1970) 3952.

7. H. M. Ledbetter, W. F. Weston, and E. R. Naimon, J. Appl. Phys., forthcoming.

8. Huntington Alloys: Inconel Alloy 718, Internat. Nickel Co., Huntington, West Virginia.

Table 1. Composition and properties of the alloy

Chemical Composition, Mill Analysis (wt. pct.)						Hardness (DPH No., 1 kg load)	Mass Density at 294 K (g/cm^3)
Ni	Cr	Fe	Nb+Ta	Mo	Ti	425	8.229
53.73	18.49	17.62	5.17	2.98	1.01		
Al	C	Mn	Si	S	Cu	Condition: As-received; hot-rolled	
0.58	0.05	0.08	0.17	0.007	0.04		

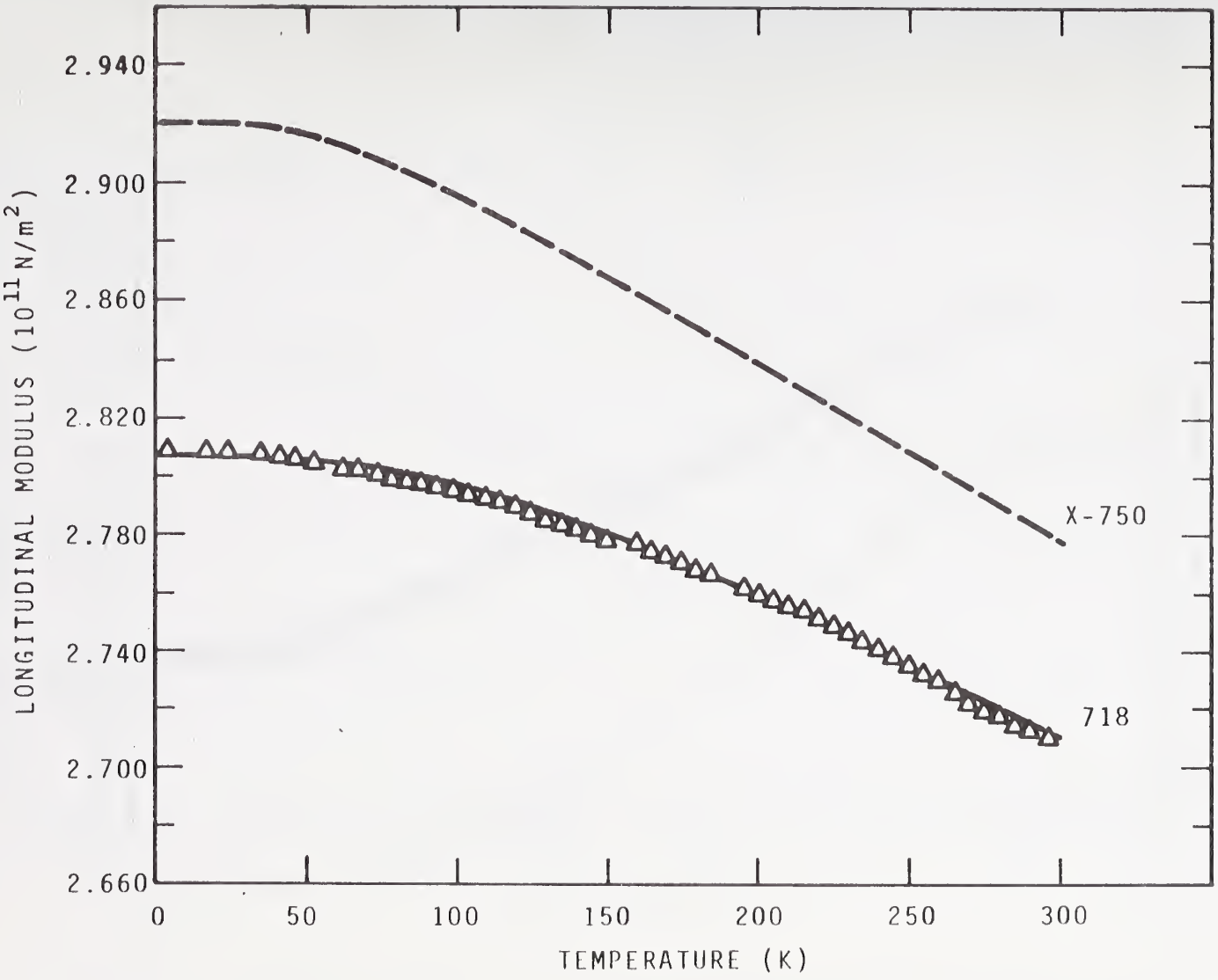

Fig 1. Longitudinal modulus versus temperature for two Inconel alloys

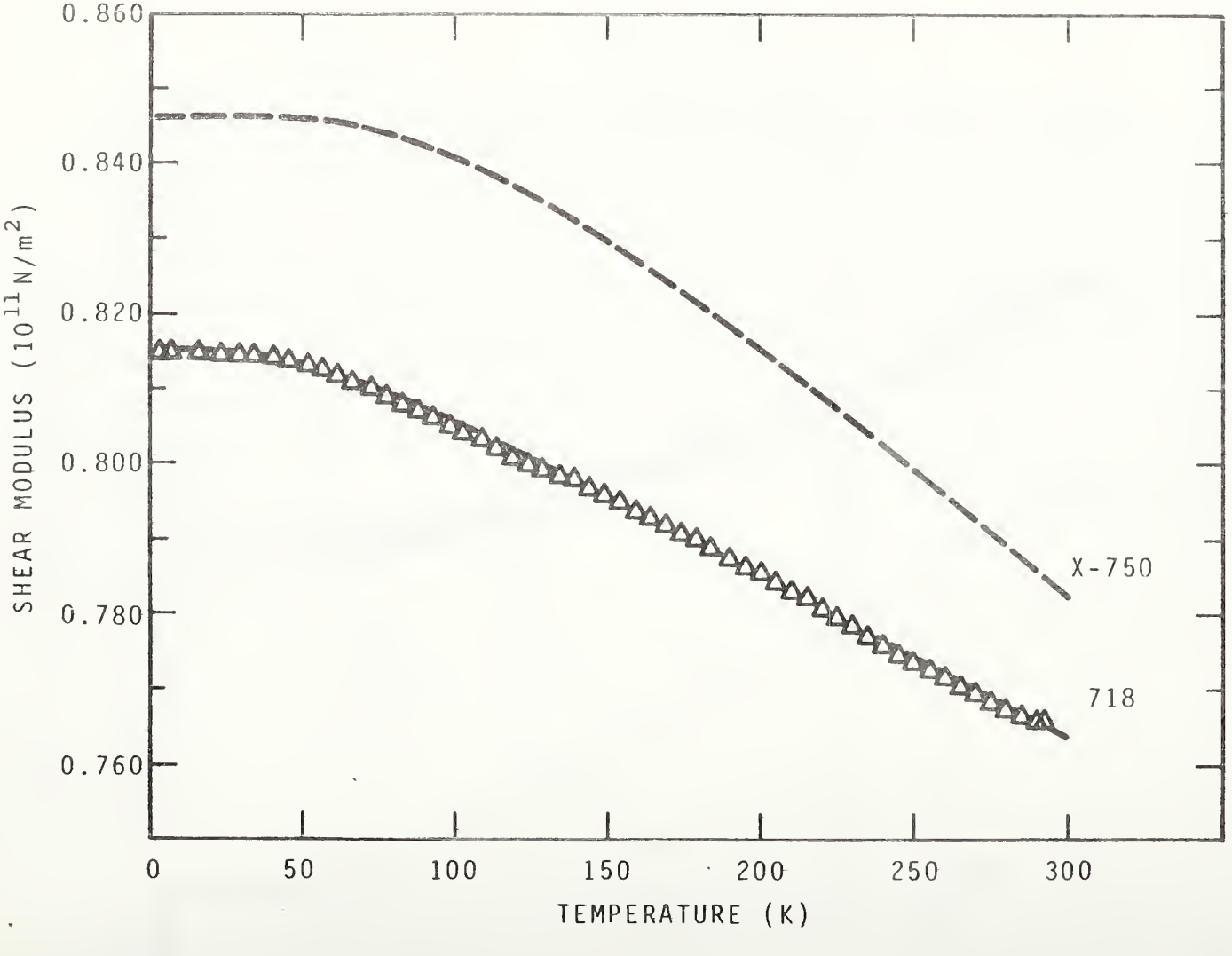

Fig. 2. Transverse (= shear) modulus versus temperature for two Inconel alloys

75X 4829

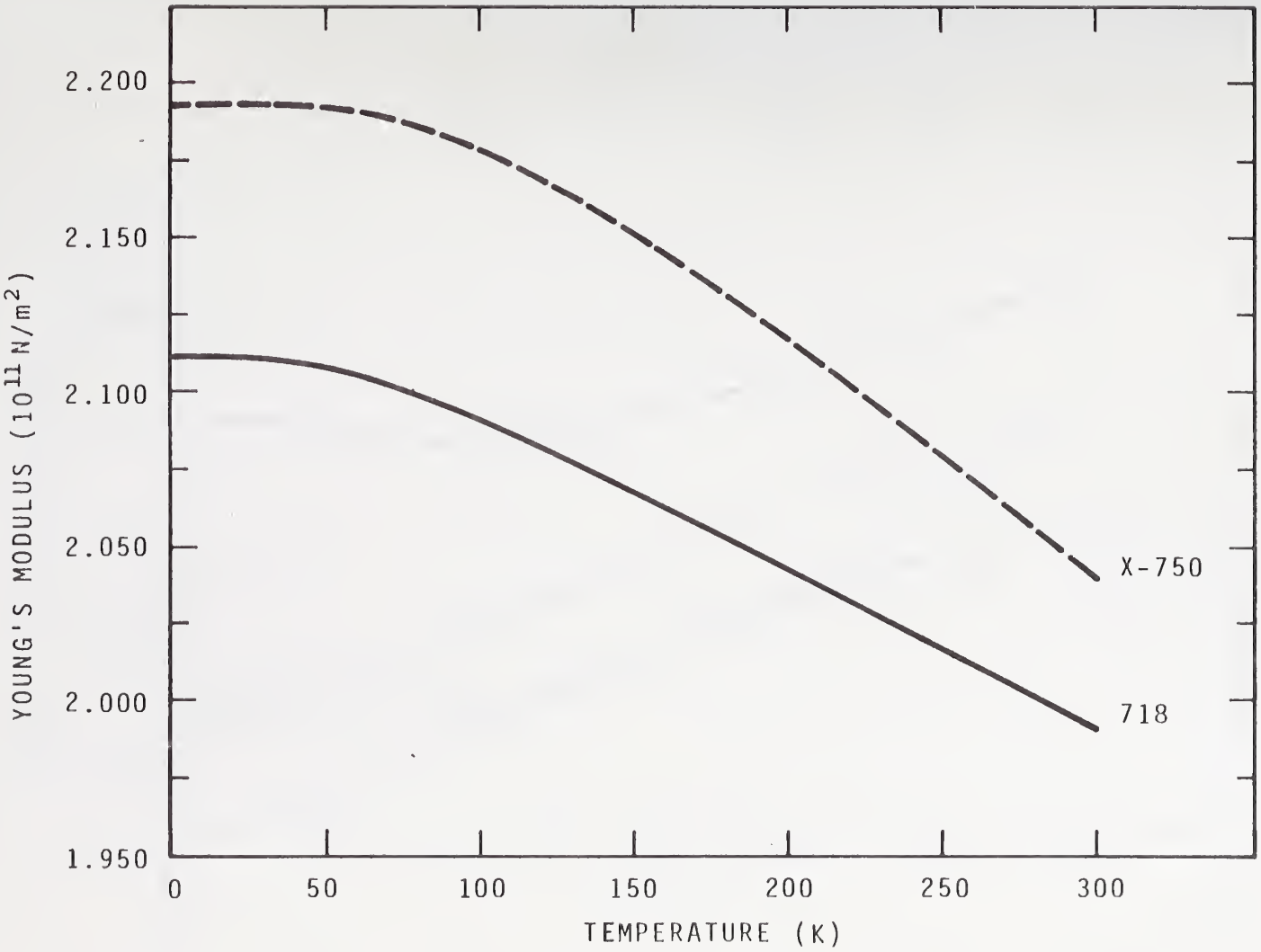

Fig. 3. Young's modulus versus temperature for two Inconel alloys

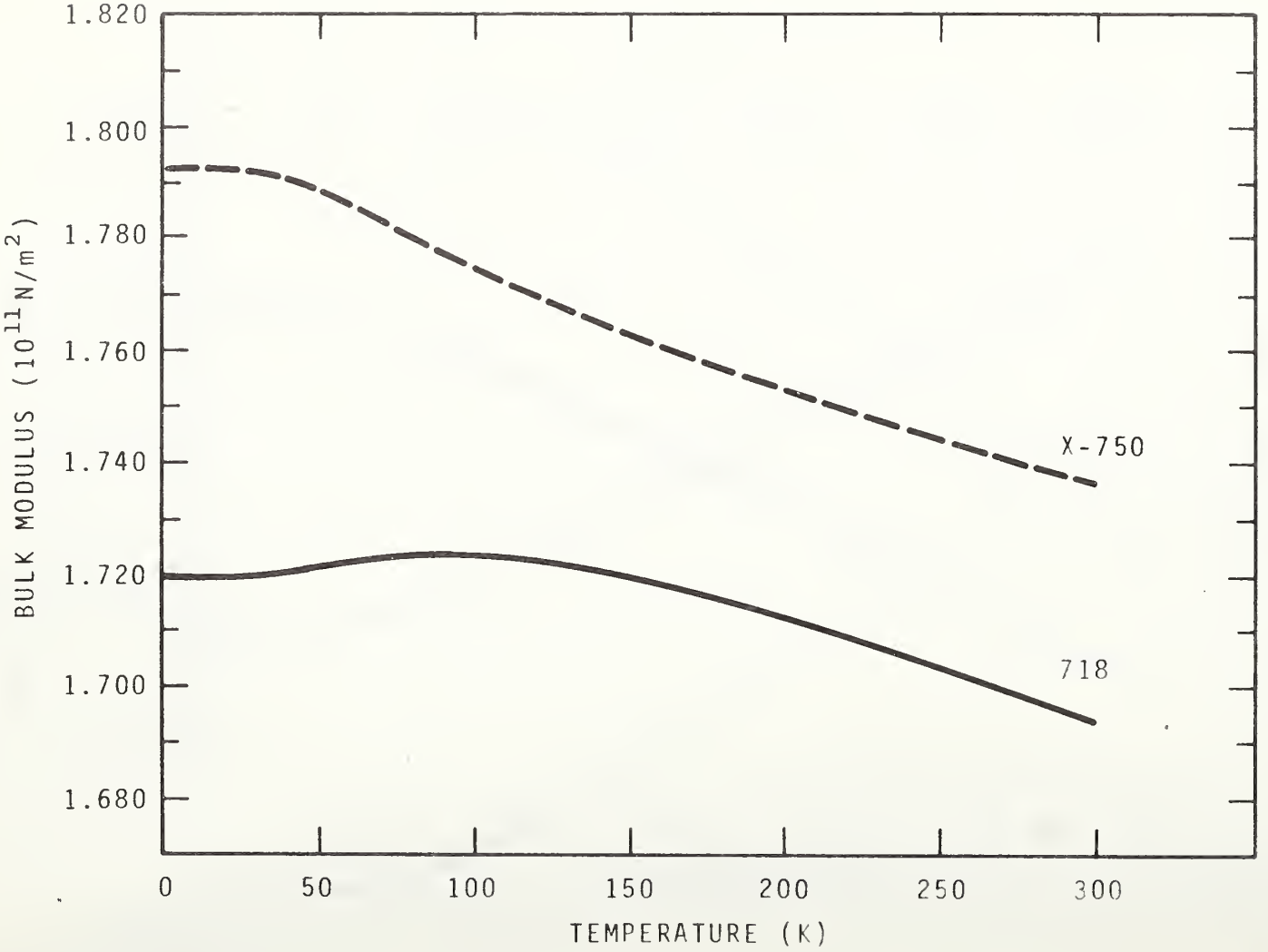

Fig. 4. Bulk modulus (reciprocal compressibility) versus temperature for two Inconel alloys

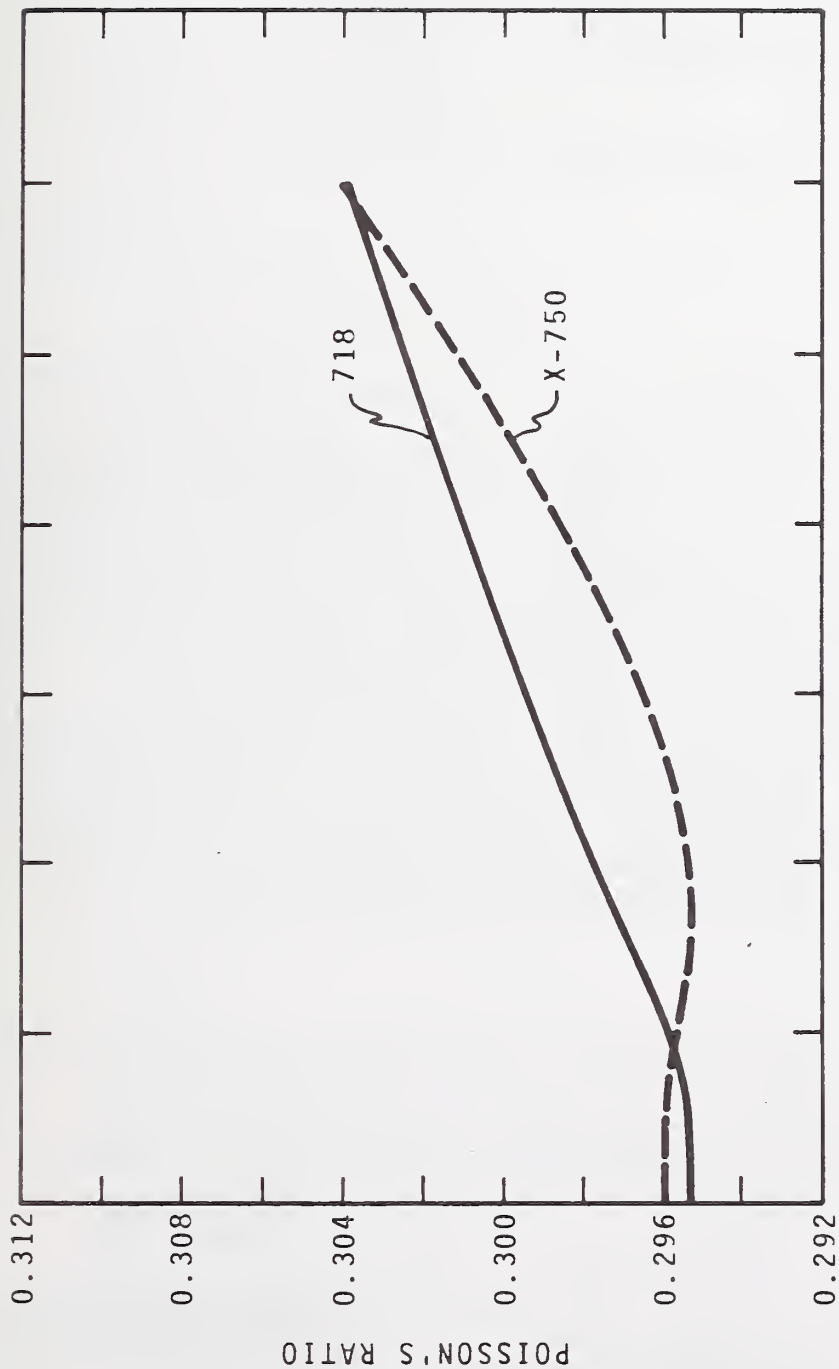

Fig. 5. Poisson's ratio versus temperature for two Inconel alloys

NBS-114A (REV. 7-73)

U.S. DEPT. OF COMM. BIBLIOGRAPHIC DATA SHEET	1. PUBLICATION OR REPORT NO. NBSIR 75-810	2. Gov't Accession No.	3. Recipient's Accession No.

4. TITLE AND SUBTITLE

Semi-Annual Report on Materials Research in Support of Superconducting Machinery

5. Publication Date: April 1975

6. Performing Organization Code: 275.03

7. AUTHOR(S) R. P. Reed, J. G. Hust, M. B. Kasen, H. M. Ledbetter, R. P. Mikesell, R. E. Schramm, L. L. Sparks, R. L. Tobler, and W. F. Weston.

8. Performing Organ. Report No.

9. PERFORMING ORGANIZATION NAME AND ADDRESS

NATIONAL BUREAU OF STANDARDS
DEPARTMENT OF COMMERCE
WASHINGTON, D.C. 20234

10. Project/Task/Work Unit No.: 2756530

11. Contract/Grant No.: ARPA Order No. 2569

12. Sponsoring Organization Name and Complete Address (Street, City, State, ZIP)

Advanced Research Projects Agency
Department of Defense
Washington, D.C.

13. Type of Report & Period Covered

14. Sponsoring Agency Code: ARPA

15. SUPPLEMENTARY NOTES

16. ABSTRACT (A 200-word or less factual summary of most significant information. If document includes a significant bibliography or literature survey, mention it here.)

Results of six months of study on materials in support of superconducting machinery (October 1974 through March 1975) are reported to the sponsor, the Advanced Research Projects Agency of the U.S. Department of Defense. The report is divided into five sections: thermal conductivity, magnetothermal conductivity, fatigue and fracture-toughness properties, properties of advanced composites, and elastic properties. The temperature range 4 to 300 K is covered by the study. Materials studied are either being used or are candidates for use in superconducting machinery and include: aluminum alloys, composites, copper, age-hardened, nickel-base superalloys, stainless steels, and titanium alloys.

Special results of the study include: thermal conductivity data for comparison of the effects of heat treatment on age-hardenable alloys, the first determination of a complete set of elastic constants for a composite at liquid helium temperature, boron-aluminum composite tensile data at 4 K, and a summary of fatigue crack-growth rate behavior at 4 K for a number of different structural alloys. These data provide considerable insight into material characteristics at extremely low temperatures, assisting in material selection and efficient design.

17. KEY WORDS (six to twelve entries; alphabetical order; capitalize only the first letter of the first key word unless a proper name; separated by semicolons)

Composites; elastic properties; fracture; liquid helium; mechanical properties; structural materials; superconducting machinery; thermal conductivity.

18. AVAILABILITY

[X] Unlimited

[ ] For Official Distribution. Do Not Release to NTIS

[ ] Order From Sup. of Doc., U.S. Government Printing Office Washington, D.C. 20402, SD Cat. No. C13

[ ] Order From National Technical Information Service (NTIS) Springfield, Virginia 22151

19. SECURITY CLASS (THIS REPORT): UNCLASSIFIED

21. NO. OF PAGES

20. SECURITY CLASS (THIS PAGE): UNCLASSIFIED

22. Price